Finite element analysis of the design and manufacture of thin-walled pressure vessels used as aerosol cans.

Abdussalam, Ragba Mohamed

University of Wales, Swansea

Finite Element Analysis of the Design and Manufacture of Thin-walled Pressure Vessels used as Aerosol Cans

By

Ragba Mohamed Abdussalam

B. Sc Eng (honours) M. Sc Eng

Thesis submitted to the University of Wales Swansea

For the degree of Doctor of Philosophy, September 2006

Civil and Computational Engineering Centre

School of Engineering

SUMMARY

Thin-walled cylinders are used extensively in the food packaging and cosmetics industries. The cost of material is a major contributor to the overall cost and so improvements in design and manufacturing processes are always being sought. Shape optimisation provides one method for such improvements.

Aluminium aerosol cans are a particular form of thin-walled cylinder with a complex shape consisting of truncated cone top, parallel cylindrical section and inverted dome base. They are manufactured in one piece by a reverse-extrusion process, which produces a vessel with a variable thickness from 0.31 mm in the cylinder up to 1.31 mm in the base for a 53 mm diameter can. During manufacture, packaging and charging, they are subjected to pressure, axial and radial loads and design calculations are generally outside the British and American pressure vessel codes. 'Design-by-test' appears to be the favoured approach. However, a more rigorous approach is needed in order to optimise the designs.

Finite element analysis (FEA) is a powerful tool for predicting stress, strain and displacement behaviour of components and structures. FEA is also used extensively to model manufacturing processes. In this study, elastic and elastic-plastic FEA has been used to develop a thorough understanding of the mechanisms of yielding, 'dome reversal' (an inherent safety feature, where the base suffers elastic-plastic buckling at a pressure below the burst pressure) and collapse due to internal pressure loading and how these are affected by geometry. It has also been used to study the buckling behaviour under compressive axial loading. Furthermore, numerical simulations of the extrusion process (in order to investigate the effects of tool geometry, friction coefficient and boundary conditions) have been undertaken.

Experimental verification of the buckling and collapse behaviours has also been carried out and there is reasonable agreement between the experimental data and the numerical predictions.

Declaration

This work has not previously been accepted in substance for any degree and is not being concurrently submitted in candidature for any degree.

Signature: .....
(Candidate)
Date: 12.12.06

Statement 1

This thesis is the result of my own investigation, except where otherwise stated. Where correction services have been used the extent and nature of the correction is clearly marked in footnote(s). Other sources are acknowledged by footnotes giving explicit references. A bibliography is appended.

Signature: .....
(Candidate)
Date: 12.12.06

Statement 2

I hereby give a full consent for my thesis, if accepted, to be available for photocopying and for the title and summary to be made available to outside organisations.

Signature: .....
(Candidate)
Date: 12.12.06

ACKNOWLEDGEMENT

I would like to express my sincere appreciation and gratitude to my advisor Dr Steve. J. Hardy for his support, guidance, encouragement and his understanding during my research years and I would like to thanks Professor David G.T. Gethin. For his professional guidance advise. Many thanks to Dr. M.K. Pipelzadeh for his technical support in my experimental work; I also want to thanks all the technicians for their assistance and patient during the experimental work.

I feel a deep sense of gratitude for my late parent who formed part of my vision and taught me the good things that really matter in life. The happy memory of my parent still provides a persistent inspiration for my journey in this life. I am grateful to my brother and sisters for all the opportunities they have given me along with their loving support without them, I would not have achieved my success today.

Finally I would like to give a special thanks to my husband for his encouragement, patient and moral support.

In my opinion, doing a PhD is a holy task and this was definitely one of the best decisions of my life, it takes a lot of effort and time but it's worth it.

CONTENTS

Chapter 3 **INTERNAL PRESSURE LOADING**

Chapter 7: **DISCUSSION**

Chapter 8: **CONCLUSIONS AND RECOMMENDATIONS**

LIST OF TABLLES

LIST OF FIGURE

NOMENCLATURE

A_{walls}	Area of can walls
D	The inside diameter
$D^{\bullet}$	Rate of dissipation of energy per unit volume
D_d	Dissipation energy
E	Young's modulus (MPa)
E_0	True modulus of elasticity
E_i	Elastic modulus of each element
FE	Finite element
FEA	Finite element analysis
F(x)	Objective function
g	Acceleration due to gravity
g_i	Inequality constraints
GNL	Geometric non- linearity
h_j	Equality constraints
I	Second Moment of Area
i	Current iteration number
L	Can length
LF	Load Factor
P	Internal pressure
P_{burst}	Burst pressure of the can
P_y	Yield pressure
P_u	Upper bound limit load
P_l	Lower bound limit load
P_c	Collapse pressure
r	Punch head radius, Radial co-ordinate direction, Can radius
r_i	Inner can radius
r_o	Outer can radius
t	Can wall thickness

$u^{\bullet}$	Displacement rates
U_d	Strain energy
σ_1	Longitudinal stress
σ_2	Circumferential stress
σ_3	Radial stress
σ_{char}	Characteristic stress within the element
σ_e	Converged stress
σ_{eq}	Equivalent stress
$(\sigma_{eq})nom$	Nominal stress
$\sigma^{\bullet}$	Stress increment
α	Arbitrary constant
σ_L	Limiting stress
σ_{UTS}	Ultimate tensile stress of aluminium
σ_{Yield}	Yield stress
σ_{cr}	Critical stress
ε	Strain
$\varepsilon^{\bullet}$	Strain increment
β	The constant of proportionality
$\dot{I}_{eq}$	Elastic stress concentration factor
μ	Coefficient of friction
Σ	Sum

Subscripts

Char	Characteristic
d	Associated with the arbitrary load(set) P_d
e	Elastic
$_{eq}$	Equivalent
I	Iteration number
L	Lower bound
r	Resident

U	Upper bound
y	Yield
1, 2, 3	Principle values

Superscript

*	Incomplete solution

Abbreviations

EIH	Elastic isotropic hardening
EKH	Elastic kinematic hardening
EPP	Elastic perfectly plastic
K_t	Stress concentration factor

Chapter 1

INTRODUCTION

1.1 Background

The use of thin-walled cylinders in the food packaging and cosmetics industries is extensive and the demand for steel and aluminium containers is such that extremely high-volume manufacturing processes have been developed over the past two decades. The cost of material is a major contributing factor to the overall cost of the container and so improvements in design and manufacturing processes are always being sought.

The early cans were hand-made by practiced artisans who could produce up to six each hour. The process was laborious and required considerable skill and strength. The craftsman would cut a rectangular body and two circular pieces (for the lids) from a sheet of tinned iron. The rectangular body would be bent around a cylindrical mould and the sides soldered together before affixing the ends. But the can opener was not invented until 1930 [1].

This project continues on from work carried out by Patten [2] in conjunction with a major manufacturer of aluminium aerosol cans for the cosmetics industry. The manufacturing process for these cans is described in detail in Chapter 2 but, in brief, they are manufactured from a cylindrical billet of almost pure aluminium using a 'back-extrusion' process. Prior to Patten's work, 'design by test' was the recognised method of proving the designs and it was acknowledged that certain regions of the can cross-section were 'over-designed' and that potential savings were to be made.

Patten carried out an analytical study of the manufacturing process and developed a constant volume model to predict the thickness profile based on billet, punch and die dimensions. He also carried out finite element analyses in order to identify regions of the cross-section where stresses were low and hence potential material savings could be made.

An aerosol can is a thin-walled cylinder with a complex shape (see Section 1.2) which limits the amount of 'design' that can be undertaken using simple thin cylinder equations to estimating the burst pressure of the can. In reality, an aerosol can is subjected to a number of loading patterns including internal pressure, axial and radial loading and although the behaviour of a plain cylinder with constant wall thickness is well understood, very little research has been conducted into the design of these more complex shapes. What is required is an analysis method that can be used to accurately predict the elastic and elastic-plastic stresses and deformation of these cylinders due to internal pressure, axial and radial loading, as well as providing details of the modes and behaviour during failure, including buckling. Finite element analysis (FEA) is such a powerful and comprehensive analysis method and has been used comprehensively in this project, supported by experimental validation.

1.2 Thin walled pressure vessels

A pressure vessel is a closed structure containing liquids or gases under pressure. An aerosol cans are one example of a cylindrical pressure vessel categorised as a shell structure due to its thin wall in comparison to its radius and length. The current practice of pressure vessel design by analysis is most commonly based on elastic finite element analysis and the rules defined in codes such as BS5500 (the British

standard for unfired fusion welded pressure vessels) [3] and Section VIII of the ASME Boiler and Pressure Vessel Code [4]. This approach gives rise to two significant problems in the design: elastic analysis is used to assess possible inelastic failure mechanisms and the design by analysis rules is essentially based on shell theory. These problems introduce the concept of stress categories into the design procedure. Some designers argued that plastic analysis should be the preferred method for assessing failure modes associated with gross distortion due to a single application of pressure. Plastic and limit analysis can be performed using non-linear finite element analysis, which is much more difficult to perform than elastic analysis.

Furthermore, an aerosol can has additional complexities due to its shape which, for a one-piece aluminium can, consists of an inverted base, a nominally constant-thickness parallel cylinder and a sloping top, as shown in Figure 1.1. The nature of the manufacturing process is such that there is a significant variation in thickness, particularly between the base and cylinder, which limits the usefulness of simple design rules. The thickness profile of an aerosol can is such that a number of design requirements have to be met:

Cylinder
- must be thick enough to withstand bursting due to overpressure
- must be thick enough to withstand radial buckling during bundling/packaging
- must be thick enough to avoid axial buckling/collapse under compressive axial load during manufacture and charging

Base
- must be thick enough to withstand bursting due to overpressure

- must be thin enough to facilitate 'dome reversal' at a specified pressure below the burst pressure

Top - must be thick enough to withstand bursting due to overpressure

- must be thick enough to avoid collapse under compressive axial load during manufacture and charging

and hence the design of such components presents some interesting problems and complex balancing of structural integrity and manufacturing economy, for which little detailed analysis has previously been undertaken.

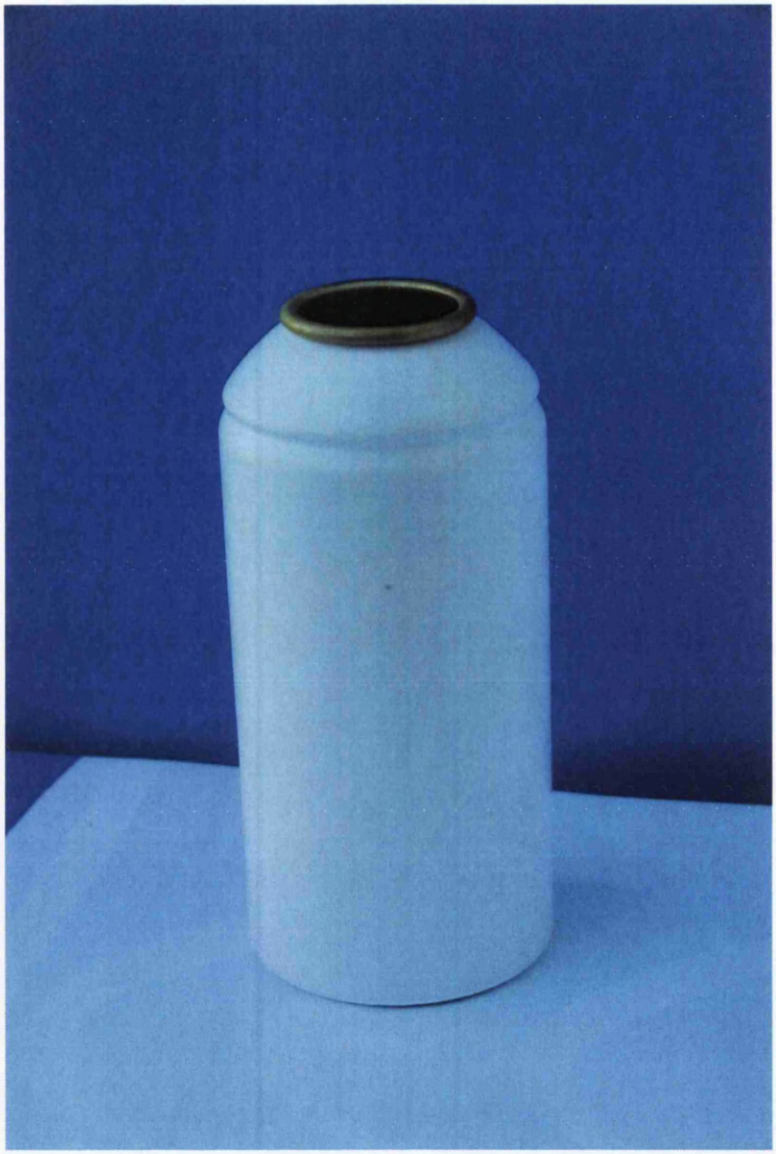

Figure 1.1: Typical aluminium aerosol can

1.3 Aims and objectives of the research

The aims of this research project have been to investigate the factors influencing the characteristic mechanical behaviour of these thin-walled pressure vessels subjected to internal pressure and axial loading and to provide a reliable analysis tool for future optimisation studies. Included in this has been an investigation into the modelling of the extrusion process by which such vessels are manufactured and an investigation

The aims of this research project have been to investigate the factors influencing the characteristic mechanical behaviour of these thin-walled pressure vessels subjected to internal pressure and axial loading and to provide a reliable analysis tool for future optimisation studies. Included in this has been an investigation into the modelling of the extrusion process by which such vessels are manufactured and an investigation. The numerical analysis used the ELFEN Non-linear finite element program, which is an established commercial package [5] apart from the development of (FE) analysis method.

The specific objectives are:

- to further the understanding of the process of dome reversal (elastic-plastic buckling) of thin-walled cylinders with inverted bases subjected to internal pressure

- to investigate the application of the elastic compensation method for estimating upper and lower bound pressure loads

- to accurately predict axial buckling loads and buckling modes using experimental results for comparison

- to use finite element analysis to model the back-extrusion process and compare the predictions with analytical solutions and experimental evidence

- to carry out a preliminary investigation into the optimisation of the can profile

1.4 Structure of thesis

This thesis consists of eight main chapters:

Chapter 1 has provided an introduction to the project, stating the aims and objectives of the research.

Chapter 2 reviews the background information and literature relevant to all areas of the project.

In **Chapter 3**, using constant thickness models and a realistic thickness profile for an axisymmetric and a full three-dimensional model, elastic and elastic plastic finite element analysis predictions for the vessel subjected to internal pressure are presented. The application of the elastic compensation method to provide upper and lower bound pressure estimates is also investigated.

The analyses in Chapter 3 are extended in **Chapter 4** to predict the buckling and collapse behaviour under axial compressive loading. Experimental tests to validate the predictions are also described.

Chapter 5 describes the modelling of the two-stage extrusion process, using billet, tool and die data from a local manufacturer, have been considered and comparisons with experimental measurements.

Chapter 6 describes a preliminary investigation into the optimisation of the thickness profile, as it is anticipated that material savings are possible, particularly in the base region. The results from a reduced thickness model are presented and an

introduction to structured optimisation, using the DOT optimisation program, is described.

Chapter 7 presents an overall discussion of the research findings and conclusions and recommendations for further study are provided in **Chapter 8**.

The appendices contain information not included in the main body of the thesis.

Chapter two

GENERAL BACKGROUND AND LITERATURE REVIEW

2.1 Introduction

This Chapter reviews the background information and the appropriate literature relevant to this research work on one-piece aerosol cans, which are a specific form of thin-walled pressure vessel. It starts by considering the design and manufacture of these pressure vessels, the basic concepts of elasticity and plasticity (with particular reference to finite element analysis) and appropriate theory for thin-walled cylinders subjected to internal pressure or axial loading (i.e. buckling loading). The relevant British and American standards for pressure vessel design are also reviewed. Also, approximate methods of determining pressure vessel limit loads, in particular the elastic compensation method, are reviewed.

An important element of the research has been the modelling of the extrusion process using finite element analysis and this subject is reviewed in Section 2.10. An initial investigation into the optimisation of a typical vessel profile is described in Chapter 6 and relevant background information is provided here. A considerable amount of research has already been carried out in the field of extrusion and optimisation of aerosol cans and this is discussed in Sections 2.10 and 2.11.

2.2 The design and manufacture of aerosol cans

Aerosol cans are generally made of tin-plated steel (normally constructed from three components; the base, the cylinder and the top, which are joined) or aluminium (normally produced in one piece [6] from a curved billet, using the 'back extrusion' process – see Section 2.10). Examples of aerosol cans are shown in Figure 2.1.

Figure 2.1: Aerosol cans [6]

The thickness of the tinplate steel varies, depending on the size, the pressure of the contents and the location (i.e. cylinder or ends). For the cylindrical section, the thickness is typically in the range 0.18 mm to 0.25 mm whereas the tops and bottoms are made from material that is typically between 0.28 mm and 0.43 mm thick [6]. Aluminium cans produced by the back-extrusion process have a typical thickness variation of 0.31 mm to 0.41 mm in the cylindrical section and 0.7 mm to 1.31 mm at the ends [6].

An aerosol can is a pressurised system and, as such, is governed by legislation. This not only covers the design and manufacture of the empty can, but also its subsequent filling [6].

Legislation governs the amount of product that may be contained in an aerosol can since, for safety reasons there must always be some space in the can, which does not contain liquid. The propellant occupies this empty space, which is greater when a compressed gas, such as air, is used since it operates at higher pressures than those for liquefied propellants.

2.2.1 Top and valves

A typical top with valve is shown in Figure 2.2. The components are:

- Valve Cup: - typically constructed from tinplate steel or aluminium
- Outer Gasket: - this is the seal between the valve cup and the aerosol can
- Valve Housing: - contains the valve stem, spring and inner gasket
- Valve Stem: - the tap through which the product flows
- Inner Gasket: - covers the hole in the valve stem
- Valve Spring: - usually stainless steel
- Dip Tube: -allows the liquid to enter the valve
- Actuator: - fitted to the top of the valve stem.

When the actuator (red in the figure) is depressed it pushes the valve stem through the inner gasket, and the hole is uncovered, allowing liquid to pass through the valve and into the actuator and out to atmosphere.

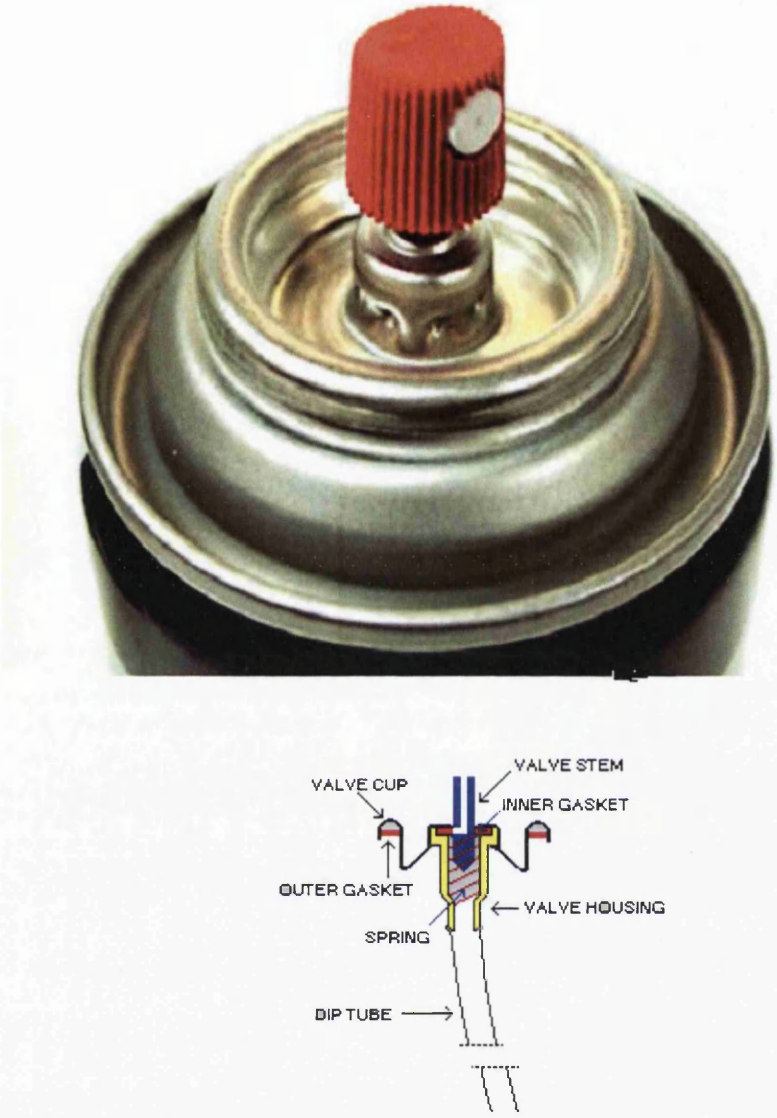

Figure 2.2: Aerosol can valve [6]

Figure 2.2 shows the top of typical tinplated steel can which is pressed from flat sheet. A typical one-piece aluminium top, shown in Figure 2.3, is less complex and is often a simple tapered section with central rim into which a valve system insert is added at a later stage.

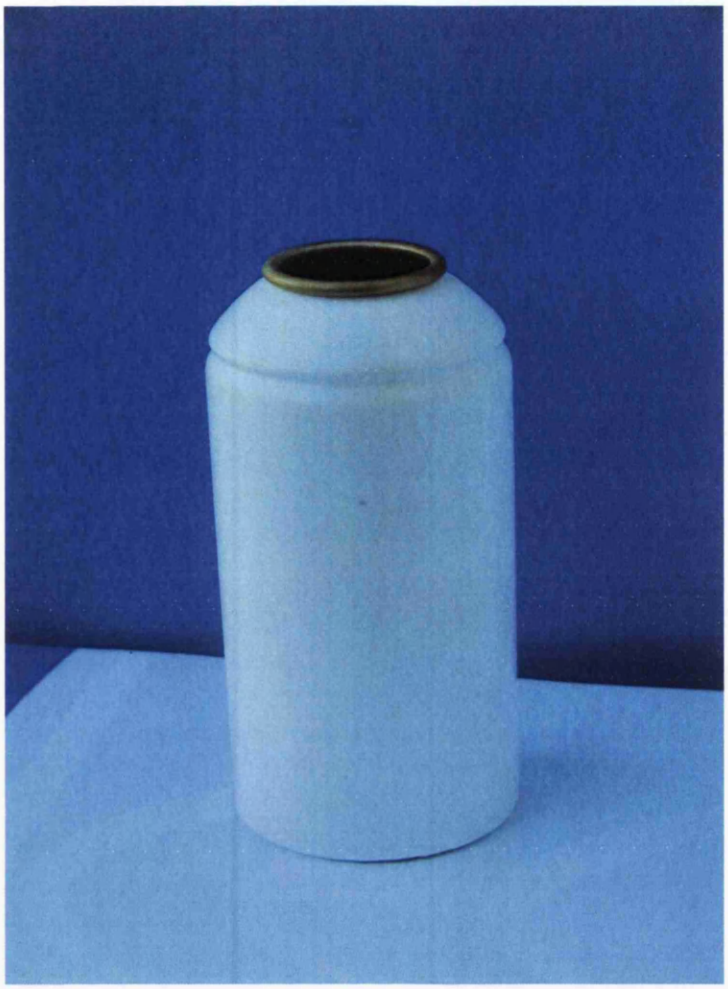

Figure 2.3: Aluminium aerosol can valve

2.2.2 Main body

The main body of a tinplated steel can is a constant-thickness rolled section, which is joined using the welded process. And the round end pieces (pressed from another sheet of steel) are then fitted by a clinching process known as double seaming-welded process [7]. Alternatively, the back-extrusion process for aluminium cans produces a thickness profile in the cylinder, which is discussed in more detail in Chapter 5.

2.2.3 Base

Most cans have bases that curve inwards and this shape strengthens the structure of the can. The inverted base design is also an inherent safety feature as it provides a natural pressure release mechanism in the event of a pressure overload, with 'dome reversal' (which is a form of elastic-plastic buckling) of the base occurring. This sudden change in geometry (a) results in an immediate fall in pressure and (b) provides a visual indication, since the can is no longer stable. In order for this pressure release mechanism to be effective, the design must be such that 'dome reversal' occurs at a pressure lower than the burst pressure [2].

Also, the last bit of the product collects in the small area around the edges of the can and this makes it easier to empty almost all of the liquid as shown in Figure 2.4.

Figure 2.4: Aerosol can bottom [6]

The bottom dome-shape of the can base is produced by the forming process. This is produced by supporting the can on a mandrel and forming the can base with a punch as shown in Figure 2.5. This process has a direct effect on the pressure that the can will withstand. The bottom forming process increases the can strength and provides a

safety feature that is required according to customer specifications [2] This states that the can base must pop out at a pressure 20% lower than the can burst pressure.

The formation of the base can take place either before or after the can is decorated and the support provided to the can during base formation is different for the two cases. The two types of formation described and obtained by using finite element method in Chapter five.

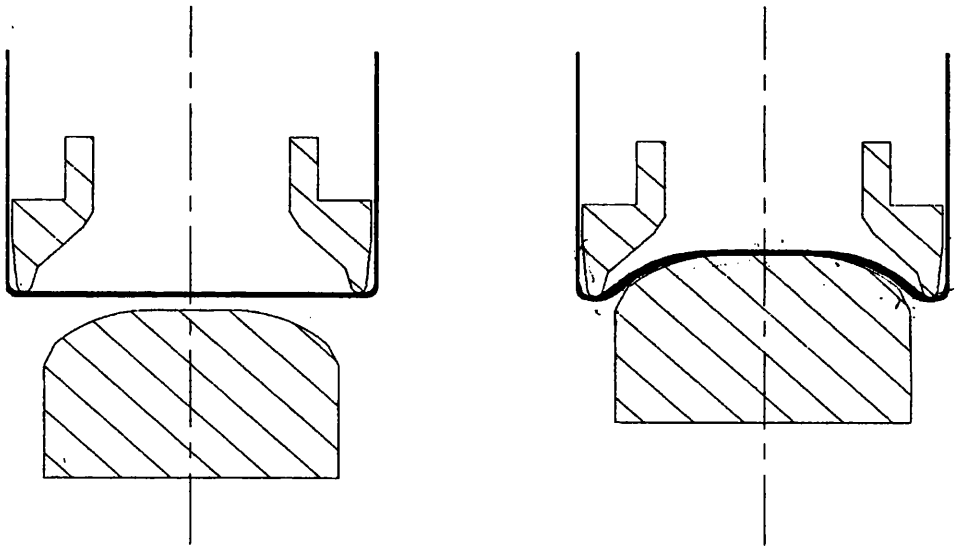

Figure 2.5: Bottom forming process

2.2.4 Principles of operation

The basic principle of an aerosol can is very simple: One fluid stored under high pressure is used to propel another fluid out of the can [8]:

- A fluid is any substance made up of free-flowing particles. This includes substances in a liquid state, such as the water from a faucet, as well as substances in a gaseous state, such as the air in the atmosphere.

- The particles in a liquid are loosely bound together, but they move about with relative freedom. Since the particles are bound together, a liquid at a constant temperature has a fixed volume.
- If the applied energy to a liquid is high enough (e.g. by heating it), the particles will vibrate so much that they break free of the forces that bind them together. The liquid changes into a gas. This is the boiling process, and the temperature at which it occurs is referred to as a substance's boiling point.

The force of individual moving particles in a gas can add up to considerable pressure. An aerosol contains two essential components (see Figure 2.6): -

- The product, in the form of a liquid, emulsion or suspension
- The propellant, which can be a liquefied or compressed gas

Liquefied propellants are gases that exist as liquids under pressure. Because the aerosol is under pressure, the propellant exists mainly as a liquid, but it will also be in the headspace as a gas. As the product is used up, some of the liquid propellant turns to gas and keeps the head space full of gas. In this way the pressure in the can remains essentially constant and the spray performance is maintained through the life of the aerosol. Compressed gas propellants occupy the headspace above the liquid in the can. When the aerosol valve is opened the gas pushes the liquid out of the can. The mass of gas in the headspace remains the same but it has more space, and as a result the pressure will drop during the life of the can.

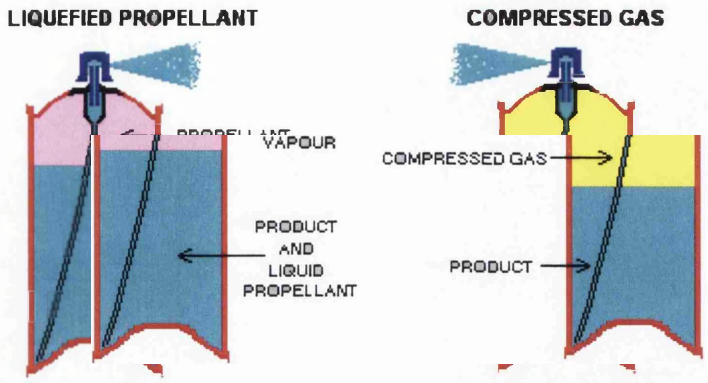

Figure 2.6: Liquid and compressed propellant [8]

2.2.5 Design

The integrity of the can is the key condition, since a failure (e.g. burst or leakage) could have catastrophic consequences. For a one-piece aluminium can, the thickness profile is the principle design consideration.

At the same time, overall weight should be minimised in order to keep material costs low (see Chapter 6). Experimental results from burst tests are discussed in Section 3.6.

2.2.5.1 Internal pressure

In practice, the customer generally specifies the minimum internal pressure, without showing any visible signs of deformation or failure. For the aluminium can geometries used in this project, internal pressures of 12, 15 or 18 bar, depending on diameter, have been adopted.

2.2.5.2 Axial loading

The aerosol cans are required to support an axial load that is applied when the valves are inserted as part of the filling and charging process (see Figure 2.7). The cans must support this load and show no visible signs of deformation (buckling). Any deformation of the can will take the form of flattening (collapse) of the top, as shown in Figure 2.8.

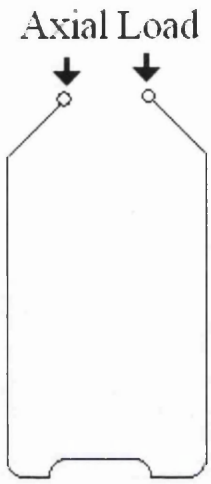

Figure 2.7: Axial loading during valve insertion and filling

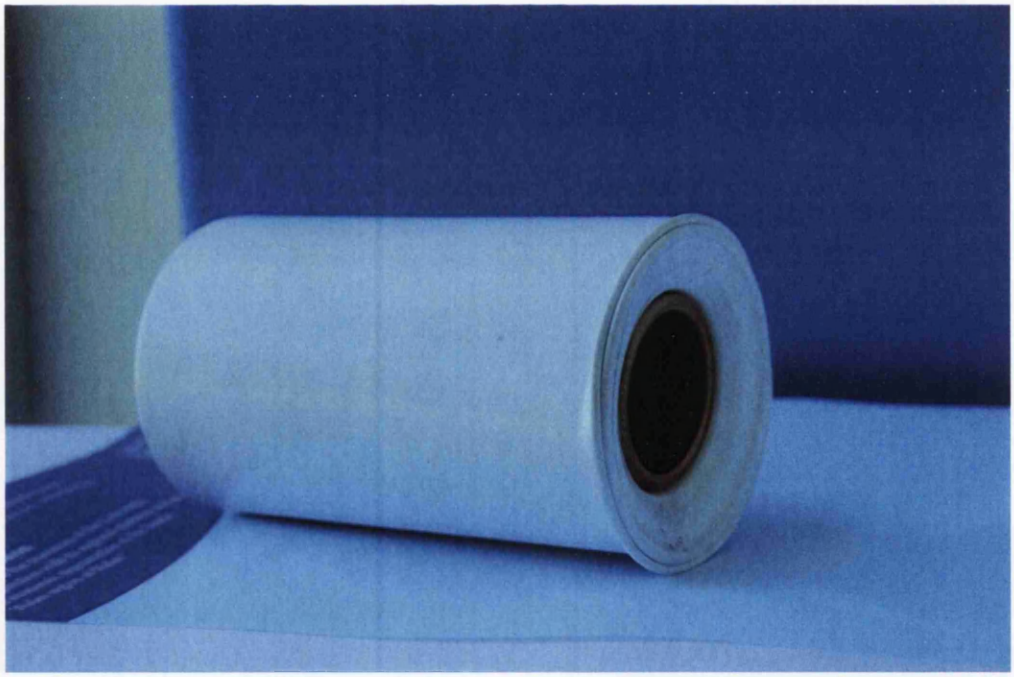

Figure 2.8: The buckling of the can top

Also, during the forming of the top, the plain can rim is also subjected to an axial force which may cause the cylindrical section to buckle, as shown in Figure 2.9.

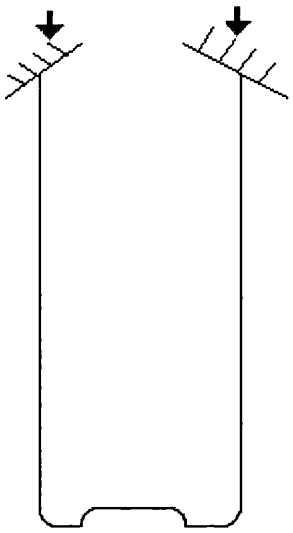

Figure 2.9: Axial loading during neck forming

2.2.5.3 Dome reversal of the inverted base

As previously stated, the dome reversal (or plastic buckling or plastic snap-through) of the inverted base is an important safety feature and design consideration. The pressure-deformation response of an aerosol can is carefully monitored (by experiment) to ensure that this plastic buckling occurs at a pressure that is at least 20% below the corresponding burst pressure for that geometry [2]. This requires a specific thickness profile, which must be controlled closely.

2.2.6 Manufacture

The production of aluminium cans starts off in the form of aluminium curved billets. The process is shown diagrammatically in Figure 2.10 which is taken from [2]. Firstly the billet is coated in dry lubricant (graphite powder) and secondly the back extrusion process forms the basic can shape with a flat base. By using tapered extrusion dies the extrusion process allows the wall thickness to vary from the top of

the can to the bottom. The cylinder is then coated internally with a protective lacquer, which is cured in an oven. The base of the can is formed, either before or after decoration and drying ovens, in the bottom-forming machine. A series of dies, for the purpose of producing the shoulder and neck on the extruded cans, are designed to work within a tolerance range of ±0.01mm on the thickness of the top of the extruded can walls. This means that any changes to the thickness of the upper third of the cans may require a complete new set of tooling for the necking machine.

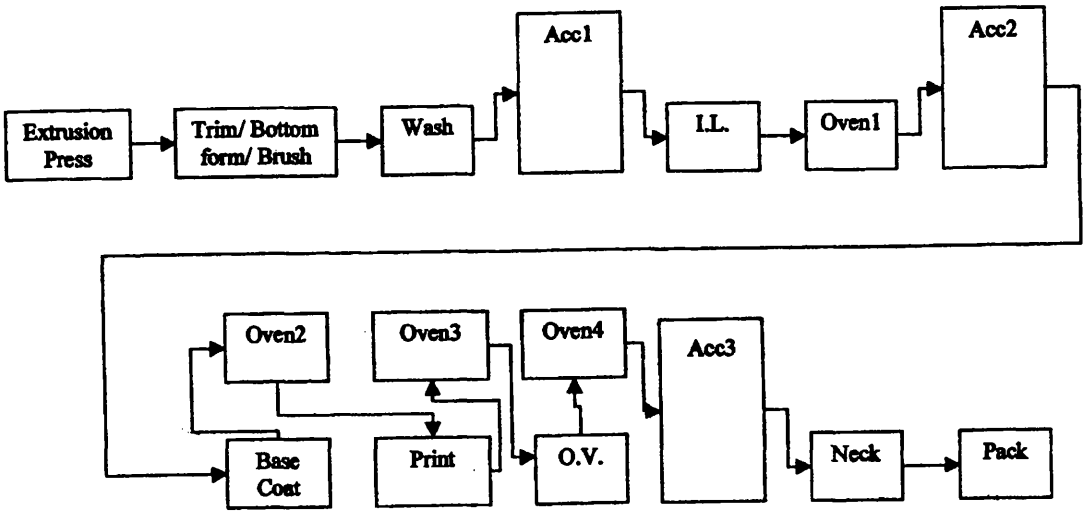

Acc = Accumulator, LL, = Inside lining, O.V = Over varnish

Figure 2.10: Schematic diagram of aerosol can production line [2]

2.3 Basic concepts of elasticity and plasticity

2.3.1 Elasticity

For a perfectly elastic material, the removal of the loads returns the component to its original form with no permanent deformation. Most of the equations used in design engineering are derived from such an assumption, where stress and strain have a

linear relationship defined by Hooke's law, [9] which is independent of time and load history. This relationship can be expressed in a generalized form as:

$$[\sigma] = [D][\varepsilon] \qquad \ldots (2.1)$$

where $[\sigma]$ is the stress matrix, $[\varepsilon]$ is the strain matrix and $[D]$ is the elasticity matrix

For a generalised three-dimensional state-of-stress:

$$[\sigma] = \begin{bmatrix} \sigma_{xx} \\ \sigma_{yy} \\ \sigma_{zz} \\ \tau_{xy} \\ \tau_{yz} \\ \tau_{xz} \end{bmatrix} \quad \textit{and} \quad [\varepsilon] = \begin{bmatrix} \varepsilon_{xx} \\ \varepsilon_{yy} \\ \varepsilon_{zz} \\ \gamma_{xy} \\ \gamma_{yz} \\ \gamma_{xz} \end{bmatrix} \qquad \ldots (2.2)$$

where σ_{xx} , σ_{yy} and σ_{zz} are the normal stresses and τ_{xy}, τ_{yz} and τ_{xz} are the shear stress also ε_{xx}, ε_{yy} and ε_{zz} are the normal strains and γ_{xy}, γ_{yz} and γ_{xz} are the shear strains

For an isotropic material with a two-dimensional plane stress assumption:

$$[D] = \frac{E}{1-\upsilon^2} \begin{bmatrix} 1 & \upsilon & 0 \\ \upsilon & 1 & 0 \\ 0 & 0 & \frac{1-\upsilon}{2} \end{bmatrix} \qquad \ldots (2.3)$$

where E is Young's modulus and ν is Poisson's ratio. Similarly, for plane strain,

$$[D] = \frac{E(1-\upsilon)}{1-\upsilon(1-2\upsilon)} \begin{bmatrix} 1 & \frac{\upsilon}{1-\upsilon} & 0 \\ \frac{\upsilon}{1-\upsilon} & 1 & 0 \\ 0 & 0 & \frac{1-2\upsilon}{2(1-\upsilon)} \end{bmatrix} \quad \ldots (2.4)$$

For an axisymmetric analysis:

$$[\sigma] = \begin{bmatrix} \sigma_z \\ \sigma_r \\ \sigma_\theta \\ \tau_{rz} \end{bmatrix} \quad \ldots (2.5)$$

$$[\varepsilon] = \begin{bmatrix} \varepsilon_z \\ \varepsilon_r \\ \varepsilon_\theta \\ \gamma_{rz} \end{bmatrix} \quad \ldots (2.6)$$

$$[D] = \frac{E(1-\upsilon)}{1-\upsilon(1-2\upsilon)} \begin{bmatrix} 1 & \frac{\upsilon}{1-\upsilon} & \frac{\upsilon}{1-\upsilon} \\ \frac{\upsilon}{1-\upsilon} & 1 & \frac{\upsilon}{1-\upsilon} \\ \frac{\upsilon}{1-\upsilon} & \frac{\upsilon}{1-\upsilon} & 1 \end{bmatrix} \quad \ldots (2.7)$$

2.3.2 Plasticity

Figure 2.11 shows a typical stress-strain curve for simple one-dimensional tension (or compression) for an elastic-plastic material [10]. The stress at point A, which separates the curve into an elastic portion and a plastic portion, is defined as the yield

stress σ_Y. Because the yield stress is not always clearly identified, it is often taken as the limit of proportionality.

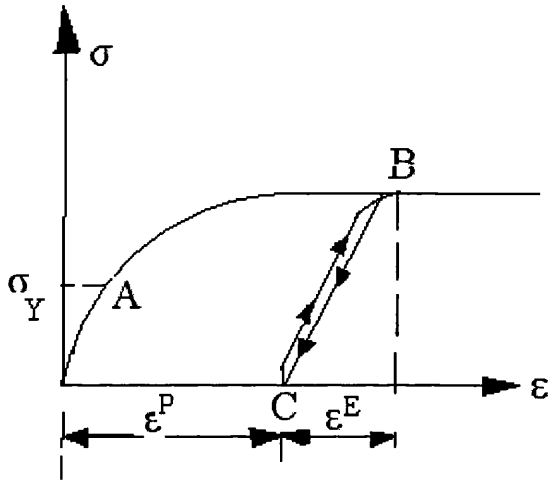

Figure 2.11: Stress-strain curve for a simple one-dimensional tension (or compression)

The general theory of plasticity requires the following:

i. A yield criterion, which defines the onset of plastic deformation under multi-axial conditions of stress;

ii. A flow rule, which relates the stress to the increments of plastic strain;

iii. A hardening rule, which describes the work hardening of the material and how the yield condition changes with progressive of plastic deformation. The hardening rule also describes the material behaviour under cyclic loading conditions;

2.3.2.1 Yield criterion

The purpose of the yield criterion is to define the point of yielding for a material subjected to general 3-dimensional multi-axial stress system [16]. In the case of uni-axial loading, yielding occurs when the axial stress reaches the uni-axial yield stress for the material. However, for multi-axial loading, the effect of all stress components must be considered. Yielding of an elastic-plastic material is defined by a scalar function termed the yield function F, which is a function of the stress invariants. The yield function is written in the form, which leads to the conditions.

$F < 0$ for elastic behaviour

$F = 0$ for initial yielding and plastic

The most commonly used criterion for metals and that adopted by most finite element programs (including the program used in this work) is the von Mises effective stress criterion [12]. As early as 1913, von Mises suggested a yield criterion of this type, which is applicable to metal plasticity. The yield criterion has been verified by a series of experiments mostly on thin metal tubes under biaxial stress states. According to von Mises:

$$F = \frac{1}{2}\{(\sigma_1 - \sigma_2)^2 + (\sigma_2 - \sigma_3)^2 + (\sigma_3 - \sigma_1)^2\} - (\sigma_y)^2 \qquad \ldots(2.8)$$

where σ_y is the uni-axial yield stress of the material. Yielding is assumed to be unaffected by the hydrostatic stress. Thus, yielding occurs when F = 0 and

$$\sigma_{eff} = \sigma_y \qquad \ldots (2.9)$$

where σ_{eff} is an effective stress for a mult-iaxial state-of-stress.

$$\frac{1}{\sqrt{2}}\sqrt{[(\sigma_1-\sigma_2)^2+(\sigma_2-\sigma_3)^2+(\sigma_3-\sigma_1)^2]} \quad \ldots (2.10)$$

In principal stress space, the yield condition F (σ_1, σ_2, σ_3) = 0 defines a yield surface. The von Mises yield criteria is independent of the hydrostatic stress and the infinitely long cylinder shown in Figure 2.12 defines its surface. The axis of the cylinder makes equal angles with the coordinate axes. Stress points, which lie inside the cylindrical yield surface, are associated with elastic stress states whereas those that lie on the surface represent yielding . The π-plane is defined by:

$$\sigma_1 + \sigma_2 + \sigma_3 = 0 \quad \ldots (2.11)$$

and the intersection of the π-plane with the von Mises yield surface, termed the yield curve, appears as a circle.

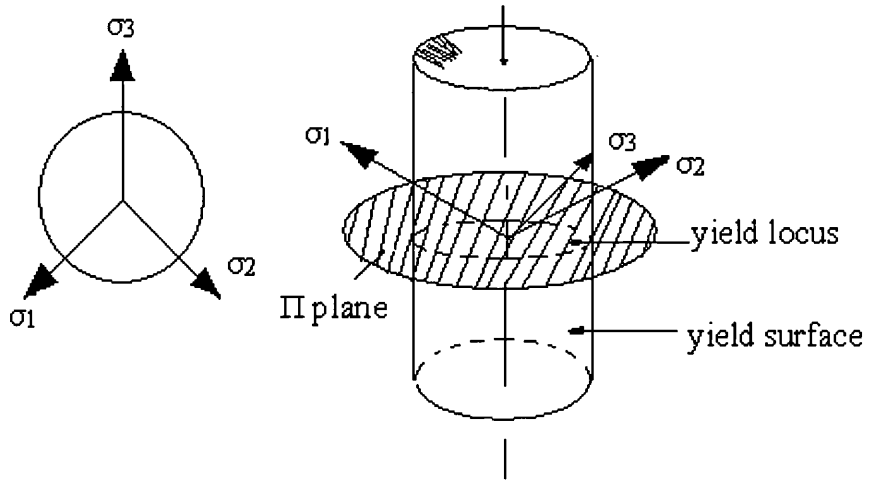

Figure 2.12: Projection of the von Mises yield surface onto the π-plane

2.3.2.2 Flow rule (normality principle)

A flow rule defines the relationship between the stress components and the corresponding plastic strain components after initial yielding. The direction of the plastic strain components is also defined through the flow rule by the plastic potentials expressed as follows [12]:

$$\{d\varepsilon^{pl}\} = \mathrm{d}\lambda \{ \frac{\partial f\{\sigma\}}{\partial\{\sigma\}} \} \quad \ldots (2.12)$$

Associating equation (2.12) with particular a yield criterion (in order to obtain the plastic strain increments) is generally known as a flow rule. The above rule is known as the normality principle because equation (2.12) requires the plastic strain rate components to be normal to the yield surface. In 1924, Prandtl [13] proposed stress and strain relationships for an elastic-perfectly-plastic material under plane strain conditions and later, in 1930, Reuss [14] generalized these relationships which became known as the Prandtl-Reuss flow rule. Thus the Prantl-Reuss flow rule is the rule associated to the von Mises yield criterion and, again, this flow rule is used extensive by finite element codes (including the one used in this work) to predict plastic strain increments.

2.3.2.3 Material hardening models

The most common material models used to analysis the behaviour of a material under elastic-plastic loading are elastic-perfectly-plastic (EPP), elastic-isotropic hardening (EIH) and elastic-kinematic hardening (EKH) [15, 16]. As shown in Figure 2.13.

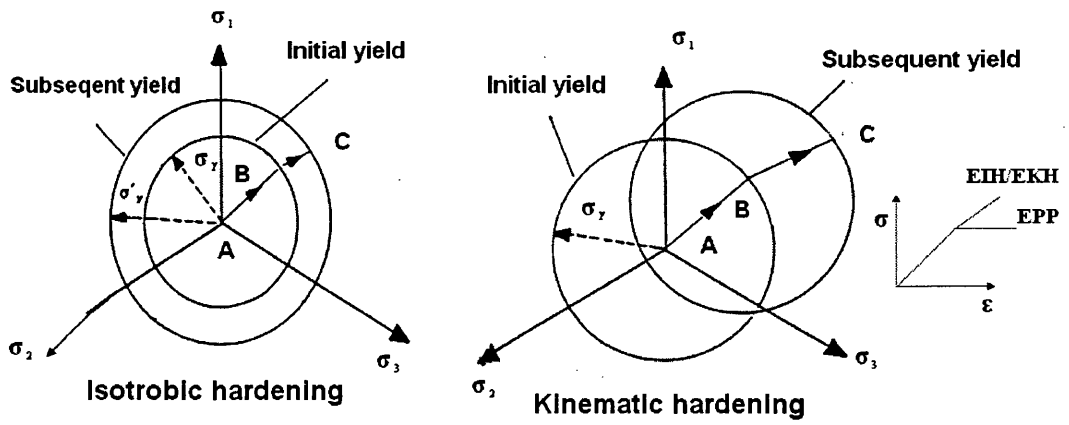

Figure 2.13: Isotropic and kinematic hardening models

Most engineering materials work-harden if taken beyond their elastic limit. If a stress reversal from tension to compression then takes place, there is a clear reduction in the compressive yield stress when compared to the original tensile yield stress of the material. This is also true for stress reversal from compression to tension. This is referred to as the Bauschinger effect. As can be seen in Figure 2.13, the isotropic hardening model is based on the assumption that the hardening effect is the same in both tension and compression, in other words ignoring the Bauschinger effect. The onset of compressive yielding will be initiated when:

$$\sigma = -\sigma_y \qquad \ldots (2.13)$$

where σ_y is the current yield stress. For isotropic hardening the yield surface increases in size but maintains its original shape under loading conditions. It can be seen in Figure 2.12 that the von Mises yield appears as a set of concentric circles.

On the other hand, the kinematic hardening model assumes a constant elastic stress range of $2\sigma_y$ and can be used to model the Bauschinger effect (see Figure 2.13)

2.4 Overview of non-linear finite element analysis

Many texts provide detailed information on the modelling of non-linear problems (e.g.[12,17]) and only a brief summary is given here.

The majority of general engineering components and structures are considered to exhibit linear elastic behaviour under load and small deflection finite element theory is used where the response of the structure or material is directly proportional to the load applied. Hooke's law [16], which is illustrated by a simple spring problem, givers a simple linear relationship between the applied force, F, and the resulting deflection, u:

$$F = k \, . \, u \qquad \ldots (2.14)$$

where k is the spring stiffness. The deflection can be calculated easily by dividing F by k. This is valid so long as the spring remains linear-elastic and the deflection is such that they do not cause the spring material to yield. Therefore, doubling the force doubles the deflection. In a finite element model, F and u are replaced by matrices and K becomes a square stiffness matrix. However, in many practical situations, the force is not equal to K.u and these are referred to as non-linear problems. There are three types of non-linear finite element modelling [17]:

- Geometric non-linearity (GNL) – where large deformations and large strains may be present. This includes snap-through buckling (see Section 2.8). The deformations are large enough to cause the loading direction and stiffness to change throughout the analysis.

- Material non-linearity – where plasticity, creep or visco-elasticity is present in the material model and stress is not directly proportional to strain.

- Boundary non-linearity – where a status-dependant problem exists, in which two surfaces come into or out of contact.

The problems being studied in this work contain geometric non-linearity, material non-linearity and boundary non-linearity.

The application in the finite element method to non-linear problems involves replacing the non-linear loading history of the structure by a sequence of linear or weakly non-linear increments. This means that instead of applying the full load in one load step, it is applied as a number of small increments. An iterative procedure is used within each load increment to ensure that the solution has converged within an acceptable level.

2.4.1 Explicit and implicit methods

Numerical solution is often referred to as being explicit or implicit. When a direct computation of the dependent variables can be made in terms of known quantities, the computation is said to be explicit. In contrast, when the dependent variables are

defined by coupled sets of equations, and either a matrix or iterative technique is needed to obtain the solution, the numerical method is said to be implicit.

The principal reason for using implicit solution method which are more complex to program and require more computational effort in each solution step, is to allow for large time-step sizes.

In an explicit numerical method would be evaluated in terms of known quantities at the previous time step n. An implicit method, in contrast, would evaluate some or all of the terms in terms of unknown quantities at the new time step n+1.

The choice of whether an implicit versus explicit method should be used ultimately depends on the object of the computation. When time accuracy is important, explicit methods produce greater accuracy with less computational effort than implicit methods. Also the implicit options are important for other methods.

Explicit is a dynamic finite element tool specifically designed for application to complex non-linear finite element simulations [5].

Explicit may be utilized for multi-phase analysis, for example a produce made from sheet steel may be formed using four sets of tools [5].

The implicit neutral file contains the entire model data associated with the application

The explicit solver is more suitable for forming simulation. The analysis cost increases in direct proportion to the size of the mesh, whereas the implicit solver cost

increased with the square of the matrix bandwidth of the mesh. In this thesis the implicit and explicit are used.

2.5 Thin cylinder formulae

Cylinders are usually considered to be either thick, where stress gradients due to relative curvature are significant, or thin in which case, stress gradients are negligible. If the ratio of thickness to internal diameter is less than about 1/20 (D_i/t >20) it is considered to be a thin cylinder.

By symmetry the three principal stresses in a thin cylinder subjected to internal pressure are the circumferential (or hoop) stress, the longitudinal stress and the radial stress [18] (see Figure 2.12) where:

hoop stress = $\sigma_1 = \frac{pD}{2t}$, longitudinal stress = $\sigma_2 = \frac{pD}{4t}$ and radial stress = σ_3 = -

$\frac{p}{2}$

These stresses only depend on pressure and the cross-section of the cylinder. The length of the cylinder has no effect, so long as the cylinder is long enough for 'end effects' to be ignored in which case these formulae are correct away from the cylinder ends. Either the inside diameter D_i, outside diameter D_o or the mean diameter, D_m, can be used in these equations since the difference between them is very small.

Using equation 2.10, yielding occurs when:

$$(\frac{pD}{2t} - \frac{pD}{4t})^2 + (\frac{pD}{4t} - -p)^2 + (-p - \frac{pD}{2t})^2 = 2\sigma_y^2 \quad \ldots (2.15)$$

2.6 BS5500

BS5500 is the British Standard for Unfired Fusion Pressure Vessels. It states wide-ranging requirements for design, construction, inspection, testing and verification of compliance for this type of pressure equipment. Grip the fluid under pressure is the mean function of pressure vessels. BS5500 provides equations to calculate minimum thickness for vessels required to withstand a given internal pressure [3].

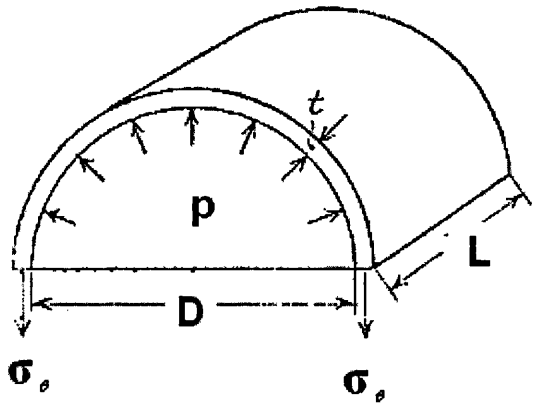

Figure 2.14: Hoop stress diagram

For equilibrium conditions from figure 2.14:

$2\sigma_\theta tl = p2rl$

$$\sigma_\theta = \frac{pr}{t} = \frac{pD_m}{2t} \qquad \ldots (2.16)$$

This is a reasonable approximation of the circumferential stress, which is used in design because it is the largest, BS5500 takes σ_θ to be the design stress f. Substituting mean diameter $D_m = D + t$ into Equation (2.16):

$$\sigma_\theta = \frac{p(D+t)}{2t} \quad \Rightarrow \quad t = \frac{pD}{2f - p} \qquad \ldots (2.17)$$

For cylindrical shells:

$$t = \frac{pD_i}{2f - p} \quad \text{or} \quad t = \frac{pD_o}{2f - p} \qquad \ldots (2.18)$$

2.7 ASME VIII

The American Society of Mechanical Engineers set up a committee in 1911 for the purpose formulating standard rules for the construction of steam boilers and other pressure vessels [4]. This committee is now called the Boiler and Pressure Vessel Committee. To determine minimum thickness of shells under internal pressure by the following formulas:

For cylindrical shells:

$$t = \frac{PR}{SE - 0.6P} \qquad \ldots (2.19)$$

where

t = minimum thickness

P = design pressure

R = inside radius

S = maximum allowable stress

E = efficiency of appropriate joint in cylindrical shells

This, ASME VIII is very similar to BS5500

2.8 Buckling

When a component or structure is subjected to compressive loading, it may experience visibly large displacements a direction perpendicular to the load at a force well below the force required to cause the material to yield. This is known as elastic buckling.

The primary path (curve oac) in Figure 2.15 load-deflection curve is the perfect structure [19]. The second phenomenon is known as bifurcation buckling and this is a very different kind of failure. At the buckling load or bifurcation point the curve will branch away from the primary path and continue on a secondary path (curve obd on Fig 2.15). The subsequent deformation will follow a new path, which differs considerably from the pre-buckling pattern.

This path will be followed if the post-bifurcation load deflection curve has a negative slope and the applied load is independent of the deformation amplitude.

To clarify this somewhat, bifurcation buckling is what could be termed elastic buckling, as the branching point may be within the linear elastic region in which case at least part of the secondary path will be elastic.

In the case of real structures, which contain unavoidable imperfections, true bifurcation buckling occurs infrequently. In fact the structure will generally fail in the snap-through manner describe later on. Imperfections will reduce the structure's strength and thus it will fail at a lower load than the perfect structure (represented by curve oac on Fig 2.15) and thus curve oef shown the response for an imperfect structure. Figure 2.15 also illustrates the varying buckling loads, where λ_{CR} is the limit load of a perfect shell, λ_{CRI} is the limit load of an imperfection structure and λ_{BIR} is the bifurcation load. [19].

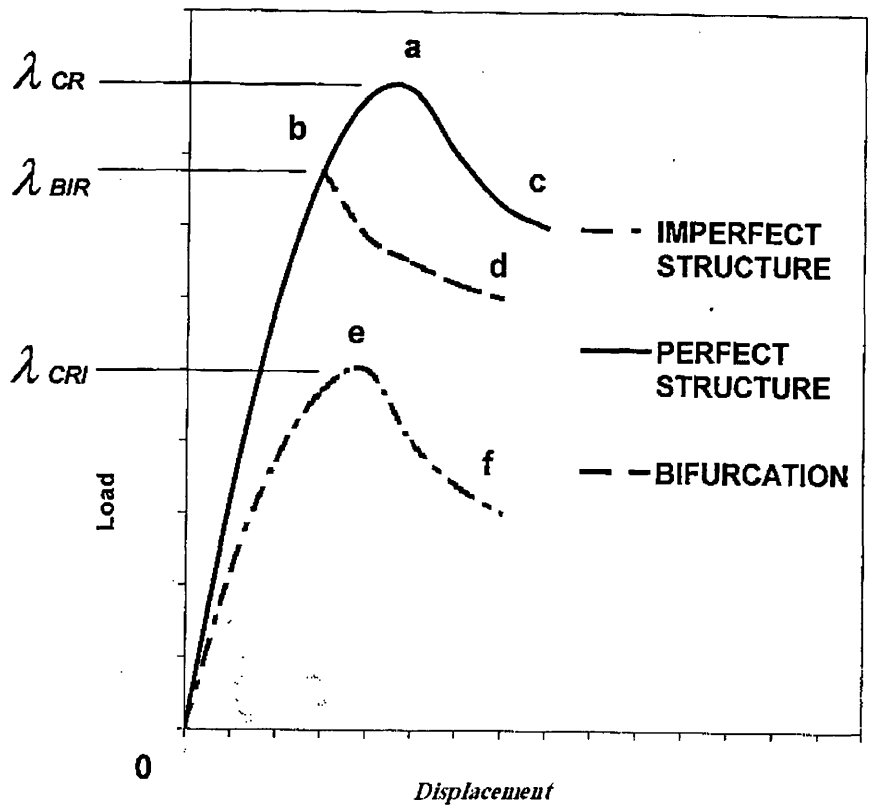

Figure 2.15: Load-deflection curves showing limit and bifurcation points [19]

2.8.1 Bifurcation buckling

At a certain stage during the compressive loading of structures, the equilibrium state of an ideal structure may reach a point beyond which two possible equilibrium paths exist. The point at which these two paths diverge is known as the 'bifurcation' point [20]. Beyond this point, the load-displacement characteristic of the structure may either follow the initial equilibrium regime (corresponding to the stress-strain curve for the material) or follow a new path (associated with a different form of deformation). In practice, the characteristic follows the path that minimizes the total potential energy of the system. An axially compressed column that fails by Euler buckling is an example of this type of failure. In a similar way, an ideal cylinder subjected to an axial compressive load reaches a critical load at which the deformation mode bifurcates from uniform axial compression into a pattern of diamond-shaped radial indentations.

The elastic buckling load for a cylindrical shell in axial compression, based on classical theory, has been determined by many researchers and reviews of early theoretical work are presented by Timoshenko [9] and Bushnell [19]. The critical stress σ_{cr}, resulting from these calculations is:

$$\sigma_{cr} = \frac{2Et}{D\sqrt{3(1-\nu^2)}} \qquad \ldots (2.20)$$

where E is Young's modulus, t is the wall thickness, D is the cylinder diameter and ν is Poisson's ratio.

The critical stress is the minimum axial stress for buckling in the cylindrical shell depending on the minimum buckling load which is a function of λ_{CR} as can be shown in Figure 2.15.

2.8.2 Pre-buckling deformation

Farshad [21] emphasises the importance that the pre-buckling solution has on the prediction of the bifurcation buckling loads by considering the pre-buckled state in an axially compressed cylinder. Bushnell [19] describes a bifurcation buckling failure mechanism of straight-walled collapse due to edge effects developed in the pre-buckled state. This type of failure is common in straight-walled cans. The edge buckling is mainly due to local hoop compression, which is greater nearer to the cylinder end. Bushnell states that in a near-perfect shell, where imperfections and end effects are negligible, edge buckling occurs before general instability remote from the edge or axisymmetric collapse near to the edge. (i.e. the plastic collapse observed in 'thick' shells). This study has shed light on the plastic failure in the can base by highlighting the mechanism of plastic hinge development.

2.8.3 Post buckling deformation

Experimental results suggest that actual collapse loads for axially compressed cylindrical shells may be as low as 10 to 20 % of the theoretical values. In 1932, Flugge [22] carried out experimental tests on cylindrical shells under axial compression in order to investigate this discrepancy. He found that his experimental buckling loads were approximately one-half of the theoretical values. Later, in 1941, von Karman and Tsies [23] provided a major contribution to the understanding of the effects of initial imperfections in cylindrical shells on the subsequent post-buckling

compressive behaviour. Their analytical results showed that the secondary equilibrium path drops sharply downward from the bifurcation point.

2.8.4 Eigenvalue analysis

Eigenvalues are a set of scalar values that are used in the solution of a linear system of equations. They are also known as characteristic roots. (Eigenvalues and eigenvectors) have particular significance in science, particularly in physics and engineering. For example, in the context of this research, they can be used to predict the critical load at which a structure will bifurcate and also the 'shape' of the subsequent buckling pattern. An eigenvalue buckling prediction is based on the determination of singularities in a linear perturbation of the structure's stuffiness matrix [24]. Because the lowest buckling mode is expected to be non-symmetrical, an initial perturbation (small change) to the geometry is required to promote non-symmetric deformation. A finite element eigenvalue analysis can be used to provide the data necessary to locally perturb a perfectly symmetric geometry of a structure in order to create the non-symmetry of loading required for buckling.

However, the eigenvalue approach is only useful if the perturbation is a realistic representation of the structural displacement prior to buckling. Consequently, the method can only be used when displacements are small (and elastic) and, therefore, the structure is stiff [24, 25].

Robotham *et al* [24, 25] used this method to investigate the elastic-plastic buckling of shafts (thin-walled tubes) subjected to torsion, using finite element analysis. They

demonstrated that accurate predictions for the collapse behaviour can be obtained using this method, which has significant advantages over existing analytical theories.

2.8.5 Rik`s method for modelling snap through

'Snap through' behaviour is associated with large elastic displacements, which result in large changes in geometry prior to collapse. Structures that exhibit 'snap through' tend to reach a maximum sustainable load, which will then decrease or increase in the post-buckling regime. At the point of 'snap through', zero stiffness is reached and a standard finite element analysis, based on the Newton-Raphson method, will predict an unbounded displacement increment which often causes the program to stop prematurely not allowing further prediction of the load deflection characteristics. The modified Riks method [26] is one approach that can be used to overcome this problem of zero stiffness.

A small imperfection (or perturbation) in the geometry is required and this is applied to the structure prior to loading. As discussed above, this comes from an eigenvalue analysis of the structure. An incremental loading process is adopted and the modified Rik's method is used to determine the quasi-static equilibrium state at each increment. However, unlike a traditional static non-linear analysis, the size of the load increment is variable in order to satisfy equilibrium conditions.

2.8.6 Buckling of thin-walled tubes

The buckling of thin-walled cylinder under axial compression and lateral pressure has been investigated by Flugge [22] who found that the effect of the internal

pressure on the buckling load is negligible. He considered a thin walled cylindrical shell of length L, and wall thickness t.

The strength and stability of a thin cylinder depends on a number of factors including the Young's modulus and yield stress of the material, the plate thickness and the cylinder diameter. The mode of failure may be buckling or yielding, whichever occurs at the lower level of applied force [7]. The compressive yield strength of the cylinder subjected to a uniform compressive force around its rim can be estimated using:

$$F_y = 2\pi R\, t\, \sigma_y \qquad \ldots (2.21)$$

where F_y = yield force

R = cylinder radius

t = cylinder thickness

σ_y = yield stress of cylinder material

But it is suggest that measured values are typically between 40 and 60% of this theoretical value [7]. Then the predicted collapse load in buckling:

$$F' = 0.4619 \frac{\pi t^2}{\sqrt{(1-\upsilon^2)}} E \qquad \ldots (2.22)$$

where F' = buckling force

2.9 Upper and lower bound analysis

The design of pressure vessels and related components is usually based on a combination of finite element analysis and rules contained within the appropriate codes of practice such as BS5500 [3] and ASME VIII [4] where yielding is generally considered to be the upper bound. Post-yield design is becoming more extensive, with techniques such as elastic-plastic finite element analysis being used in order to study shakedown and ratchet-ting regimes as well as collapse conditions. To avoid the added complexities of non-linear analysis, a limit load approach has been suggested [27]. The lower limit is based on the lower-bound limit load theorem:

"If for a given load P_L, a statically admissible stress field exists in which the stress nowhere exceeds the yield stress of the material, then P_L is a lower bound limit load"

Correspondingly, the upper limit is based on the upper-bound limit-load theorem

"If, for a given load set, the rate of dissipation of internal energy in a body is equal to the rate at which external forces do work in any postulated mechanism of deformation, the applied load set will be equal to or greater than the plastic collapse load"

Direct calculation of limit loads using upper and lower bound theories is very difficult because it requires a statically admissible stress field and a kinematically admissible strain field. In order to determine the equilibrium equations between the external forces and internal stresses and the stress-strain relationships, a complicated collapse solution is required. To avoid this, several alternative approaches have been investigated see review in [30]. The reduced modulus method (see, for example, [29]) has been modified [30] such that the elastic-plastic solution is replaced by a series of elastic solutions. After each elastic computation, the modulus of elasticity is

reduced until the conditions of admissible stress and strain fields, as lower and upper bound criteria respectively, are satisfied.

This method has been further developed by Mackenzie and Boyle [31] and Mackenzie *et al* [32], who have presented an elastic compensation method, where a series of elastic finite element analyses are used to predict a converged solution, which meets either the lower or upper bound criteria. Applications such as beams in bending and/ or tension, nozzles in spheres and torispherical heads are considered. Gowhari-Anaraki and Adibi-Asl [33] have used the method to estimate upper and lower limit and shakedown loads for beam members and a thick sphere.
Hardy *et al* [34] have used the method to estimate upper and lower bounds for hollow tubes with axisymmetric internal projections under axial loading. They found that this method could be used successfully to determine upper and lower bounds for both limit and shakedown loading, when compared with elastic-plastic finite element predictions.

Seshadri and Kizhatil [35] have suggested that if the procedure could not be verified for simple components, it was unsafe to use it for more complex design. Hence, in this work, a relatively simple geometry is used to further investigate the validity of the method.

2.9.1 Elastic compensation method

The aim of the method, as described in [31], is to systematically re-distribute the predicted stress field, while still remaining statically admissible, by carrying out an iterative elastic analysis and modifying the local elastic modulus at each stage. An

initial elastic finite element analysis is performed with an arbitrary load set (e.g., P_d), using the true modulus of elasticity for the material, E_0. This is taken to be the zero-th iteration in a series of linear elastic analyses. In each of the subsequent analyses, the elastic modulus of each element is modified according to the equation:

$$E_i = E_{i-1} \ \sigma_L \ / \sigma_{char} \qquad \ldots \quad (2.23)$$

where subscript 'i' is the current iteration number, σ_L is a limiting value of stress and σ_{char} is some characteristic stress within the element. It is suggested that this limiting stress is related to the material yield stress, σ_Y, by:

$$\sigma_L = \alpha \ \sigma_Y \qquad \ldots (2.24)$$

where α is an arbitrary constant between 0 and 1 ($^2/_3$ being found to provide suitable convergence. It is also suggested that the characteristic stress is the maximum (unaveraged) nodal equivalent stress associated with the element calculated in the previous iteration, defined as σ_{i-1}. Hence the iteration on element modulus of elasticity becomes:

$$E_i = 2 \ E_{i-1} \ \sigma_y / (3 \sigma_{i-1}) \qquad \ldots \quad (2.25)$$

The iterative procedure redistributes the stresses in the component and, over a number of iterations; the net effect is to decrease the maximum stress in the model to reach a converged constant value σ_d.

2.9.2 Application to lower bound limit load

The lower bound limit load is calculated by applying the lower bound limit load theorem. The converged elastic compensation solution satisfies the first requirement of the lower bound theorem in that it is statically admissible. Because the solution is linear elastic, there is a linear relationship between stress and applied load. A lower bound load, P_L, can therefore be established as the load required giving a maximum (nodal equivalent) stress in the component/structure that is equal to the uni-axial yield strength of the material, σ_y. for the worst point in the model and using proportionality:

$$\sigma_d = \beta\ P_d$$

and $$\sigma_Y = \beta\ P_L$$

(where β is the constant of proportionality)

hence:

$$P_L = P_d\ \sigma_Y / \sigma_d \qquad \ldots (2.26)$$

The applied load set P_d, is not restricted to single loads and may represent multiple forces, moments, pressure etc., in the form of proportional loading.

2.9.3 Application to upper bound limit load

The upper bound limit load theorem for a complete plastic collapse solution can be expressed as:-

$$\sum P\,\dot{u} = \int_V \dot{D}\,dV \qquad \ldots (2.27)$$

where $\dot{D}$ is the rate of dissipation of energy per unit volume, P is the set of equilibrium external loads and $\dot{u}$ is the compatible set of displacement rates, which requires details of that complete plastic collapse solution.

Alternatively, an upper bound solution can be found when an incomplete or partial plastic collapse solution is available [32] and Equation (2.27) can be re-written in the form:

$$\sum P\,\dot{u}^* \leq \int_V \dot{D}^*\,dV \qquad \ldots (2.28)$$

where the asterisk denotes an incomplete solution (i.e. a geometrically possible mode of deformation in which the stress field is not necessarily defined).

For this incomplete solution, compatible sets of displacement and strain rate increments are required and an iterative elastic finite element analysis, employing the elastic compensation method, will provide such information. However, the finite element predictions required to obtain the left hand side of Equation (2.28) are not always readily available. However, since the solutions are elastic, the elastic strain energy increment can be substituted, i.e.:

$$\int_V \dot{\sigma}^*\dot{\varepsilon}^*\,dV \leq \int_V \dot{D}^*\,dV \qquad \ldots (2.29)$$

where $\dot{\sigma}$ and $\dot{\varepsilon}^*$ are the elastically calculated stress and strain increments, respectively. Also, the increment of energy dissipation per unit volume for an elastic-perfectly plastic material, using the von-Mises yield criterion, can be expressed as [32]:

$$\dot{D} = \sigma_y \sqrt{\frac{2}{3}(\dot{\varepsilon}_1^{\,2} + \dot{\varepsilon}_2^{\,2} + \dot{\varepsilon}_3^{\,2}} \qquad \ldots \quad (2.30)$$

where $\dot{\varepsilon}_i$ (i = 1, 2, 3) are the three principal strain rates.

Equation (2.28) can be re-written in simple form as:

$$U \leq D$$

and, as shown in Figure 2.16, the dissipation energy, D, is linearly related to the applied load whereas the strain energy, U, varies with the square of the load. Furthermore, the intersection of the two lines represents the upper bound on the limit load.

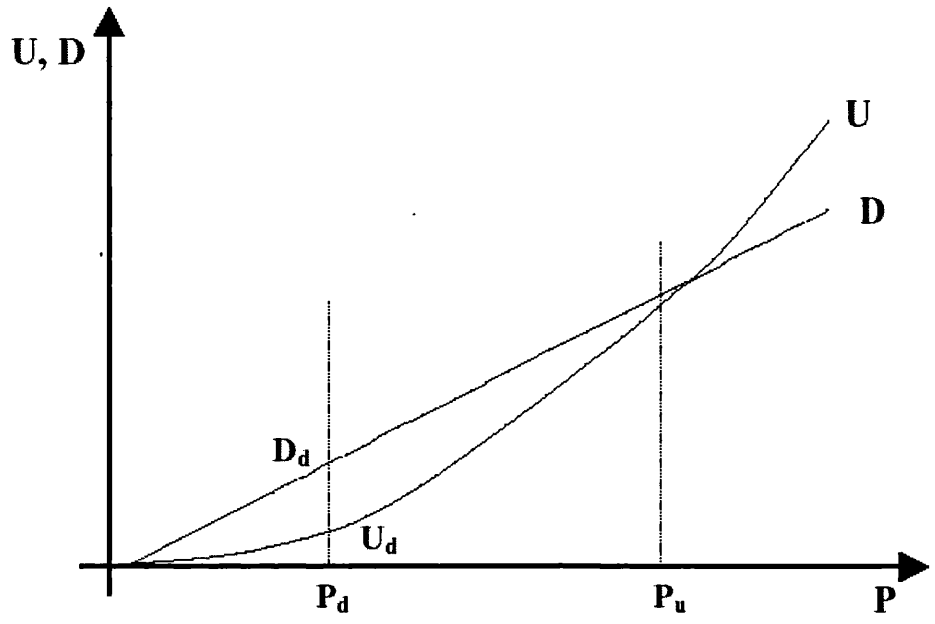

Figure 2.16: Variation in strain energy and dissipation energy with applied load, used in the calculation of the upper bound limit load

The upper bound limit load is therefore obtained using predictions from the converged elastic compensation finite element solution with the arbitrary load set, P_d , i.e.

since $U \alpha P^2$ and $D \alpha P$

then $U_d \alpha P_d^2$ and $D_d \alpha P_d$

and because the solutions are elastic:

$$U = \frac{U_d}{P_d^2} P^2 \text{ and } D = \frac{D_d}{P_d} P \qquad \text{for any load set, P}$$

Equating U and D at the upper bound limit load, P_u, gives:

$$P_U = \frac{D_d}{U_d} P_d \qquad \ldots (2.31)$$

where D_d and U_d are found from the converged elastic compensation finite element solution.

2.10 Extrusion process and modelling

2.10.1 Process description

In 1797, Bramah [see [36]] described a press in which lead, maintained molten in an iron pot, was forced by a pump into a long projecting tube, which served as a die. This was the earliest example of the extrusion process. A tapered mandrel was supported concentrically with the tube by bridge in its enlarged end.

Extrusion is a forming method that is widely used in industry for producing a large variety of products such as window frames, tubes, cans and cables. The cross-sections that can be produced vary from solid round, rectangular, to L shapes, T shapes, tubes and many other different shapes. The extrusion process is a simple method, which involves using a punch to press a ductile material through a die, thus causing gross plastic deformation and forming the required shape.

The essential feature of the extrusion process is the occurrence of extremely high pressures during the process, this being due to the constraints imposed by rigid tools. This high pressure may increase the ductility of the material, which in turn enables large deformations to take place in one operation without the material cracking, achieving at the same time precise dimensional accuracy and shape of the product. The process is particularly suited to high volume requirements and produces components free from porosity. Working the metal in the cold state creates a fine grain structure, which improves toughness, strength and hardness, and the high quality finish is ideal for polishing and anodising. These features combine to give price, quality and delivery advantages over other methods of manufacture such as turned parts, castings and deep drawn components [37].

Although extrusion is a modern process it precedes the development of aluminium, which was only commercially available since 1886. There are two types of extrusion commonly used in industry: direct and indirect extrusion as shown in Fig 2.17. In direct extrusion, the die is located at one end of the container and the metal to be extruded is pushed towards it, hence moving relative to the container. In the case of indirect extrusion, the die is placed on the end of the ram, and moves through the container from one end (see Figure 2.17).

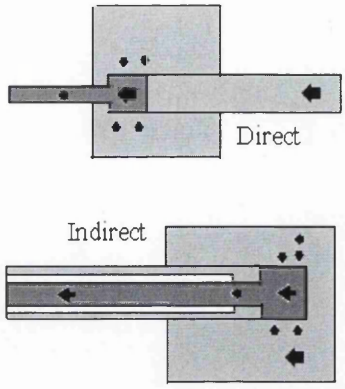

Figure 2.17: Direct and indirect extrusion [36]

In indirect extrusion of aluminium alloys, the process is characterized by the absence of friction between the billet surface and the container. The load required is therefore always decreased, compared with direct mode (as illustrated in Figure 2.18) and can be reduced by as much as 50%. The advantages of indirect extrusion are partly related to the lower load needed and partly to the more uniform flow pattern developed because of the absence of relative motion between the billet and the container such that no heat is produced by friction [36].

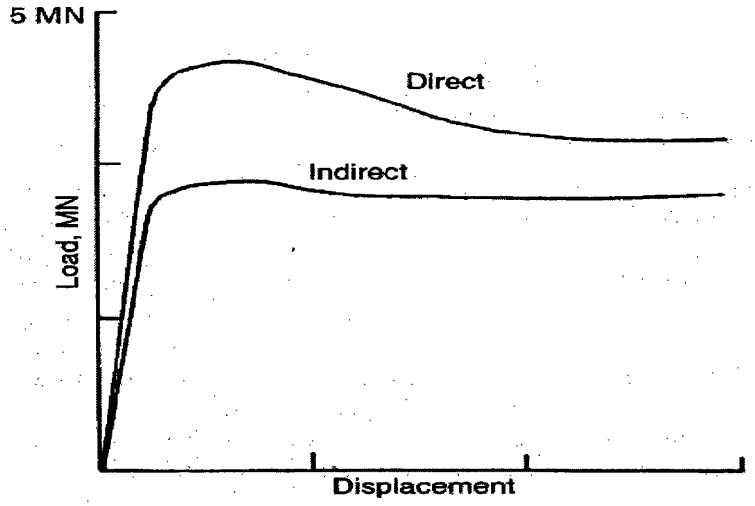

Figure 2.18 Extrusion load/displacement curves for direct and indirect extrusion [36]

Impact (or back) extrusion is a type of indirect extrusion process that produces components by striking a cold billet, or slug, of metal contained in a die cavity. The metal slug is forced to flow around a punch by a single high-speed blow. The wall thickness is controlled by the clearance between the punch and die [37]. This type of extrusion process is used to form aluminium aerosol cans (see Section 2.2.6). The aluminium aerosol cans are manufactured in one piece by reverse-extrusion process and the tool used for manufacturing is shown in Figure 2.19.

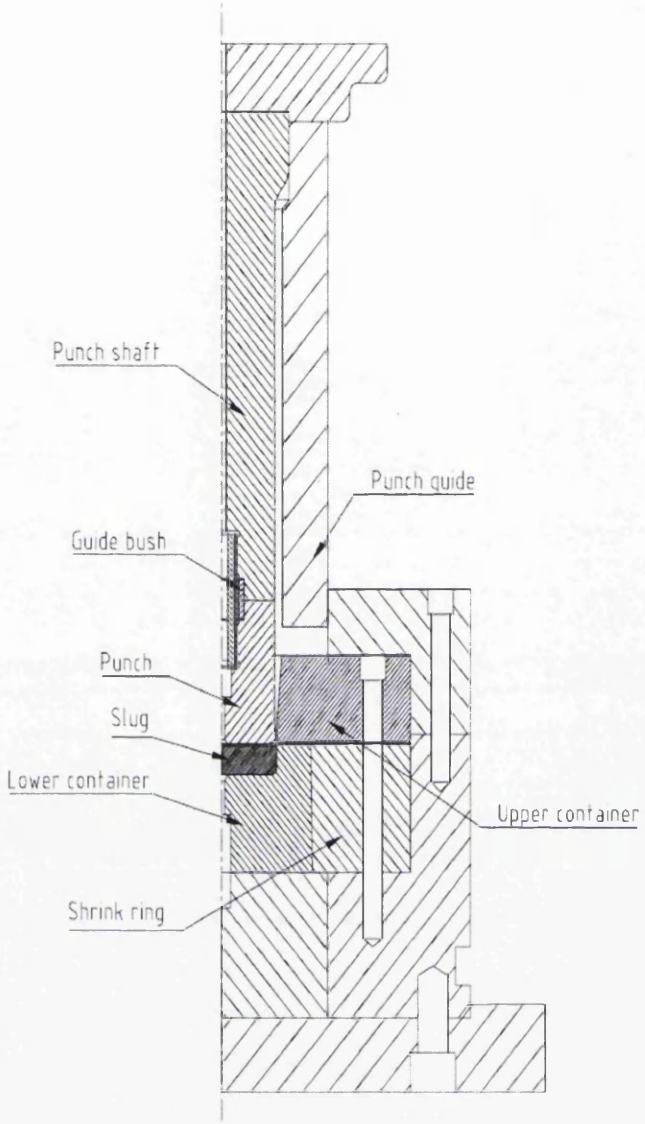

Figure 2.19: Tool setup used for the manufacturing of the aluminium cans

2.10.2 Constant volume analytical approach

Patten [2] developed a program to predict the height and thickness variation in the first stage of the back-extrusion process for aluminium aerosol cans, using a constant volume approach. The mathematical method involved the development of a volumetric model of the extrusion process based on billet, punch and die dimensions coupled with information on the punch travel. The profile is split into sections and a cumulative volume conservation principle applied. The results produced were validated through experimental measurement.

2.10.3 Finite element modelling

The application of the finite element method to metal forming problems began as an extension of structural analysis techniques into the plastic deformation regime. Thus early applications of the finite element method to metal forming problems were based on the plastic stress-strain matrix developed from the Prandtl-Reuss equations. Hydrostatic extrusion, compression, and indentations were analysed using this matrix and the infinitesimal variation formulations [38]. In recent years, a trend can be observed towards a more objective documentation of the empirical knowledge available on extrusion components. The development of automated design applications or expert systems can be seen as a part of this trend. These systems require the explicit formulations of the design rules. To formulate such rules more knowledge of the mechanics behind the extrusion process is required. The finite element method can be a valuable tool in obtaining such knowledge, providing insight into the process that cannot easily be obtained in any other way [39].

The use of the finite element method (FEM) is becoming increasingly important in understanding the processes that occurs during aluminium extrusion.

Joeri [39] in 2000 described the finite element simulation of the extrusion process for aluminium prismatic sections with some new developments in the simulation of aluminium extrusion for complex sections and simple sections also hollow profiles was produced using the finite element method being reported. The simulation can be used to investigate particular aspects of the extrusion process. The simulation can also be used directly in the design process to improve the design of specific dies in order to improve the performance of these dies.

Joachim in 2005 [40] studied the backward cans extrusion process. The study discusses the type of punch used in the backward cans extrusion process, which is commonly made with a cylindrical punch land. Using finite element analysis, the radial contact force of the punch has been determined. The results the finite element simulations of the process employing a new punch design show that a slight change in the angle of the punch land causes a drastic change in the contact conditions between the punch land and can wall and the change in contact condition gives rise to a net radial force on the punch, which will deflect the punch off centre leading to variations in the can wall thickness. He does not consider the effects of friction coefficient or the relationship between punch force and punch travel.

2.10.4 Friction considerations

The effect of friction in metal forming operations is fairly complex. Friction occurs between the processed specimen and the forming tool in the appearance of surface shears, and therefore directly affects the position of the planes of principal stresses. The effect increases with the increasing area of contact between the specimen and the tools, and with the reduction thickness of the processed material [41].

According to the Coulomb friction law [39] the standard coulomb friction model assumes that no relative motion occurs if the equivalent frictional stress is less than the critical frictional stress. In the rough friction model for non-slipping case, it can be further assumed that there seems to be no relative motion as long as the two surfaces remain in contact. A penalty contact algorithm in the Lagrangian multiplier method was adopted to remove the relative motion by dividing the friction force by the penalty stiffness [42]. The effect on thickness of friction coefficient is shown in Figure 2.20. The thickness decreased with increasing coefficient of friction.

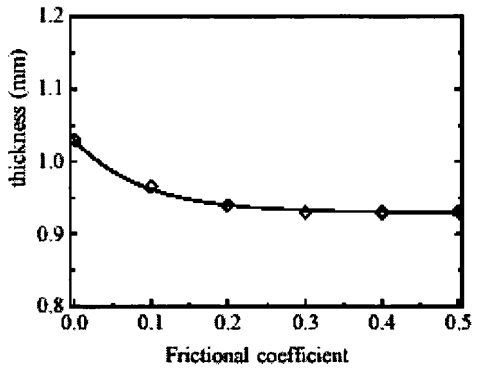

Figure 2.20: Effect of friction on the thickness of the sheet model [42]

The effect of friction in the direct extrusion process is important in the commercial process because it determines the billet size, either by pressure limitation or by the surface at the end of the ram stroke. During the extrusion process the normal pressure on the interface between the aluminium and the die is so high that no slipping friction occurs [39].

The higher the contact friction the higher the forming costs, see Figure 2.21. Therefore, it is necessary to ensure that the contact friction is as low as possible in the forming process [43]. This is achieved by applying a dry lubricant to the billet before it enters the die.

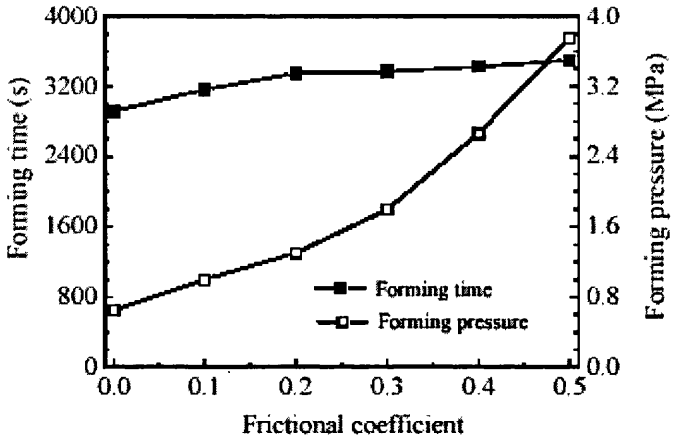

Figure 2.21: Effect of friction on the final forming time and pressure [42]

2.10.5 Unloading (spring back)

The unloading process following extrusion is primarily elastic. However, because the sheet is bent and unbent around the die and punch corners, some secondary yielding may occur. Spring back is additional deformation of the material that happens during unloading. In the extrusion process, spring back is a phenomenon, which takes place when the work-piece is removed from the tools after completing forming [44]. The degree of change in the shape depends on the material properties as well as the technological parameters: restraining force, friction between the sheet and the tools. It is an important consideration in both pressing and forming since the final shape of the component is (slightly) different to that created by the punch and die geometry.

R. Akbari, *et al* [45] described the finite element code used to simulate the spring back and sidewall curl in 2-D draw bending. Five stages have been applied for the simulation of the whole process.

The results showed that the springback and sidewall curl phenomena could be completely simulated by ELEFEN software for sheet metal forming of high strength steel.

Mercer *et al* [46] have illustrated the effective use of different solvers in the simulation of material forming processes. By combining the advantages of the explicit and direct solvers, an effective solution scheme is obtained for simulating the complete sheet forming process as well as subsequent analysis of in service loads.

Joannic and Glin [47] used finite element analysis to simulate stamping or deep drawing operations. A 3-D simulation code was used to design appropriate tools in sheet metal forming. They found that the springback procedure proposed can evaluate the amount of springback in deep drawing processes in a realistic manner.

Narasimhan [48] studied numerical techniques for predicting springback deformation in sheet metal forming. He used implicit and explicit finite element methods to analyse the formation of an actual automotive module. He found that a finite element procedure that couples the implicit and explicit finite element methods accurately predicted spring back in the stamping of an automotive component. The overall number of iterations involved in the design of die components could be significantly reduced. Hence the simulation saved design and production time for manufacturers.

Arwidson [49] studied the numerical simulation of sheet metal forming for high strength steels very deep drawing situation was investigated both experimentally and by numerical simulation for four high-strength steels. He observed that the

simulation is highly sensitive in the critical bending region. Also, varying the friction coefficient between 0 and 0.1 had a significant influence on the results.

In the case of the back extrusion of aluminium aerosol cans and after these vessels have been formed, there will be a small amount of elastic strain left within the aluminium. This will cause a very slight reduction in the dimensions and change in shape. Since these are thin-walled cylinders, where the wall thickness is very much less than the cylinder diameter, the mechanical elastic effects are very small and therefore can be neglected.

2.10.6 Other issues

2.10.6.1 Effects of punch speed

During the extrusion process, the punch speed should be selected to make sure that the dynamic effect on the deformable body is minimal. The final kinetic energy of the blank should be less than 5% of the internal energy. Even in the initial contact stage, the kinetic energy should not exceed 10% of the internal energy. Usually the peak punch speed is chosen to be in the range of 1m/s-5m/s. [39].

2.10.6.2 Thermal effects

During the extrusion process, the temperature of the aluminium increases. A significant portion of this heating takes place during the early stages. The rest occurs when the material flows around the punch. Because the thermal conductivity of aluminium is high, it is expected that localised heating is limited.

When the aluminium is plastically deformed, there is considerable heat generation. This will affect the tooling dimensions. However, it is considered that these changes in dimensions are small and are generally assumed to be negligible

2.11 Optimisation

Optimisation is the act of obtaining the best results under the given or prevailing circumstances [50]. In the design, construction, maintenance and operation of process plant, technological and managerial decisions must be taken at several stages. The ultimate goal of such decisions is either to minimise the effort required or maximum the desired benefit. The effort required or benefit desired can generally be expressed as functions of certain decision variables. Thus optimisation can be thought of as the process of finding the conditions that produce the maximum or the minimum of such functions. (Note that maximisation and minimisation are interchangeable since the maximum of a function can be determined by seeking the minimum negative of the same function).

There is no single method for solving all optimisation problems successfully or indeed efficiently. Hence, it is important to identify the type of optimisation problem involved and then apply the appropriate procedure for its solution. Some of the basic building blocks of optimisation were developed in the time of Newton, Lagrange and Cauchy [50], including the use of calculus to obtain maxim and minima. There have been spectacular advances since the advent of digital computers. Currently, optimisation in engineering covers a wide range of applications.

The general optimisation problem may be stated as [50]:

$$X = \begin{Bmatrix} X_1 \\ X_2 \\ \bullet \\ \bullet \\ \bullet \\ \bullet \\ X_n \end{Bmatrix} \quad \text{which minimises } f(X) \qquad \ldots (2.33)$$

subject to the constraints:

$$g_i(X) \leq 0 \qquad i = 1, 2 \ldots, m \qquad \ldots (2.34)$$

$$h_j(X) = 0 \qquad j = 1, 2, \ldots, p$$

where X is a non-dimensional vector

$f(X)$ is the objective function or performance index

$g_i(X)$ are inequality constraints

$h_j(X)$ are equality constraints

An objective function is a function associated with an optimization problem that determines how good a solution is.

One particular area of optimisation, which is of particular interest to this project, is the area of shape optimisation where optimised shapes are investigated in order to reduce stress variations in components and to reduce the amount of material used.

2.11.1 Previously published work

In 1984 Sodeik [51] published literature is not particularly helpful towards the specific the design issue of optimisation of aerosol cans. He developed an equation for axial collapse based of a bead on the application of the theory of the point of metal yield. In the development of equation he considers a single triangular bead with three yield points but does not take into account the circular nature of the problem and the development of hoop stresses.

In 1992, Jing Han *et al* [52] studied the application of structural optimisation techniques to aluminium beverage bottle design to investigate the influence of the design parameters to the buckling strength and rigidity of the base under an axial load and internal pressure. His paper dealt with the shape optimisation of the bottom of aluminium beverage bottles by applying the structural optimisation technique. He used non-linear finite element analysis to study the influence of the design parameter on the buckling strength and rigidity of the bottom under an axial load and internal pressure. The thickness of the bottom and the top parts of sidewall are t = 0.4 mm and 0.135 mm. The objective function which he used for optimisation to maximize the column strength of the bottom is:

$$F = P(X)$$

With design variables

$$X = \{x_i\}, \quad i = 1...n$$

where n is the number of design variable

The results obtained a 50% increase in column strength. Also he established that using the progressive optimisation method can help designers to understand the optimisation problem more clearly and the computational cost was reduced.

In 1999, Benjamin [53] studied the computational strategies for the design and optimisation of three-piece steel food cans. He described the performance of the finite element models across a range of bead-depths. He used the suite to provide consultancy services to a number of can-makers to study the effect of geometry and material changes. This study calculated that using the current can material and geometry specifications finite element models should be constructed. He studied the effect of imperfections on the post buckling behaviour of food cans and the axial collapse of the beaded cans in 2-D and 3-D model

2.12 Closure

The background information and published literature relevant to this project have been reviewed. In particular, information on thin-walled cylinders under internal pressure and thin-walled cylinders subjected to axial loading has been presented and will be referred to in later chapters of this thesis. The areas of extrusion modelling and optimisation analysis have also been explored, since they also feature in this work.

Several observations are made based on this review:

1. there is a requirement for further understanding of the process of dome reversal (elastic-plastic buckling) of thin-walled cylinders with inverted bases subjected to internal pressure;

2. similarly, a need for greater accuracy in the modelling and prediction of axial buckling loads has been identified;

3. the British and American standards do not cover such design considerations;

4. further applications of the elastic compensation method are required in order to validate the approach;

5. there is little evidence of finite element analysis being applied to the modelling of the back-extrusion process;

6. the raw material costs associated with the manufacture of aluminium aerosol cans are very high and, at the same time, the cans are often considered to be over-designed. Consequently, there is a requirement for the optimisation of the can thickness profile such that material can be reduced while, at the same time, maintaining the same critical pressures for dome reversal and bursting.

These six issues are investigated further in the remaining chapters.

Chapter three

INTERNAL PRESSURE LOADING

3.1 Introduction

This chapter describes the results of an analysis of the aerosol can under internal pressure loading using finite element analysis, together with details of the experimental validation of the predictions. The analysis focuses on the base of the can, since this is the critical area for improvements to be made. Elastic analysis is used to study the elastic stress distributions and the onset of yielding and elastic-plastic analysis is used to investigate the post-yield behaviour up to dome reversal and eventual failure. The application of approximate methods, such as the upper and lower bound techniques, to this type of component and loading is also investigated.

Full details of geometries, loading, boundary conditions and material models considered are given in Sections 3.2.1 to 3.2.3. The mechanisms are described in detail using one particular geometry-load combination and an elastic-perfectly-plastic material model. The maximum internal pressure that the charged pressure vessel will withstand is presented together with upper and lower bound estimates.

The finite element predictions have been obtained using ELFEN Version 3.0.4, [5] a finite element program for Microsoft Windows NT. The program allows pre-processing, analysis and post-processing stages to be completed within a single application. The program can be used to model a large number of situations including buckling, plastic deformation, forming and stress analysis problems, etc.

3.2 Elastic finite element analysis using axisymmetric models

3.2.1 Geometry and finite element models

In order to fully understand the stress response, predictions have been obtained for a series of constant thickness can profiles as well as for an actual profile. This has been developed using the measured outside profile of an actual can [2] and assuming a constant thickness throughout. The model used for the actual profile analysis and the corresponding results are presented in Section 3.3.5.

The basic shape is assumed to be axisymmetric about the Y-axis. The geometry of the base is described using six dimensions; H (the dome depth), t (the wall thickness), L (the flat base length), R (the major arc radius), r (the minor arc radius) and the angle θ, as shown in Figure 3.1. Seven geometries have been considered in this analysis and the relevant geometric parameters are listed in Table 3.1. A detailed investigation of geometry G4 is described and a summary of results presented for the other geometries.

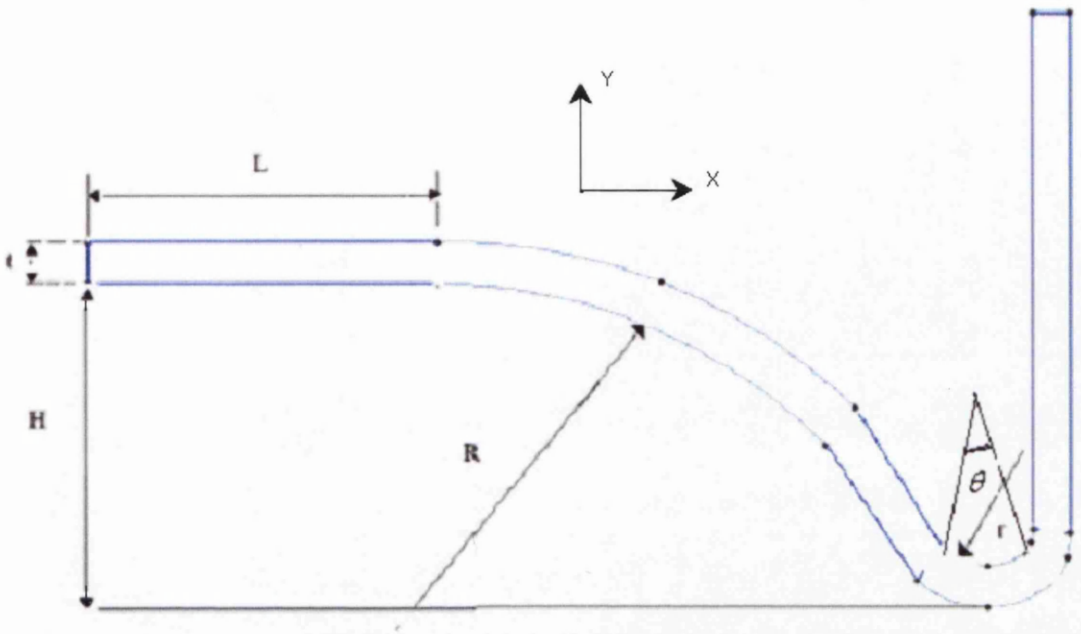

Figure 3.1: Can base geometry (constant thickness)

Geometries	H (mm)	t (mm)	L (mm)	R(mm)	r (mm)	θ (degree)
G1	7.5	0.4	8.924	13.75	3.20	87.8°
G2	8.5	0.6	8.924	13.75	3.18	86.7°
G3	8.5	0.8	8.924	13.75	2.73	67.3°
G4	8.5	1.0	8.924	13.75	1.94	50.5°
G5	8.5	1.2	8.924	13.75	1.62	30.4°
G6	8.5	1.4	8.924	13.75	1.50	25.2°
G7	8.5	vary	8.924	14.13	3.23	64.2°

Table 3.1: Geometric parameter

The basic finite element model is shown in Figure 3.2. During mesh generation, these "super elements" are sub-divided to create a suitable mesh, a typical mesh being presented in Figure 3.3 and discussed later in this chapter.

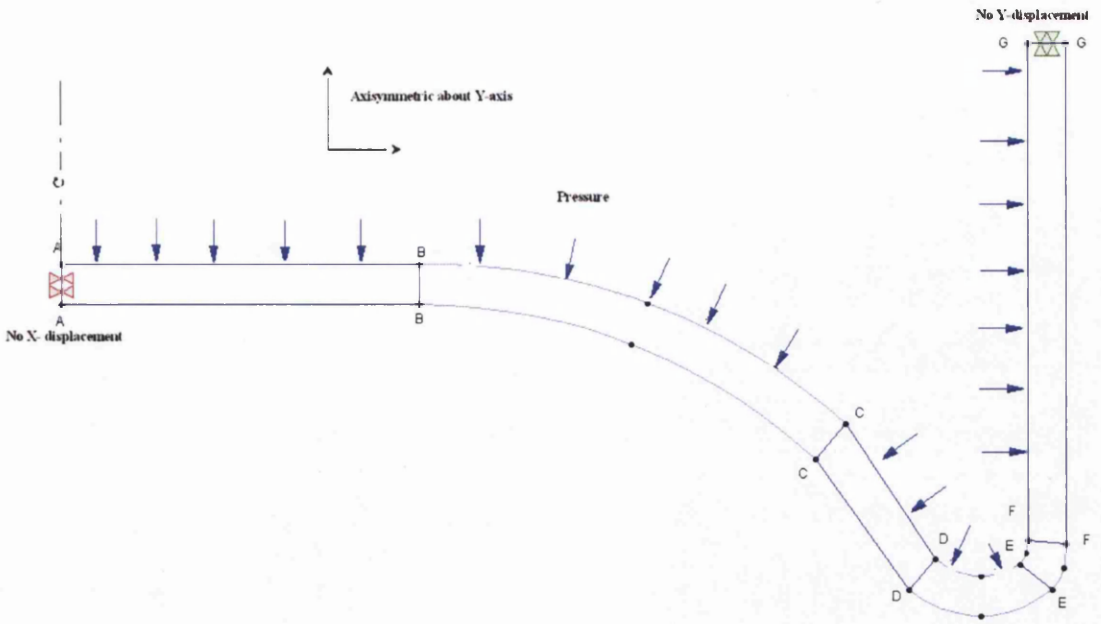

Figure 3.2: Basic finite element model of can base (constant thickness)

The top section of the can is not included at this stage to simplify the model. This will have little effect on the results, as it is known from experimental testing that the base of the aerosol can deforms first. On the basis of preliminary predictions, the cylindrical section was made long enough to ensure that a uniform stress distribution was reached away from the corners. Additionally, by removing the top section of the can, the model accuracy and computation time is increased. 8 noded, axisymmetric, isoparametric elements have been used because of their efficiency and increased accuracy.

3.2.2 Loading and boundary conditions

The axisymmetric model shown in Figure 3.2 is constrained in the X direction along the plane AA to represent symmetry. It is also constrained in the Y direction along the plane GG. These constraints on the displacement are sufficient to prevent a singularity occurring in the finite element solution. Elastic finite element calculations

have been performed for a pressure load of 1 bar (0.1 MPa) applied uniformly on the inner surface of the model.

3.2.3 Materials models

The material assumed for the elastic analysis is aluminium 1050, which is commonly used in this type of application. This means that the aluminium is 99.50% pure, with 0.5 % natural impurities [54] (and therefore no added impurities). The mechanical properties are given in Table 3.2 [2]. The results are generally normalized with respect to these material properties.

Material properties	Value
Density, ρ (kg/m^3)	2700
Young's modulus, E (GPa)	68.3
Poisson's ratio, υ	0.33
Yield stress (MPa)	100
Ultimate tensile strength (MPa)	156

Table 3.2: Mechanical properties of 1050 aluminium [2]

3.2.4 Constant thickness models

The region of the component under investigation is the can base, which is subjected to uniform pressure loading. In addition, the whole component is analysed in order to obtain 'nominal' predictions. Geometry G4, having t = 1 mm, is selected for a full review and a summary of the results is given for the other geometries. The mesh was generated using the ELFEN mesh generator and the mesh for G4, containing 1267 elements, is shown in Figure 3.3(a).

In finite element modelling, a better-quality mesh typically results in a more accurate solution. However, as a mesh is made better, the computation time increases. There is one way to perform a mesh convergence study as follows:

- Create a mesh using the fewest reasonable number of elements and analyze the model.
- Recreate the mesh with a denser (biggest number of element) element distribution, re-analyze it and compare the results to those of the previous mesh.
- Keep increasing the mesh density and re-analyzing the model until the results converge satisfactorily.

This type of mesh convergence enables an accurate solution with a mesh that is sufficiently dense and not overly demanding of computing resources. the mesh convergence for this analysis as shown in Figure 3.3(b).

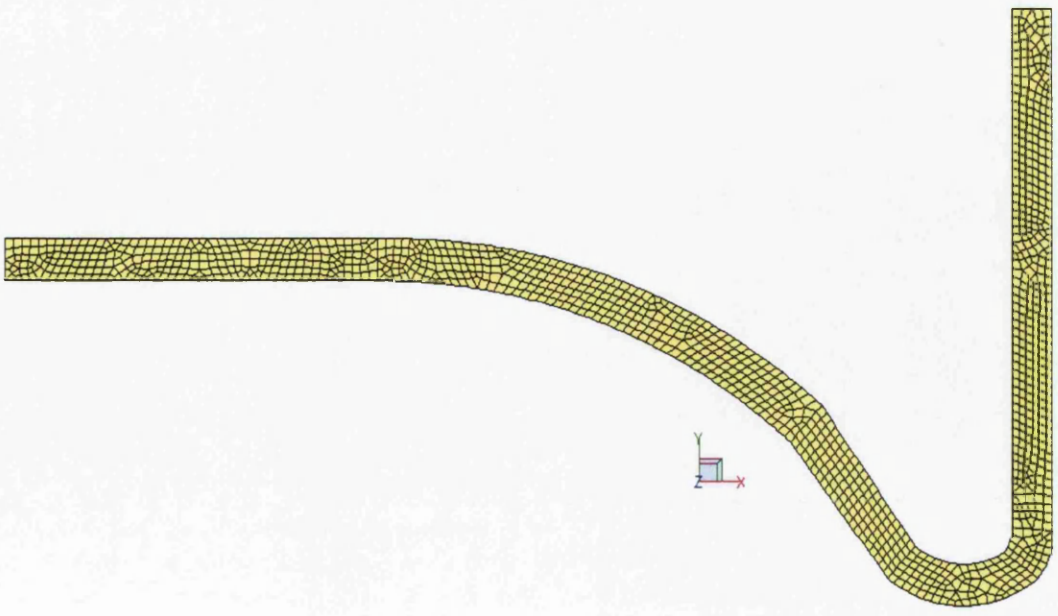

Figure 3.3(a): Finite element mesh for geometry G4

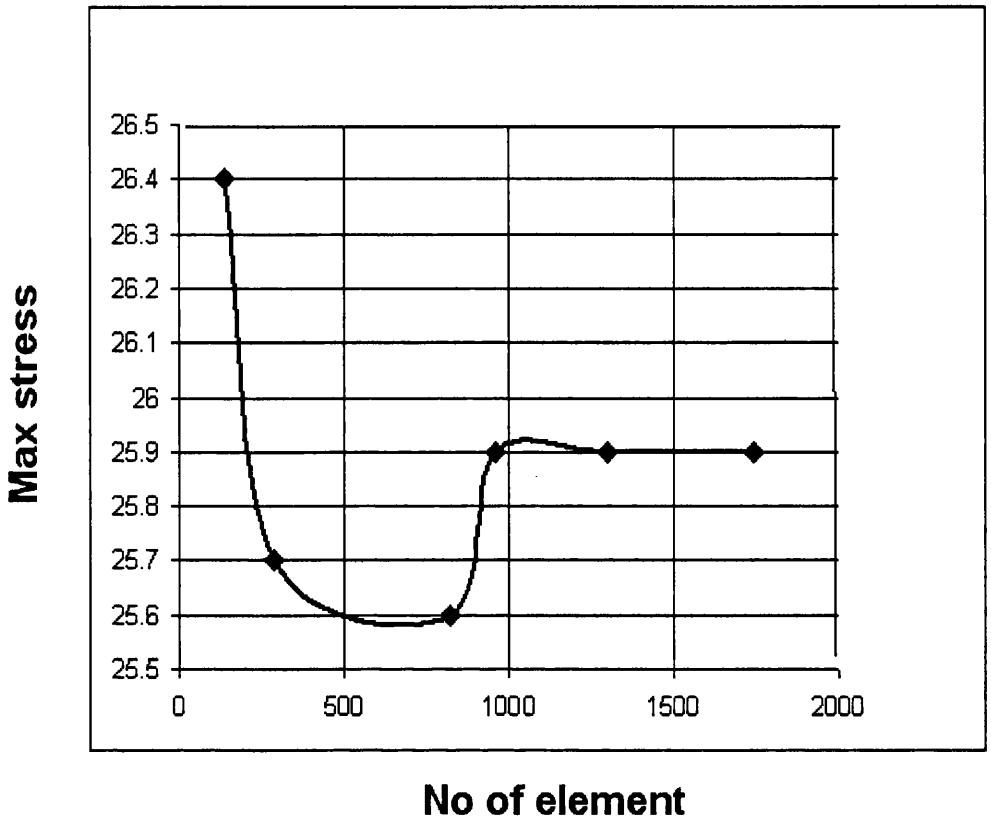

Figure 3.3(b): Mesh convergence

3.2.4.1 Results for geometry G4 (t = 1 mm)

Elastic principal stress contour plots for G4 for an internal pressure of 0.1 MPa are presented in Figures 3.4, 3.5 and 3.6. It can be seen that σ_1 has a maximum localized value of +15.72 MPa on the inside surface close to the intersection between the base and vertical sides (section EE in Figure 3.2). Elsewhere, σ_1 is reasonably uniform and of low value. σ_2 varies between +2.02 and –14.46 MPa with the maximum compressive value on the inside surface between sections CC and DD in Figure 3.2. σ_3 varies between +9.26 and –11.43 MPa with a maximum tensile value close to section DD in Figure 3.2 and generally compressive stresses in the uniform base

region, σ_1 is the hoop stress, σ_2 is the longitudinal stress and σ_3 is the radial stress approximately.

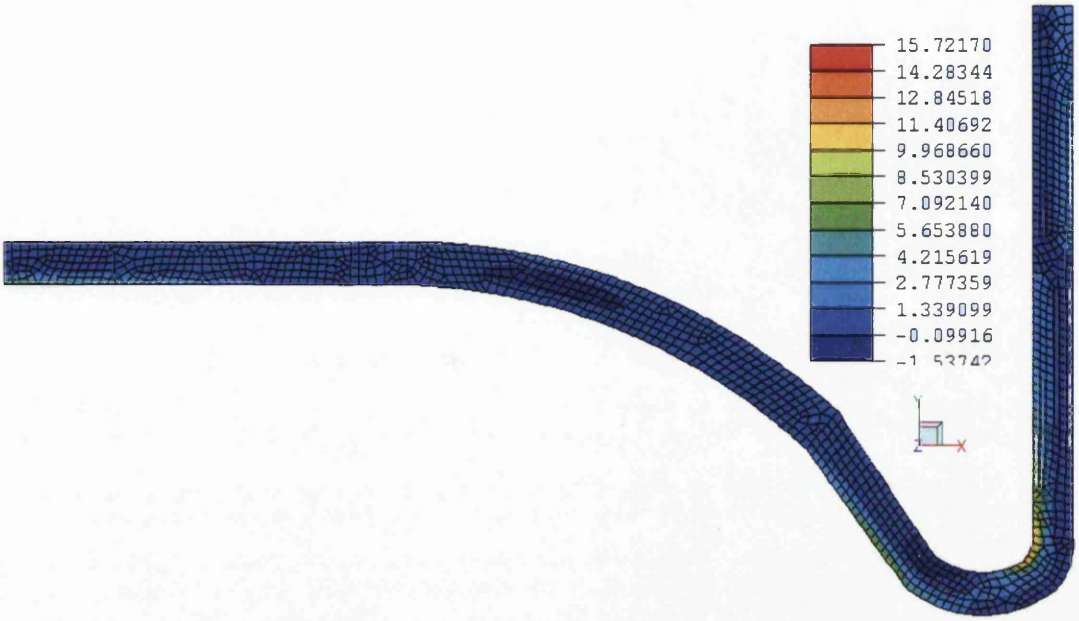

Figure 3.4: σ_1 contour plot (G4, p =0.1 MPa)

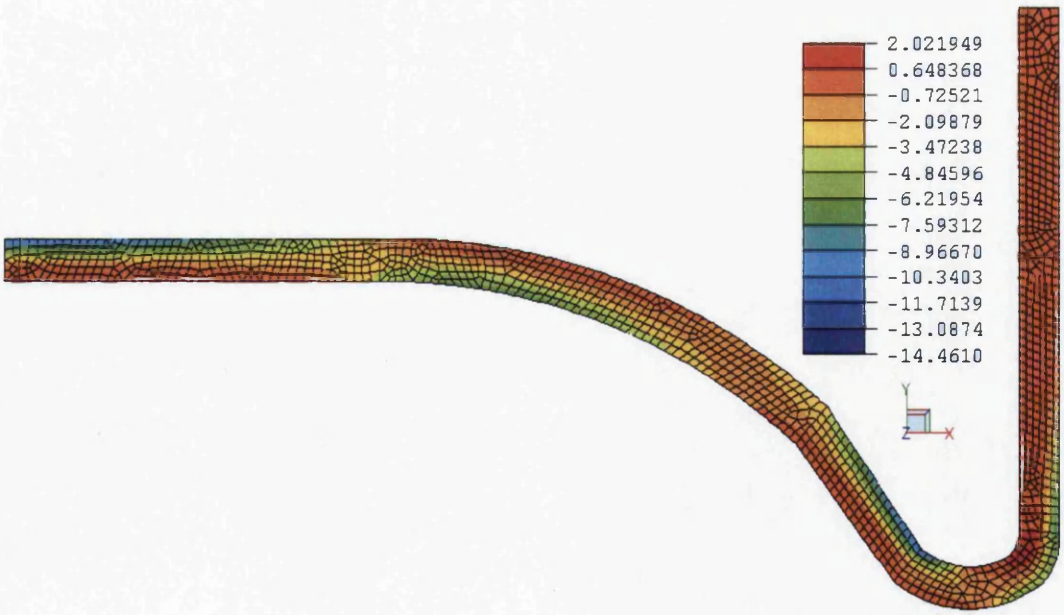

Figure 3.5: σ_2 contour plot (G4, p = 0.1 MPa)

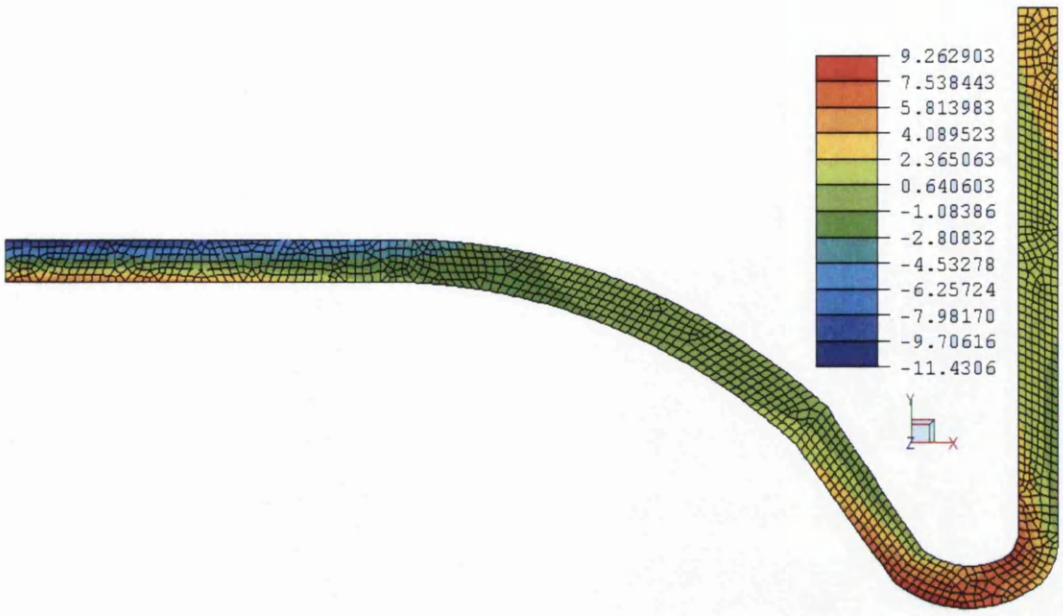

Figure 3.6: σ_3 contour plot (G4, p = 0.1 MPa)

The corresponding principal stress distributions around the inside and outside surfaces between points A and G (see Figure 3.2) are shown in Figures 3.7 and 3.8 respectively. It can be seen from figure 3.8 that the highest principal stress (σ_1) is at Section FF. Also σ_2 is higher at Section CC then σ_3 at Section EE. As can be seen from the figure, there are very sharp rise in σ_2 at point E compared to the other stresses. The flat sections of these curves occur when two of the principal stresses are negative and the other (maximum) must therefore be zero.

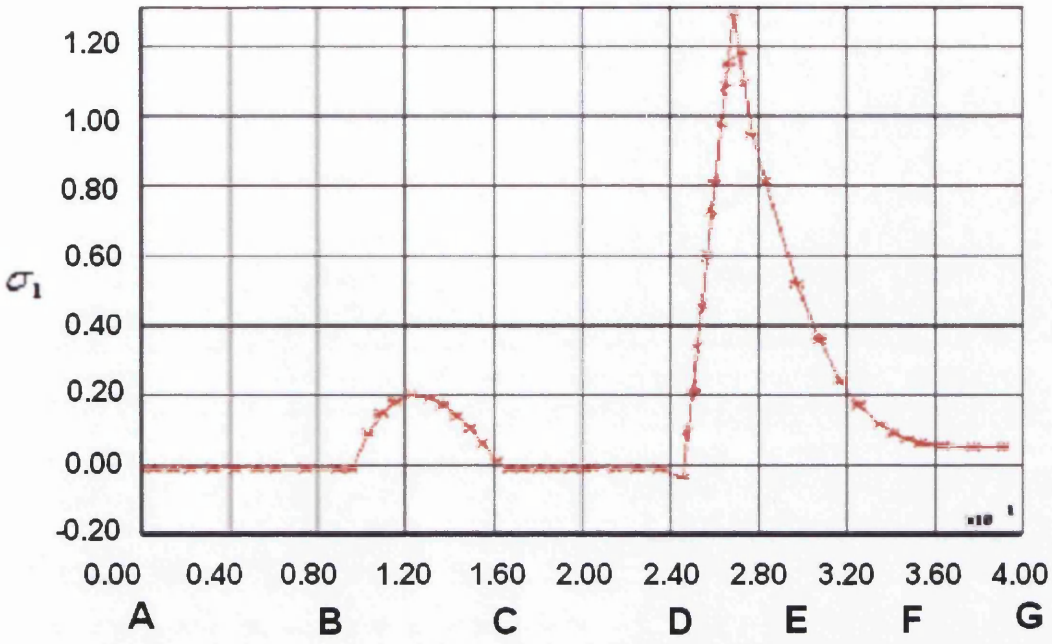
1.20
1.00
0.80
0.60
0.40
0.20
0.00
-0.20
σ_1
0.00 0.40 0.80 1.20 1.60 2.00 2.40 2.80 3.20 3.60 4.00
A B C D E F G

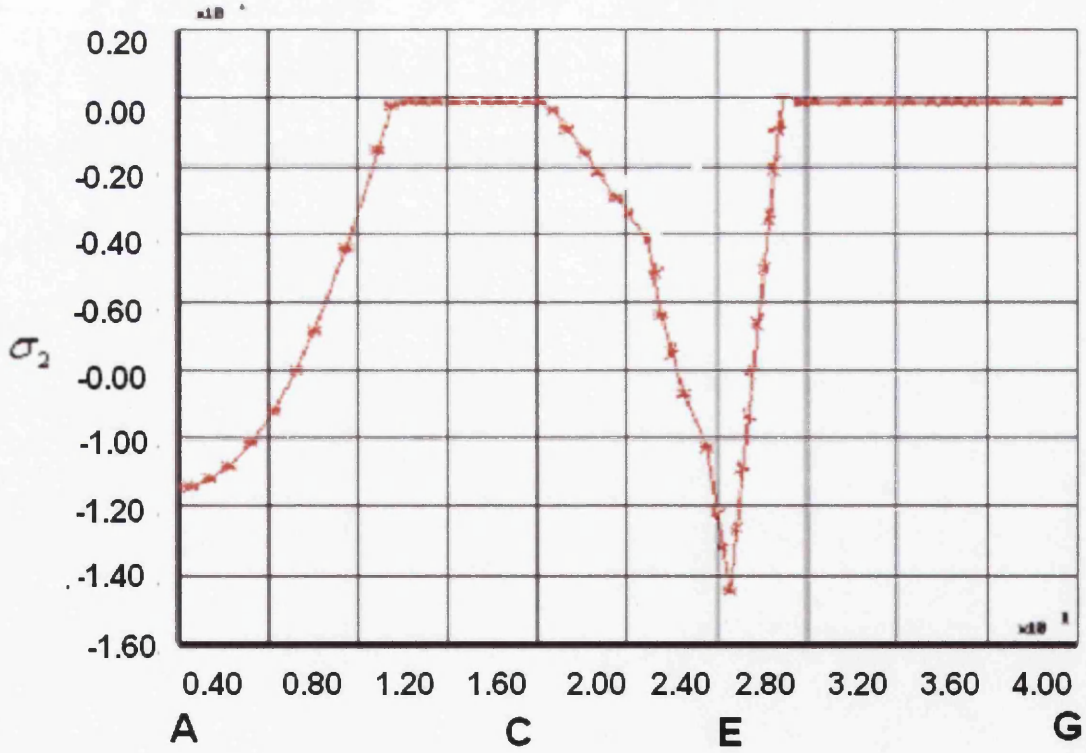
0.20
0.00
-0.20
-0.40
-0.60
-0.00
-1.00
-1.20
-1.40
-1.60
σ_2
0.40 0.80 1.20 1.60 2.00 2.40 2.80 3.20 3.60 4.00
A C E G

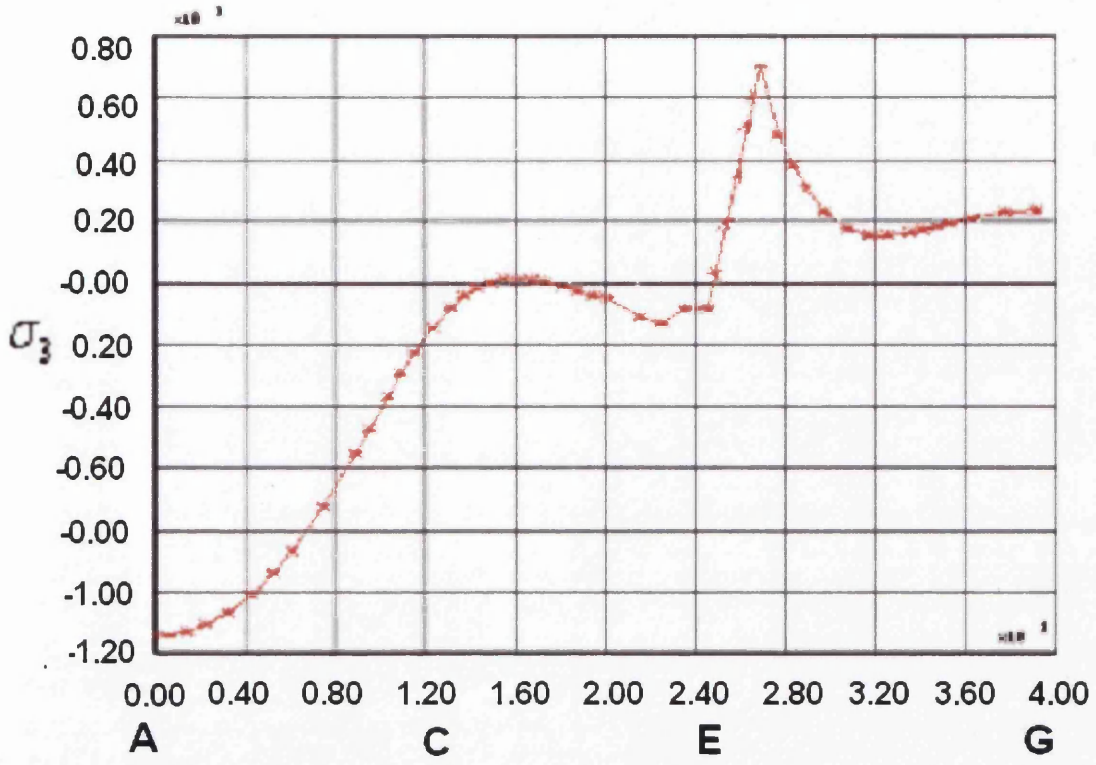

Figure 3.7: Principal stress distributions around the inside surface (G4, p = 0.1 MPa)

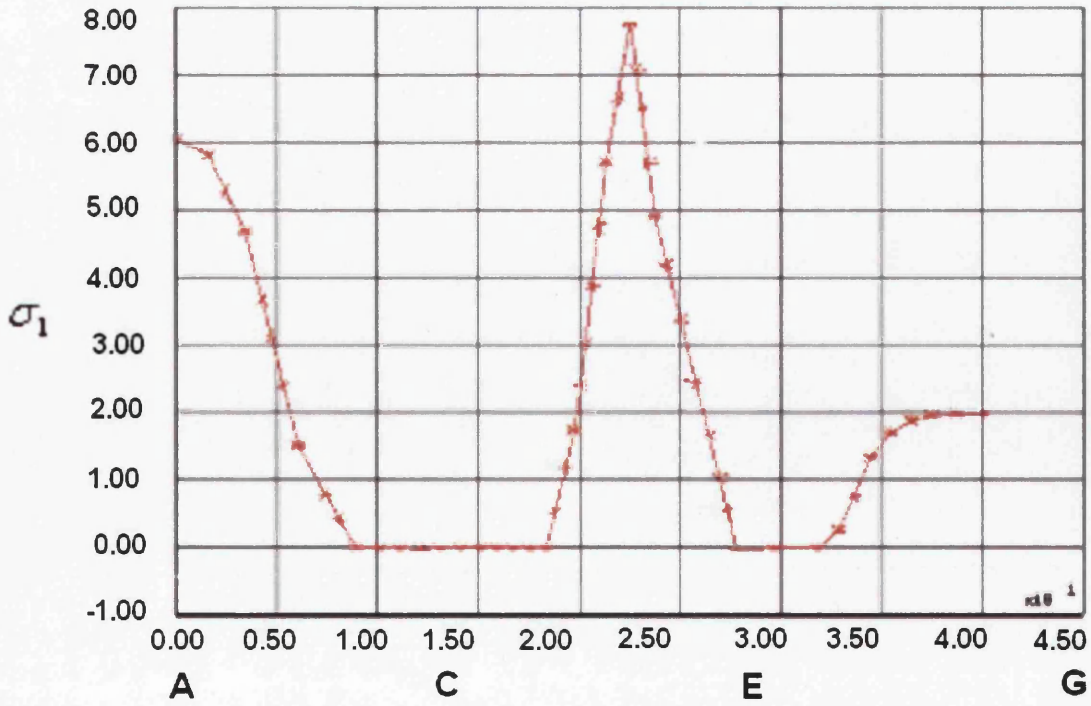

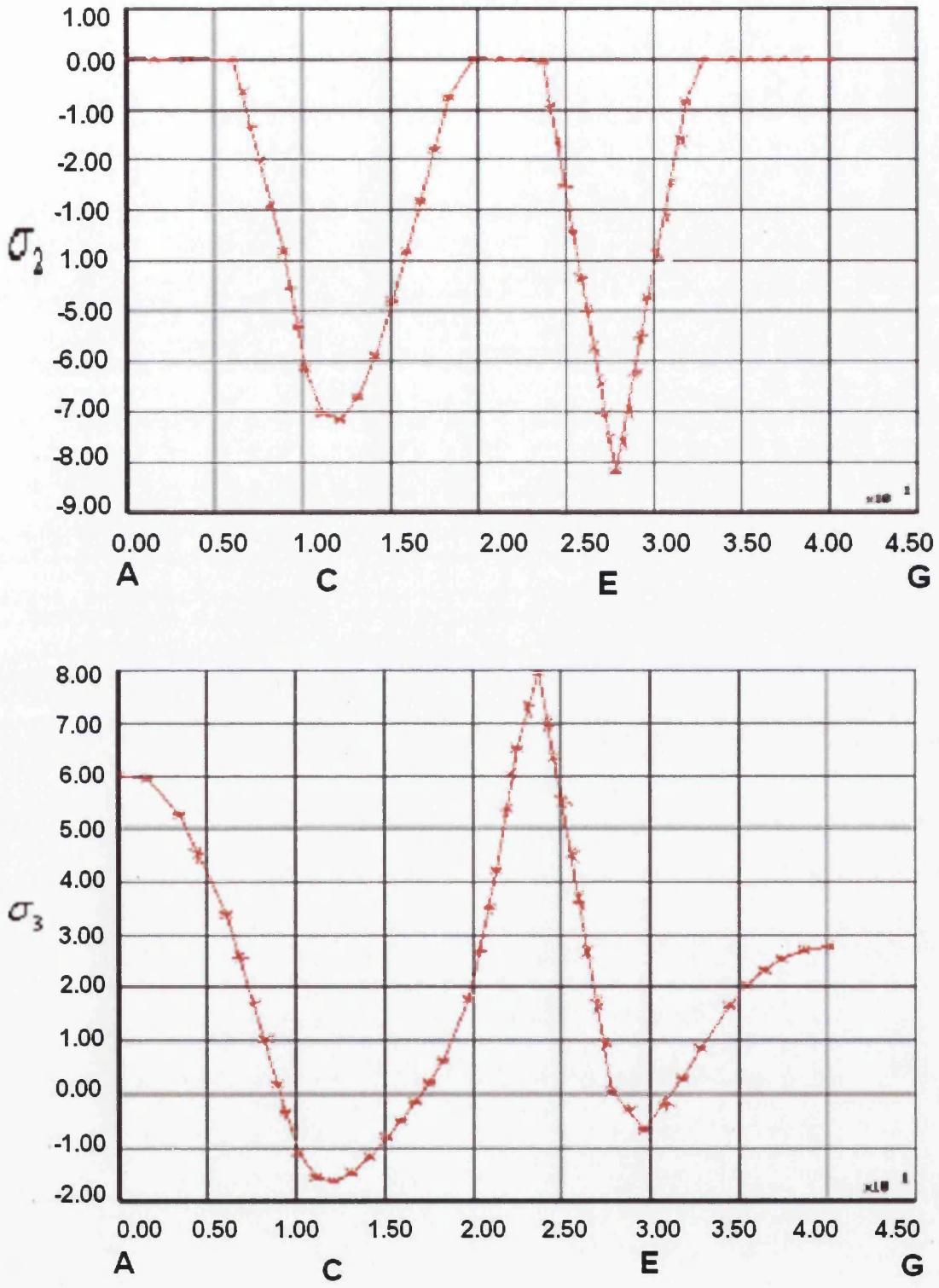

Figure 3.8: Principal stress distributions around the outside surface (G4, p = 0.1 MPa)

The von Mises equivalent stress contour plot, for p = 0.1 MPa, is shown in Figure 3.9. The equivalent stress distributions around the inside and outside surface are shown in Figure 3.10. The maximum equivalent stress is 13.88 MPa and occurs on the inner surface close to the point E in Figure 3.2. The maximum equivalent stress index, $\hat{I}_{eq}$ (or elastic equivalent stress concentration factor), is obtained by dividing the maximum equivalent stress by the nominal stress:

$$\hat{I}_{eq} = \frac{\hat{\sigma}_{eq}}{(\sigma_{eq})_{nom}} \qquad \ldots (3.1)$$

where the nominal stress is found from:

$$(\sigma_{eq})_{nom} = \frac{1}{\sqrt{2}} \sqrt{[(\sigma_1 - \sigma_2)^2 + (\sigma_2 - \sigma_3)^2 + (\sigma_1 - \sigma_3)^2]} \qquad \ldots (3.2)$$

$$\text{where} \quad \sigma_1 = \frac{pD}{2t}, \quad \sigma_2 = \frac{pD}{4t}, \quad \sigma_3 = -\frac{p}{2} \qquad \ldots (3.3)$$

and D is the inside diameter.

Using p = 0.1 MPa, D = 53 mm and t = 1 mm:

σ_1 = 2.65 MPa, σ_2 = 1.325 MPa, σ_3 = -0.05 MPa, $(\sigma_{eq})_{nom}$ = 2.34 MPa and hence $\hat{I}_{eq}$ = 5.93.

It is clear that yielding will occur here first at a pressure which is well below the yield pressure for the plain tube region of the can with 1 mm wall thickness, which is

when $(\sigma_{eq})_{nom}$ = 100 MPa. Hence, scaling up these elastic results, first yield occurs when:

$$p_y = \frac{100}{13.88}.0.1 = 0.720\ \text{MPa}$$ - for the base

compared with:

$$p_y = \frac{100}{2.34}.0.1 = 4.27\ \text{MPa}$$ - for the plain tube

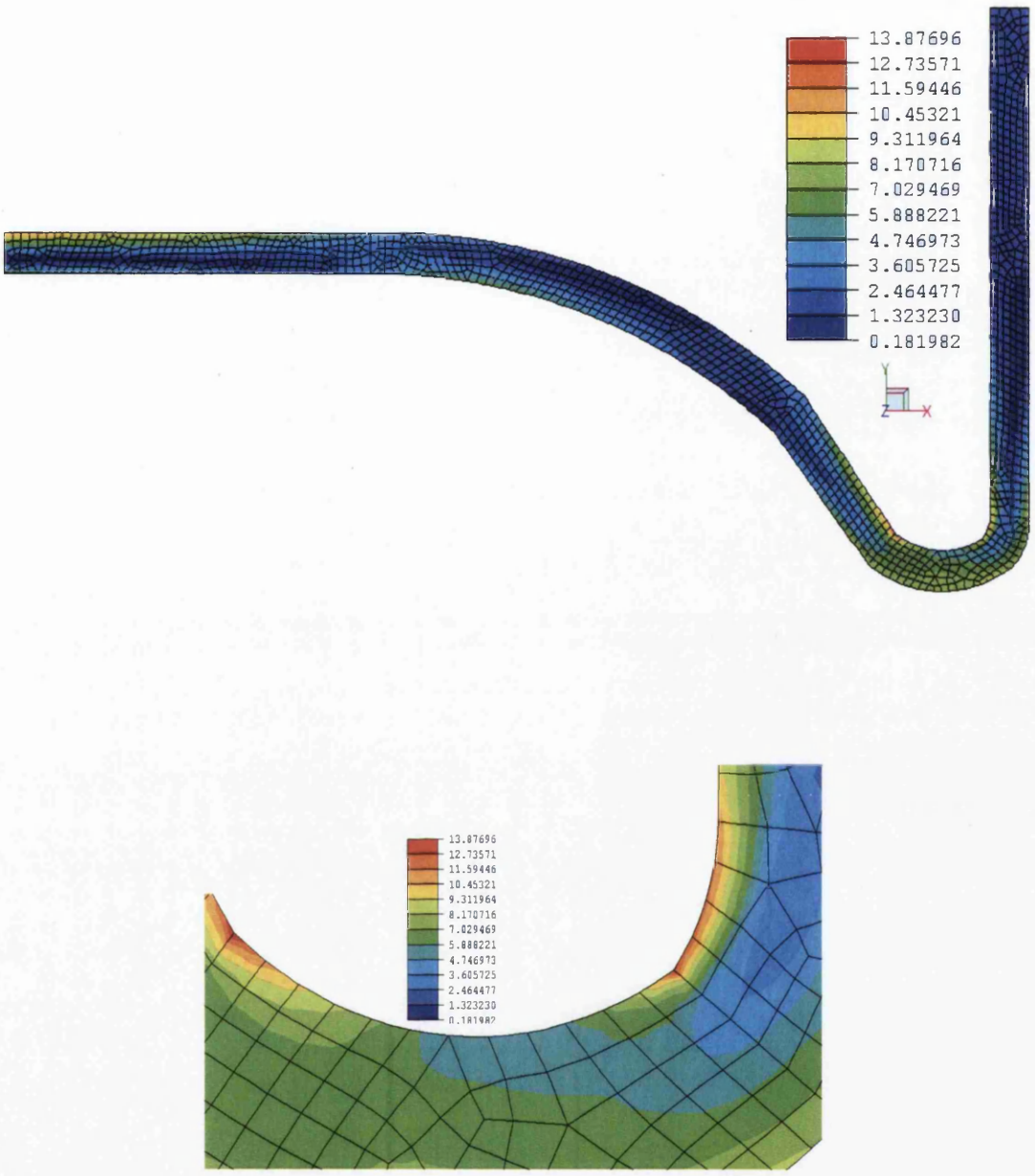

Figure 3.9: Equivalent stress contour plot (G4, p = 0.1 MPa)

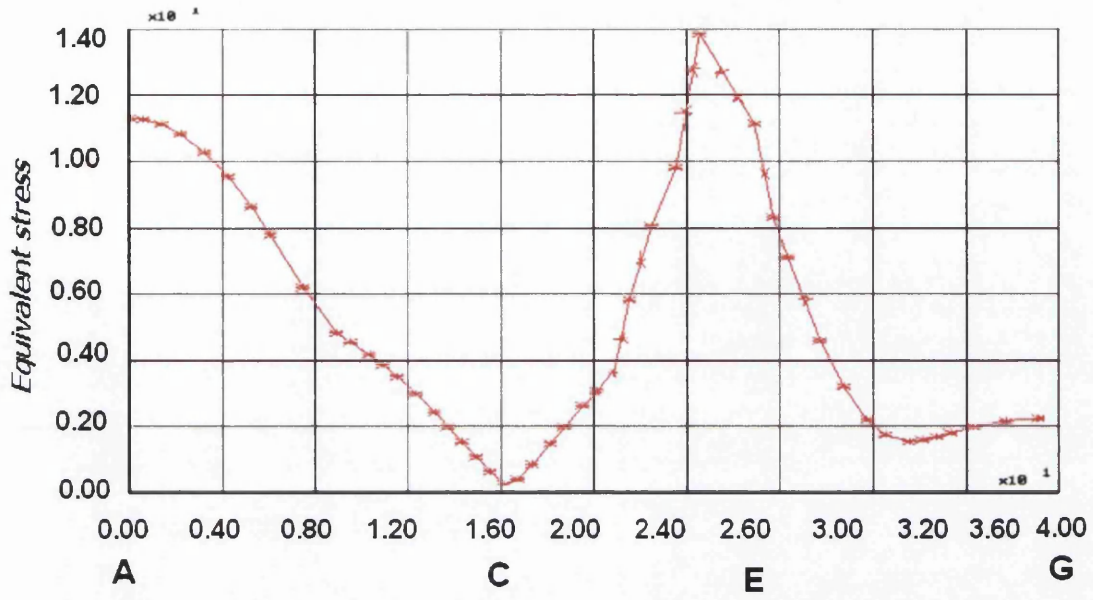

(a) Inside surface

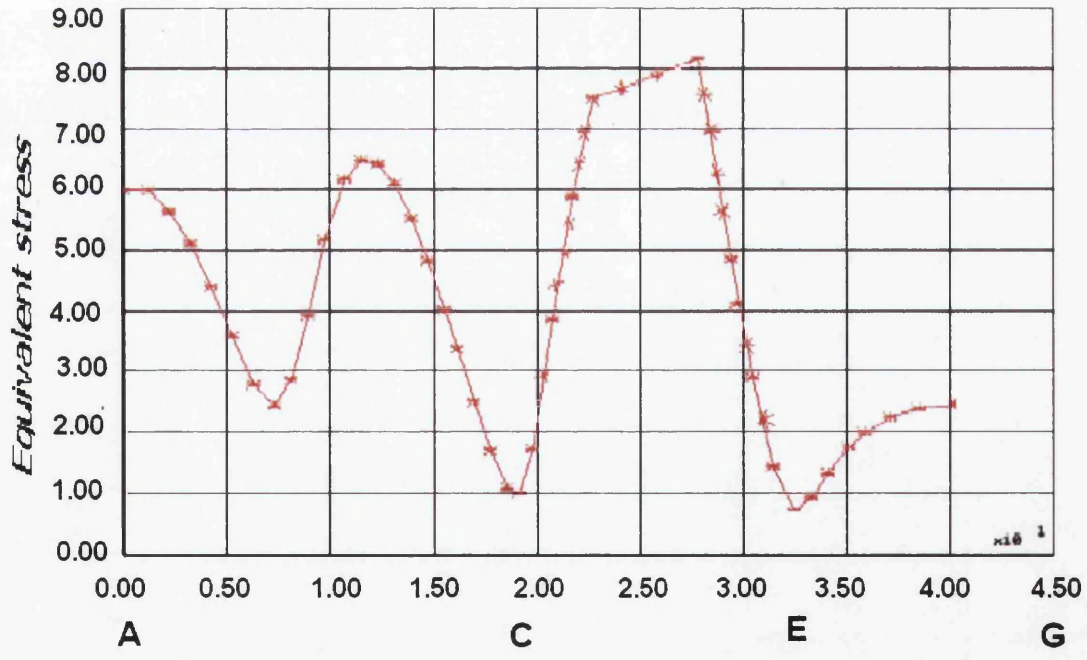

(b) Outside

Figure 3.10: Equivalent stress distribution (G4, p =0.1 MPa)

3.2.4.2 Effects of wall thickness

Equivalent stress contour plots for t = 0.4, 0.6, 0.8, 1.2 and 1.4 (which represents the variation in thickness seen in actual cans), with an internal pressure of 0.1 MPa are shown in Figures 3.11, 3.12, 3.13, 3.14 and 3.15 respectively.

The maximum equivalent stresses in each case are in the corner region close to the point E (see Figure 3.2) and decrease with increasing thickness. The equivalent stress for t = 0.4 mm (Figure 3.11) varies between 62.2 and 0.13 MPa close to the Sections DD and EE in Figure 3.2. For t = 0.6 mm, (Figure 3.12), the equivalent stress varies between 43.5 and 0.27 MPa close to the Section EE. For t = 0.8 mm (Figure 3.13), the equivalent stress varies between 24.9 and 0.03 MPa close to the Section DD and EE. For t = 1.2 mm (Figure 3.14) the equivalent stress varies between 8.48 and 0.06 MPa close to the Section DD and EE, and for t = 1.4 mm (Figure 3.15) the equivalent stress varies between 6.72 to 0.02 MPa close to the Section DD and in the Section AA in Figure 3.2. The relationship between thickness and maximum stress is clearly non-linear.

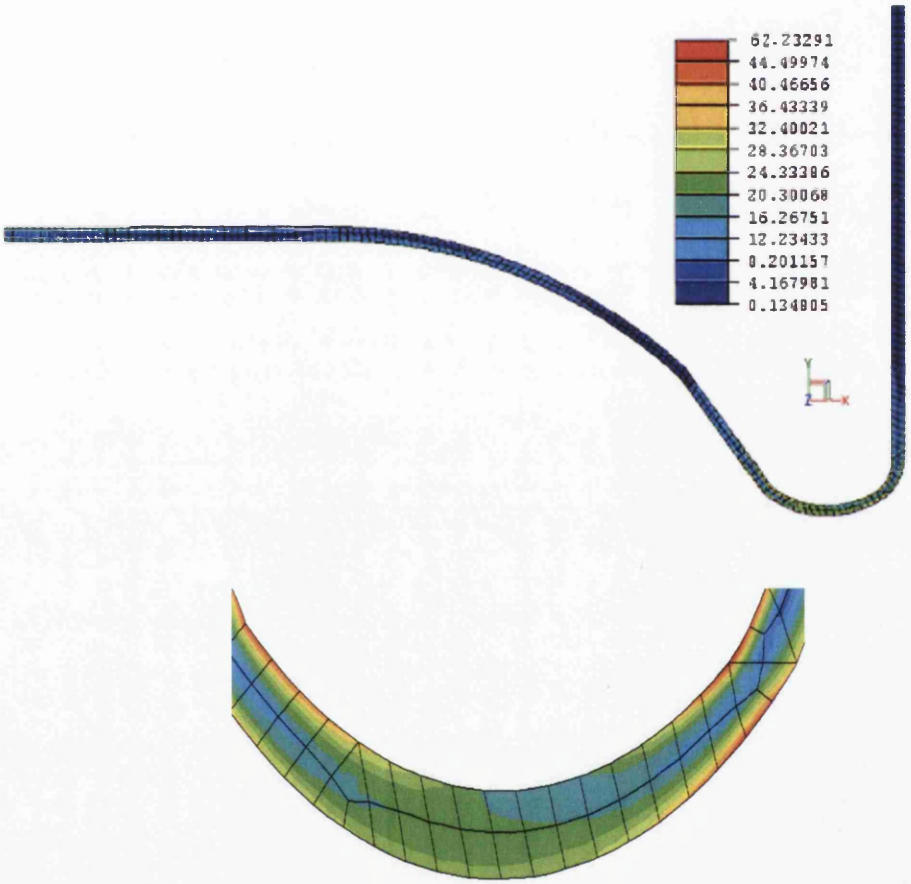

Figure 3.11: Equivalent stress contour plot (G1, p = 0.1MPa)

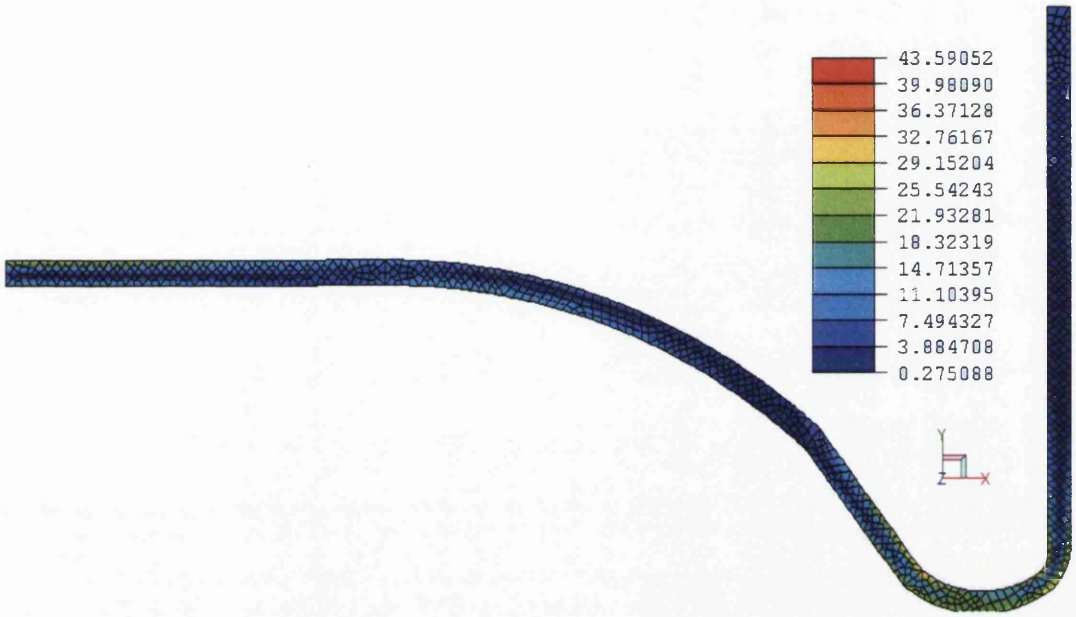

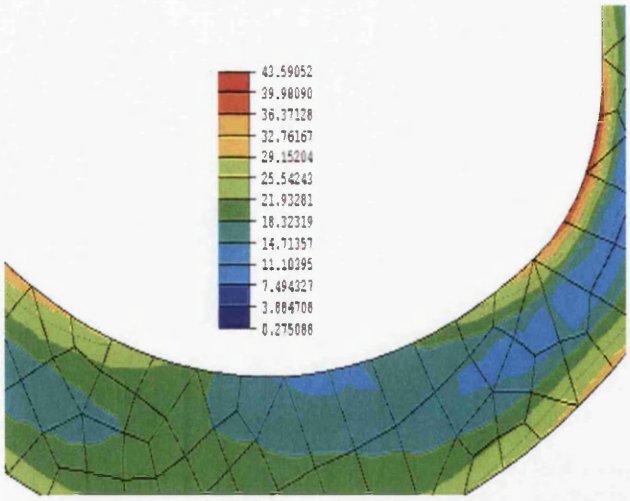

Figure 3.12: Equivalent-stress contour plot (G2, p = 0.1 MPa)

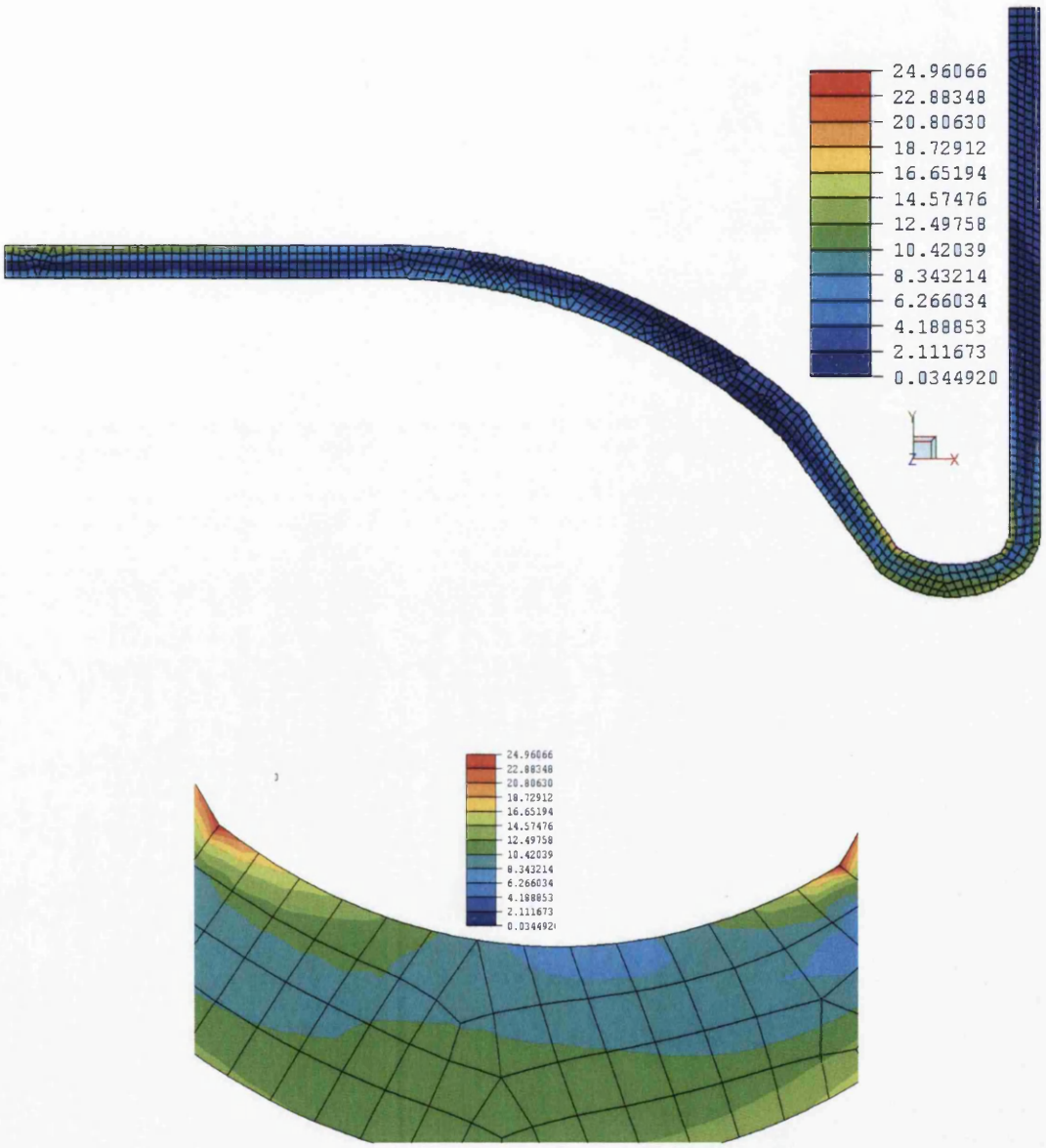

Figure 3.13: Equivalent stress contour plot (G3, p = 0.1MPa)

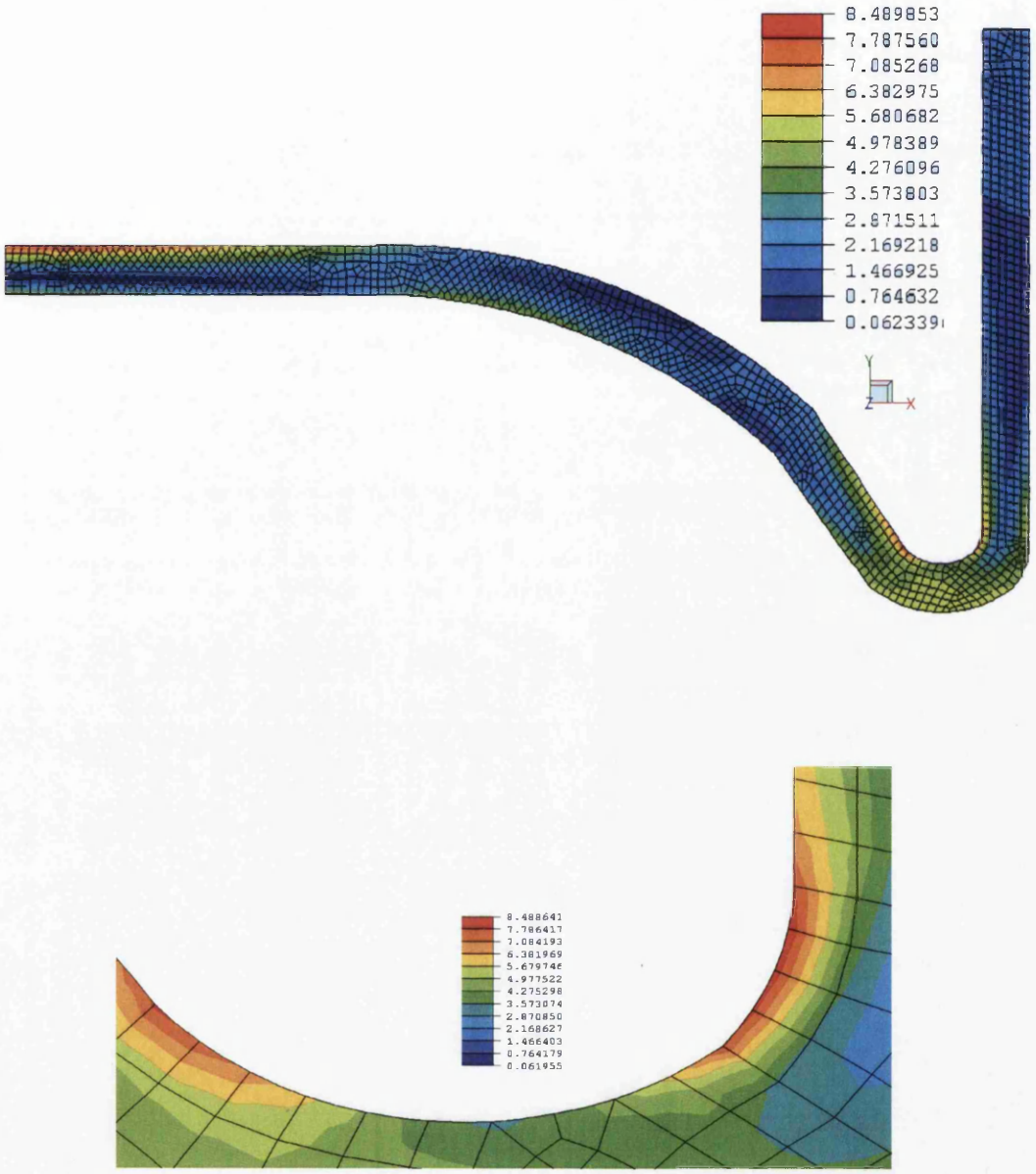

Figure 3.14: Equivalent stress contour plot (G5, p = 0.1 MPa)

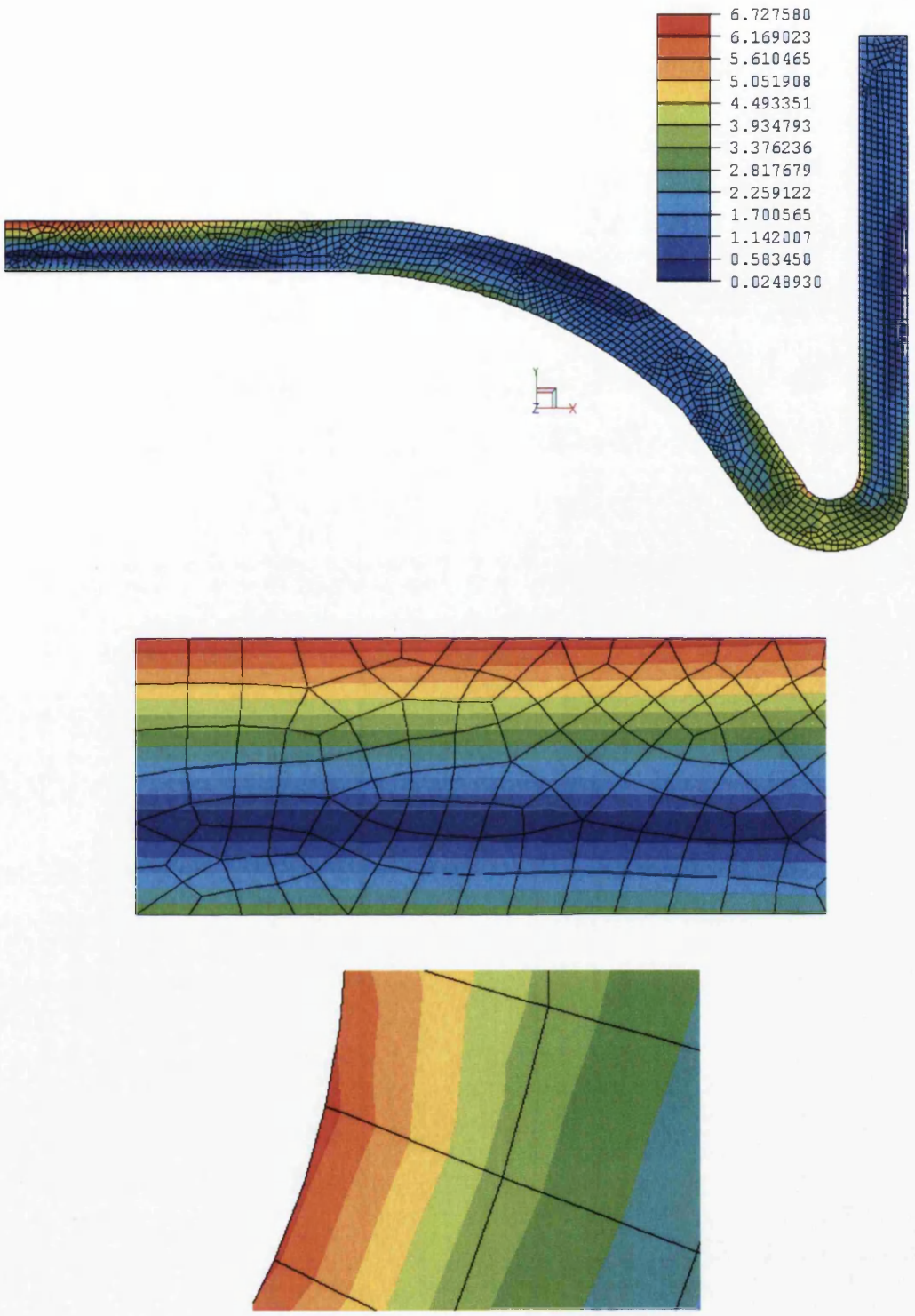

Figure 3.15: Equivalent Stress Contour plot (G6, p = 0.1 MPa)

A summary of the maximum equivalent stresses, nominal stresses and maximum equivalent stress indices, together with the number of elements in each mesh, is

presented in Table 3.3. These results are presented graphically in Figures 3.16 and 3.17. It is clear that the relationship between $\hat{I}_{eq}$ and thickness is reasonably linear for t in the range 0.4 to 1.4 mm, whereas changes in thickness have a more marked effect on maximum equivalent stress particularly when the value of thickness is at the higher end of the range considered.

These results are presented in an alternative form in Figure 3.18. Here, the diameter has been normalised by dividing by the thickness to give the dimensionless parameter D/t.

Geometry	**G1**	**G2**	**G3**	**G4**	**G5**	**G6**
Thickness (mm)	0.4	0.6	0.8	1.0	1.2	1.4
D/t	132.50	88.33	66.25	53	44.16	37.85
$\hat{\sigma}_{eq}$	62.23	43.59	24.96	13.88	8.48	6.72
$(\sigma_{eq})_{nom}$	5.77	3.86	2.91	2.34	1.95	1.65
$\hat{I}_{eq}$	13.83	11.29	8.58	5.93	4.34	4.07
No of elements	424	889	894	1267	1514	1787

Table 3.3: The variation of maximum equivalent stress index with wall thickness

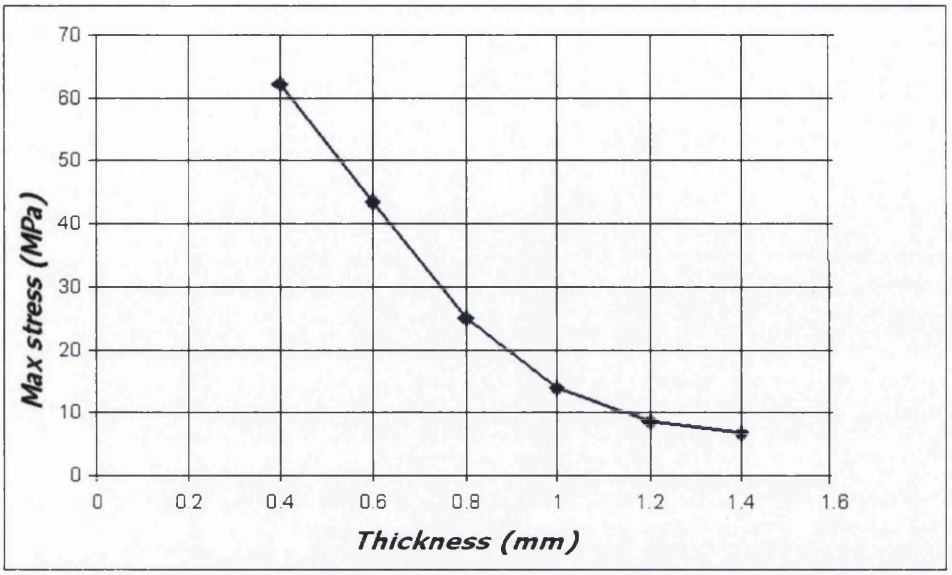

Figure 3.16: The relationship between wall thickness and maximum equivalent stress

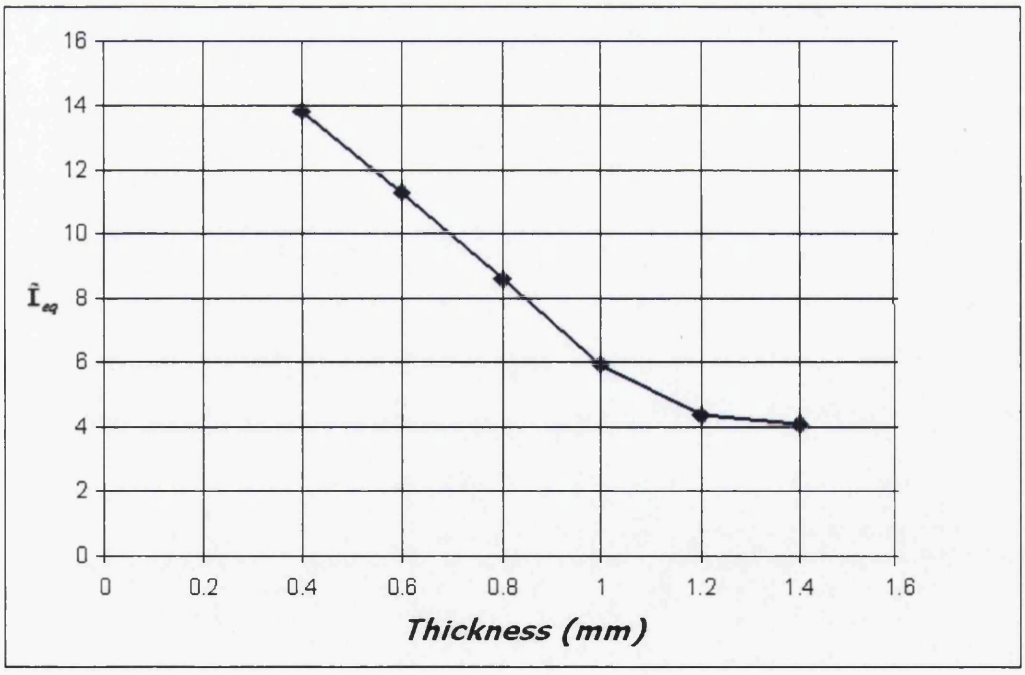

Figure 3.17: The relationship between maximum elastic equivalent stress index and the wall thickness

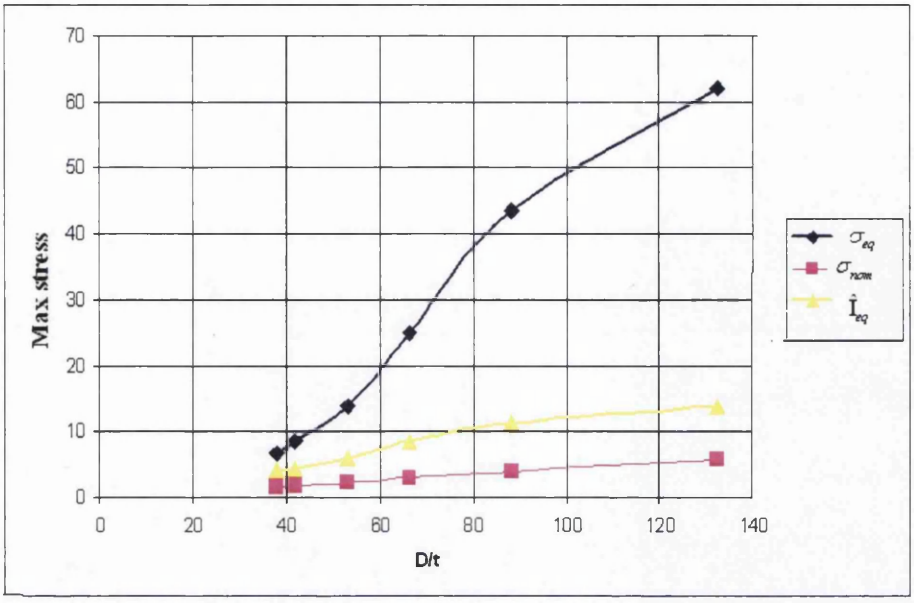

Figure 3.18: Maximum equivalent stresses, nominal stresses and maximum equivalent stress indices versus D/t ratio

3.2.4.3 Limiting pressures

Using the method of analysis discussed in Section 3.2.4.1, the elastic predictions have been scaled linearly in order to obtain values of the limiting pressure (the pressure at which yielding will first occur) for the can base as well as for the plain tube region. These predictions are presented in Table 3.4 and Figure 3.19. It can be seen that the relationship is reasonably linear over the range 0.4 mm $\leq$ t $\leq$ 1.4 mm.

Thickness (mm)	D/t	Limiting pressure (MPa)	
		Can Base	Plain Tube
0.4	132.50	0.16	1.73
0.6	88.33	0.22	2.59
0.8	66.25	0.40	3.43
1.0	53	0.72	4.27
1.2	44.16	1.17	5.12
1.4	37.85	1.49	6.06

Table 3.4: Limiting pressures for constant thickness cans

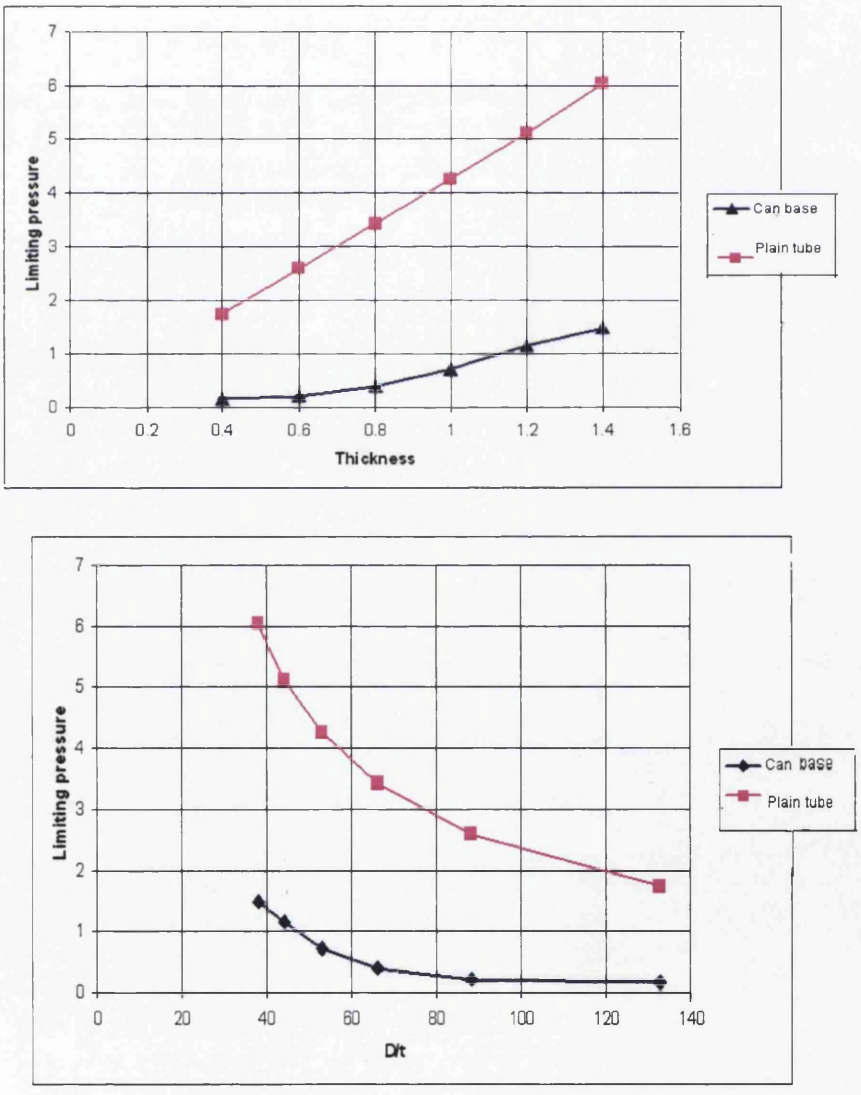

Figure 3.19: Variation of limiting pressure with wall thickness and D/t

3.2.5 Can with varying thickness

In practice, the actual thickness profile of a can is highly non-uniform for a number of reasons. Based on experimented measurements, Patten [2] obtained a thickness profile and this has

been used here to obtain realistic values of stress and limiting pressure. It was found that the thickness varies in the range from 0.31 mm to 1.31 mm. A variable thickness model, which reflects the true thickness profile of measured cans has been used and it is clear that there is a significant difference between the thickness of the cylindrical section (0.31 mm minimum) and that of the base (1.31 mm maximum). The basic finite element model is shown in Figure 3.20. The constraints, loading conditions and material properties are as discussed in Sections 3.2.2 and 3.2.3 for the constant thickness models. A suitable mesh of 8 noded, axisymmetric, isoparametric elements was generated using the ELFEN mesh generator and is shown in Figure 3.21.

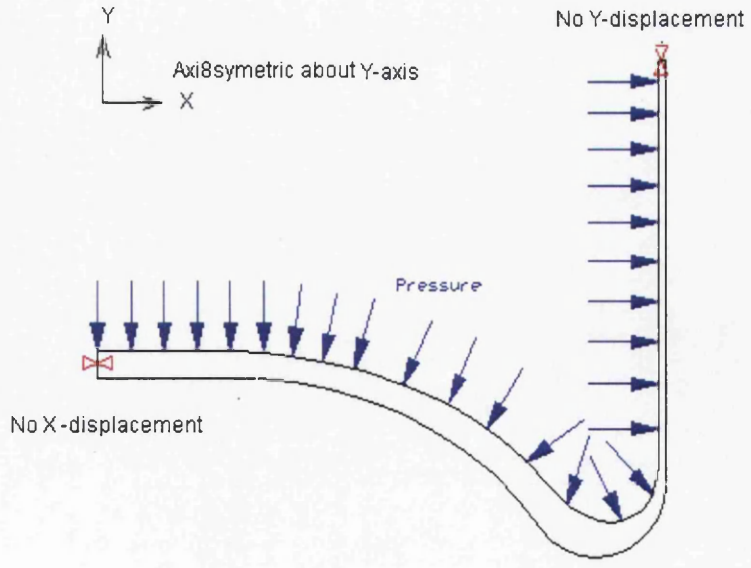

Figure 3.20: Finite element model of can with varying thickness

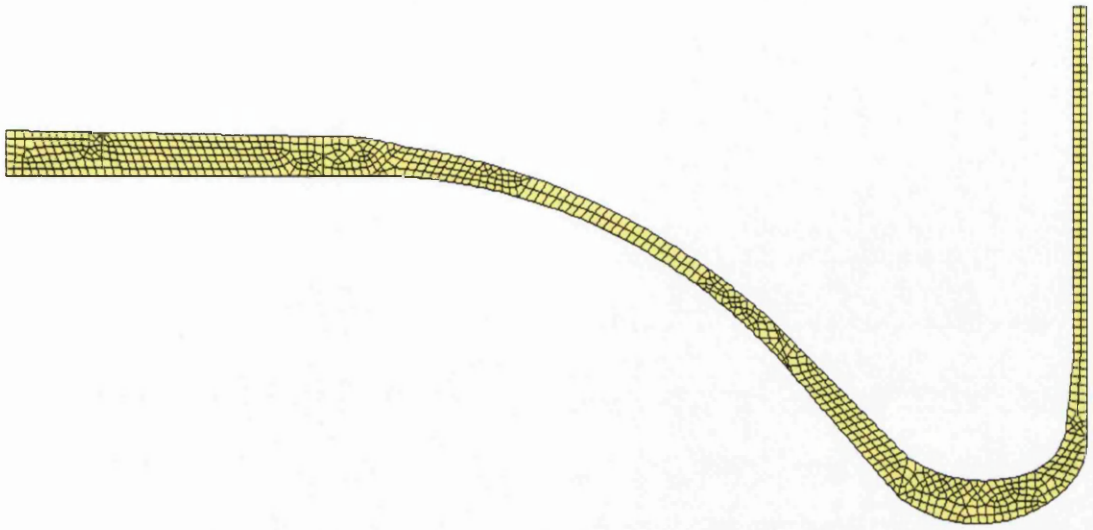

Figure 3.21: Finite element mesh for can with varying thickness

3.2.5.1 Results

The predicted variation in maximum equivalent stress, for an internal pressure of 0.1MPa, is shown in the form of a contour plot in Figure 3.22. There are large stress gradients close to the regions CC and FF in Figure 3.2 and the maximum value of equivalent stress is 25.68 MPa at the interface between the base and the cylinder. The distribution of equivalent stress around the inside and outside surfaces is shown in Figures 3.23 and 3.24 respectively. Inner surface equivalent stresses are generally greater than the corresponding outer surface values.

From the experimental measurements, it is seen that the thickness in the plain region of an actual can is approximately 0.31 mm and this gives a nominal stress of 7.43 MPa (Equation 3.2) and, therefore, a maximum equivalent stress index of 3.45.

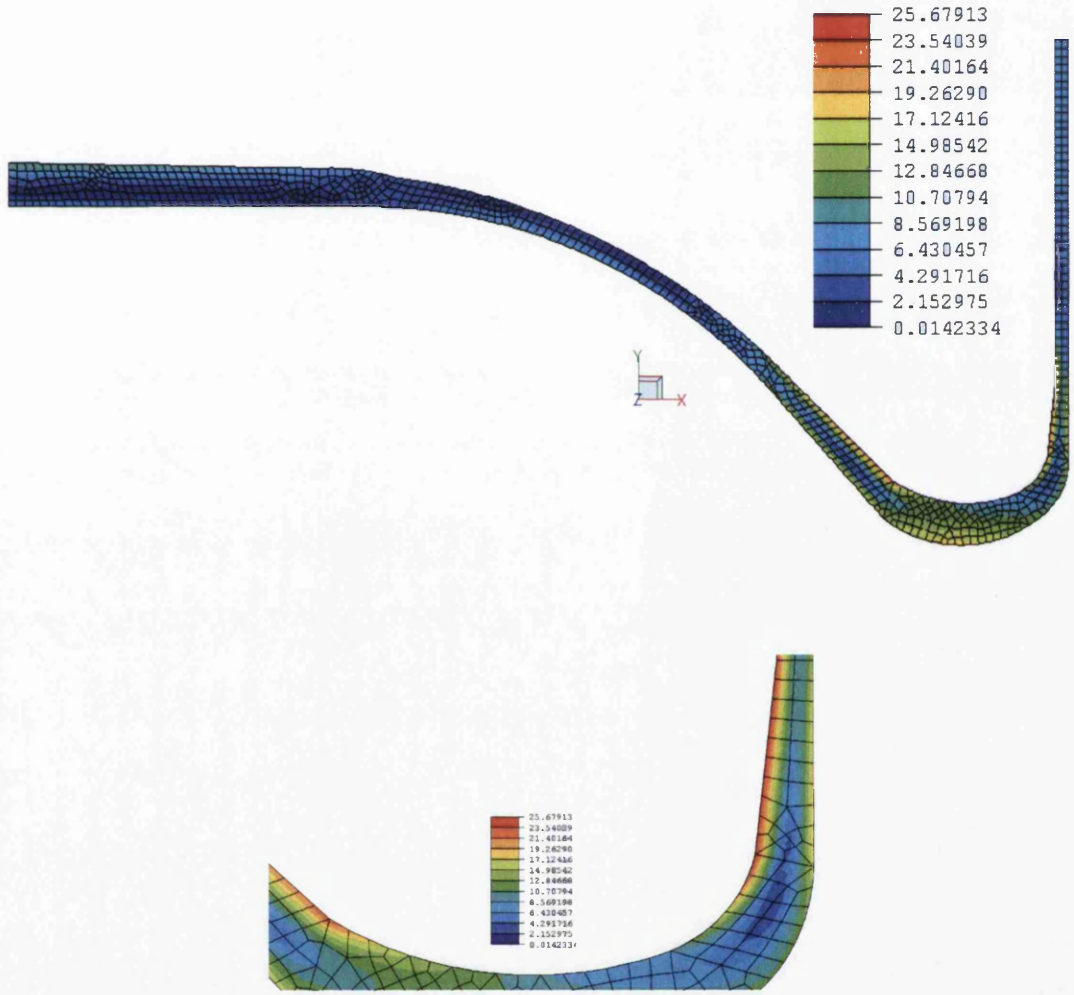

Figure 3.22: Equivalent stress contour plot at internal pressure of 0.1 MPa

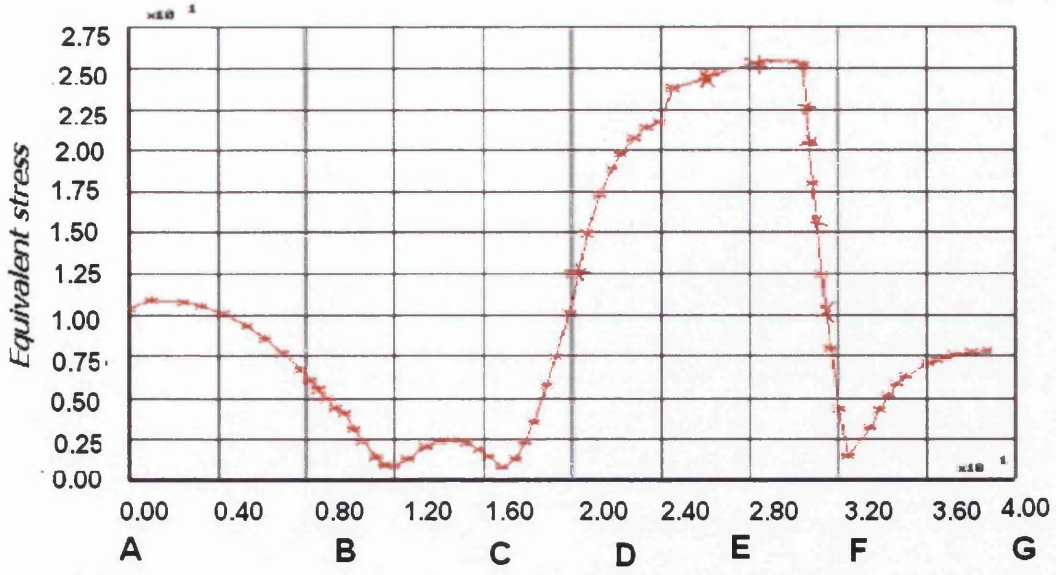

Figure 3.23: Equivalent stress distribution around inside surface

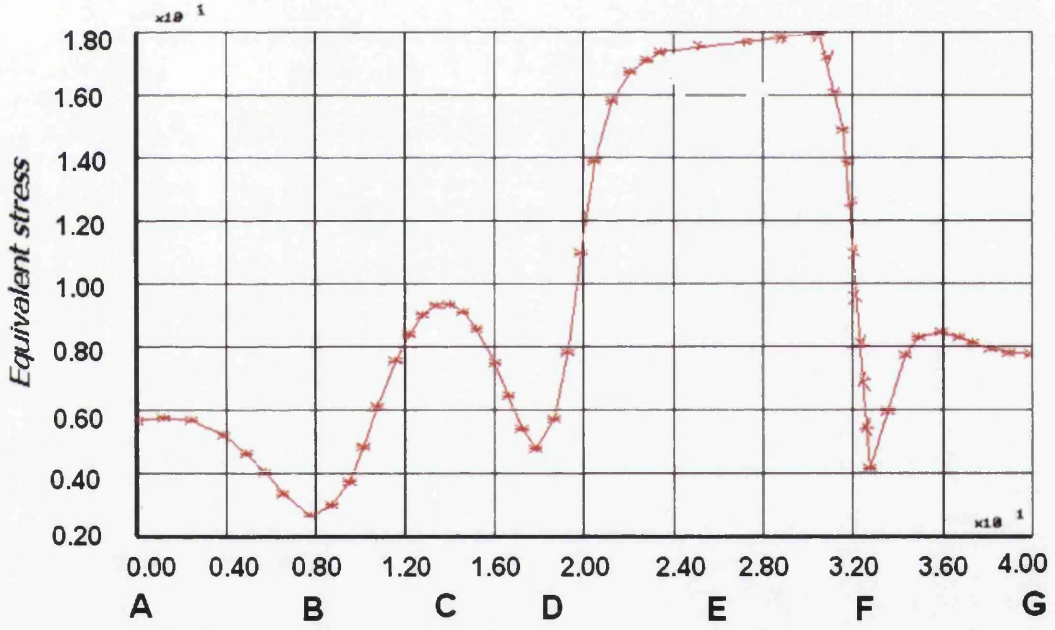

Figure 3.24: Equivalent stress distribution around outside surface

The limiting pressure (the pressure at which yielding will first occur) has been obtained using the method described in Section 3.2.4.1 and a value of 0.38 MPa is predicted. This result is seen to compare to an average thickness of 0.73 mm. It is clear from Figure 3.22 that there are very low stresses in the central region of the base of the actual can, compared to the intersection region, and thus the amount of

the aluminium in this region can be reduced with no significant effect on the integrity of the can. This will be the subject of the optimisation analysis discussed in Chapter 6.

3.3 Elastic-plastic finite element analysis using axisymmetric models

The finite element models and loading conditions considered here are the same as those used for the elastic analysis discussed in 3.2.1and 3.2.2.

3.3.1 Constant thickness model

The objective of this model is to predict the maximum possible internal pressure the pressurised can will withstand before plastic buckling (plastic snap-through) of the base occurs. This model was used initially to investigate the stress concentrations, optimise the mesh density and provide a better understanding of how to improve the can base strength. The basic geometry is identical to that used in the elastic analysis and shown in Figure 3.1. An identical mesh to that used for the elastic analysis and seen in Figure 3.3 has been used here. The finite element mesh was generated automatically using the ELFEN mesh generation. In the modelling of aluminium cans, the deformation of the can base is non-linear. The material deforms plastically and also the deformations are large enough to cause the loading direction and stiffness to change throughout the analysis. This change in loading direction and geometry-dependent stiffness is referred to as a geometric non-linearity (GNL) and the GNL option within ELFEN was selected for these analyses. The non-linear finite element analysis is achieved by incrementing the applied load in very small steps allowing the stresses to be calculated at each load increment.

3.3.2 Material models

The multi-linear uni-axial stress-strain characteristic for the aluminium used in can production is shown in Figure 3.25 and was derived by Patten [2] from experimental results. Two types of finite element model have been used to represent this data:

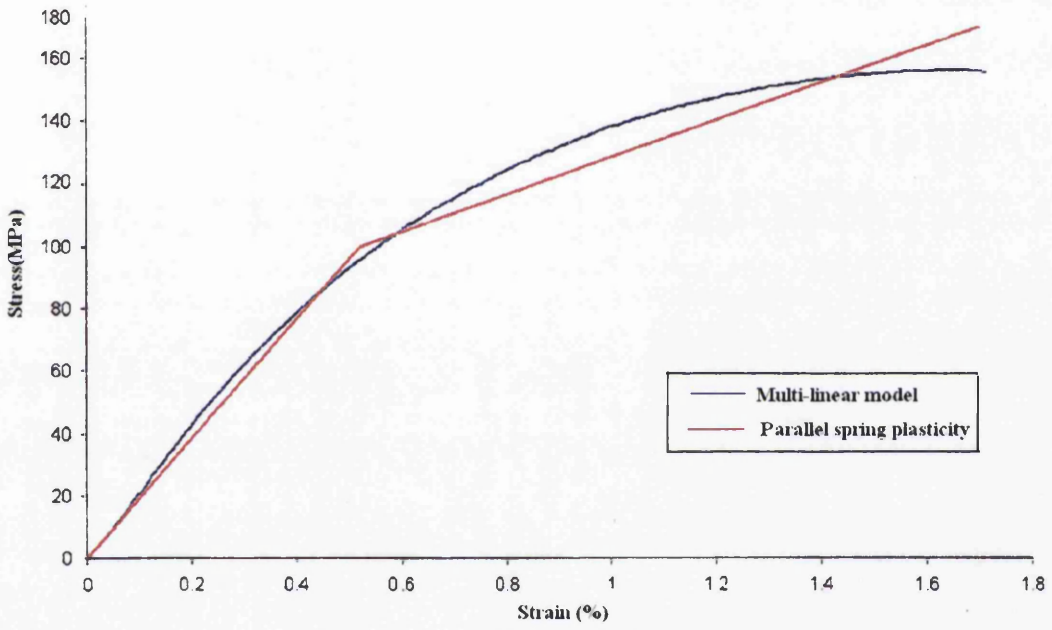

Figure 3.25: Parallel spring plasticity Vs multi-linear model

a) Elastic-perfectly-plastic (Figure 3.26)

Using this model, the von Mises equivalent stress cannot exceed yield stress (σ_y = 100 MPa). Once yielding occurs across a section of the tube, the finite element procedure will no longer converge since the model predicts infinite strains and the 'plastic collapse' condition is reached. This model is extremely conservative and under predicts stresses.

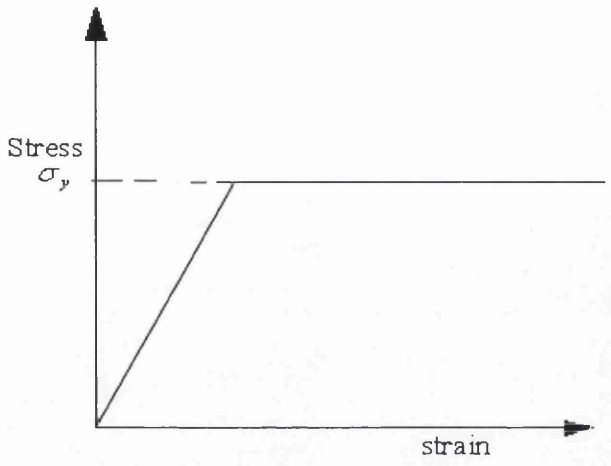

Figure 3.26: Stress-Strain relationship for an elastic-perfectly-plastic material model

b) Bi- and multi-linear work hardening

In order to improve the accuracy of the model, a simple solution is to assume a bi-linear relationship. This is known as a parallel spring model [17] as can be seen in Figure 3.27. The model will now predict stresses above the yield stress and the material is said to work (or strain) harden. However, this model will not predict collapse since the stress can continue to increase with increasing load.

The most accurate model is the one that uses a series of straight lines to model the true σ-ϵ behaviour up to the ultimate tensile strength of the material (156 MPa). The data for this multi-linear σ-ϵ curve is shown in Table 3.5.

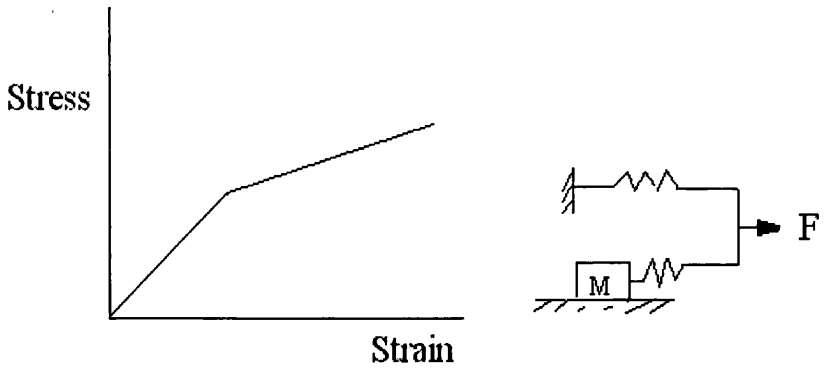

Figure 3.27: Parallel-springs plasticity model

Plastic strain (%)	Stress (MPa)
0	100
0.08	106
0.18	115
0.28	124
0.38	132
0.48	138
0.58	143
0.68	148
0.78	151
0.88	153
0.98	155
1.08	156
1.18	156

Table 3.5: Plastic stress-strain data for multi-linear material model [2]

3.3.3 Finite Element results for geometry G4

A typical geometry (i.e. Geometry 4) having t = 1mm is selected for a full review. The pressure load was increased from 0 up to failure (collapse). The load was incremented from an initial time factor of 0.1 to a total stage time 1.0. A Newton-Raphson iteration method [17] was used to perform an equilibrium check, to ensure that the predicted results satisfy the underling differential equation.

3.3.3.1 Elastic-perfectly-plastic model

The results of the analysis are shown as stress contours in Figures 3.28 to 3.31 for pressure increments of 0.22 MPa and starting at 1.0 MPa. Equivalent stresses slightly higher than the uni-axial yield stress (100 MPa) are predicted due to the convergence criteria within the ELFEN program. These figures indicate that major plastic zones develop in the regions AA to BB and DD to FF (see Figure 3.2) and that failure ultimately occur when a plastic hinge forms between DD and FF. From these predictions, it was established that first yield and plastic hinge occur at pressures of 0.72 and 1.60 MPa respectively.

These figures indicate the regions of high stress and also the growth of the plastic zone. Yielding first occurs when p = 0.72 MPa, (Figure 3.28). As the pressure is increased, four plastic zones are clearly seen to develop, at points labelled A, B, C & D in Figure 3.2, for p = 1.2 MPa. A further increase in pressure to 1.4 MPa results in a 'plastic hinge' where the whole of Section XX (see Figure 3.30) has yielding because of the merger of zones B, C, & D. The size of zone A has also increased. However, the pressure can be further increased to 1.6 MPa before final collapse occurs (Figure 3.31) with further growth of the plastic zones.

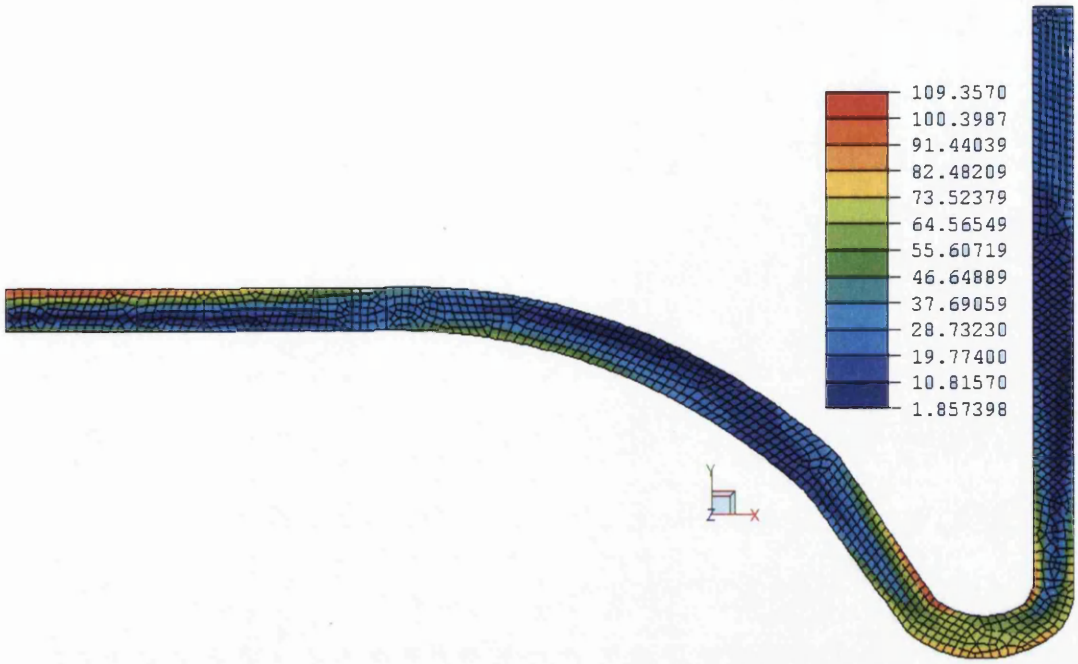

Figure 3.28: Von Mises stress contour plot for G4 with internal pressure = 1.0 MPa and EPP material model

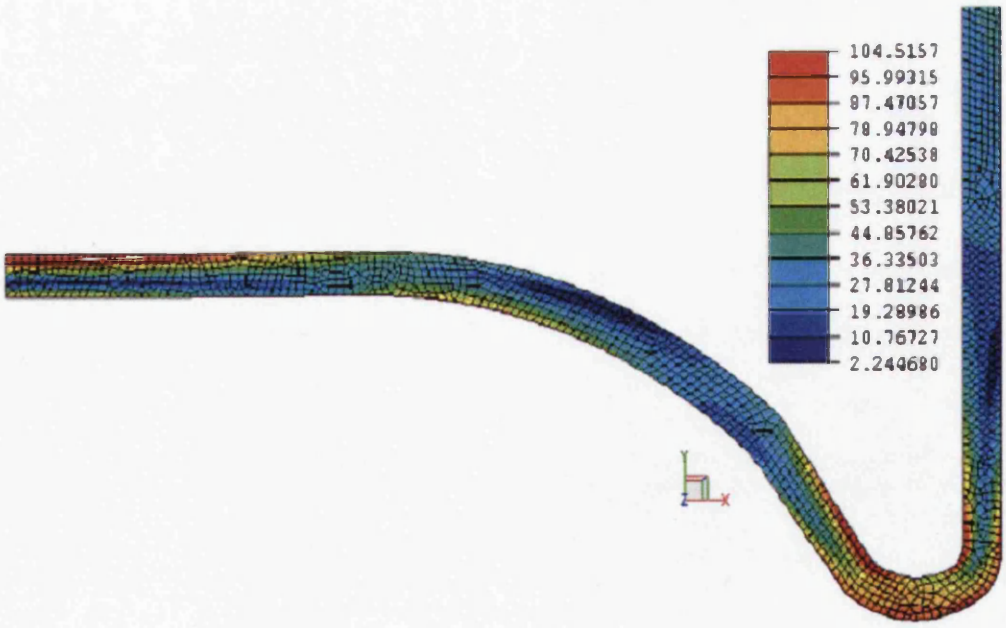

Figure 3.29: Von Mises stress contour plot for G4 with internal pressure = 1.2 MPa and an EPP material model

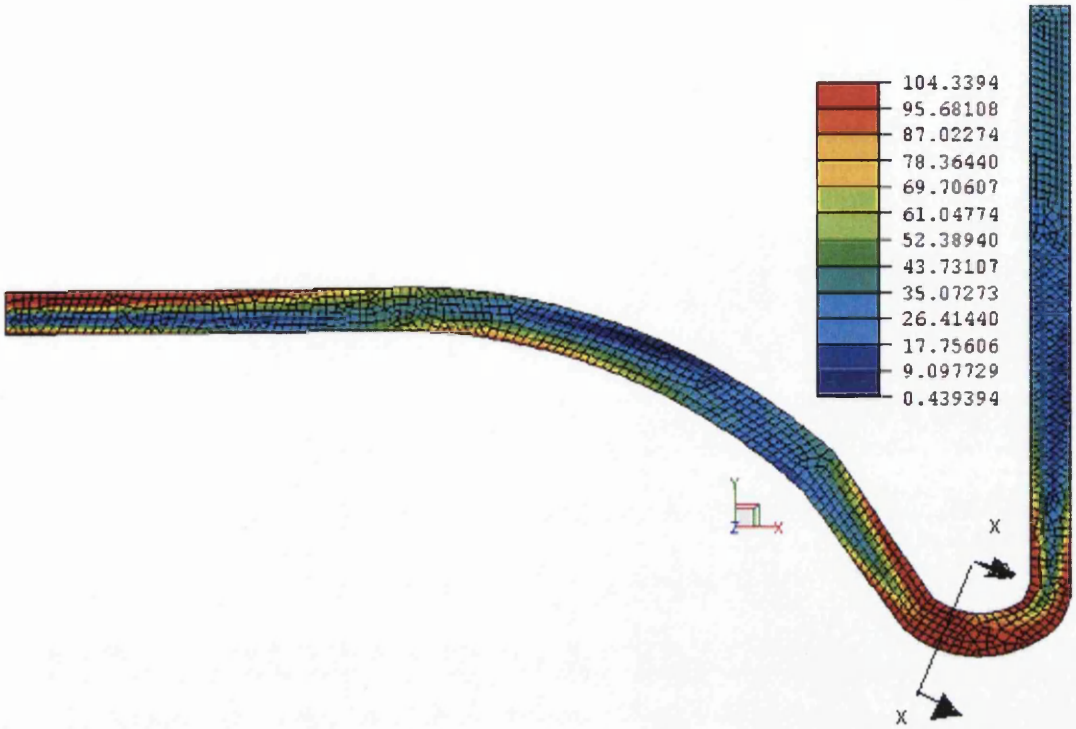

Figure 3.30: Von Mises stress contour plot for G4 with pressure = 1.4 MPa and an EPP material model

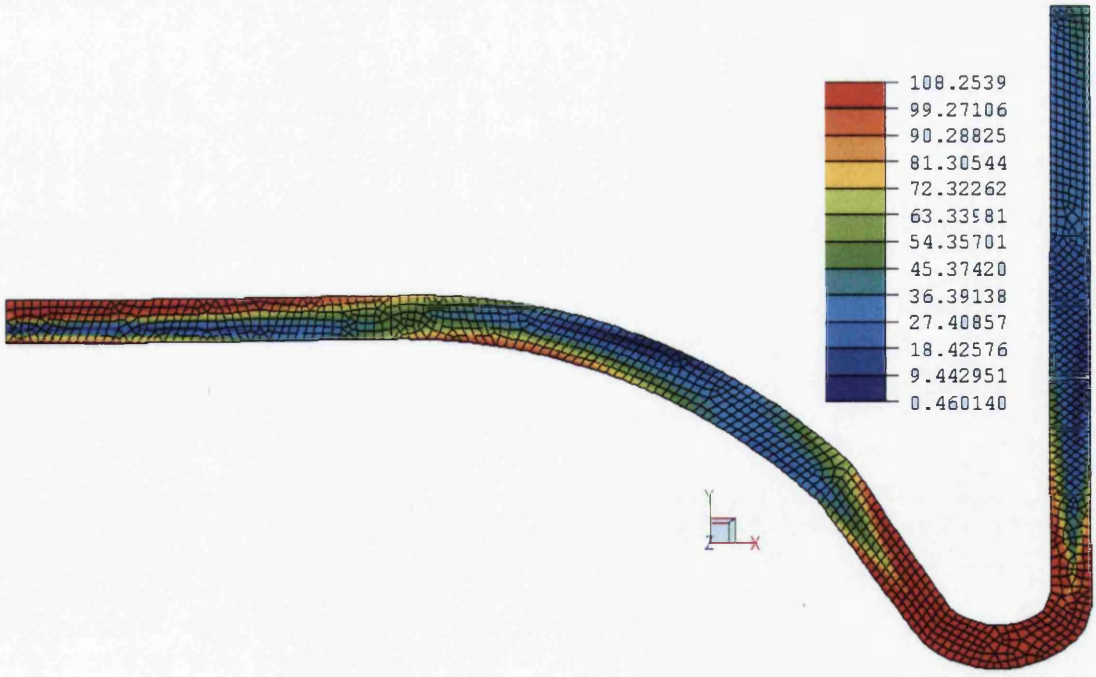

Figure 3.31: Von Mises stress contour plot for G4 with internal pressure = 1.6 MPa and an EPP material model

The corresponding equivalent stress distributions around the inside and outside surfaces are shown in Figures 3.32 and 3.33 respectively. It can be seen that the maximum stresses not exceed the yield stress when the pressure is 1.6 MPa. This is to be expected since the equivalent stress (which cannot exceed the yield stress) is a combination of the three principal stresses, which can therefore individually be greater that the yield stress.

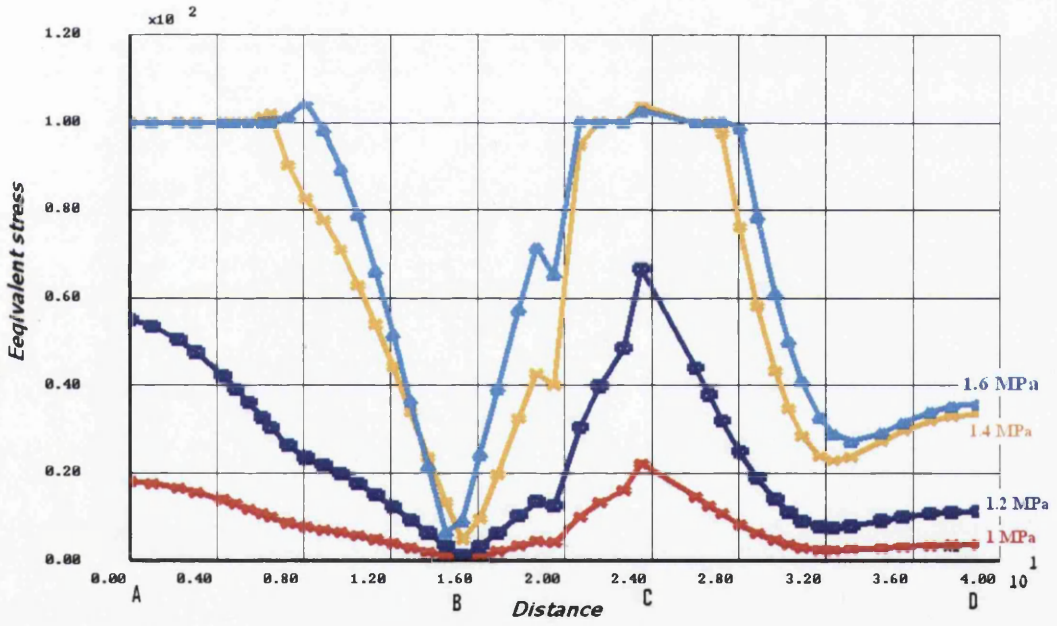

Figure 3.32: Equivalent stress distribution around the inside surface for G4 and an EPP material model

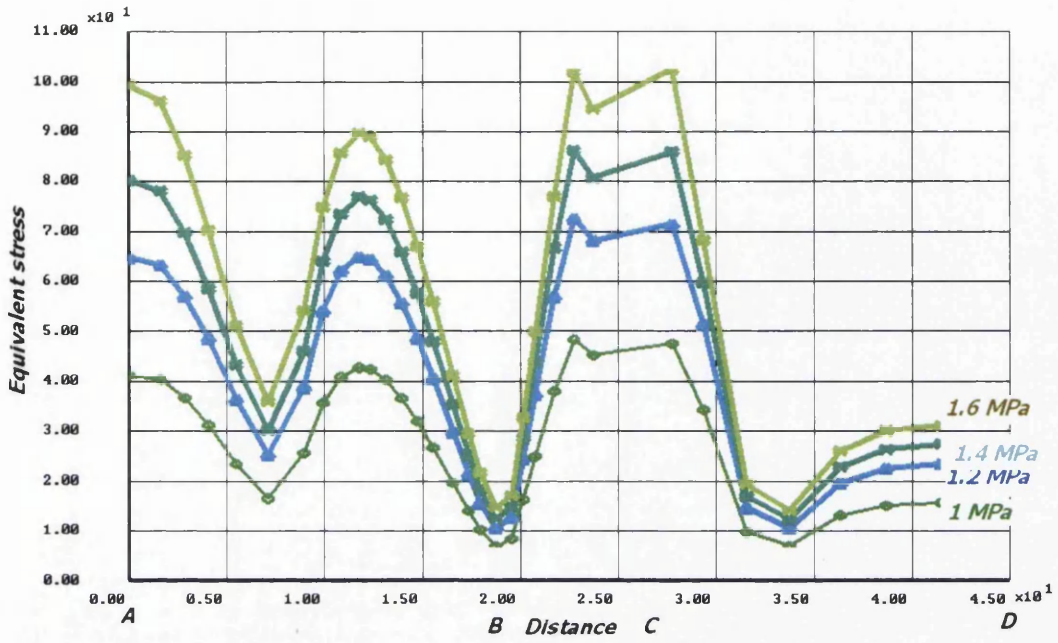

Figure 3.33: Equivalent stress distribution around the outside surface for G4 and EPP material model

3.3.3.2 Multi-linear work-hardening model

The results of the elastic-plastic analysis using a work-hardening material model are shown as equivalent stress contour plots in Figures 3.34 and 3.35 for pressures of 1.50 MPa (just before collapse) and 1.59 MPa (at collapse) respectively. The plastic hinge is clearly seen in Figure 3.34 to occur at the sharp radius close to the intersection of base and cylinder. The shape after collapse is also clearly seen in Figure 3.35. Very large deformation has taken place in the region of the plastic hinge, allowing the base to plastically buckle from a convex shape to a concave one.

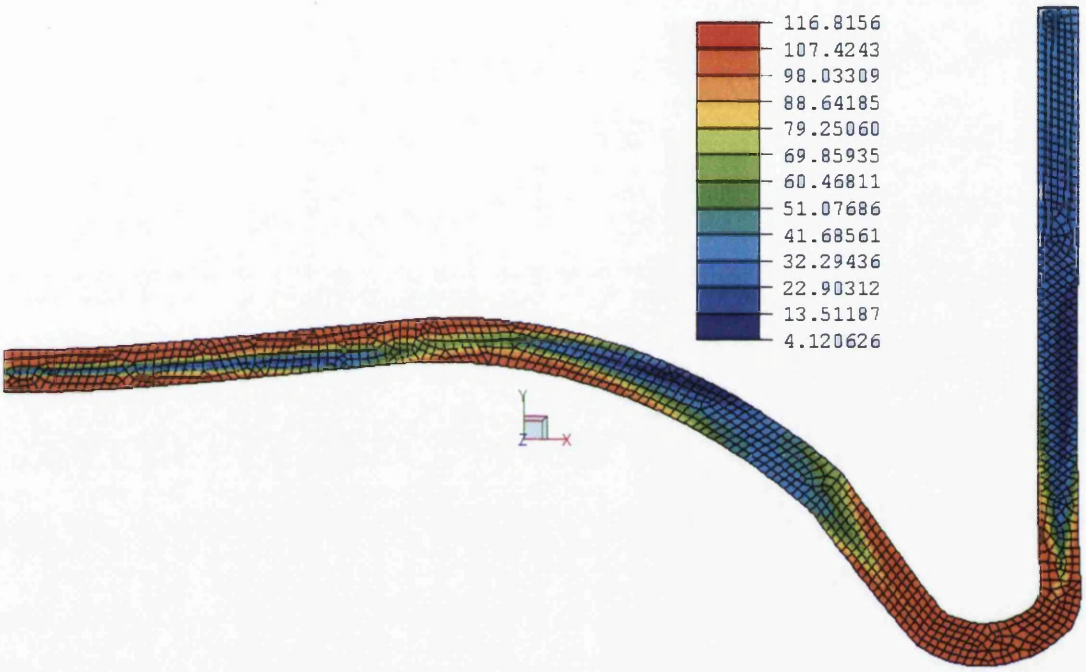

Figure 3.34: Equivalent stress contour plot (P = 1.50 MPa) for a multi- linear hardening material model

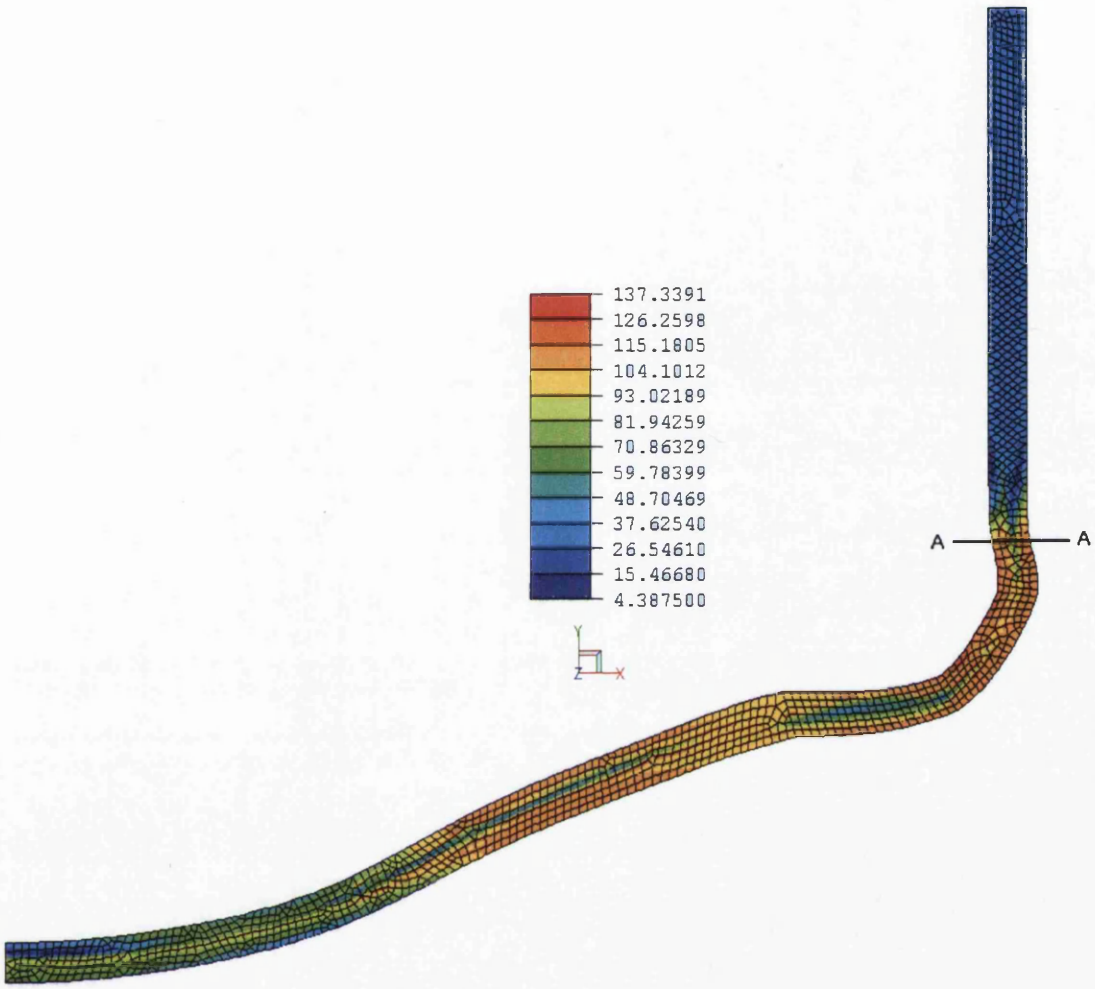

Figure 3.35: Equivalent stress contour plot (collapse, p =1.59 MPa)

3.3.4 Effects of wall thickness

The above analyses have been repeated for the other thickness values, using the multi-linear hardening model. The EPP model was not considered because it is not realistic and was only included for t = 1 mm for illustration. A summary of the results for the range of wall thickness is presented in Table 3.6 and Figure 3.36. Whereas the variation in limiting pressure is reasonably linear, the curve for collapse pressure shows a clear increase in slope with increasing thickness. This is important for material optimisation, as discussed in Chapter 6.

Wall thickness (mm)	Limiting pressure (MPa)	Collapse pressure (MPa)
0.4 (G1)	0.16	0.73
0.6 (G2)	0.22	0.93
0.8 (G3)	0.40	1.18
1.0 (G4)	0.72	1.59
1.2 (G5)	1.17	2.37
1.4 (G6)	1.49	3.56

Table 3.6: First yield and collapse pressures for different wall thickness

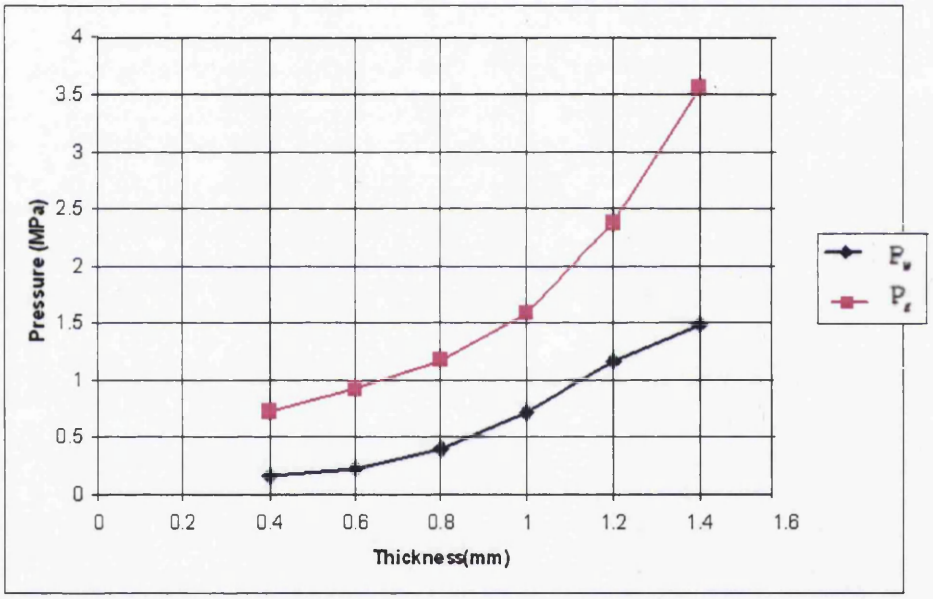

Figure 3.36: The relationship between wall thickness first yield and collapse pressure

3.3.5 Can with varying thickness

The geometry of the finite element model has previously been described in Section 3.2.5 and the finite element model is shown in Figure 3.20. The equivalent stress distribution just prior to collapse (at p = 1.50 MPa) and at collapse (p = 1.53 MPa) using the multi-linear work hardening material model previously described in

Section 3.3.2 are shown in Figures 3.37 and 3.38 respectively, superimposed on the displaced shape.

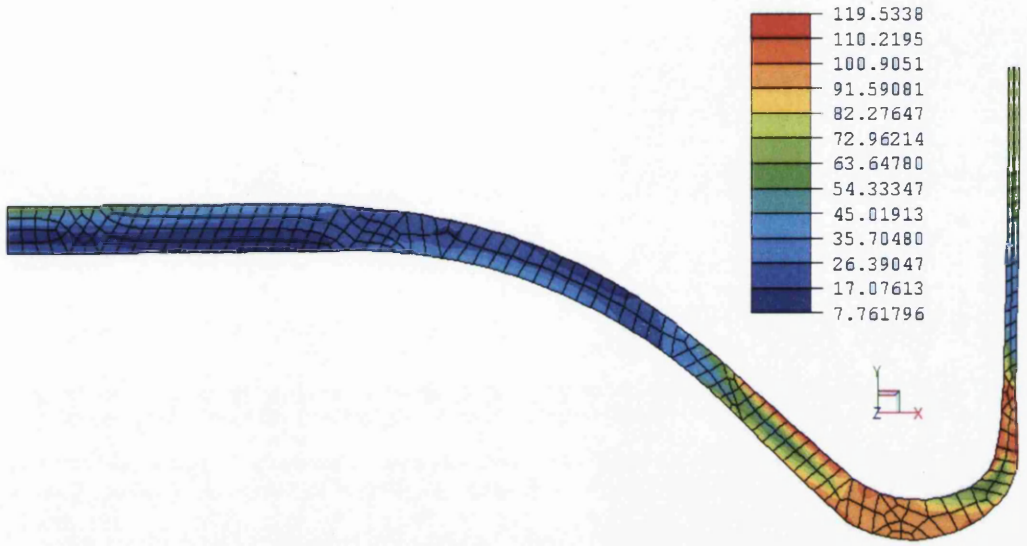

Figure 3.37 Equivalent stress contour plot (pre-buckling, pressure =1.50 MPa)

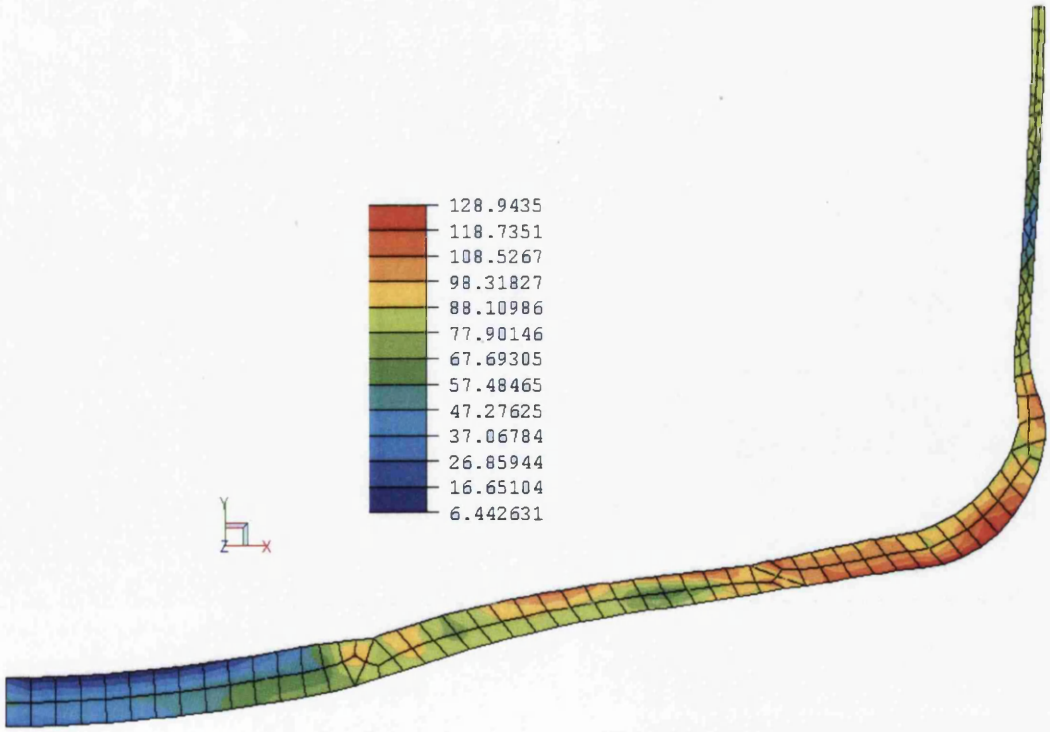

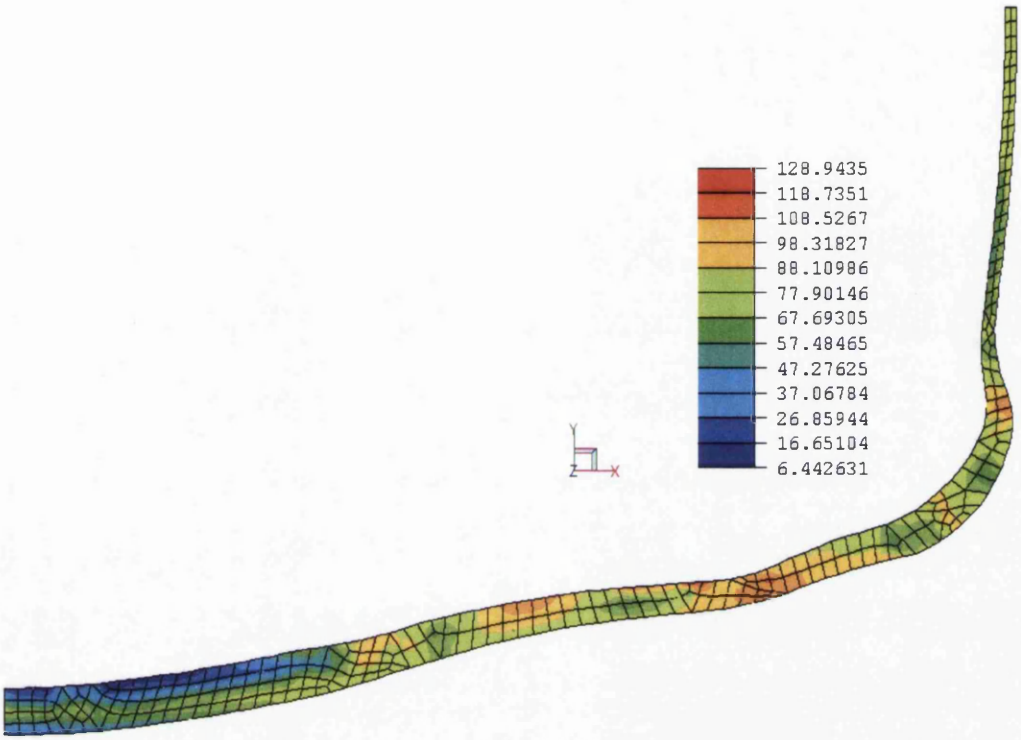

Figure 3.38: equivalent stress contour plot (collapse, pressure =1.53 MPa

As for the constant thickness models, regions of high stress are apparent in the DD to EE region of the base (see Figure 3.2). Also, the stress levels close to the axis of symmetry of the base are generally low because this region is significantly thicker than elsewhere. It is considered that shape optimisation could result in a significant reduction in material, while still retaining the plastic buckling and collapse characteristic of the can. This has been investigated in Chapter 6.

The internal pressure is a function of volume therefore any large deformation will cause the pressure inside the can to reduce.

This cannot easily be modelled, therefore the assumption is made that the pressure in the pressure test is increased very slowly such that the water pump will prevent a reduction in pressure due to increased volume.

3.4 Elastic-plastic finite element analysis using 3D models

The analyses discussed previously in this chapter, although useful in studying the mechanisms involved and the accuracy of the upper and lower bound estimates is not truly representative in one important respect. Experimental evidence suggests a slightly unsymmetrical buckling mode, due to minor radial variations in profile and there is a clear distinction between the elastic-plastic buckling of the base and burst (collapse) pressures, where bursting occurs in the plain tube region. This behaviour cannot be predicted using an axisymmetric model. Therefore a full three-dimensional model was developed and elastic-plastic buckling of the base replicated by the introduction of a small imperfection in a similar way to that reported by Robotham *et al* [25] for plain shafts in torsion.

3.4.1 Finite element model

The basic cross-section shown in Figure 3.20 using 6 super-elements has been used to create a three-dimensional model as shown in Figure 3.39 (half model shown for clarity). The boundary conditions are shown in Figure 3.40. The model was constrained along its line of symmetry in the X direction see Figure 3.39 (plane ABCD). This does not allow X displacement of these elements, to model the can as symmetrical. The top section of the can was constrained in the Z direction (plane ADE) to simulate the gripping of the can in the pressure testing equipment. In reality the can is gripped at the shoulder during the pressure tests not in the midsection as in

the model. Again, due to the large deformations, it was necessary to use a geometric non-linear analysis since the loading will change direction during the buckling process and the stiffness of the base changes significantly.

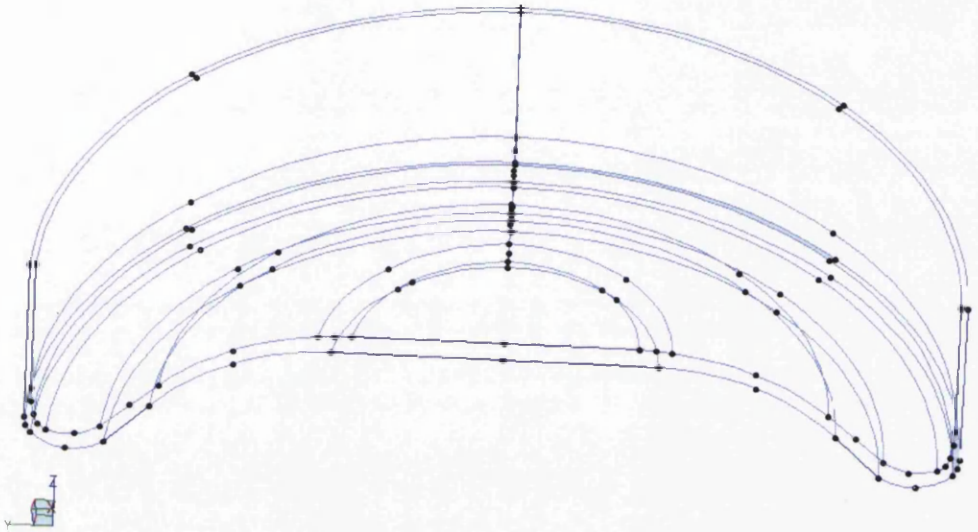

Figure 3.39: 3D finite element model geometry

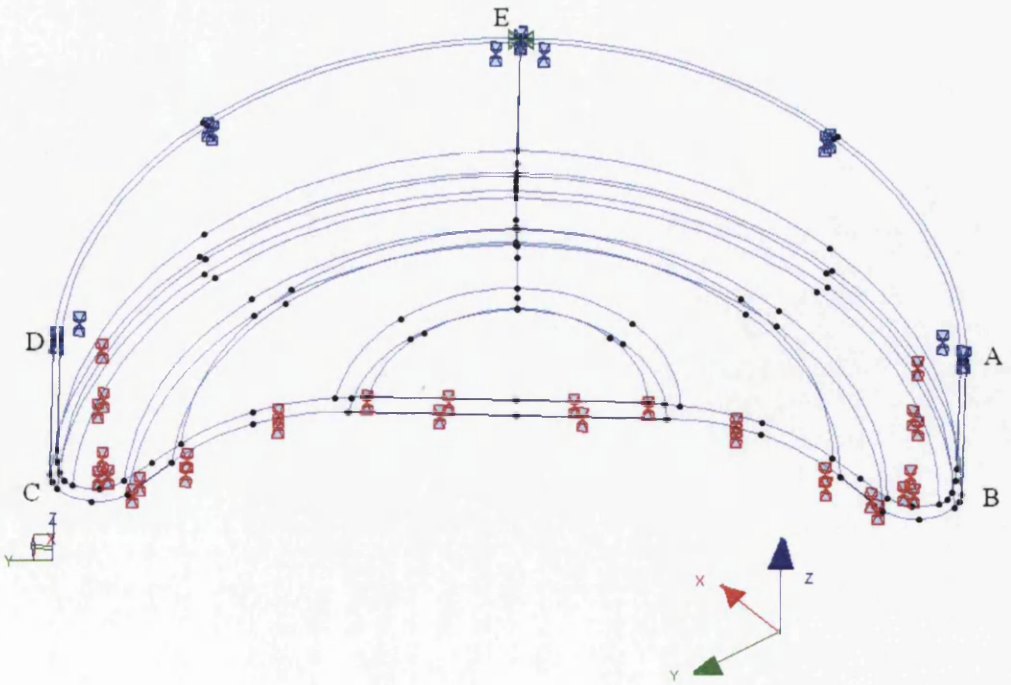

Figure 3.40: Finite Element Constraints

3.4.2 Material model and loading

The multi-linear material model for aluminium 1050, shown in Table 3.5, has been used. An incremental uniform pressure load was applied to the internal surface of the can. The mesh made up of 6315 four-noded three-dimensional elements, the finite element mesh is shown in Figure 3.41.

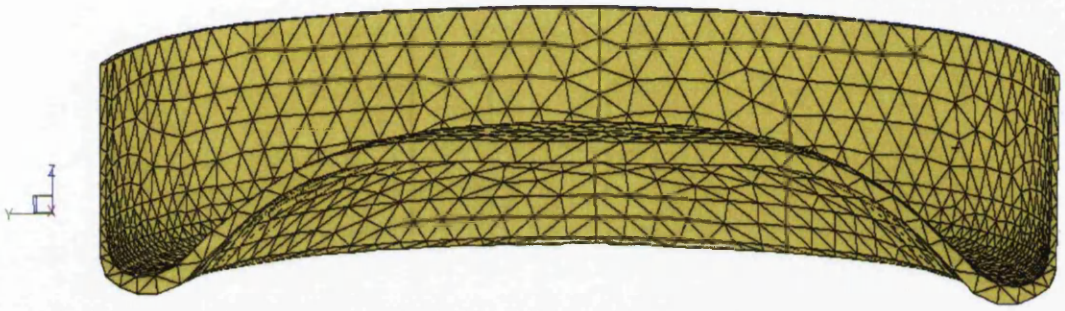

Figure 3.41: 3-D Finite element model mesh.

3.4.3 Eigenvalue analysis

From a preliminary eigenvalue analysis (i.e. lowest mode) and supported by experimental evidence, a small perturbation was introduced into the geometry to prevent a symmetrical deformation mode giving an increased load prediction at the limit point. This was achieved by increasing the radial coordinates of the nodes lying on one side of the half-model cutting plane from the centre to the edge of the base by 0.1mm (~10% of the wall thickness at that point). This provided a bifurcation point and enabled the snap-through buckling mode to be investigated. Robotham *et al* [24] showed that imperfections in the range 1 to 10% produced very similar results. In the

snap-through model, the load/displacement function will be cubic having a maximum at the point of buckling and a minimum after complete snap-through is achieved.

3.4.4 Results

The analysis resulted in stress contours plots for a number of incremental pressures. Finite element predictions of yield and elastic-plastic buckling pressures were predicted. Unlike the axisymmetric model, this model is able to resist a further increase in pressure, prior to collapse and the predicted collapse pressure is 2.02 MPa.

It can be seen from Figure 3.42 that the stresses are high enough such that
The can base yields when the internal pressure is 1.50 MPa since the yield stress for the aluminium is 100 MPa.

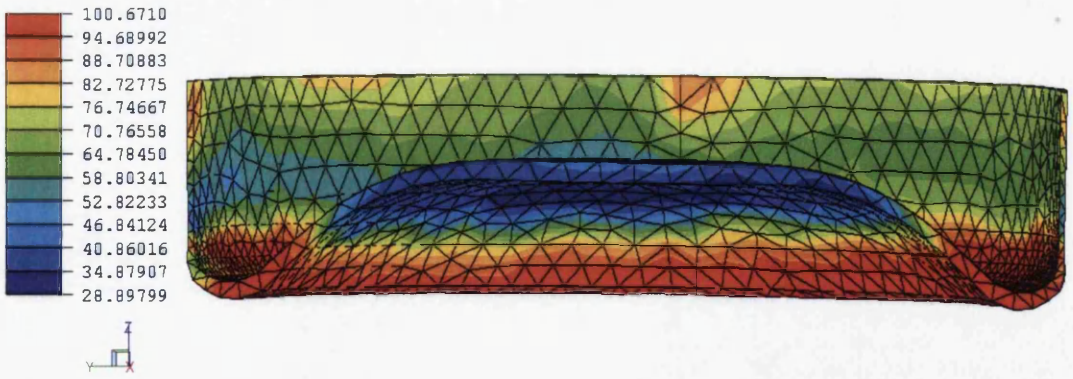

Figure 3.42: Von Mises Stress Contour Plot at internal pressure of 1.50 MPa

When the internal pressure is increased to 1.70 MPa Figure 3.43 shows that the deformation due to this pressure is clearly unsymmetrical, since it is not possible for an object to be perfectly symmetrical and will ultimately enable plastic collapse (snap-through) to occur at a pressure of 2.02 MPa, as shown in Figure 3.44, this

shows that the finite element analysis predicts that the aerosol can base will be fully deformed at 2.02 MPa and that the stresses are now concentrated in the lower section of the can walls.

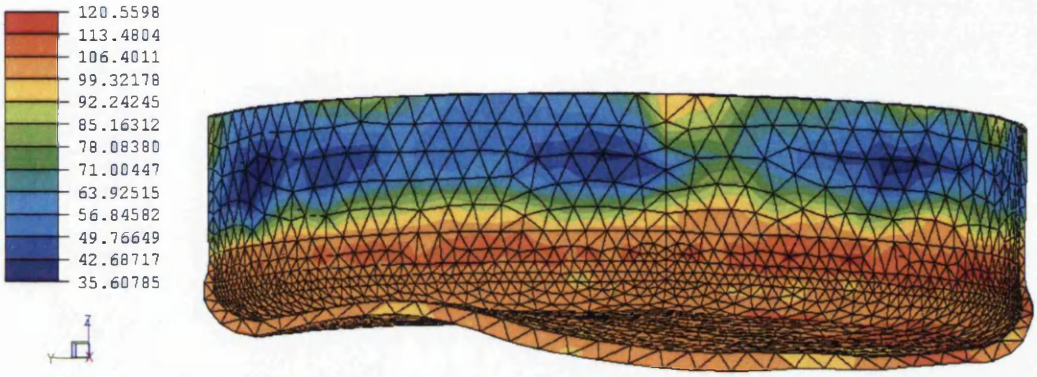

Figure 3.43: Von Mises stress contour plot at internal pressure of 1.70 MPa before snap-through

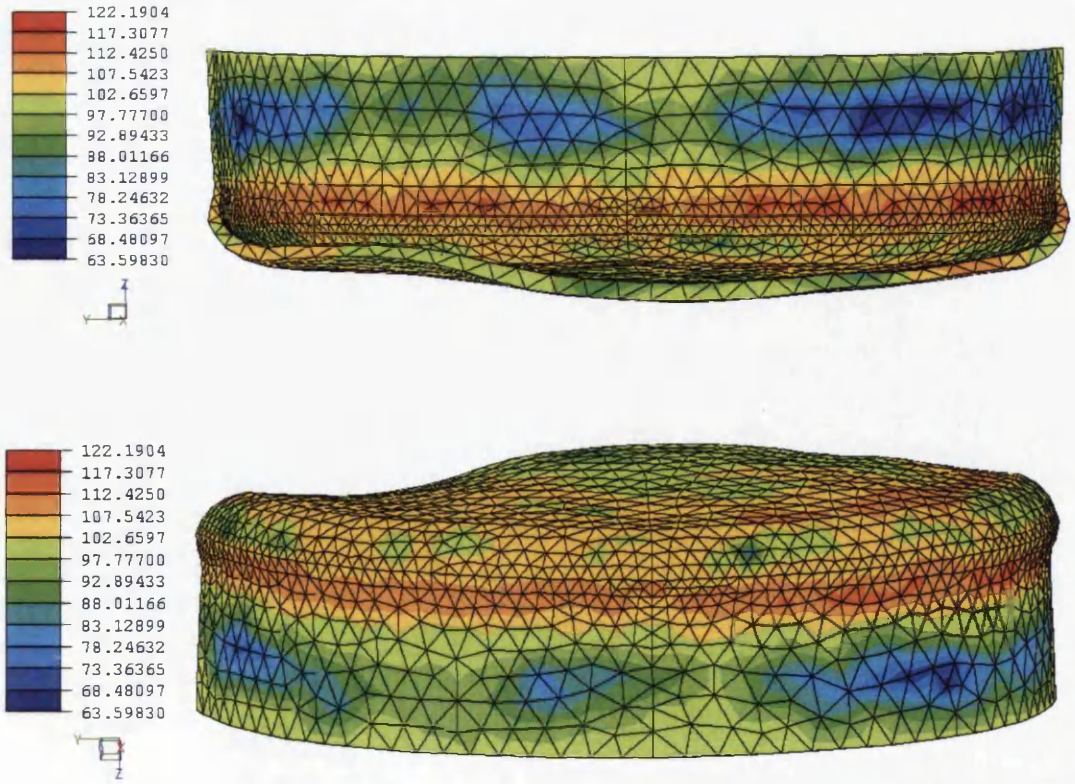

Figure 3.44: Final von Mises Stress Prediction at pressure of 2.02 MPa

For further investigation and information, two 3-D constant thickness models, for t = 0.6 mm and 1.0 mm were created and analysed, using the same approach but without the nodal perturbations to produce the geometrical asymmetry. It can be seen from Figures 3.45 and 3.46 that the plastic collapse (snap-through) occurs at a pressure of 0.83 MPa and 1.20 MPa for t = 0.6 and 1.0 mm respectively. These results show that the deformations due to this pressure are clearly symmetrical. This confirms the need for the original asymmetry in order to generate a realistic response.

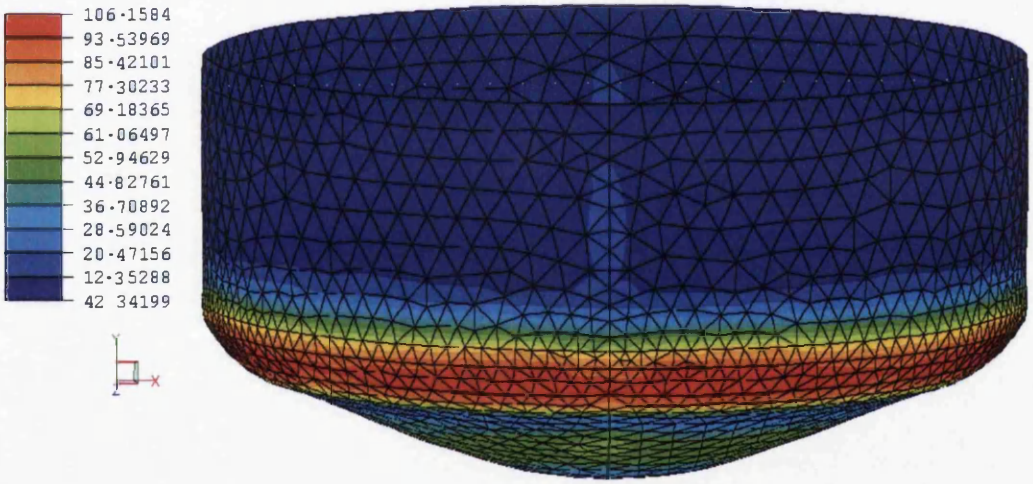

Figure 3.45: Von Mises stress contour plot at internal pressure of 0.83 MPa and 0.6 mm constant thickness

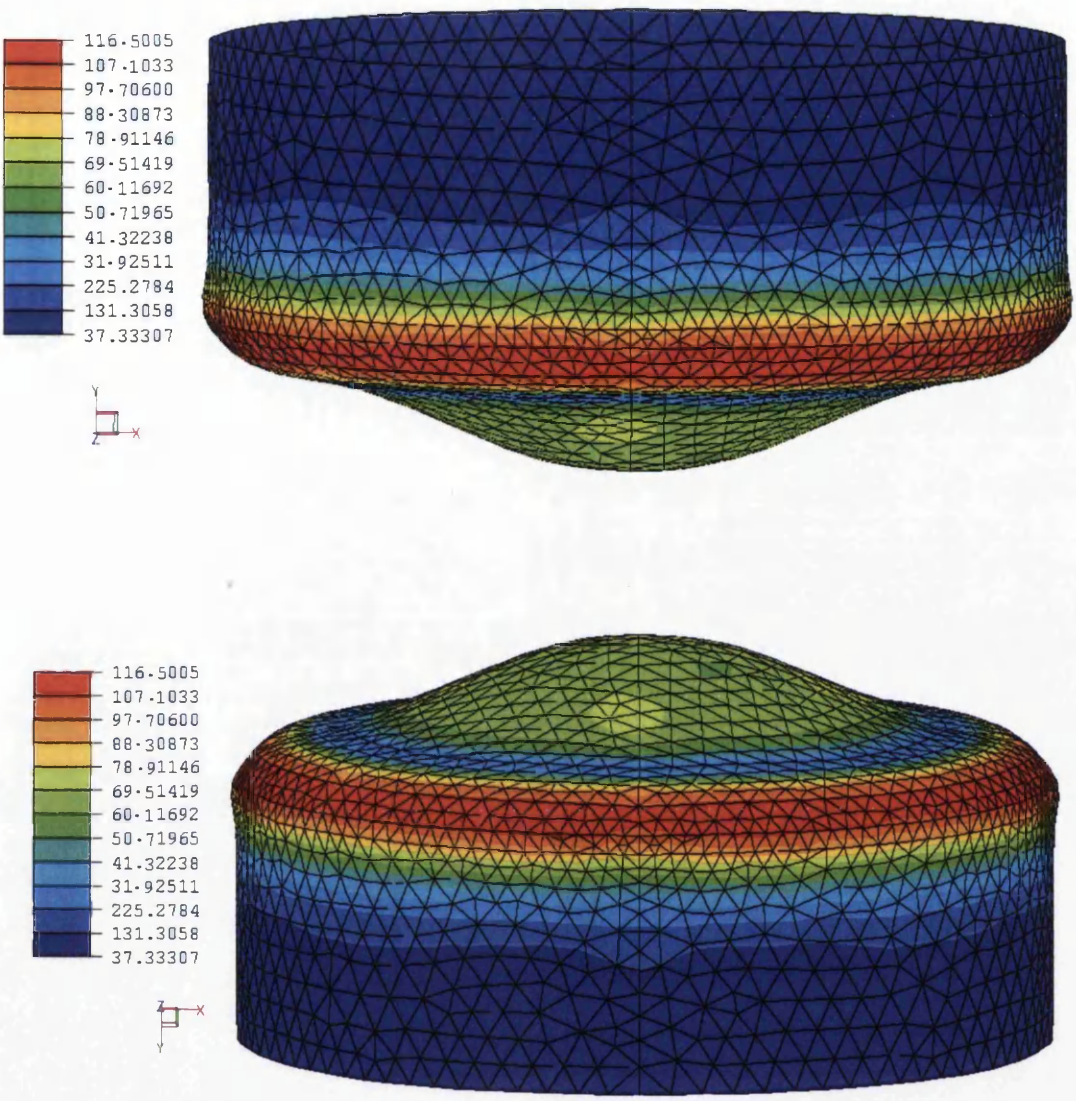

Figure 3.46: Von Mises stress contour plot at internal pressure of 1.20 MPa and 1.0 mm constant thickness

3.5 Upper and lower bound pressures

In this section, the elastic compensation method proposed by Mackenzie and Boyle and discussed in Chapter 2 is used to estimate the upper and lower bound limit (collapse) loads for the one-piece aluminium aerosol cans subjected to internal pressure loading. As in Sections 3.2 and 3.3, the wall of the can is initially assumed

to be of constant thickness and results for six thickness values are presented. A realistic thickness profile is also used in a seventh model. Upper and lower bound pressures are found using axisymmetric models.

3.5.1 Material models, loading and boundary conditions

Since the analyses are elastic, only values for Young's modulus and Poisson's ratio of 68.3 GPa (zeroth iteration) and 0.33 respectively (as before) are required. The loading and boundary conditions are as discussed in Section 3.2.2.

3.5.2 Constant thickness model

The basic finite element model, made up of six 'super elements' and shown in Figure 3.2 for a can section that has a constant thickness of 1 mm, has been used. Since the methodology involves an iterative finite element procedure, it was necessary to choose a mesh that meets both the condition of convergence and that of economy of the solution. A preliminary investigation, starting with a mesh of 296 elements (four through-thickness), was undertaken in order to establish a suitable mesh for which mesh convergence had been reached. For the elastic compensation method analysis, 296 8-noded, axisymmetric elements were generated manually from the basic mesh in Figure 3.2 and the mesh for this analysis is shown in Figure 3.47.

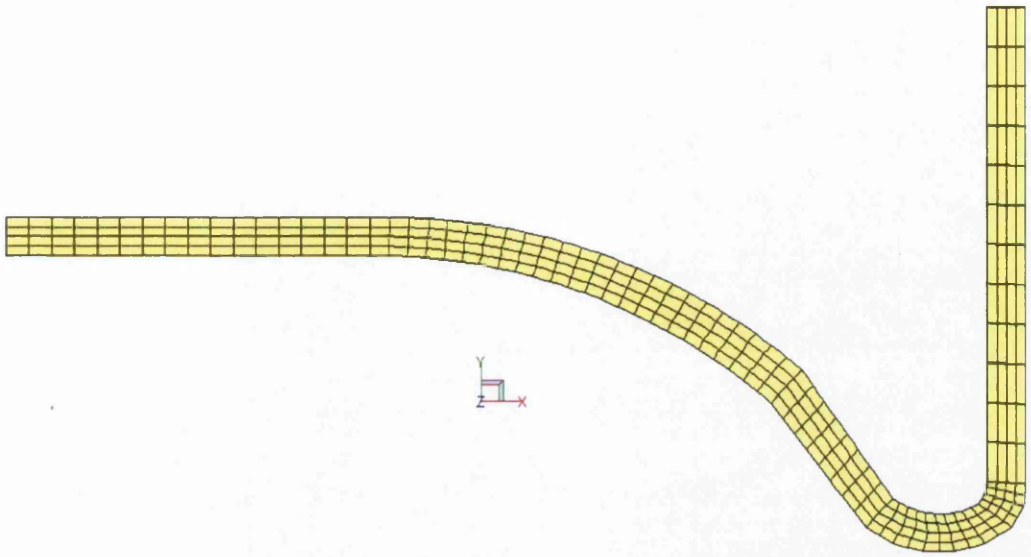

Figure 3.47: simple finite element mesh for geometry G4

3.5.2.1 Geometry G4 (t = 1 mm)

Figure 3.48 shows the von-Mises equivalent stress contour plot for the initial elastic solution (i.e. zero-th iteration in the elastic compensation method) for an arbitrary pressure of 0.1 MPa. Regions of above-average stress occur in the transition region between cylinder and base and at the base centre. On the basis of the results shown in Figure 3.48, an internal pressure at which first yield occurs was found to be 0.75 MPa.

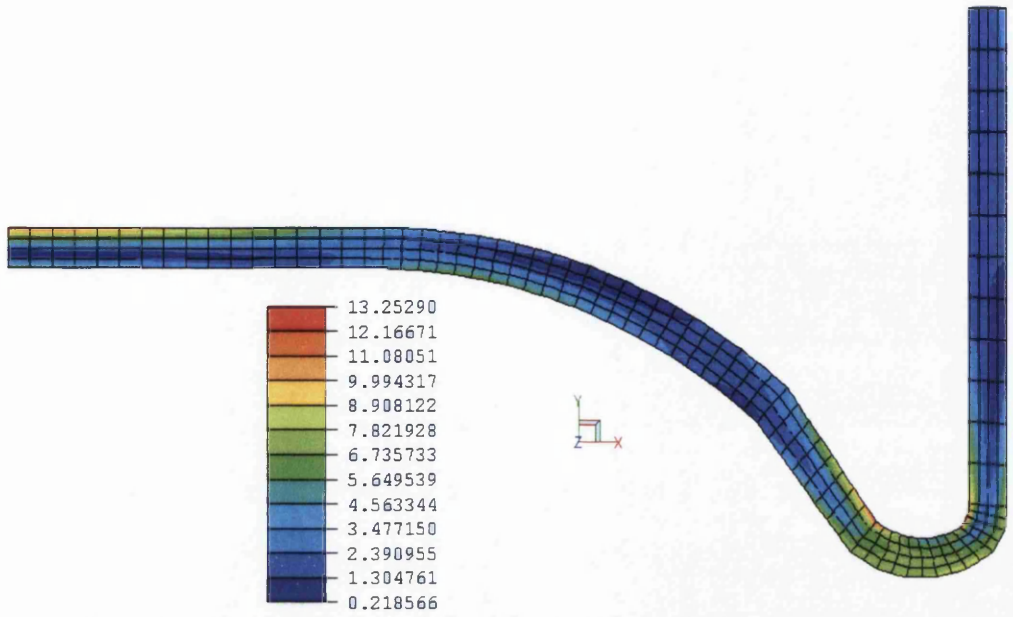

Figure 3.48: Equivalent stress contour plot for iteration 0

The iterative procedure described in Section 2.9 has then been employed (with the aid of a FORTRAN program) and the modulus of elasticity in each element modified according to Equation (2.25). The maximum equivalent stress at the end of the each subsequent iteration is shown in Figure. 3.49, from which it is clear that a converged solution occurs after 4 iterations with σ_d = 10.72 MPa. The elastic compensation method may, depending on the function used, caused the maximum stress to increase or decrease, but by careful selection of the function it is generally found that over a number of iterations there will be a net decrease in maximum stress with respect to the initial elastic solution.

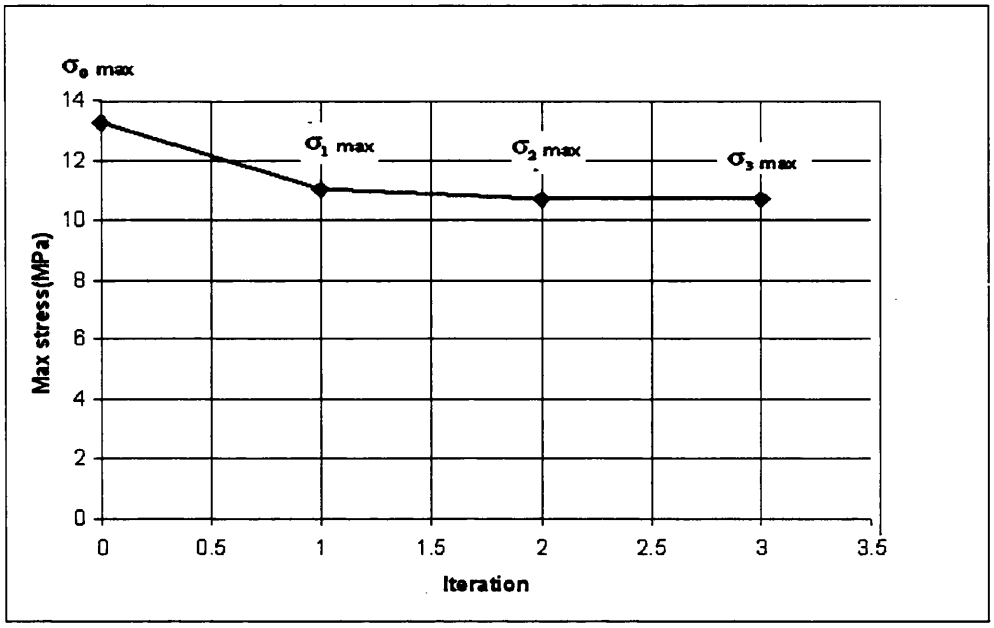

Figure 3.49: Maximum equivalent stress at the end of each iteration for t = 1 mm

The steady-state (converged) equivalent stress contour plot is shown in Figure 3.50. A redistribution of stress has occurred with an initial stress range of 0.21 – 13.25 MPa (see Fig. 3.48) reducing to 0.02 – 10.72 MPa. It is also apparent that the stress discontinuities at element boundaries have become more pronounced since the values of elastic modulus can now significantly vary from element to element.

3.5.2.2 Method of implementation of elastic compensation method

The procedure used in this approach is as follows:

(a) zero-th iteration. The initial elastic analysis is carried out with an arbitrary pressure, P_d, using E_0 throughout.

(i) store the elastic stress field, σ_e.

(ii) identify the maximum stress in each element and use them to update elemental E values, using Equation (2.25)

(iii) identify the maximum stress in the model, σ_d

(iv) re-create the finite element program input data file, using the new E values

(b) i th iteration

(i) – (iv) as above

(v) compare σ_d with the value from the previous iteration (i.e. for convergence)

(c) converged solution. This occurs when σ_d becomes constant

(i) calculate P_L using Equation (2.26)

(ii) obtain U_d and D_d from the finite element program output (see note below)

(iii) calculate P_U using Equation (2.31).

Note that:

1. Strain energy values are obtained directly from the finite element program output file. The dissipation energy for each element is obtained from the three principal strains, the yield stress and the element volume, using a version of Equation (2.30) based on total values, not rates. A simple FORTRAN program was therefore written to perform this calculation.

2. The procedure in (i) to (iv) above is time consuming and prone to error, when performed manually. A FORTRAN program was written to perform these tasks automatically.

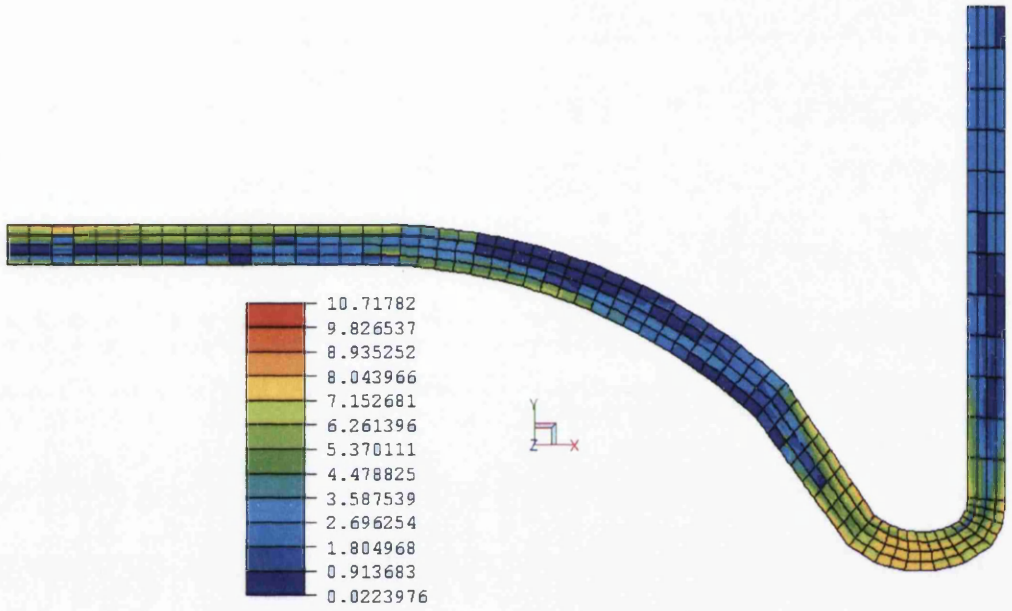

Figure 3.50: Steady state equivalent stress contour plot for t = 1 mm

From Equation (2.26), it follows that:

$$p_L = \frac{\sigma_y}{\sigma_d} p_d = \frac{100}{10.72} \text{ x } 0.1 = 0.93 \text{ MPa}$$

In order to obtain an upper bound estimate, values of dissipation energy and strain energy, for the converged solution, are required. A FORTRAN program was written to extract the stress and strain predictions from ELFEN and from which the

dissipation energy was derived, using the method described in Section 2.9. Having done this and using Equation (2.30) and (2.31):

$$p_U = \frac{D_d}{U_d} p_d = \frac{0.001405}{0.00006384} \times 0.1 = 2.20 \text{ MPa}$$

3.5.2.3 Effects of wall thickness

This process was repeated for constant thickness models of 0.4, 0.6, 0.8, 1.2 and 1.4 mm, using 296 elements in each case. The resulting upper and lower bound pressures are summarised in Table 3.7. A comparison between the upper and lower bounds pressures and the yield and collapse pressures are presented in Table 3.8 and Figure 3.51.

The results presented in Figure 3.51 show that the FE predicted collapse pressures lie between the upper and lower bound estimates, closer to the upper bound, and this provides a degree of confidence in these approximate methods. However, the range between the upper and lower bounds is large and, furthermore, the lower bound is always greater than the yield stress. This limits the use of these approximate methods for this type of geometry and loading to collapse pressure estimates. Nevertheless, the elastic compensation method is useful since it only requires elastic analyses.

Compensation method		
t (mm)	p_L (MPa)	p_U (MPa)
0.4	0.52	1.16
0.6	0.61	1.37
0.8	0.72	1.66
1.0	0.93	2.20
1.2	1.64	2.72
1.4	2.65	3.95
Variable	0.81	2.59

Table 3.7: Upper and lower bound pressures using elastic compensation method

Compensation method			Finite element	
t (mm)	P_L (MPa)	P_u (MPa)	P_y (MPa)	P_c (MPa)
0.4	0.52	1.16	0.16	0.73
0.6	0.61	1.37	0.22	0.93
0.8	0.72	1.66	0.40	1.18
1.0	0.93	2.20	0.72	1.59
1.2	1.64	2.72	1.17	2.37
1.4	2.65	3.95	1.49	3.56
Variable	0.81	2.59	0.38	1.53

Table 3.8: Results of elastic compensation and finite element analyses

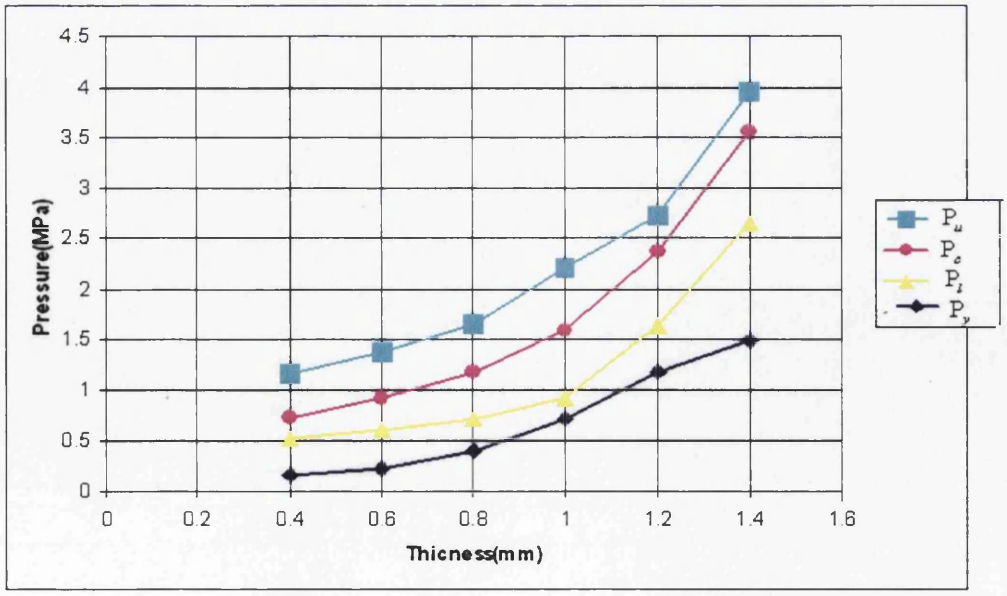

Figure 3.51: Comparison of finite element method and compensation method

3.5.3 Can with varying thickness

A finite element mesh containing 296 8-noded, axisymmetric elements was generated manually from the basic mesh shown in Figure 3.21. The iterative procedure previously described for constant thickness models was repeated using this variable thickness model. A steady-state maximum equivalent stress of 12.4 MPa was predicted and from Equation (2.26):

$$p_L = \frac{\sigma_y}{\sigma_d} p_d = \frac{100}{12.4} 0.1 = 0.81 \text{ MPa}$$

Values for the steady state dissipation and strain energies were obtained using the procedure described above and using Equation (2.30) and (2.31):

$$p_U = \frac{D_d}{U_d} p_d = \frac{0.001712}{0.0000659} 0.1 = 2.59 \text{ MPa}$$

The upper pressure bound estimate of 2.59 MPa is higher than the predicted yield pressure of 0.38 MPa (Section 3.2.5) and higher than the elastic-plastic buckling pressure prediction of 1.53 MPa (Section 3.3.5). Therefore, the upper bound estimate has good application. In this variable thickness example, however, the lower bound estimate of 0.81 MPa is higher than the yield pressure.

By comparing variable thickness results with those for constant thickness models, it is apparent that the upper and lower bound estimates for the variable thickness model fall between the 0.7 to 1.0 mm constant thickness results, which might be considered to be reasonable since the region with the highest stress concentration and where buckling ultimately occurs (i.e. the corner between cylinder and base) has a thickness

varying between 0.7 and 1.3 mm. However, the upper bound pressure estimate exceeds the collapse pressure.

3.6 Experimental testing

Experimental pressure testing of cans having various dimensions has previously been carried out by Patten and full details of the test procedure, the test equipment and results can be found in [2]. A typical burst can is shown in Figure 3.52, which also shows the buckling of the base, prior to failure. The non-symmetric nature of the deformed shape is clear and comparable with finite element predictions (see Figure 3.44). There is a requirement that the buckling pressure is at least 20% below the actual burst pressure. In this practical situation, minimum burst pressures are specified by the customers.

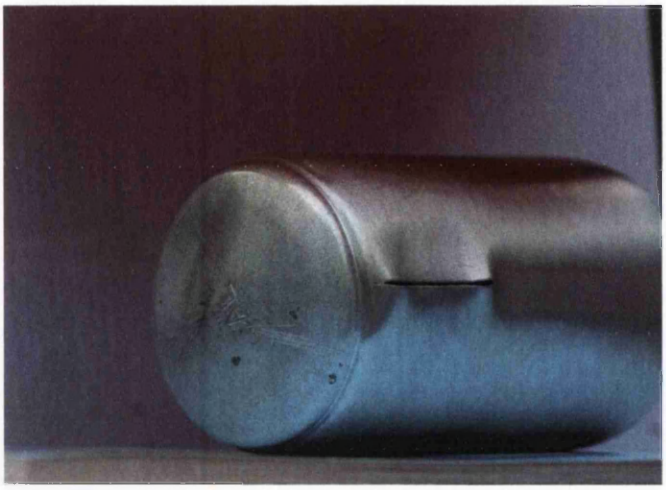

Figure 3.52: Deformation and burst pressure of can base

A typical pressure-time curve, taken from [2], is shown in Figure 3.53 and a summary of Patten's findings are presented in Table 3.9. The results for the 53 mm can (which has been modelled here) shown very good agreement between the experimental burst pressure obtained by Patten and the analytical solution and finite element predictions obtained here. Similarly, the experimental buckling pressure of 1.6 MPa compares favourably with the finite element prediction of 1.7 MPa.

Diameter (mm)	**Wall thickness (mm)**	**Average actual burst pressure (bar)**	**Predicted burst pressure**(bar)
38	0.32	28	29.6
44	0.30	24	23.4
50	0.33	23	23.1
53	0.30	21	21.0
59	0.35	21	20.8
59	0.41	24	24.4
60	0.44	24	23.4

Table 3.9: Comparison between measured and predicted burst pressures of cans [2]

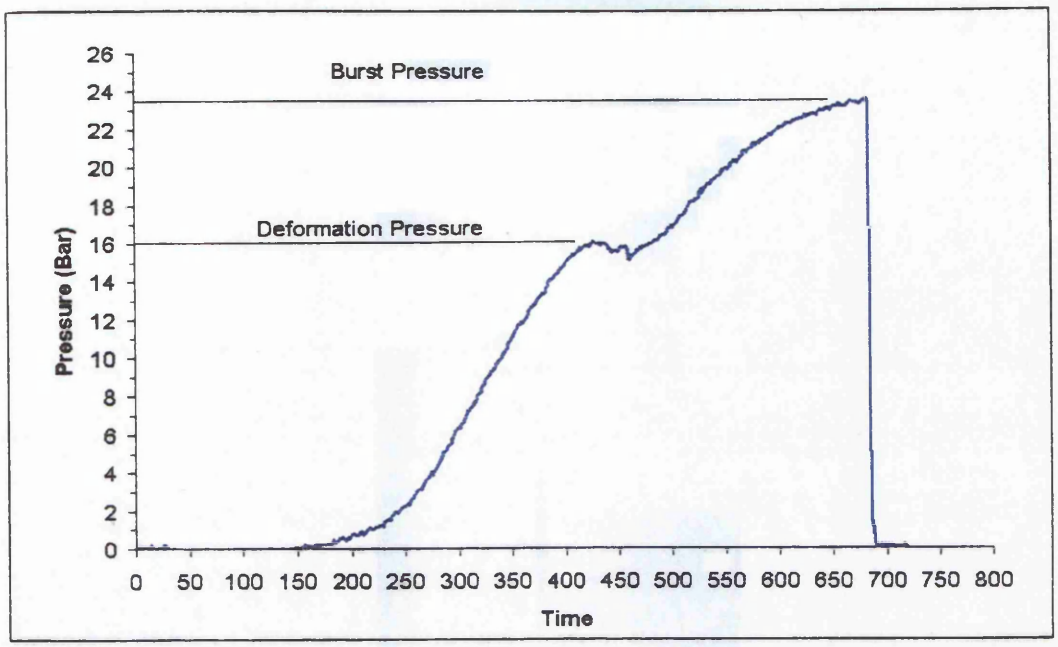

Figure 3.53: Deformation and burst pressure [2]

3.7 Closure

This chapter has described the elastic and elastic–plastic analysis of the thin cylindrical component under internal pressure loading. Initially, axisymmetric constant-thickness models have been used to investigate the stress distributions that are set up, the yield pressures and the way in which the plastic zones develop, after yielding, leading up to elastic-plastic buckling. In addition, a realistic thickness profile has been modelled in order to more accurately study the pre- and post-yield characteristics. Emphasis has been placed on the base of the cylindrical can, since this is where the major deformation occurs.

However, the axisymmetric models are not capable of distinguishing between the elastic-plastic buckling of the base and the ultimate bursting of the can. In fact, these two events are predicted to be coincident, whereas experimental evidence suggests a

slightly unsymmetrical buckling mode and a clear distinction between the elastic-plastic buckling of the base and burst (collapse) pressures. A three-dimensional half-model was developed in order to investigate the elastic-plastic buckling of the base. Finite element predictions of yield, elastic-plastic buckling and collapse (burst) pressures have been compared with experimental evidence and analytical solutions and there is generally good agreement between them. Reasons for any discrepancies will be discussed in Chapter 7.

Finally, the elastic compensation method has been adapted in order to estimate upper and lower bounds on pressure for this type of geometry and loading conditions. The method has been found to be of limited use since the lower bound pressure is generally higher than the yield pressure.

In Chapter 4, the elastic-plastic behaviour of these cylinders, when subjected to axial compressive loading, will be investigated.

Chapter Four

AXIAL LOADING

4.1 Introduction

This chapter describes the analysis of a thin-walled cylinder with inverted base (typically used as aerosol cans) under axial compressive loading in order to predict the limit and failure loads for this type of loading. Such an analysis is important because aerosol cans are subjected to axial compressive loading:

a) when the neck is formed during the manufacturing process

b) when the valves are inserted and the vessel is charged

as shown in Figure 4.1. Elastic and elastic-plastic finite element analysis is used to predict the buckling behaviour and results are compared with those obtained from experimental testing, which is also described in this chapter. Case (a) is discussed in Section 4.3 and Case (b) in Section 4.4.

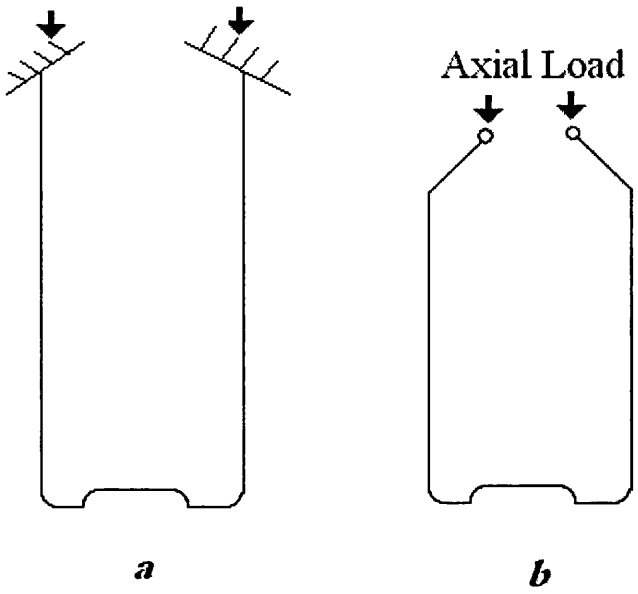

Figure 4.1: Axial compressive loading on the can

4.2 Potential failure modes

The straight section is basically a thin-walled cylinder and it is thought that the base has little or no effect on the buckling process. Most of the previous research has been conducted on plain cylinders and is directly applicable to cans. The collapse of a cylinder under an axial load may occur in a number of ways [21]. If the cylinder is slender (i.e. if the height to radius ratio is sufficiently large) then it will fail in a long-wave bending mode over its entire length (see Figure 4.2(a)). If the cylinder is moderately long with sufficiently thick walls, failure occurs plastically with an axisymmetric 'diamond type' buckling mode (see Figure 4.2(b)). For short cylinders with adequately thin walls, failure occurs elastically with an axisymmetric 'ring type' buckling mode as shown in Figure 4.2(c).

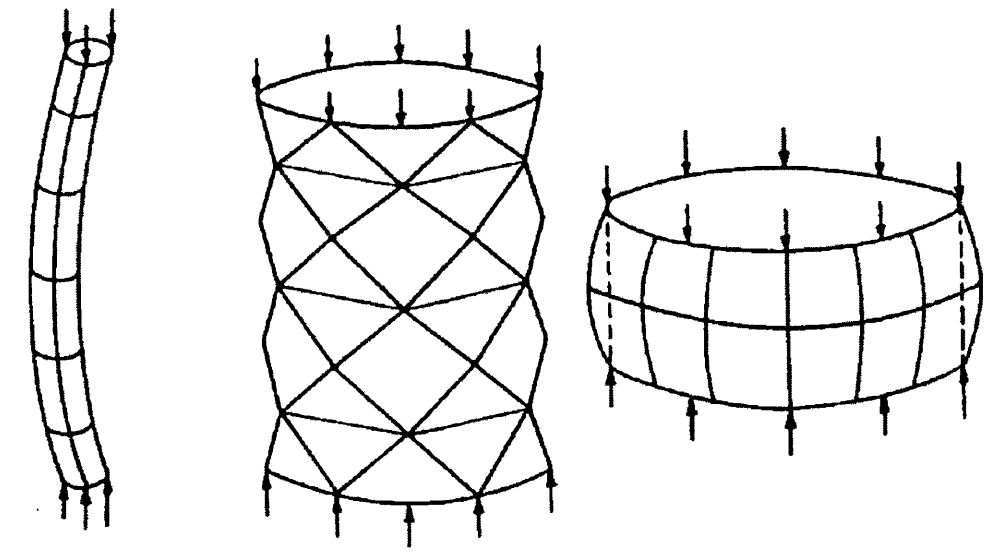

Figure 4.2: Effect of cylinder length on the buckling modes [21]

4.3 Case (a) - Compressive behaviour during neck formation

At the very start of the neck formation process, it can be assumed that the loading is applied to the rim, as shown in Figure 4.1(a). At this point, the overall length is at a maximum and the cylinder will fail at the lowest axial load.

As the load is increased there comes a point at which the deformation mode suddenly bifurcates into a pattern running around the circumference of the vessel (see Section 2.8.1) and the deformation of the buckle pattern is near the cylinder base.

4.3.1 Geometry and finite element model

The finite element model was produced in three dimensions by rotation of the cross section geometry shown in Figure 4.3 through 360° about the Y-axis. The cross section is based on measurements made by Patten [2] and so provides a realistic

model of the cylinder thickness profile. As with the dome reversed failure mode described in Chapter 3 the model needs to be 'seeded' with an imperfection in order to reproduce the correct buckling behaviour. A small perturbation in the shape of a known buckling pattern to the geometry produces the corresponding failure mode upon collapse. The cylinder geometry was modified by shifting the radial positions of the nodes as one proceeds around the circumference by 0.2 mm (see Section 2.8.4 for more information). The resulting three-dimensional shape is shown in Figure 4.4.

4.3.2 Loading and boundary conditions

At the rim of the cylinder, displacement is permitted along the axis but the rim is restrained in the X and Z directions. The bottom of the model is completely constrained to maintain a circular cross-section, as shown in Figure 4.5.

A face loading is applied normal to the horizontal rim surface of the vessel as shown in Figure 4.6 to model axial loading. The loading is ramped up linearly with time. The user need only specify the loading rate since all other loading data for the analysis is generated automatically.

4.3.3 Material model

The material data described in Section 3.3.2 including the data for the multi-linear σ-ϵ curve, as shown in Table 3.5, was used for this analysis. A finite element mesh of 7488 rectangular 4-noded shell elements and one element through the thickness was generated automatically using the ELFEN mesh generator and the mesh study result is shown in Figure 4.7.

4.3.4 Finite element predictions

Predictions have been obtained using the elastic and elastic-plastic analysis facilities within ELFEN [5]. A geometric non-linear (GNL) analysis was performed since large deformations and strains, which can have a significant effect on the load-deflection characteristics of the component, were anticipated. GNL considerations may have an influence on both the static and dynamic behaviour of structures [17]. Also in snap-through buckling, deflections of the structure are large compared with the original dimension of the structure. Changes in stiffness and load occur as the structure deforms. Geometry non-linearity occurs when the change in the geometry of the structure due to its displacement under load are taken into account in analysing its behaviour. The equilibrium equations take into account the deformed shape, whereas in small strain analysis the equilibrium equations are based on the original un-deformed shape.

The von Mises equivalent stress contour plot for a pre-buckling (elastic) face load of -29.3N/mm^2 and with a total load of 3247 N is shown in Figure 4.8. It is clear that the highest stresses occur close to the base of the cylinder. The corresponding von Mises equivalent stress contour plot and deformed shape at buckling are shown in Figures 4.9 and 4.10 respectively. It can be seen form these figures that the buckling of the cylinder is occur near the base and the mode shape has seven modes.

The load is increased and the load-displacement curve for the rim of the cylinder is shown in Figure 4.11. A reasonably linear response is seen up to a load of ~2500 N and above this, the buckling process begins with failure occurring at a load of 3247 N. The three stages of pre-buckling, buckling and post-buckling are clearly seen.

Figure 4.3: Cross-section geometry for the analysis of Case (a) axial loading during neck forming

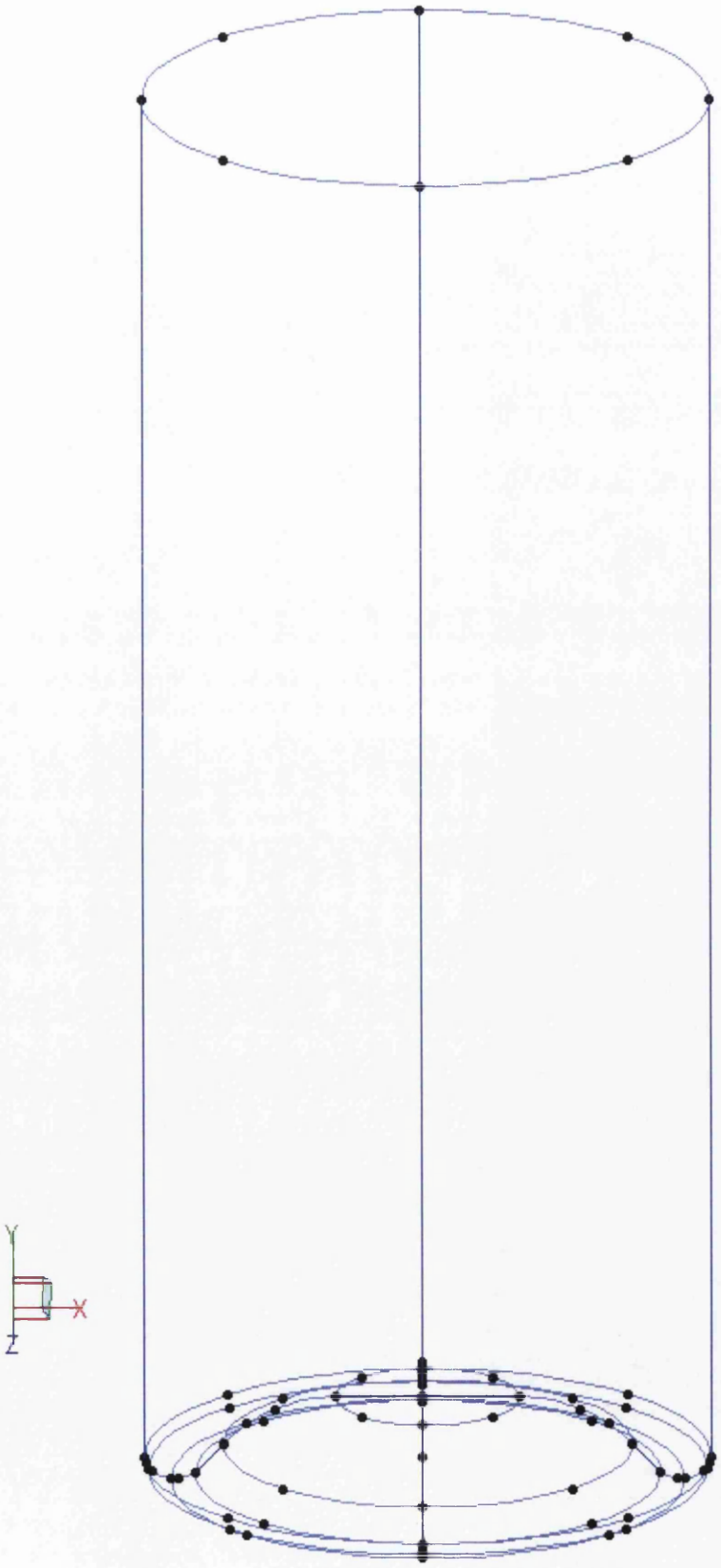

Figure 4.4: Three-dimensional model for Case (a) axial loading analysis

Figure 4.5: Structural constraints for Case (a) axial loading analysis

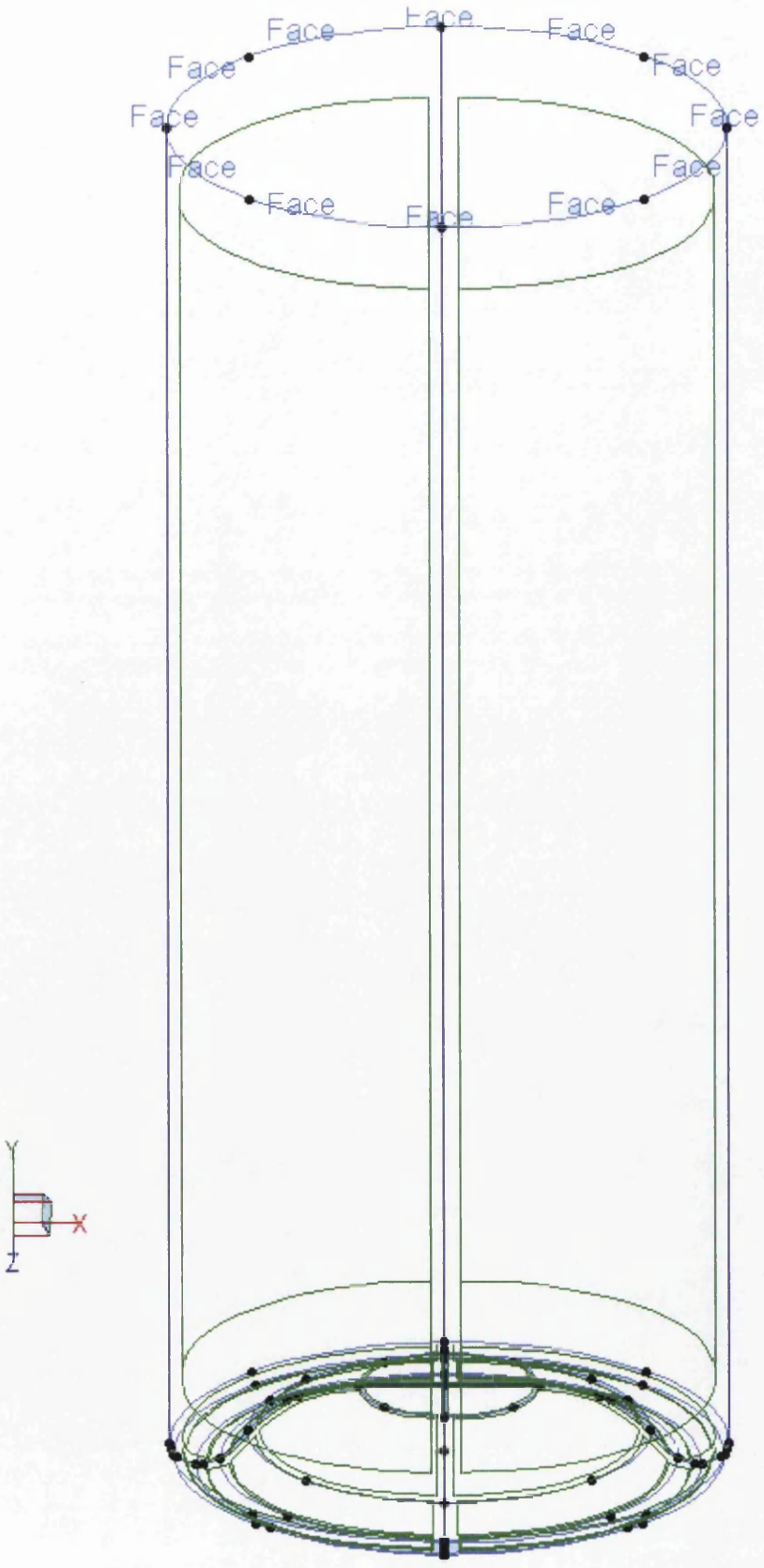

Figure 4.6: Applied loading for Case (a) axial loading analysis

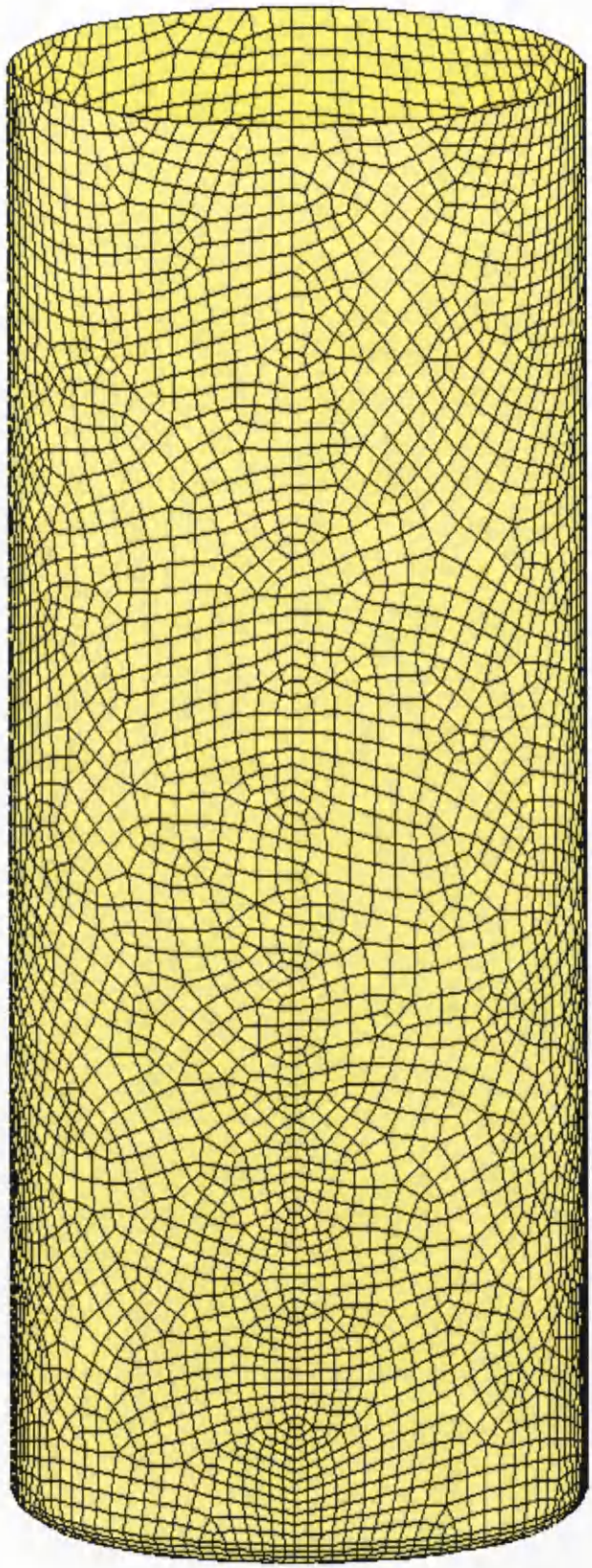

Figure 4.7: Finite element mesh for Case (a) axial loading analysis

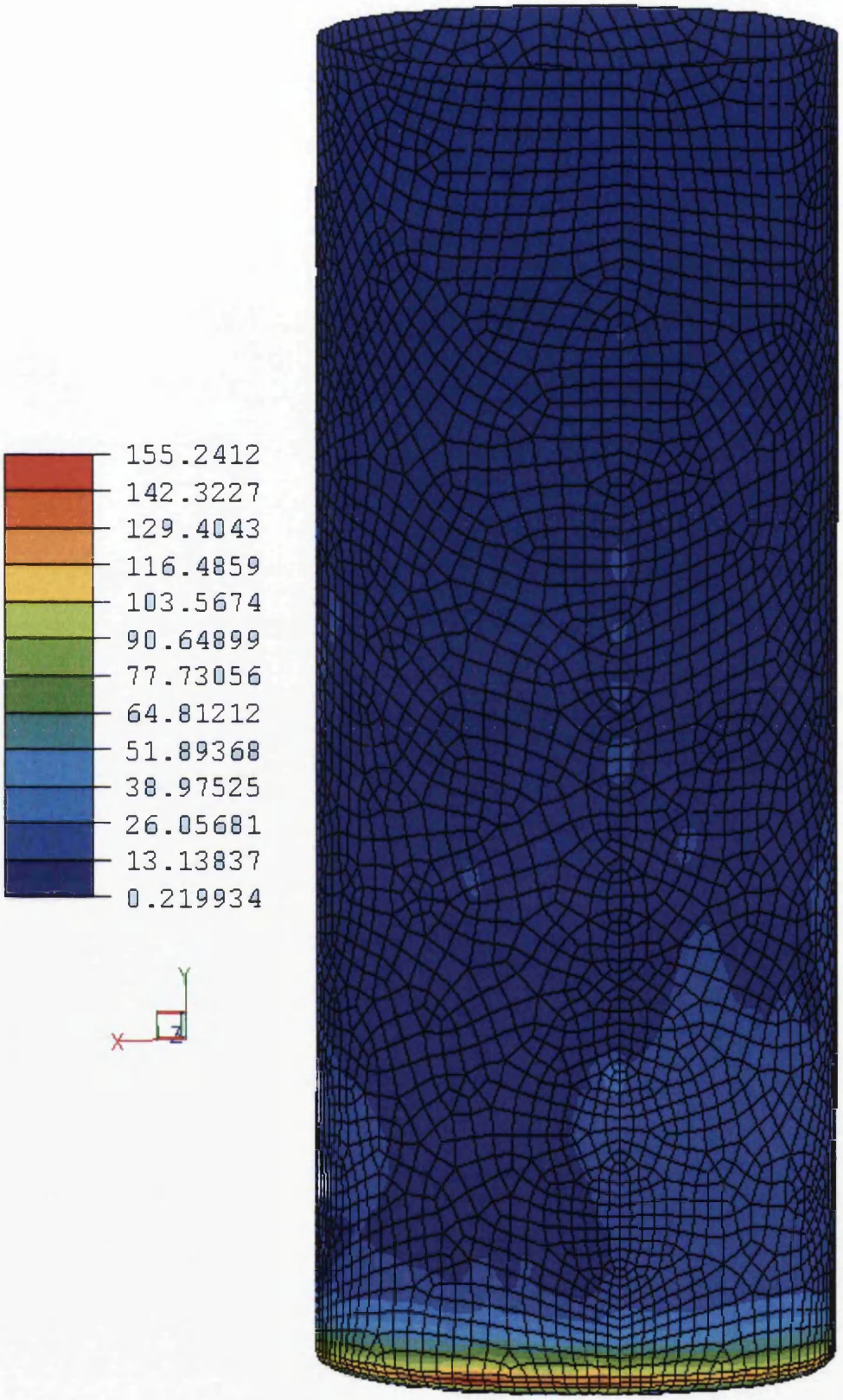

Figure 4.8: Pre-buckling equivalent stress contour plot for Case (a) axial loading analysis

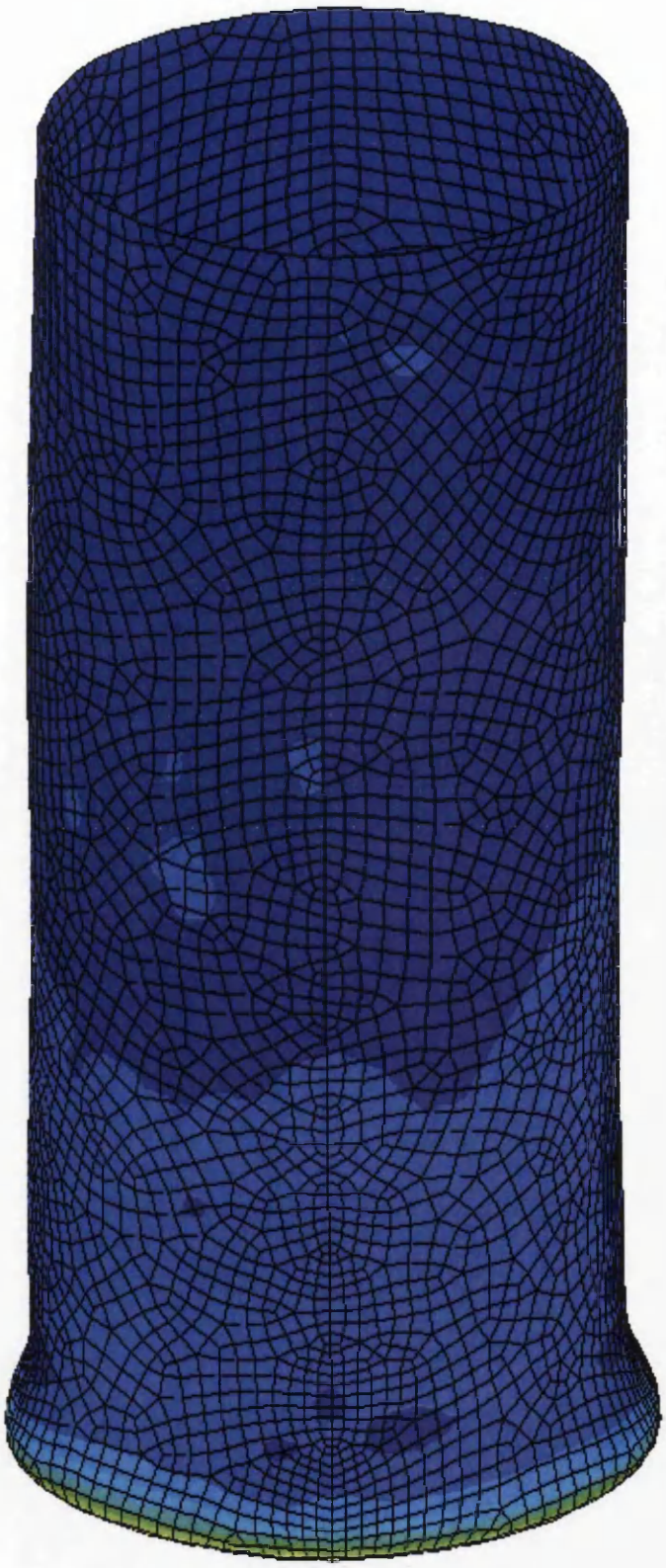

Figure 4.9: Equivalent stress contour plot at the point of buckling for Case (a) axial loading analysis

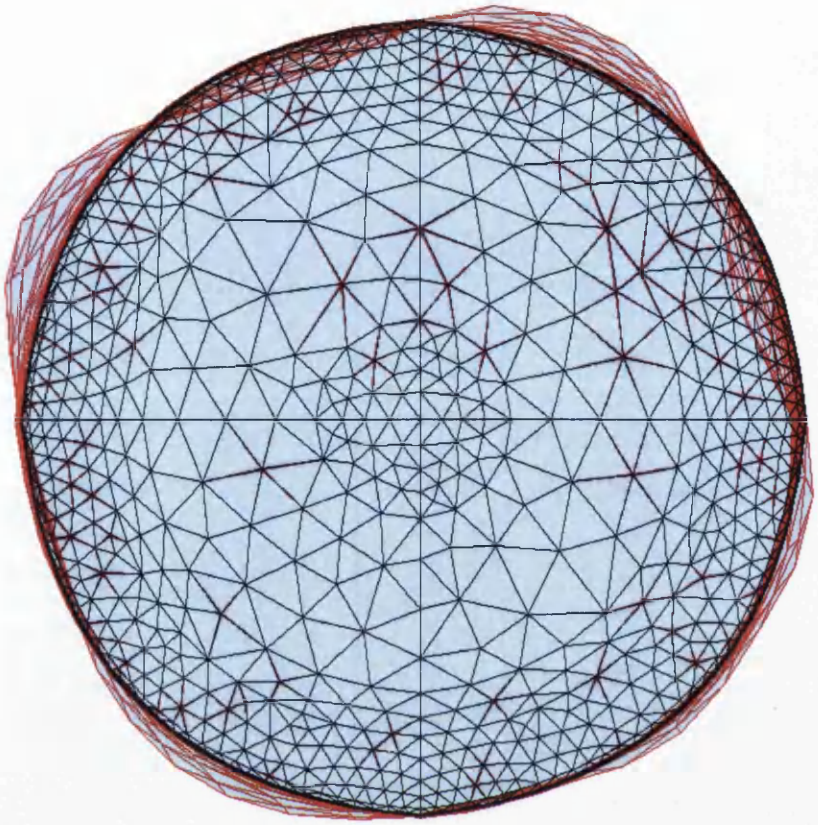

Figure 4.10: Buckling mode shape for Case (a) axial loading analysis

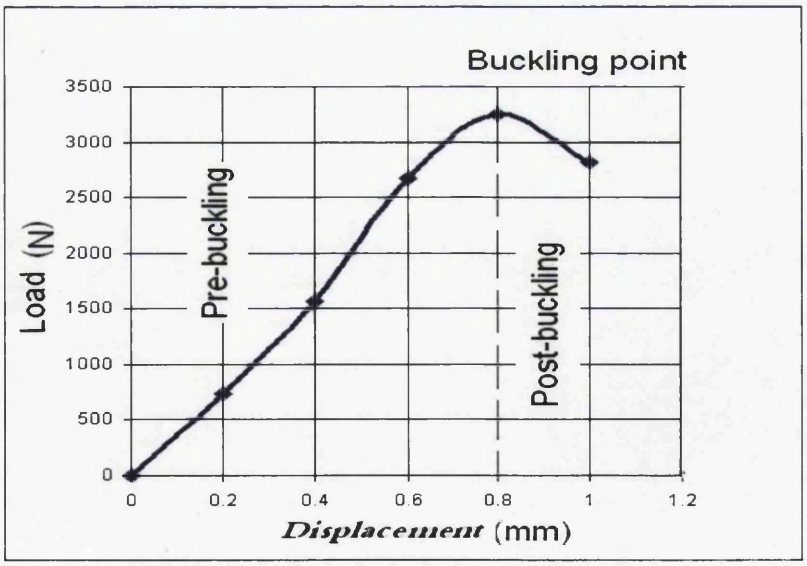

Figure 4.11: Predicted rim load-displacement curve for Case (a) axial loading analysis

4.3.5 Experimental testing

Experimental testing on a can with outer diameter 53 mm, inner diameter 52.4 mm, wall thickness 0.315 mm and length 125 mm (see Figure 4.12) has been carried out in order to validate the finite element prediction in Section 4.3.4.

A Zwick 20 kN electrically driven tensile test machine has been employed with a compressive load being applied, as shown in Figure 4.13. A compressive load was applied to the rim of the cylinder using a steel insert which was fixed to the uppermost part of the cylinder using a standard jubilee clip (see Figure 4.14).
During the test the crosshead movement and the applied load, using a 15000 N load cell, were logged and a typical resulting load-displacement curve is shown in Figure 4.15. A maximum load of 3230 N was noted at a rim displacement of ~0.86 mm, after which the load began to reduce until reach 2800 N approximately. The resulting deformed cylinder is pictured in Figure 4.16. The test was then repeated several times and very similar results were obtained.

In one case, the test was continued well beyond the point of first buckling and the resulting load-displacement curve is shown in Figure 4.17. It is clear that once a significant change in shape has occurred (i.e. for a displacement of approximately 3 mm) the can stiffness starts to increase and an increase in load is seen up to approximately 2000 N for a total displacement of ~5.5 mm. After this, a second buckling mechanism is observed with the load decreasing until the test was stopped when the rim displacement was approximately 6.8 mm. The final deformed shape is shown in Figure 4.18. It can be seen from the figure that the buckling occurs near the base and with a seven-lobed collapse pattern.

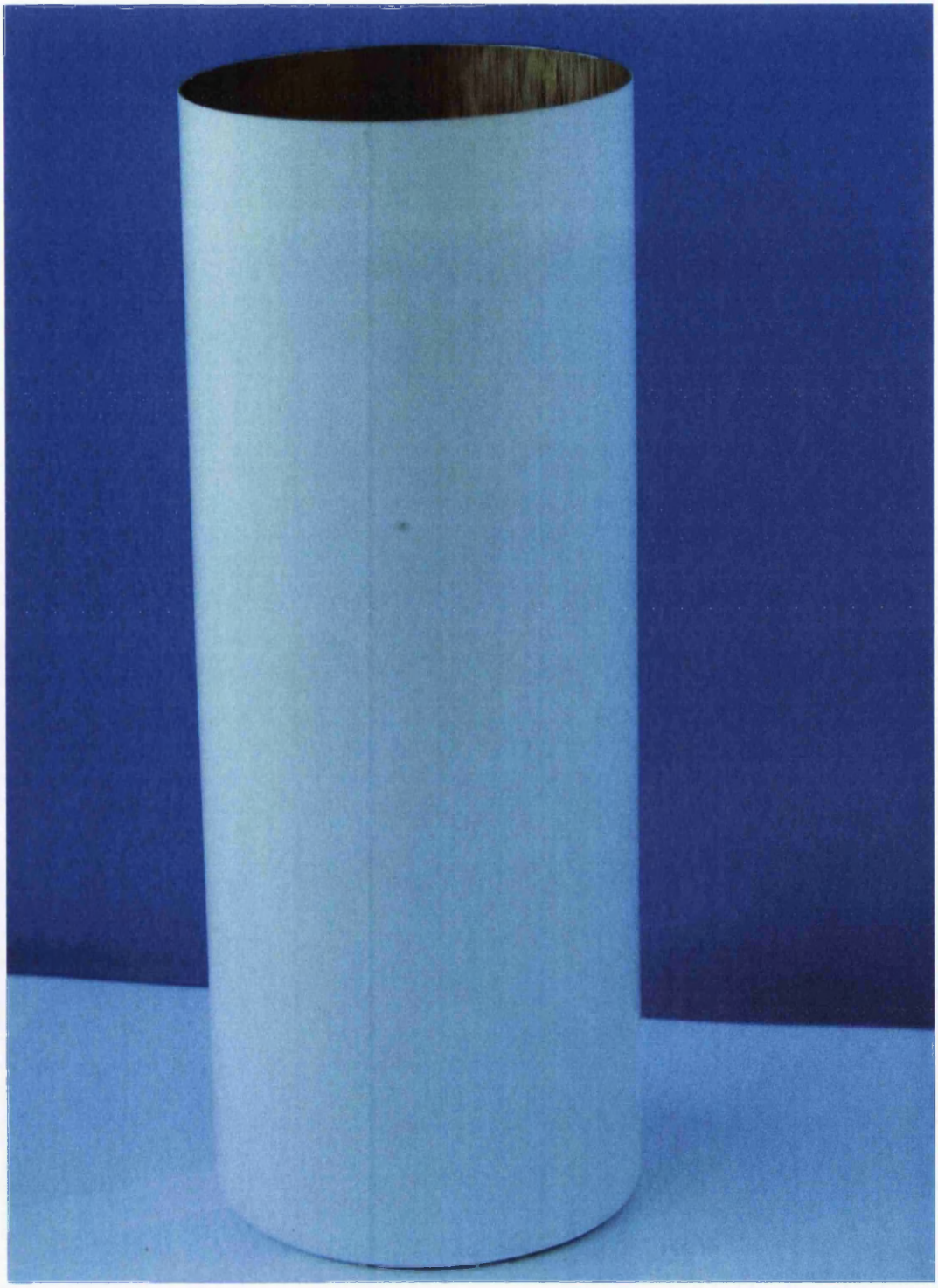

Figure 4.12: Aluminium aerosol can used in experimental testing for Case (a) axial loading analysis

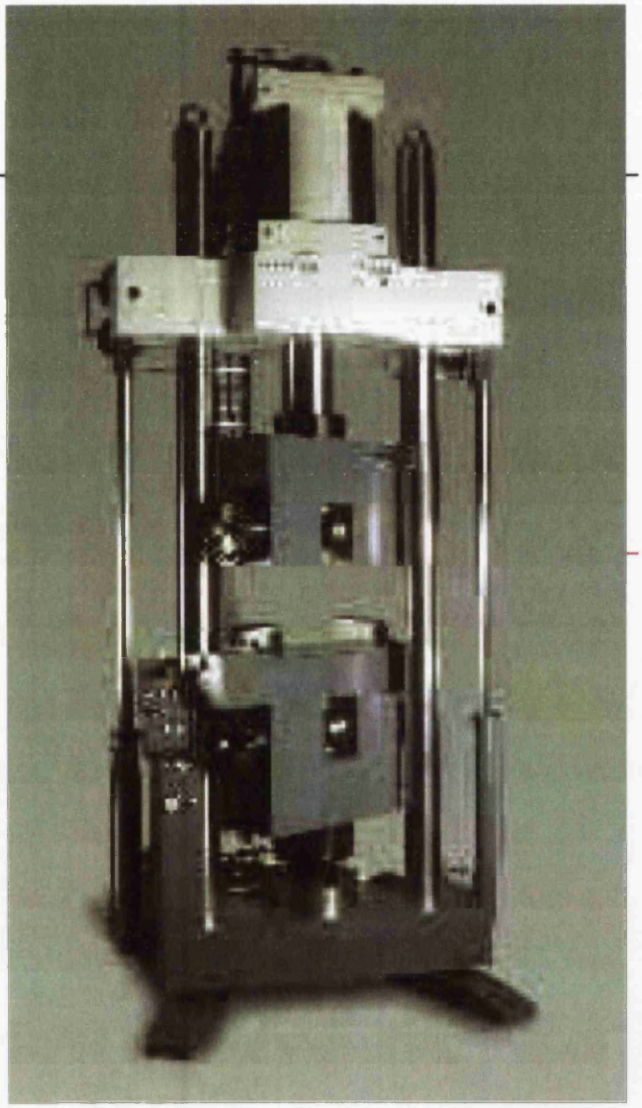

Figure 4.13: Zwick 20 kN tensile test machine

Figure 4.14: Steel insert and jubilee clip arrangement used in experimental testing for Case (a) axial loading analysis

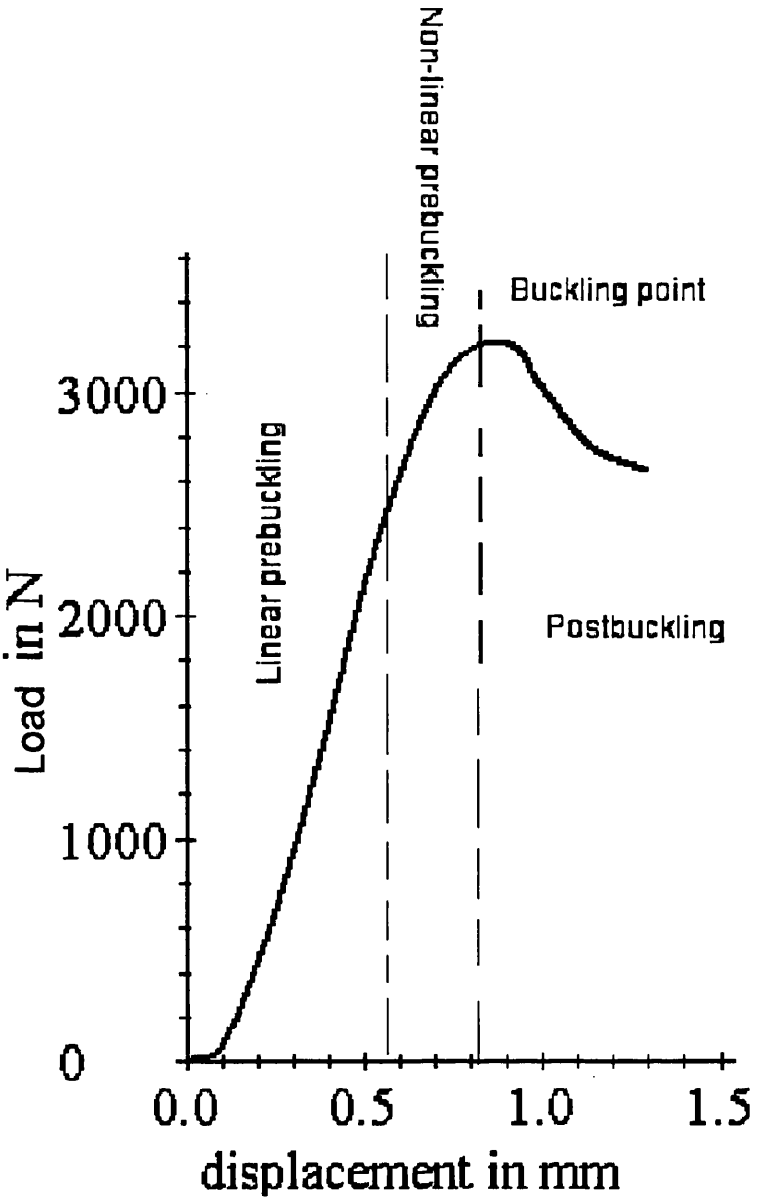

Figure 4.15: Experimental rim load-displacement curve for Case (a) axial loading analysis

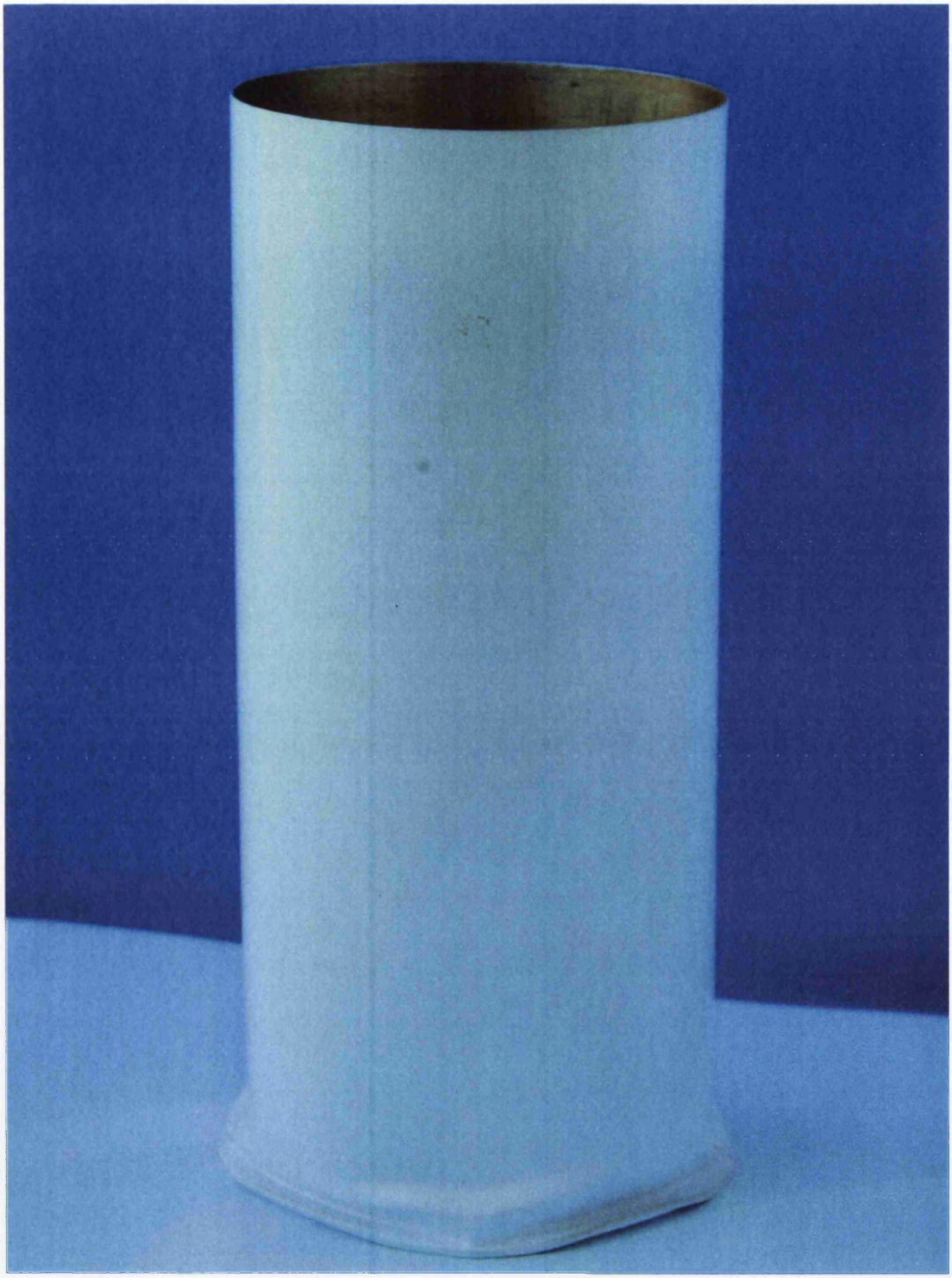

Figure 4.16: Buckled can for Case (a) axial loading analysis

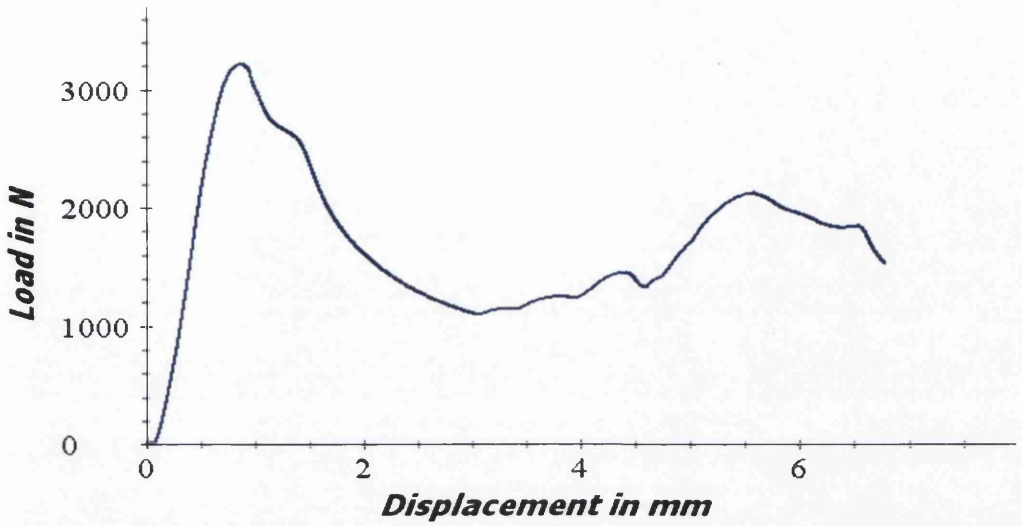

Figure 4.17: Extended experimental rim load-displacement curve for Case (a) axial loading analysis

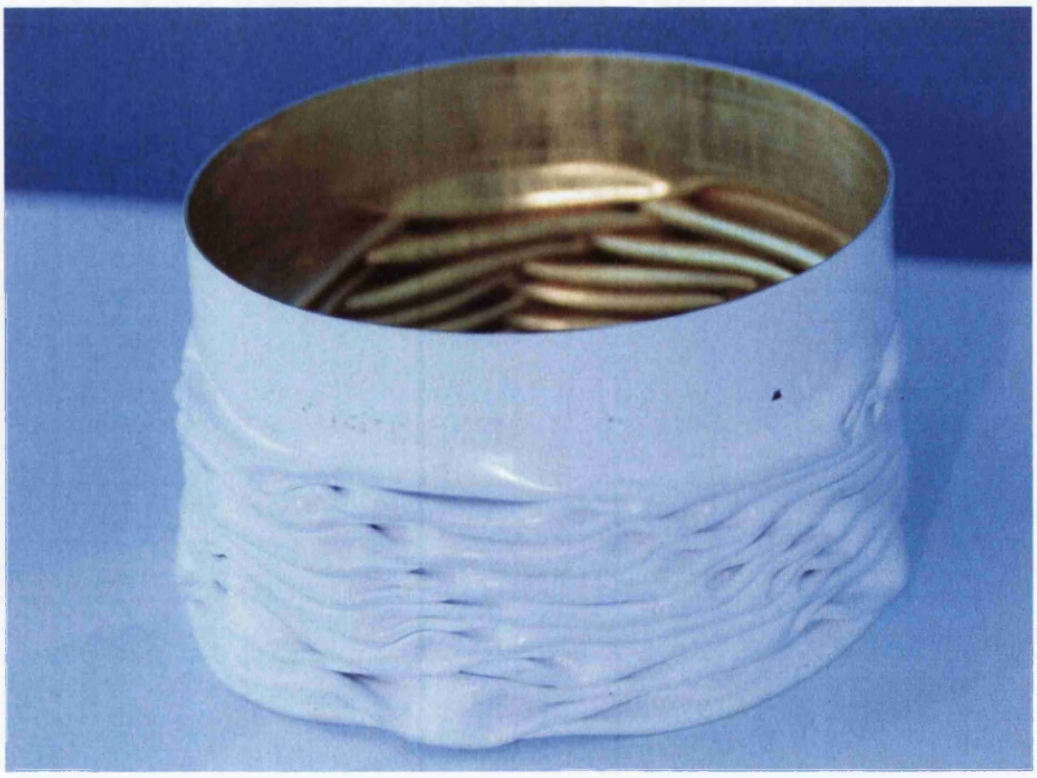

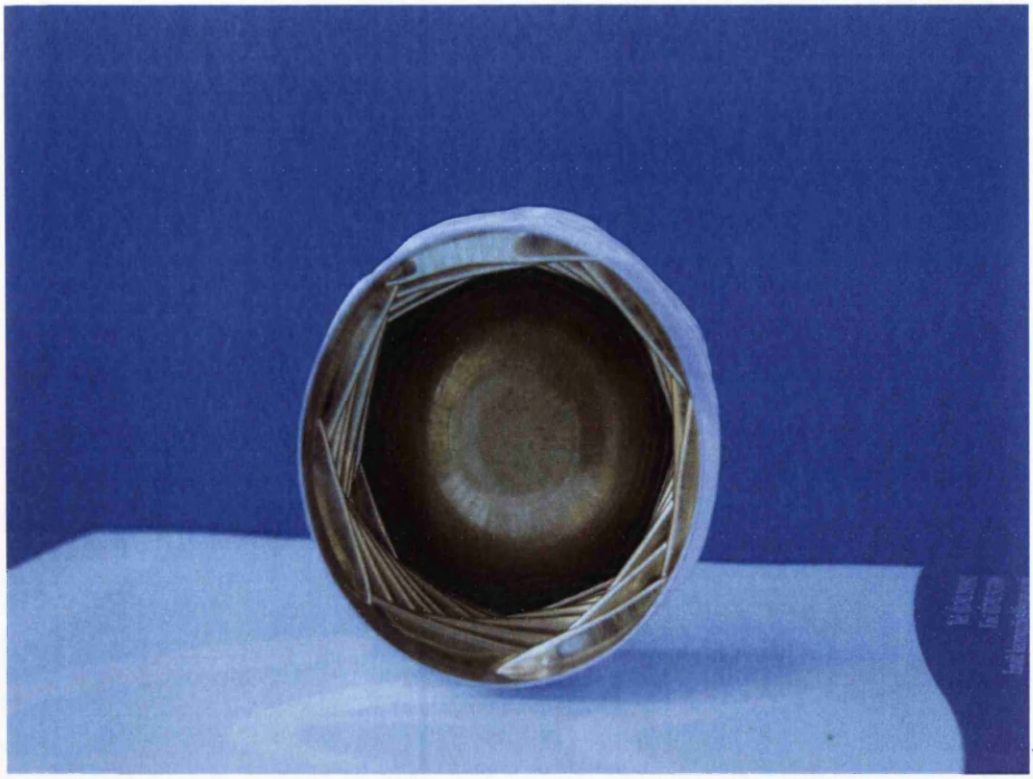

Figure 4.18: Buckled can for Case (a) axial loading analysis

4.3.6 Analytical solution

For constant thickness thin walled tubes, the maximum buckling force can be calculated from the following formula [9]:

$$F_{max} = \frac{2\pi E t^2}{\sqrt{3(1-\upsilon^2)}} \qquad \ldots (4.1)$$

Using this equation and assuming the aluminium material properties in Table 3.2 and a constant thickness of the 0.315 mm, the theoretical maximum buckling force is 26,043 N.

4.3.7 Comparison and discussion of results

4.3.7.1 Load-displacement characteristics

By comparing Figure 4.11 with Figure 4.15, it can be seen that the shape of the experimental load-deflection curve is very similar to that predicted by finite element analysis. Furthermore, the predicted elastic-plastic buckling load of 3247 N is less than 1% greater than the experimentally observed buckling load of 3230 N. Also, the predicted buckling displacement of ~0.8 mm is similar to the observed value of ~0.86 mm. There is excellent correlation between the two characteristics.

However the analytical solution, which is for the elastic buckling of a plain open cylinder with a constant wall thickness of 0.315 mm (based on experimental measurements [Patten]), is 26,043 N. This higher value is to be expected as there is clearly a stress concentration at the base of the actual cylinder (see Figure 4.8) which acts as the catalyst and causes elastic-plastic buckling at a load far less than that estimated for elastic buckling of the corresponding plain open cylinder.

4.3.7.2 Buckling mode shape

As the load increases there comes a point at which the collapse mode suddenly initiates. A linear buckling analysis indicates that for the lowest modes obtained from an eigenvalue analysis, the buckling mode for the open cylinder is a 'diamond type' inward and outward deformation see Figure 4.2(b) [21]. The predicted collapse mode of the cylinder with inverted base is shown in Figure 4.10 and the corresponding experimental results are shown in Figure 4.18.

In both cases, the buckling modes are very similar but buckling occurs close to the base, unlike that shown in Figure 4.2(b), with a seven-lobed collapse pattern.

4.4 Case (b)-Compressive behaviour during valve insertion and charging

During valve insertion and charging of an aerosol can, the loading is applied to the inner rim, as shown in Figure 4.1(b). As the load is increased, it is anticipated that the top will act as a belleville spring (washer) and will 'flatten' under load. Finite element predictions of this behaviour are compared with experimental results from tests on an aluminium aerosol can.

4.4.1 Geometry and finite element model

The finite element model was produced in three dimensions by rotation of the cross section geometry shown in Figure 4.19 through 360° about the Y-axis. The cross section is based on measurements made by Patten [2] and so provides a realistic model of the cylinder thickness profile. The resulting three-dimensional shape is shown in Figure 4.20.

4.4.2 Loading and boundary conditions

The nodes at bottom of the model are completely constrained to maintain a circular cross-section, as is see in Figure 4.21.

A face loading is applied normal to the rim of the vessel as shown in Figure 4.22. This load was incremented using the arc length method such that the pressure load was increased from zero up to failure. The load was incremented from an initial time factor of 0.01 to a total stage time of 1. For the non-linear solution of the problem, an arc load incrementing method was used to increase the applied load such that the maximum load could be found. A Newton-Raphson iteration method was used to perform an equilibrium check. A residual level of 0.1 was specified which would give sufficient accuracy for the analysis.

4.4.3 Material model

The material data described in Section 3.3.2 including the data for the multi-linear σ-ϵ curve, as shown in Table 3.5, was used for this analysis. A finite element mesh of 8548 triangular 4-noded shell elements and one element through the thickness was generated automatically using the ELFEN mesh generator and the mesh is shown in Figure 4.23.

Figure 4.19: Cross-section geometry for the analysis of Case (b) axial loading during valve insertion and charging

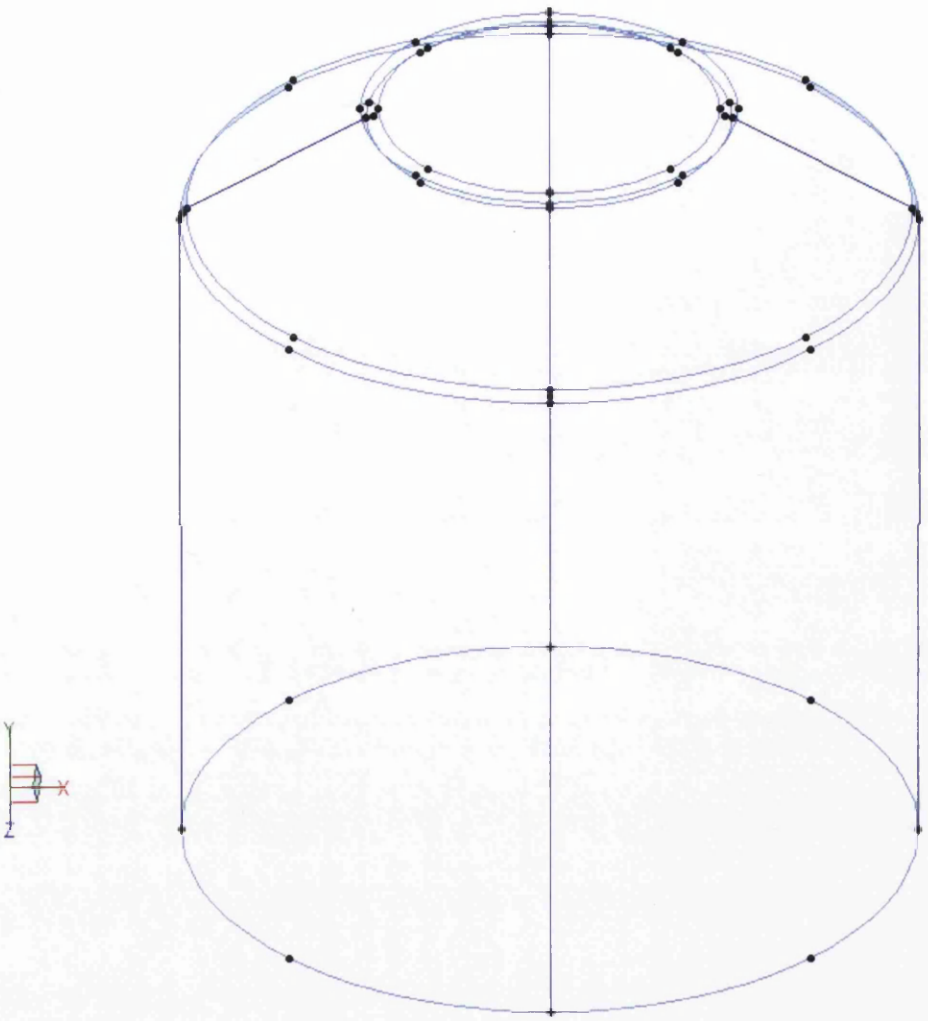

Figure 4.20: Three-dimensional model for Case (b) axial loading analysis

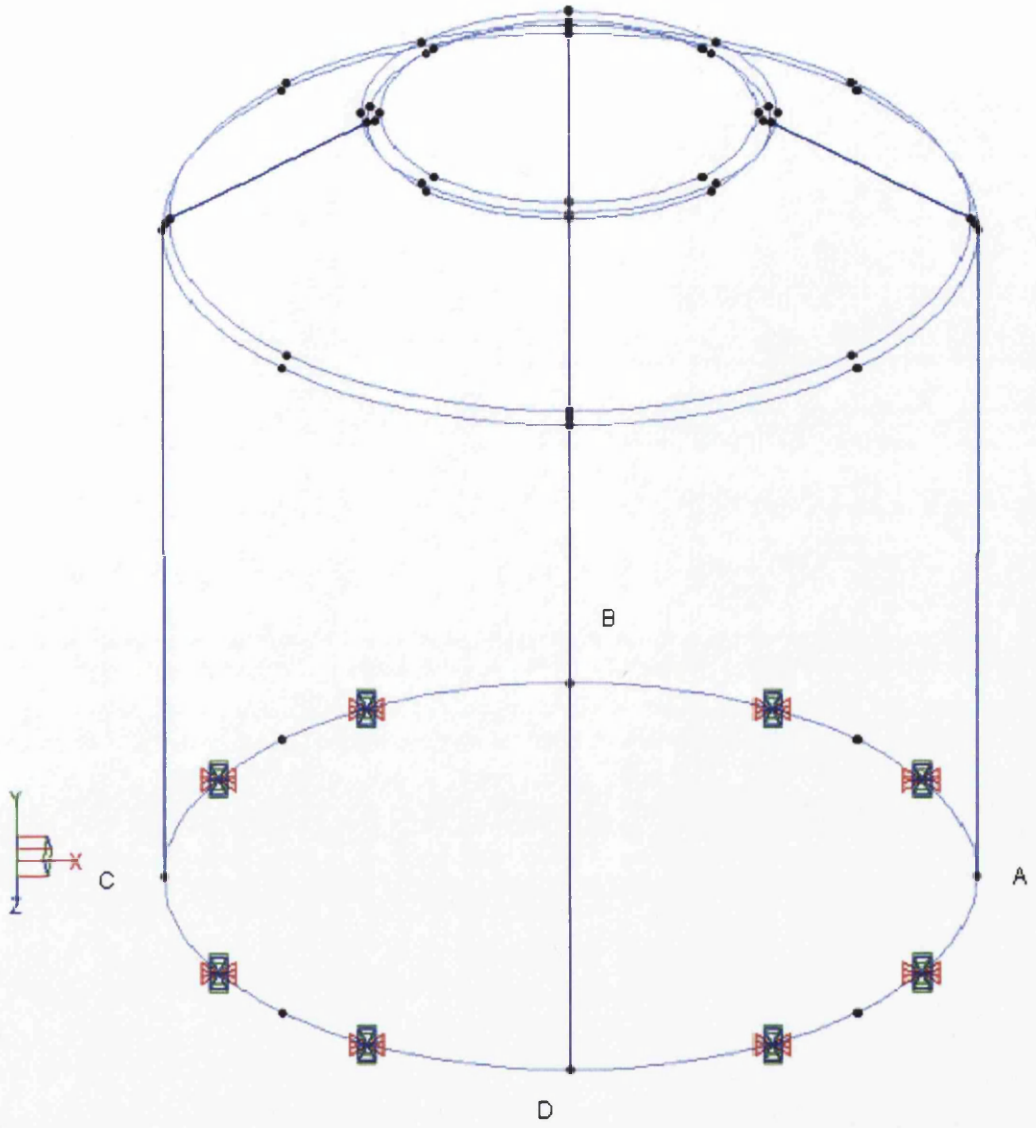

Figure 4.21: Structural constraints for Case (b) axial loading analysis

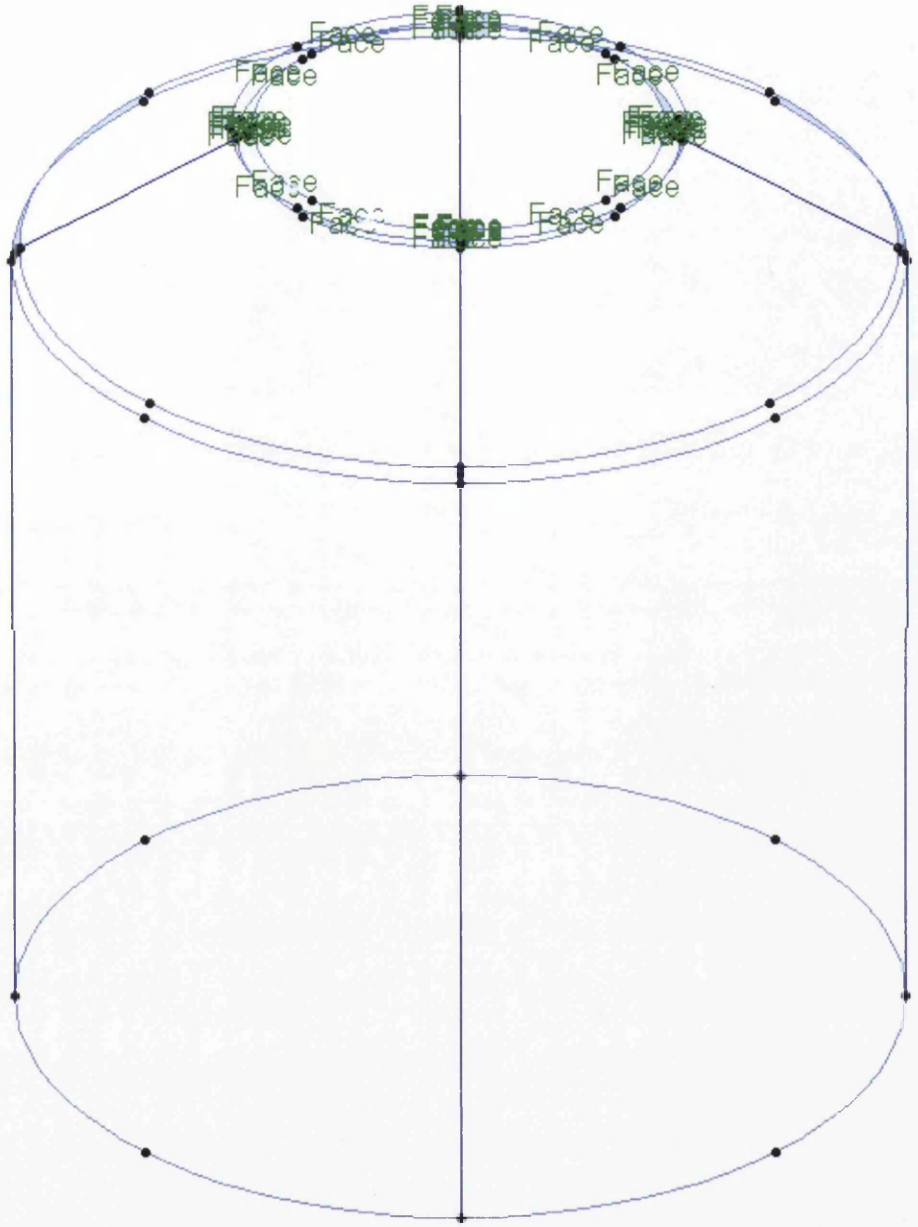

Figure 4.22: Applied loading for Case (b) axial loading analysis

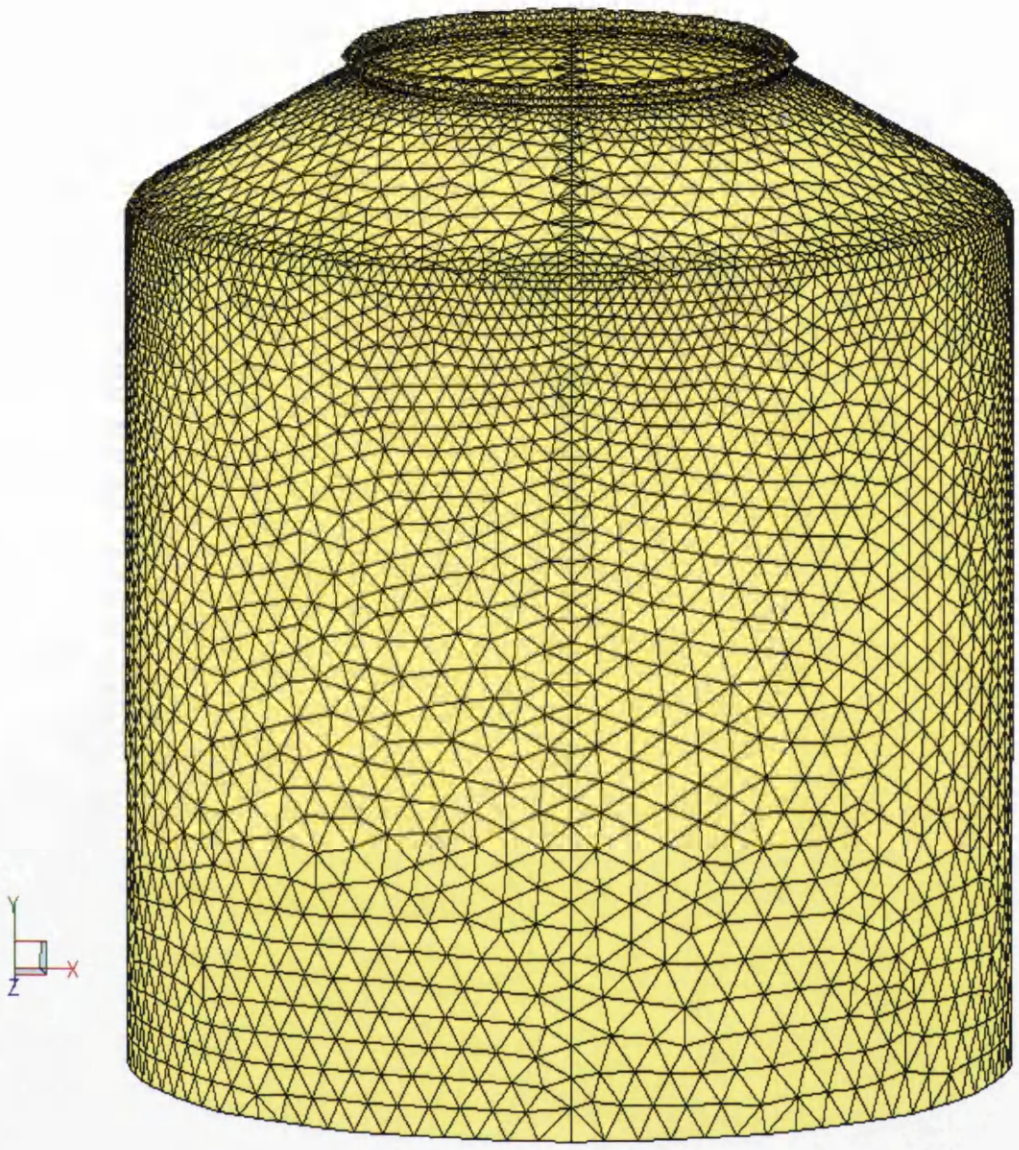

Figure 4.23: Finite element mesh for Case (b) axial loading analysis

4.4.4 Finite element predictions

Again, elastic and elastic-plastic GNL analyses have been performed using ELFEN [5]. The von Mises equivalent stress contour plot for a pre-buckling (elastic) face load of – 4.5 N/mm^2 and with a total load of 1617 N is shown in Figure 4.24. In this case, the highest stresses occur at the rim and at the intersection of the top and

parallel sections of the cylinder. The load is increased and the load-displacement curve for the rim of the cylinder is shown in Figure 4.25. A reasonably linear response is seen up to a load of 1617 N and above this, the top buckles and a reduction in load is clear. The corresponding von Mises equivalent stress contour plot and deformed shape at buckling are shown in Figures 4.26 and 4.27 respectively. It can be shown from the figures that the buckling occur in the ring top until reached the shoulder of the can.

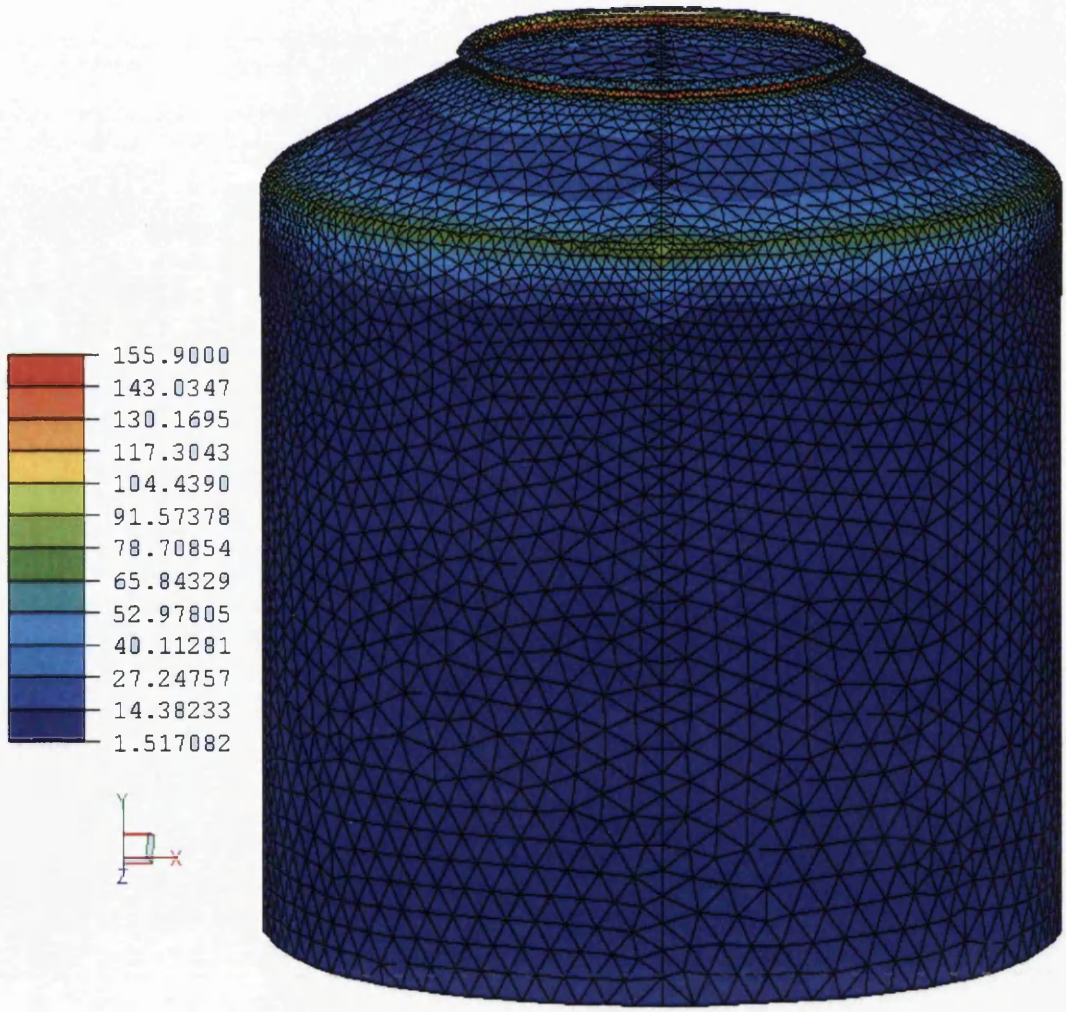

Figure 4.24: Pre-buckling equivalent stress contour plot for Case (b) axial loading analysis

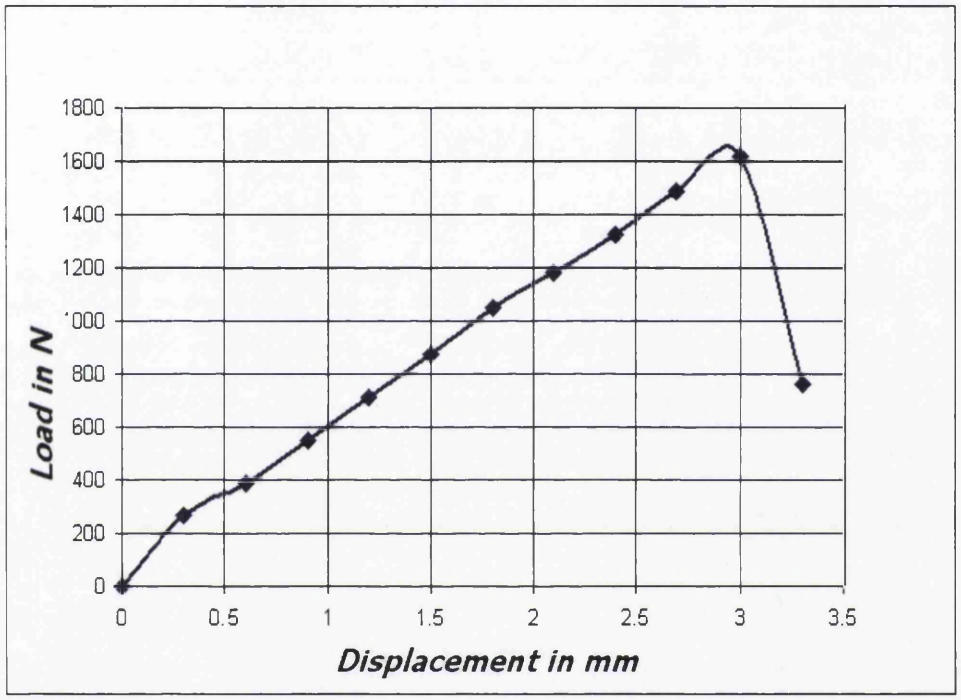

Figure 4.25: Predicted rim load-displacement curve for Case (b) axial loading analysis

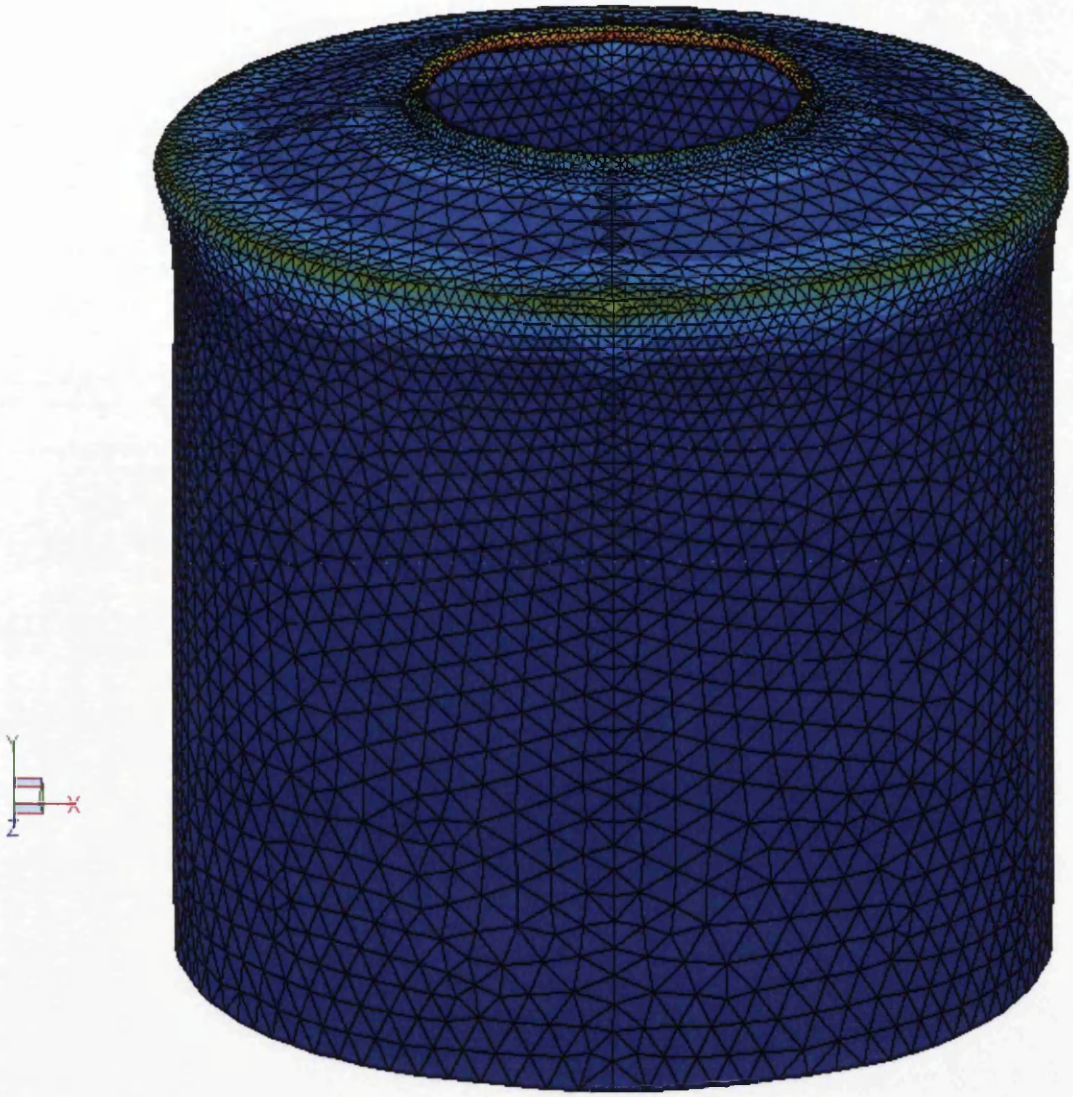

Figure 4.26: Exaggerated equivalent stress contour plot at the point of buckling for Case (b) axial loading analysis

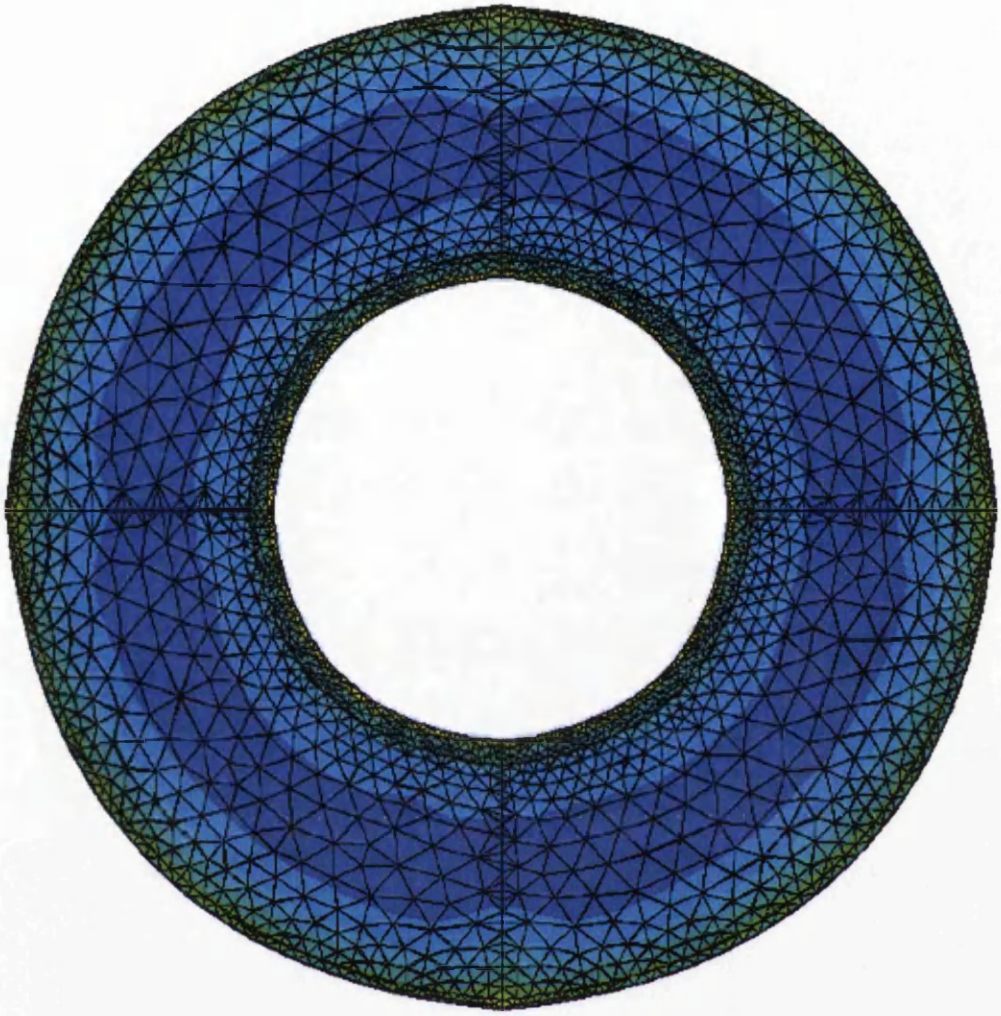

Figure 4.27: Deformed shape for Case (b) axial loading analysis

4.4.5 Experimental testing

Experimental testing on a can with outer diameter 53 mm, inner diameter 52.4 mm, wall thickness 0.315 mm (see Figure 4.28) has been carried out in order to validate the finite element predictions in Section 4.4.4. Again, the Zwick 20 kN electrically driven tensile test machine was used with a compressive load being applied.

A typical resulting load-displacement curve is shown in Figure 4.29. As the load is increased, the can is compressed until a maximum load of 1650 N is reached. Over the first 2 mm of the displacement, the load appears to increase linearly with displacement then the slope increases sharply until the point of buckling, with reducing load, is reached for displacement of approximately 2.9 mm. A second stage of buckling appears to start when the load is approximately 700 N. The load may increase again when the necked section is completely crumpled as can be seen in Figure 4.30. For this size of can, the minimum axial load that must be supported, as required by the customer specifications, is 1180 N [2] This suggests that it may be possible to make the top of the can thinner, therefore leading to further saving in material usage.

A number of compression test were carried out to investigate the axial loading that the aluminium cans are able to support.

4.4.6 Analytical solution

For a simple larg cylinder under purly compressive axial loading, the buckling load can be calculated from the following formula [55]:

$$P = \frac{\pi^2 EI}{L^2} \qquad \ldots (4.2)$$

The second moment of area for a tube section is given by:

$$I = \frac{\pi}{4}(r_o^2 - r_i^2) \quad \ldots(4.3)$$

Also, the maximum longitudinal compressive load may be calculated from:

$$F = UTS * A_{walls} \quad \ldots (4.4)$$

the predicted maximum compressive load based on Equations 4.2 to 4.4 and actual failure loads for the cans is given in Table 4.1 below.

Diameter(mm)	Length(mm)	Wall thickness (mm)	Actual failure load(N)	Predicted maximum compressive load(N)
53	110	0.41	1355	10644.2
53	125	0.315	1617	8177.8

Table 4.1: Comparison of actual failure load to buckling and compressive models

Table 4.1 shows that the cans are too short for failure to be caused by buckling and also, the failure is not caused by compressive stress in the can walls. Inspection of the aerosol cans after axial testing show that the compressive failure was concentrated on the can shoulder, as shown in finite element analysis.

It has been shown that the simple stress analysis equations cannot be used to model the deformation of the can base or axial loading.

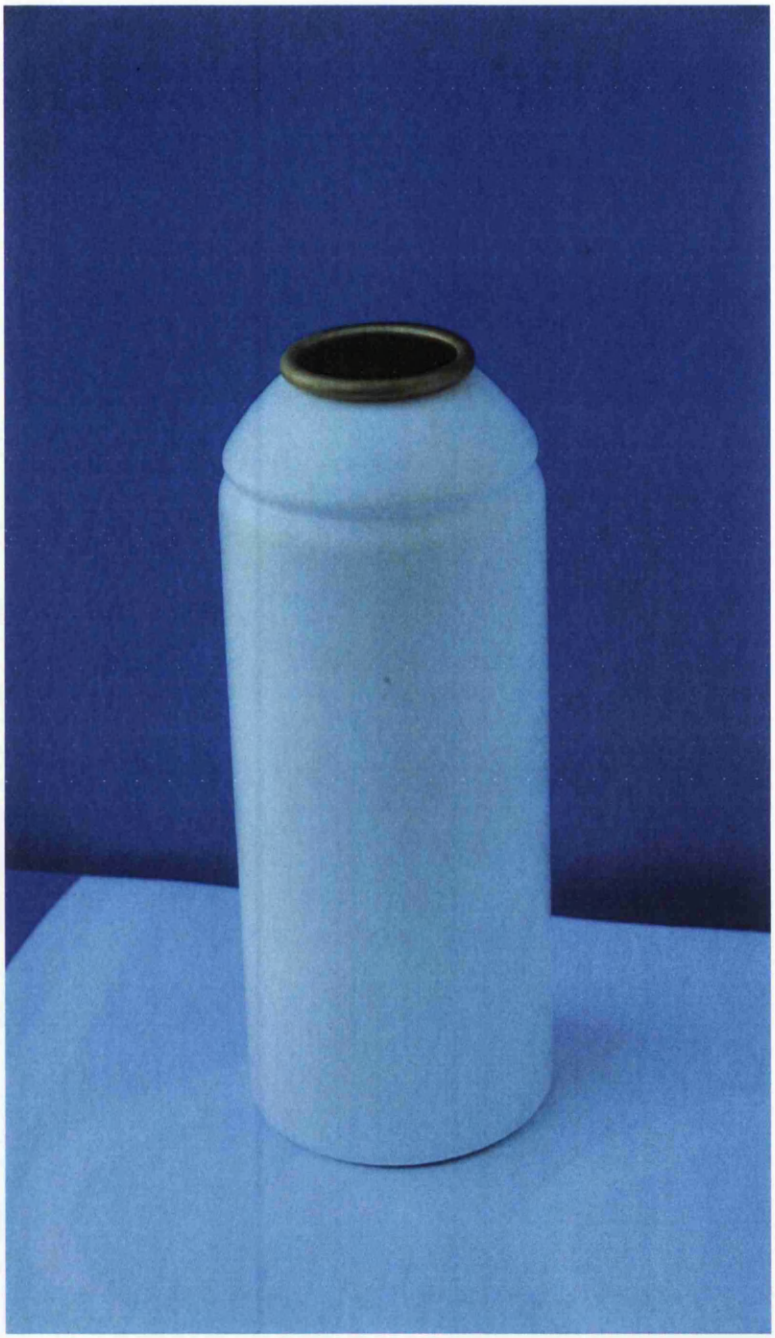

Figure 4.28: Aluminium aerosol can used in experimental testing for Case (b) axial loading analysis

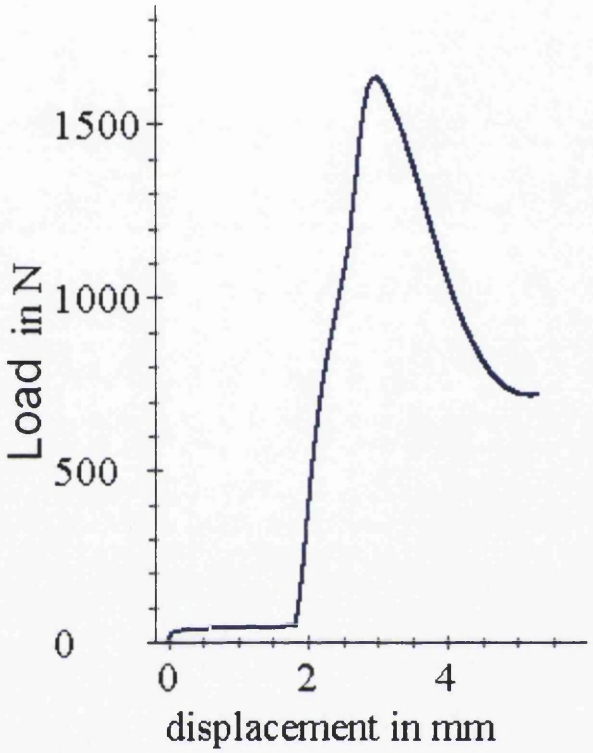

Figure 4.29: Experimental rim load-displacement curve for Case (b) axial loading analysis

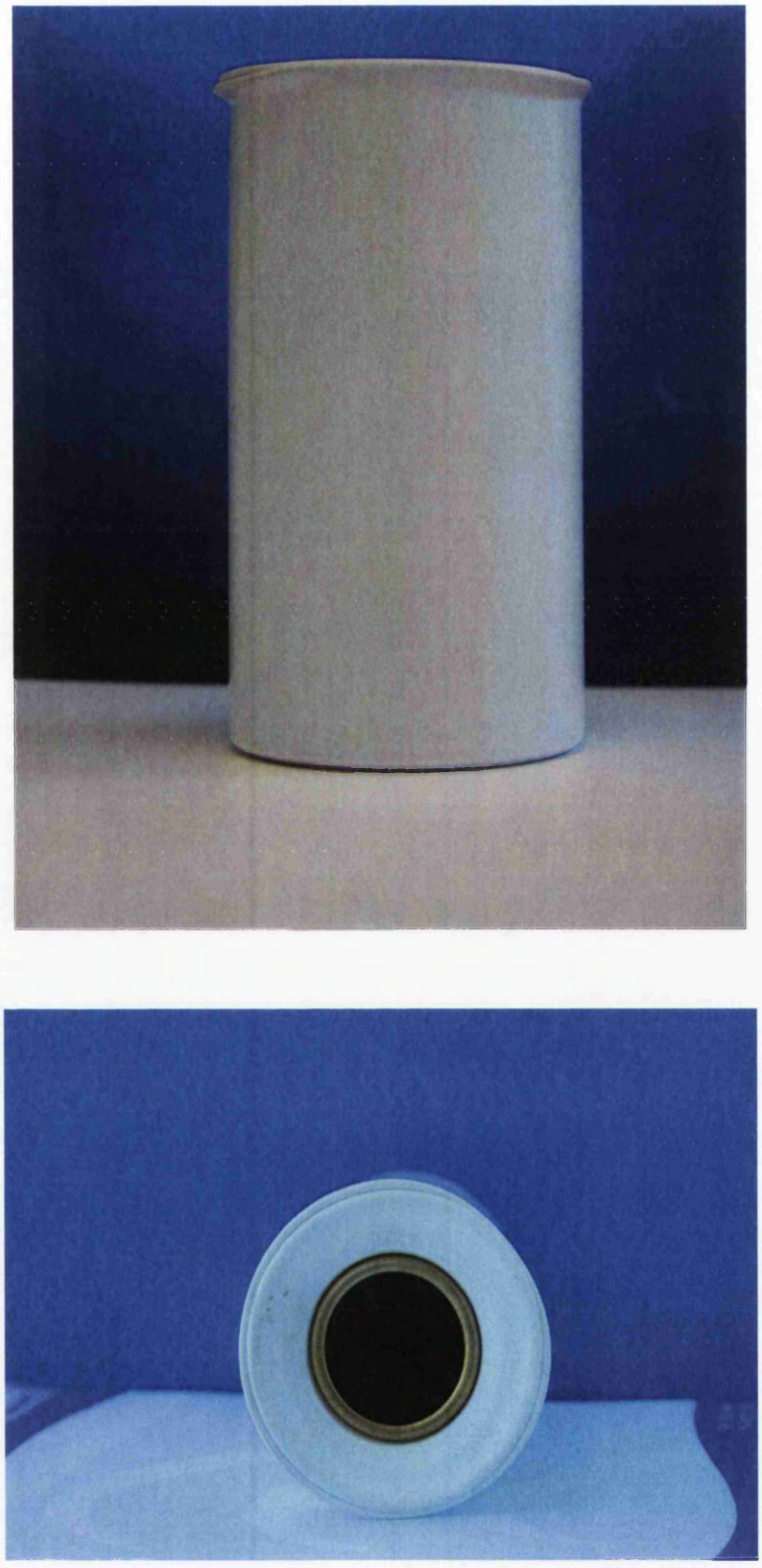

Figure 4.30: Buckled can for Case (b) axial loading analysis

4.4.7 Comparison and discussion of results

4.4.7.1 Load-displacement characteristics

By comparing Figure 4.25 with Figure 4.29, it can be seen that the shape of the experimental load-deflection curve is slightly different to that predicted by the finite element analysis in the first 2 mm of the displacement no relation visible, although they both shown buckling at a rim deflection of ~3 mm with predicted and actual buckling loads of 1617 N and 1650 N respectively.

4.4.7.2 Deformed shape

Both finite element predictions and experimental results show that, as expected, progressive failure occurs with the top of the can/cylinder taking all the deflection up to a point where the top becomes flat.

4.5 Closure

This chapter has dealt with the elastic-plastic analysis of a thin-walled cylinder (a) with inverted dome base and (b) with inverted dome base and tapered top, in both cases subjected to axial compressive loading, using a multi-linear material hardening model. Predictions have been compared with the results of experimental testing on aluminium aerosol cans and, for Case (a), with an analytical solution (which is found to be inappropriate for reasons given).

In both cases, there is reasonable agreement between the predicted and experimental collapse loads, although the Case (b) load-deflection curves are slight different. The next chapter will consider modelling of the extrusion process.

Chapter five

MODELLING OF THE EXTRUSION PROCESS

5.1 Introduction

In this Chapter, the finite element modelling of the can extrusion process is discussed. With reference to Chapter 1, there are two independent stages to the extrusion process:

Stage 1 – formation of the side walls and (flat) base,

Stage 2 – formation of the inverted dome base.

Furthermore, Stage 2 can be undertaken either before or after can decoration. In which case, although the punch and die geometries are identical, the boundary conditions are different and this leads to different profiles.

The application of finite element analysis to the extrusion process is well established and details of previous investigations are reported in Chapter 2. The aims of the modelling work described here are:

1. to validate the approach by comparing the numerical predictions with analytical predictions from Patten's constant volume model [2] and with experimental data;

2. to study the influence of the coefficient of friction and the boundary conditions on the resulting profile;

3. to obtain predictions for the forces required by the process;

4. to study the effects of punch and die slug (billet) geometry on the resulting profile.

Once a validated model has been produced, this will enable further investigation of punch, die, and aluminium billet geometries in order to generate an optimised can profile, an initial investigation in to which is presented in Chapter 6. Currently, industrial practice is based on a 'trial and error' method and relies heavily on extensive knowledge and experience to match the desired can profile with that of the slug, punch and die geometry.

A 53 mm diameter can made from aluminium 1050. has been selected for analysis. Clearly, there is a relationship between the accuracy of the predictions and the size of the can since a larger can requires a larger slug of material and greater deformation takes place.

5.2 Stage 1 modelling the base and side wall

5.2.1 Geometry and finite element model

The basic punch, die and billet geometry for a 53 mm can are shown in Figure 5.1, based on information provided by Envases (UK) Ltd. `Although it is virtually impossible to produce a perfectly axisymmetric profile (due to tool wear, deflection of the punch etc.), an axisymmetric model has been adopted because of the benefits of reduced model size and consequent reduction in computing time that can be achieved.

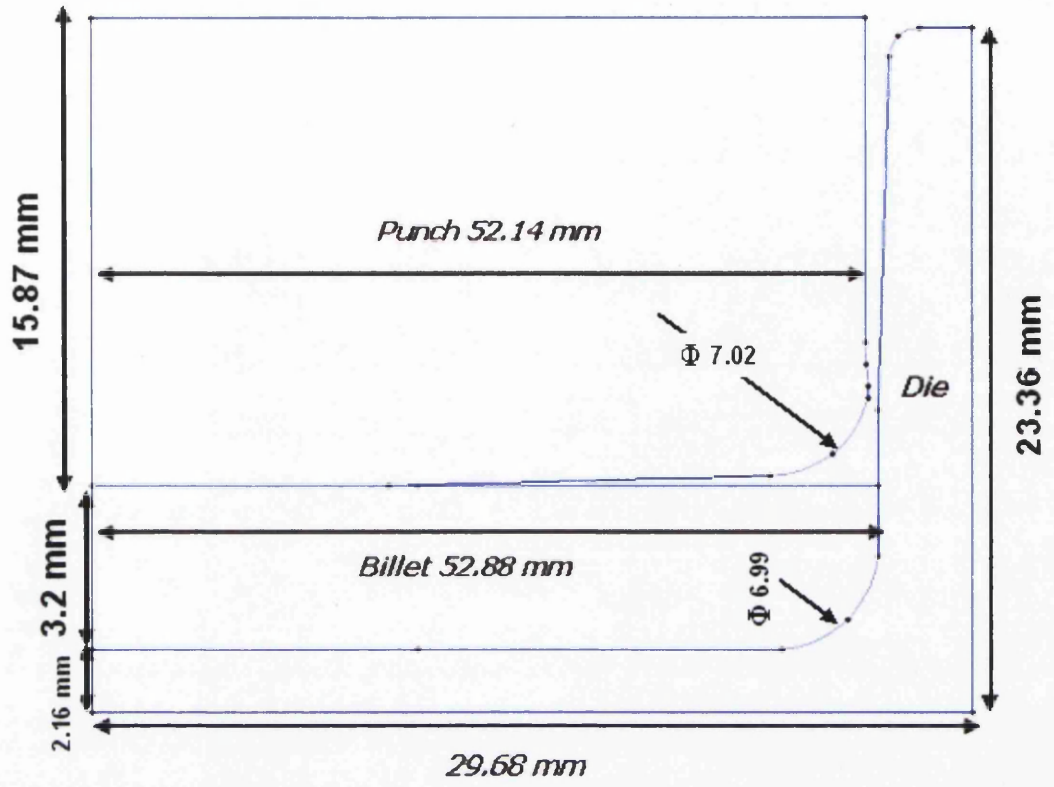

Figure 5.1: Die and punch geometry

Finite element predictions have been obtained using the large displacement elastic-plastic facilities in the ELFEN [5] suite of programs. The geometry in Figure 5.1 was then drawn into AutoCAD and the file was then transported in DXF format to ELFEN. The resulting model has 2309 eight-noded axisymmetric isoparametric elements.

5.2.2 Loading and boundary conditions

With reference to Figure 5.2, the model is constrained as follows:

1. the surface ABCDE (which represents the die) was fully restrained

2. the surface FGHJ (which represents the punch) was restrained in the X direction.

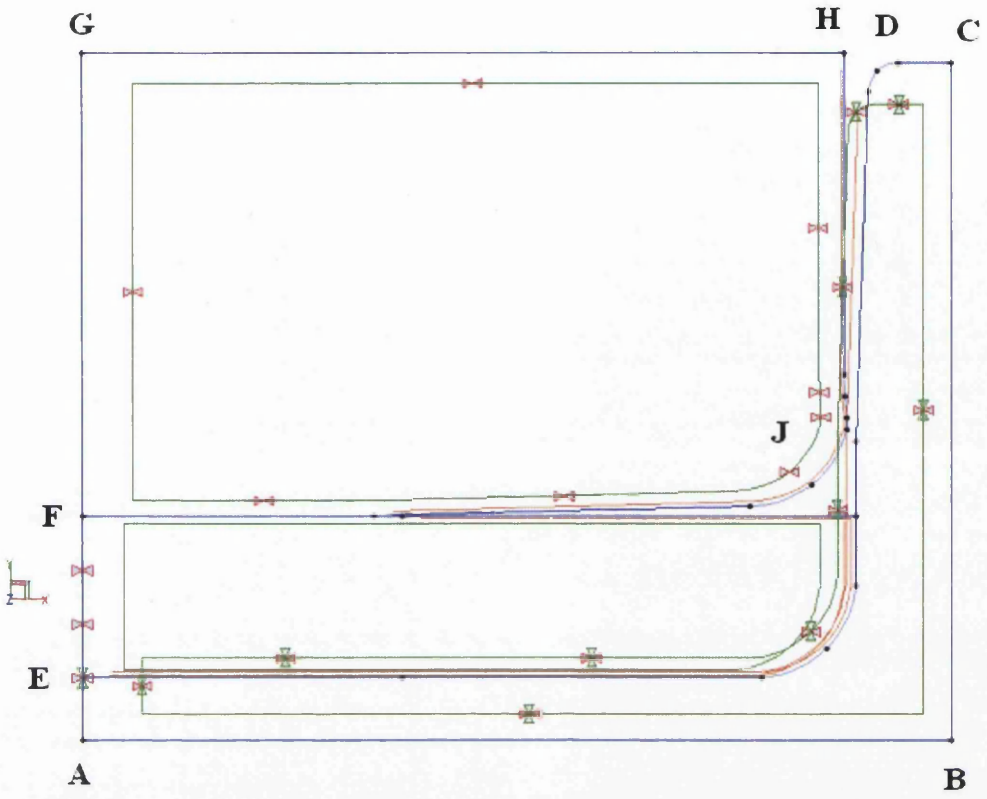

Figure 5.2: Finite element model boundary conditions

Three contact sets are created for this analysis:

- Die-Slug
- Punch-inner slug
- Punch-outer slug

Contact with friction was used in this analysis. Objects defining the contact between the slug, punch and die were defined as:

Ob-die

Ob-punch_inner

Ob-punch_outer

Ob-slug_bottom

Ob-slug_inner-top

Ob-slug_outer-top

A negative displacement of the punch in the Y direction was used to model the punch movement. A displacement in the Y direction of -4.5 mm was therefore applied to the punch using a rigid body load assigned to the top surface of the punch as shown in Figure 5.3.

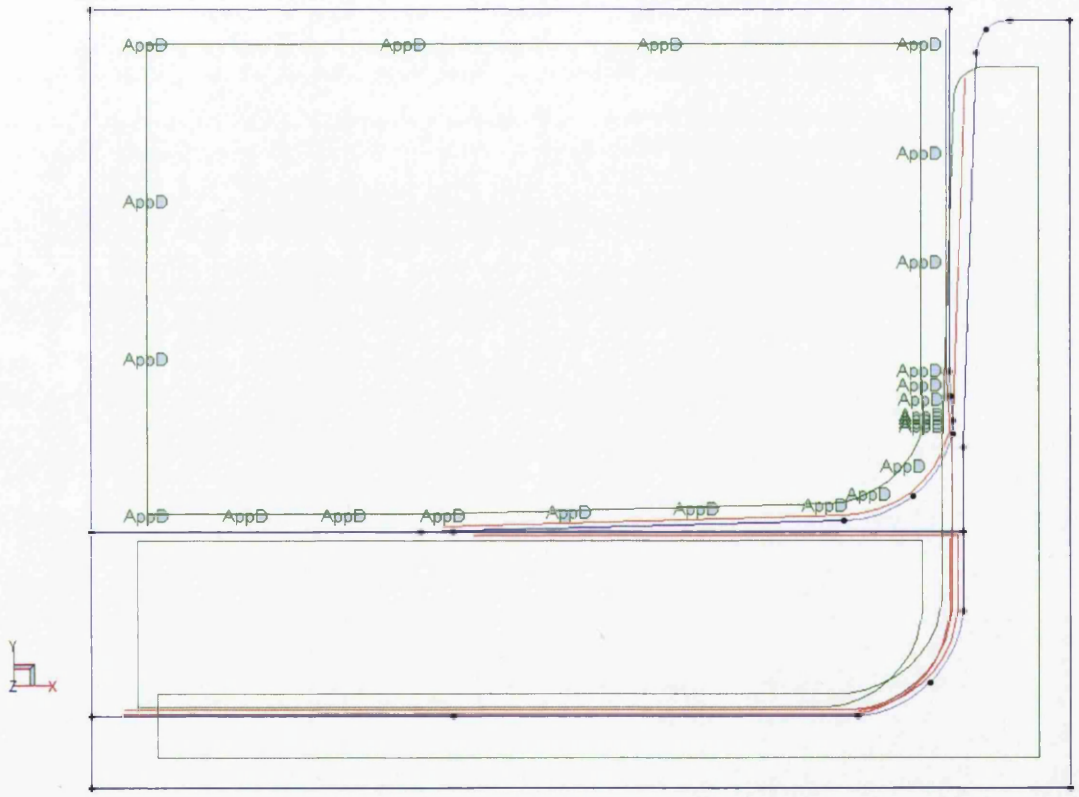

Figure 5.3: Displacement loading and contact objects

5.2.3 Material models

The elastic-plastic material properties of the slug (billet) are those for aluminium, as discussed in Section 3.3.2 and presented in Tables 3.2 and 3.5. As before, yielding is

determined using the von Mises yield criterion and post-elastic behaviour is based on the Prantl-Reuss flow rules (see Section 2.3). The material properties for the punch and die are based on steel. Values for the coefficient of friction at the contacting surfaces of 0, 0.1 and 0.25 have been assumed. The automatic mesh generation facilities were used to create the mesh shown in Figure 5.4.

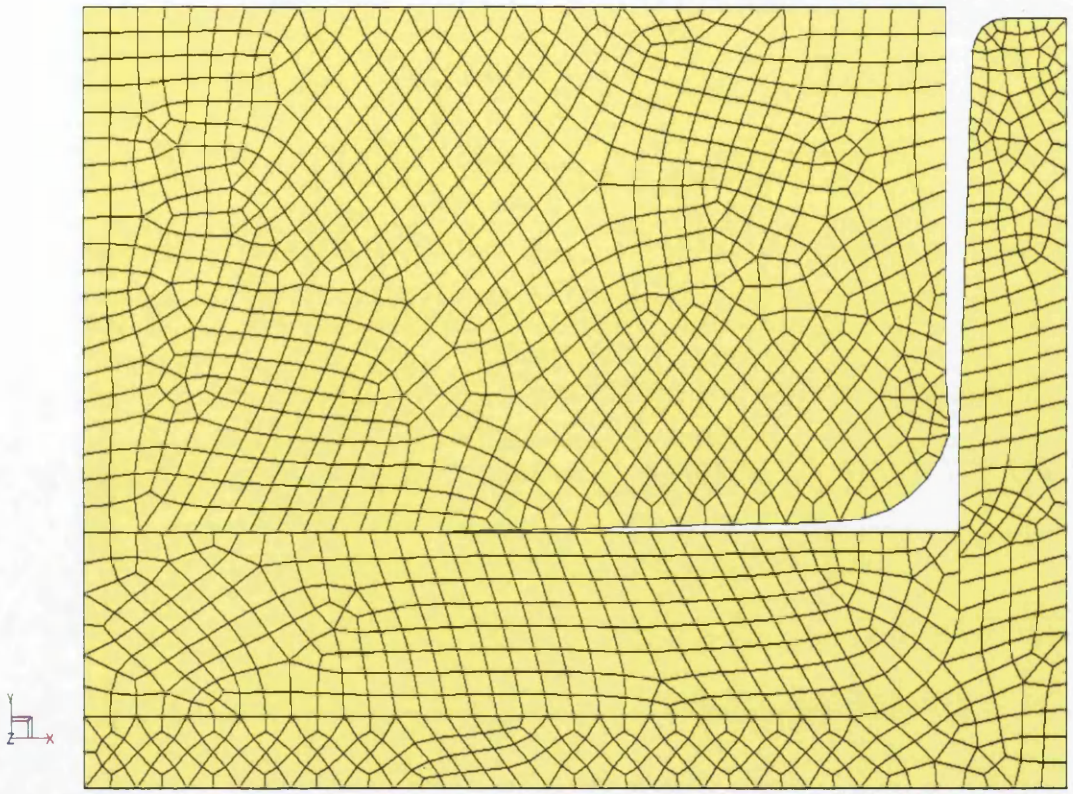

Figure 5.4: Finite element mesh

After the cans have been formed, there will be a small amount of elastic strain left within the aluminium, which will cause a very slight reduction in the can size. Since the cans are thin walled cylinders the diameters are small, thus the mechanical elastic effects are very small and therefore can be neglected.

The aluminium is plastically deformed and then there is considerable heat generation. This will affect the tooling dimensions, since there are considered in this analysis however, it is very small and therefore can also be negligible.

5.2.4 Finite element predictions ($\mu = 0.25$)

Figure 5.5 shows the development of the extruded can for punch displacements of -4.5 mm with a coefficient of friction of 0.25. When the punch is moved down it pushes the aluminium billet down in to the die and the aluminium billet will start to deform. The punch is now in contact with the billet and the billet is drawn through the die to producing a profile as can be seen in Figure 5.5(a).

Also when the punch moves down by a distance the parallel section of the aerosol can is formed. Although the tapered section of the can is formed, as can be shown in Figures 5.5(b) and 5.5(c).

At the point when the can walls are about to be made, the aluminium fills the gap between the extrusion punch and the die base. Also the tapered section of the can is predicted see Figures 5.5(d) and 5.5(e).

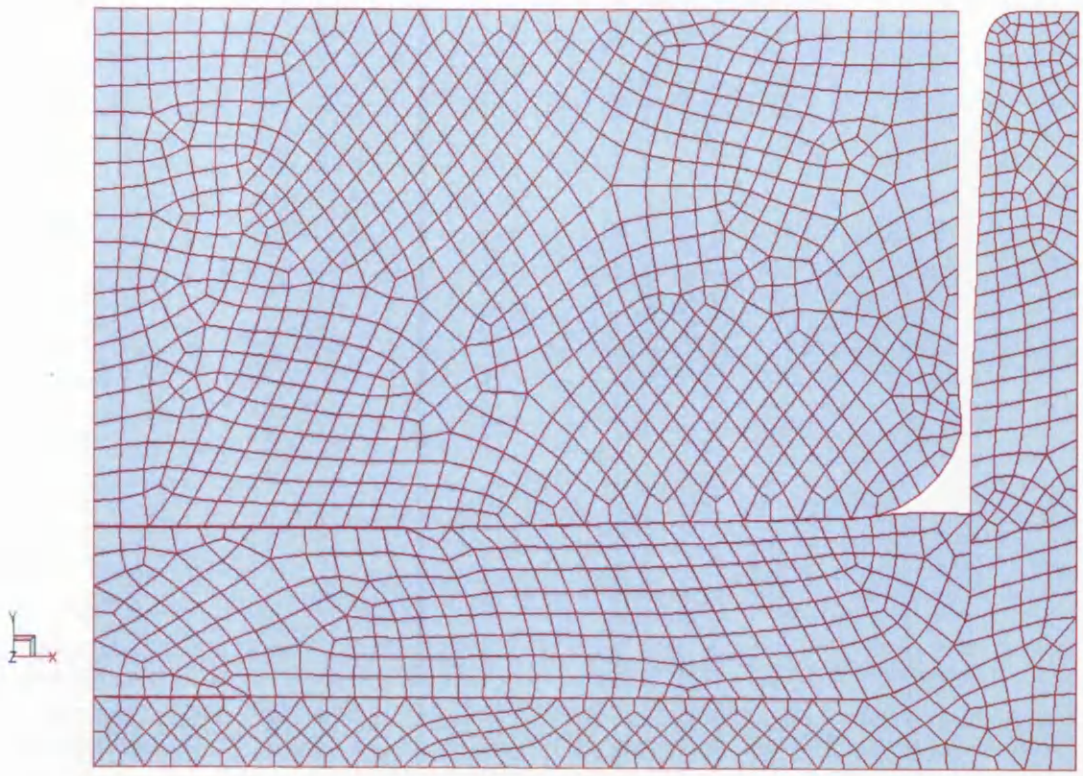

Figure 5.5(a): Stage 1 partially deformed mesh

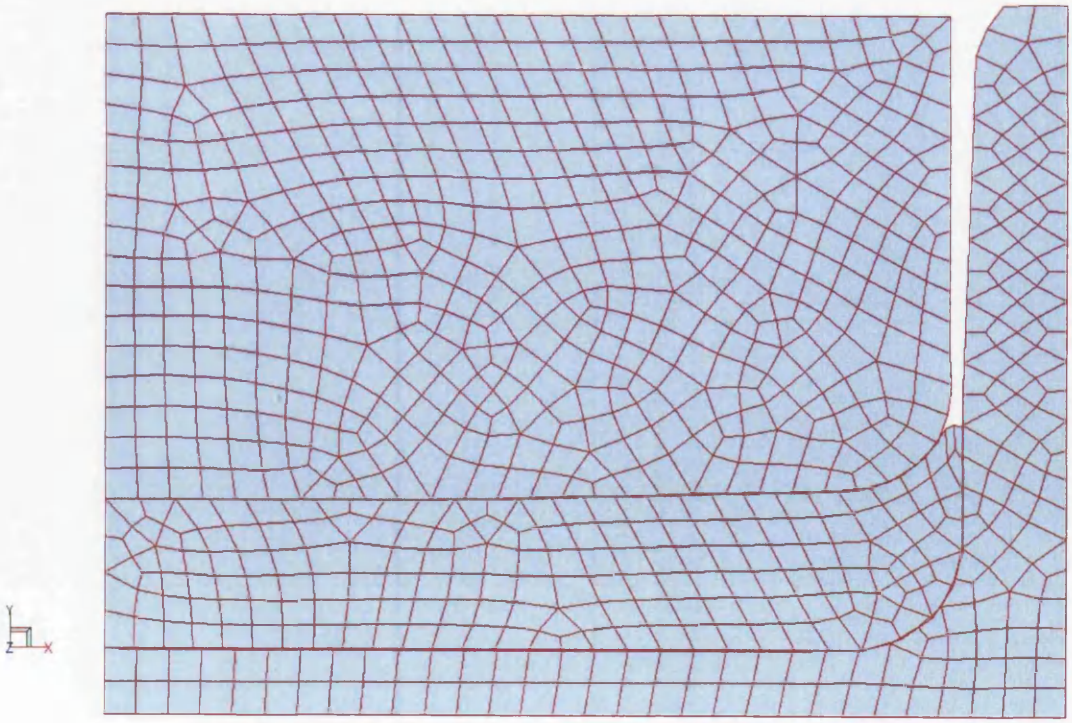

Figure 5.5(b): Stage 1 partially deformed mesh

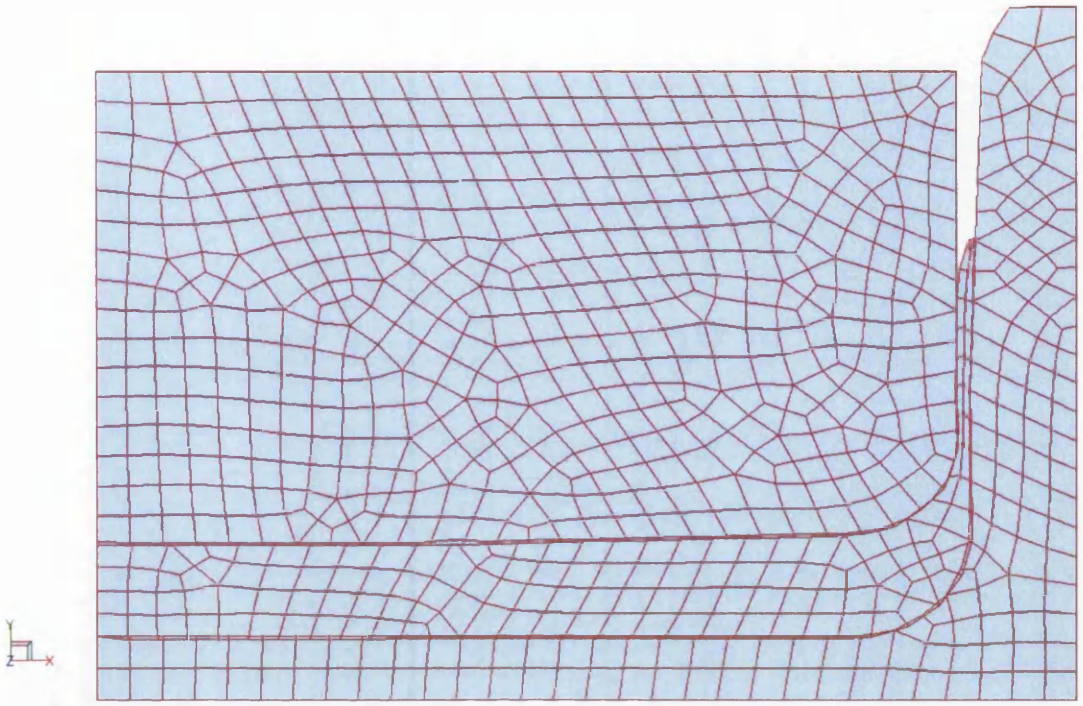

Figure 5.5(c): Stage 1 partially deformed mesh

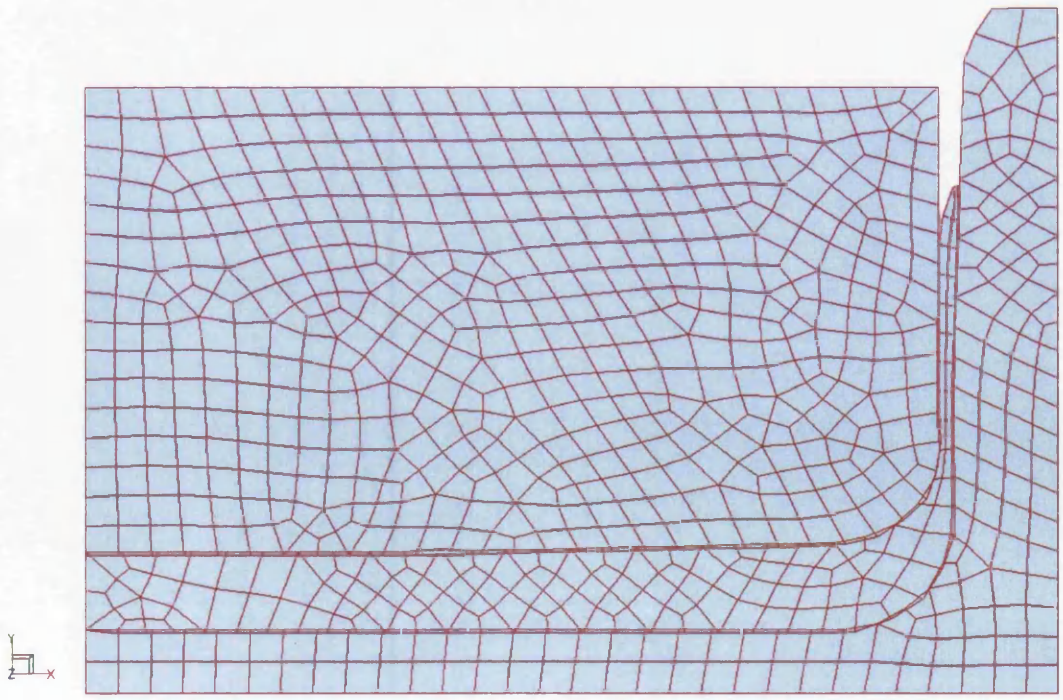

Figure 5.5(d): Stage 1 partially deformed mesh

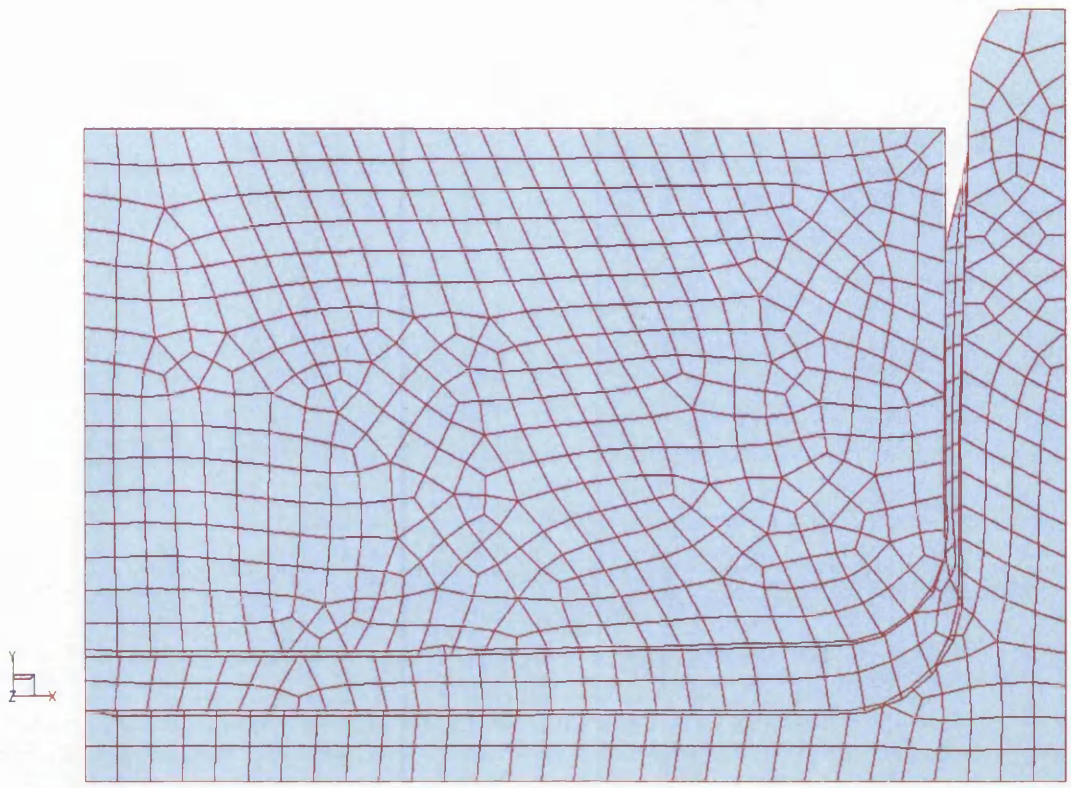

Figure 5.5(e): Stage 1 partially deformed mesh

The profile at the end of the punch travel with load still applied is shown in Figure 5.6, which also includes the corresponding details when the punch is retracted. It can be seen from the figures that the can walls and base are completely formed. The maximum equivalent stress at the end of the punch travel is shown in Figure 5.7, from which it is clear that gross yielding has occurred throughout the material. The force-displacement characteristic for the punch is shown in Figure 5.8. It can be seen from this figure that the displacement increases with increasing punch force and this increase depends on the value of the coefficient of friction, μ. As the coefficient of friction increases, the force required for any given punch travel increases.

The force-displacement curve was obtained by re-running the analysis using an applied force to the punch, as shown in Figure 5.9. An incrementally increasing force was applied and the punch displacement noted after each increment. Hence it was possible to determine the force at various stages of the extrusion process, knowing the punch displacement. The results of the analysis, shown in Figure 5.8, indicate that a maximum force of -45.7 kN is required to produce this profile. Up to a displacement of 1 mm the curve has a sharp rise with increasing force and displacement. Until reaches the highest point.

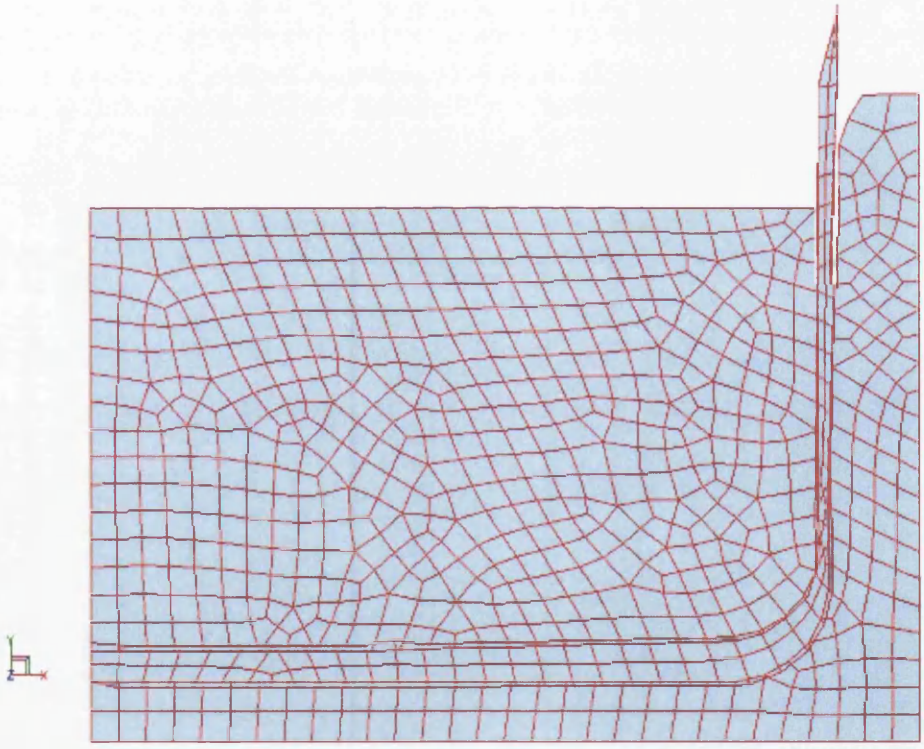

Figure 5.6(a): Stage 1 at the end of the punch travel

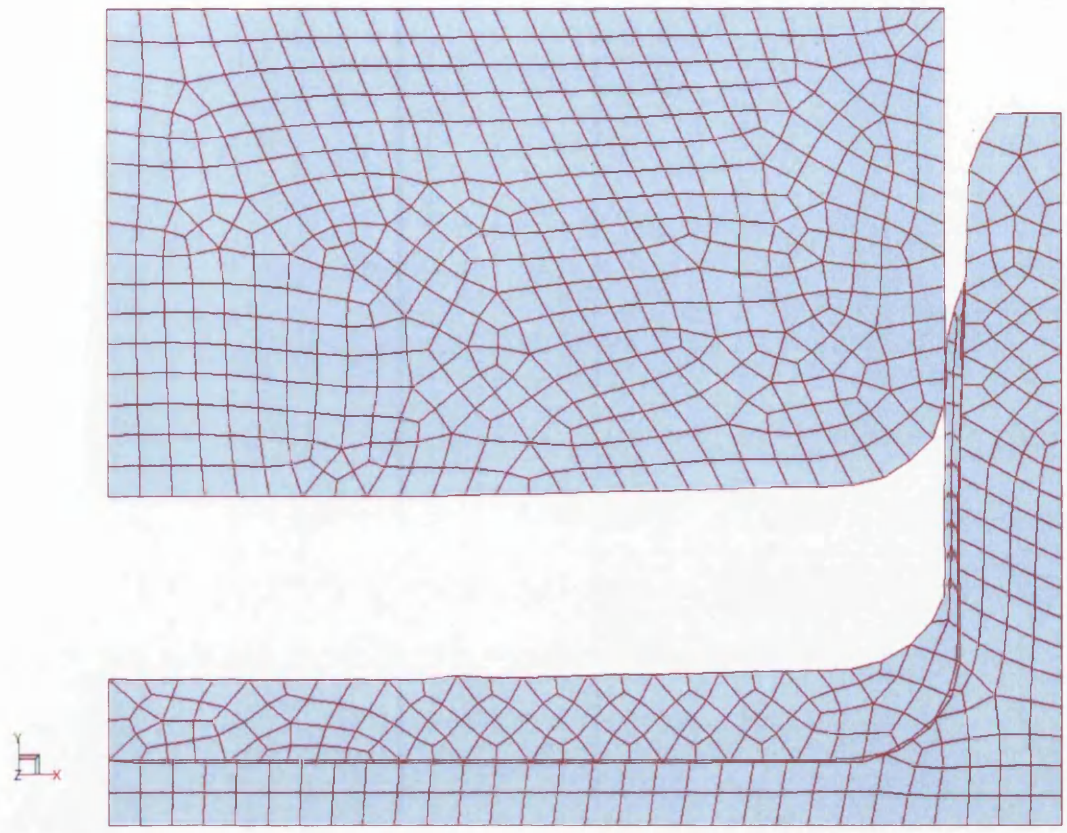

Figure 5.6(b): When the punch retracted

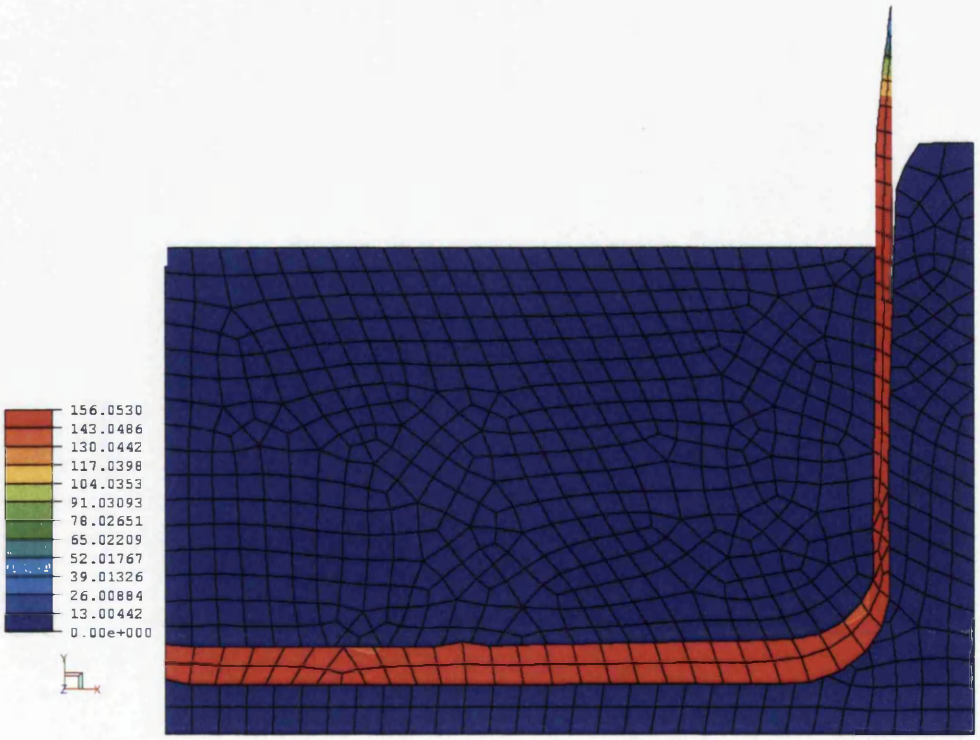

Figure 5.7: Von Mises max equivalent stress contour plate at the end of punch travel

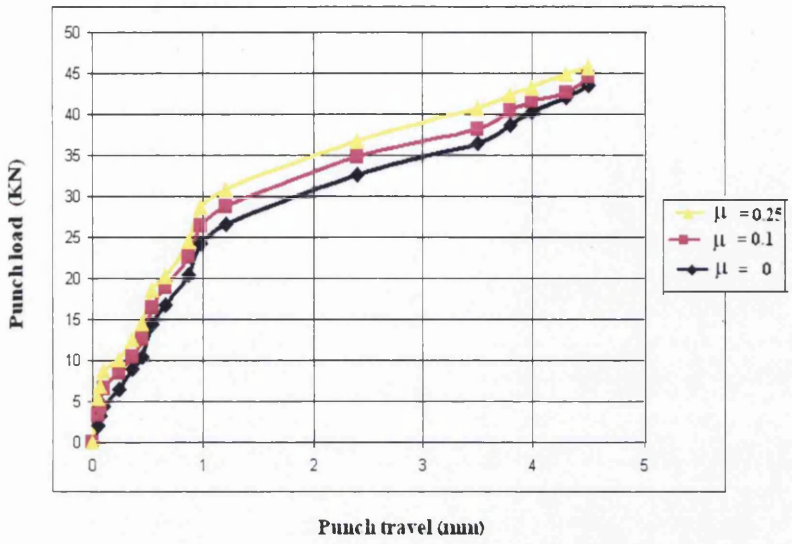

Figure 5.8: Comparison of punch load Vs punch travel displacement for various coefficient of friction

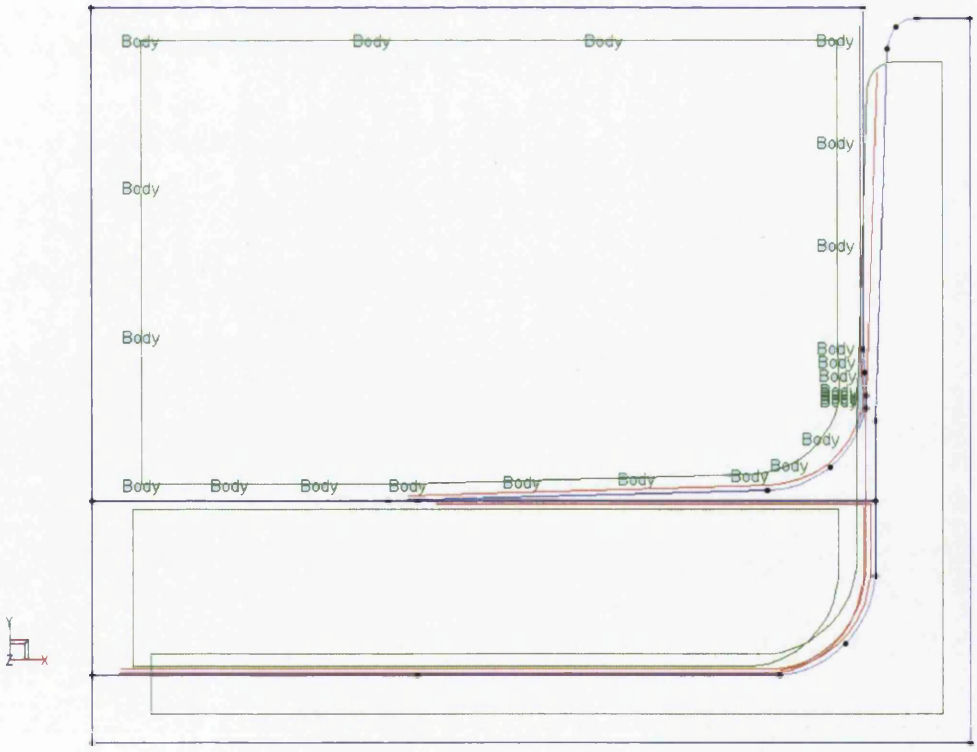

Figure 5.9: Stage 1 model with force loading

The thickness profile, starting at the centreline of the base and moving along the base, around the corner and up the cylinder, is shown in Figure 5.10. This figure includes finite element predictions for μ = 0, 0.1 and 0.25 (discussed in Section 5.2.5). Figure 5.10 also included the results from [2], which is discussed in Section 2.10.2.

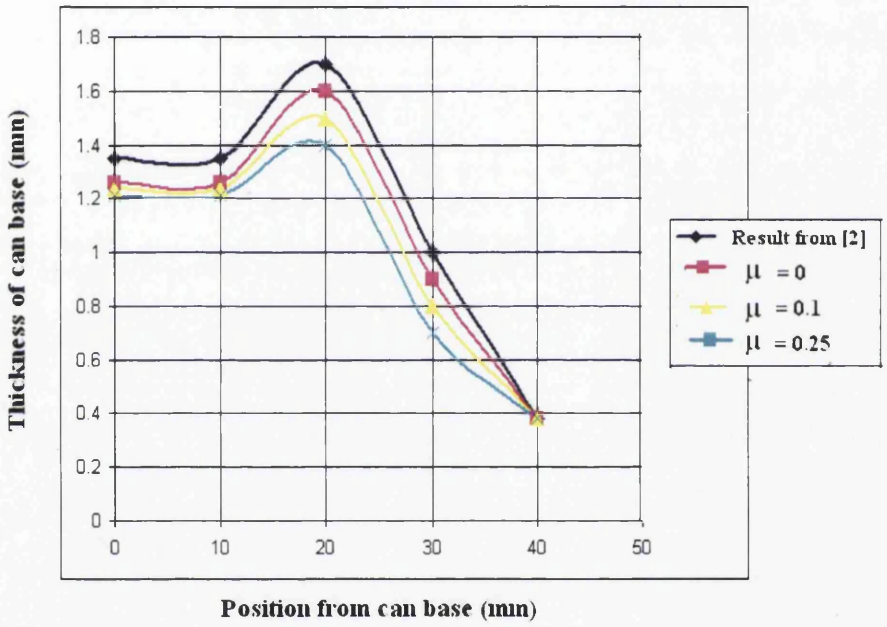

Figure 5.10: Comparison of the effect of coefficient of friction on the Stage 1 extruded thickness profile with that predicted by the result from [2]

5.2.5 Effect of coefficient of friction

The effect of friction in the direct extrusion process is important in the commercial process because it determines the billet size and hydraulic pressure requirements, either by pressure limitation or by surface at the end of the ram stroke.

The basic extrusion process was simulated with three different values for the friction coefficient on the contacting surface and the comparisons of punch force and resulting thickness profiles are shown in Figures 5.8 and 5.10 respectively. From Figure 5.8 it can be seen that the variation in punch load with μ during the process can be significant (up to 5 KN) although the maximum force variation is less significant (45 KN). Figure 5.10 indicates that thicker sections in the base are produced when μ is low but that the thickness at the start of the cylindrical section is less affected by the friction. Also the effect increases with the increasing area of contact between the specimen and the tools, and with the reduction thickness of the processed material [43].

5.2.6 Comparisons with analytical solution

The results of this validation are shown in Figure 5.10. It can be seen from the figure that the extrusion model is reasonably accurate with the lower friction giving the best correlation with the constant volume results of [2].

5.3 Stage 2 modelling

The bottom forming process produces the dome in the can base. This is produced by supporting the can on a mandrel and forming the can base with a punch.

5.3.1 Geometry and finite element models

The basic punch and die geometry for the base of a 53 mm can are shown in Figure 5.11, based on information provided by Envases (UK) Ltd. Again, an axisymmetric

model has been adopted because of the benefits of reduced model size and consequent reduction in computing time that can be achieved.

Finite element predictions have been obtained using the large displacement elastic-plastic facilities in the ELFEN [5] suite of programs. The geometry in Figure 5.11 was replicated in AutoCAD [56] and the file was then transported in DXF format to ELFEN.

5.3.2 Loading and boundary conditions

Two sets of boundary conditions have been considered. The formation of the base can take place either before or after the can is decorated and the support provided to the can during base formation is different for the two cases. Experimental observations indicate that a different base profile is generated for these two cases and an additional objective of this work is to confirm (or otherwise) this variation.

5.3.2.1 Stage 2(a) – base formation before decoration

With reference to Figure 5.12, the model is constrained as follows:

The die is fully restrained in the X and Y directions, the punch is restrained in the X direction, and the can was constrained in the X-direction along the centre line.

5.3.2.2 Stage 2(b) – base formation after decoration

With reference to Figure 5.13, the model is constrained as follows:

The vessel is restrained in the X and Y directions in the inside of the cylindrical section. The punch is restrained in the X direction and the die restrained around the edge.

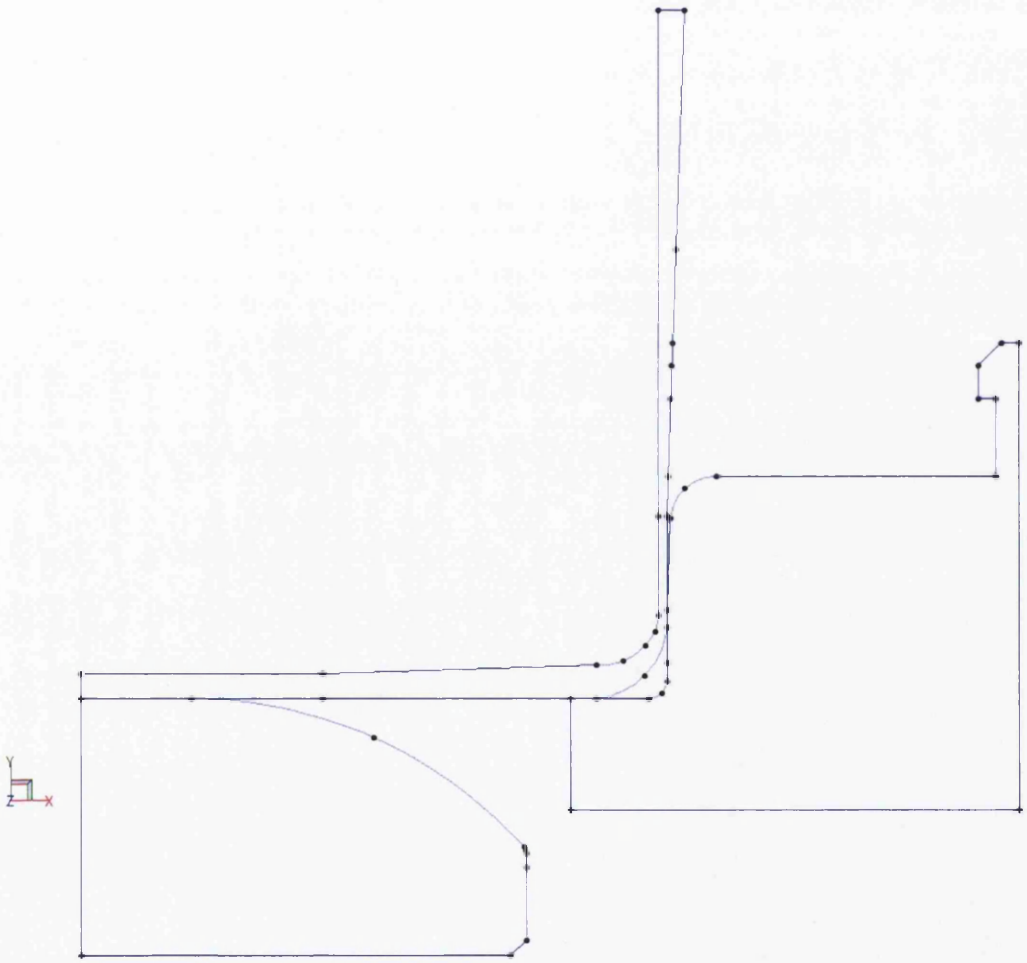

Figure 5.11: Impact extrusion dome base

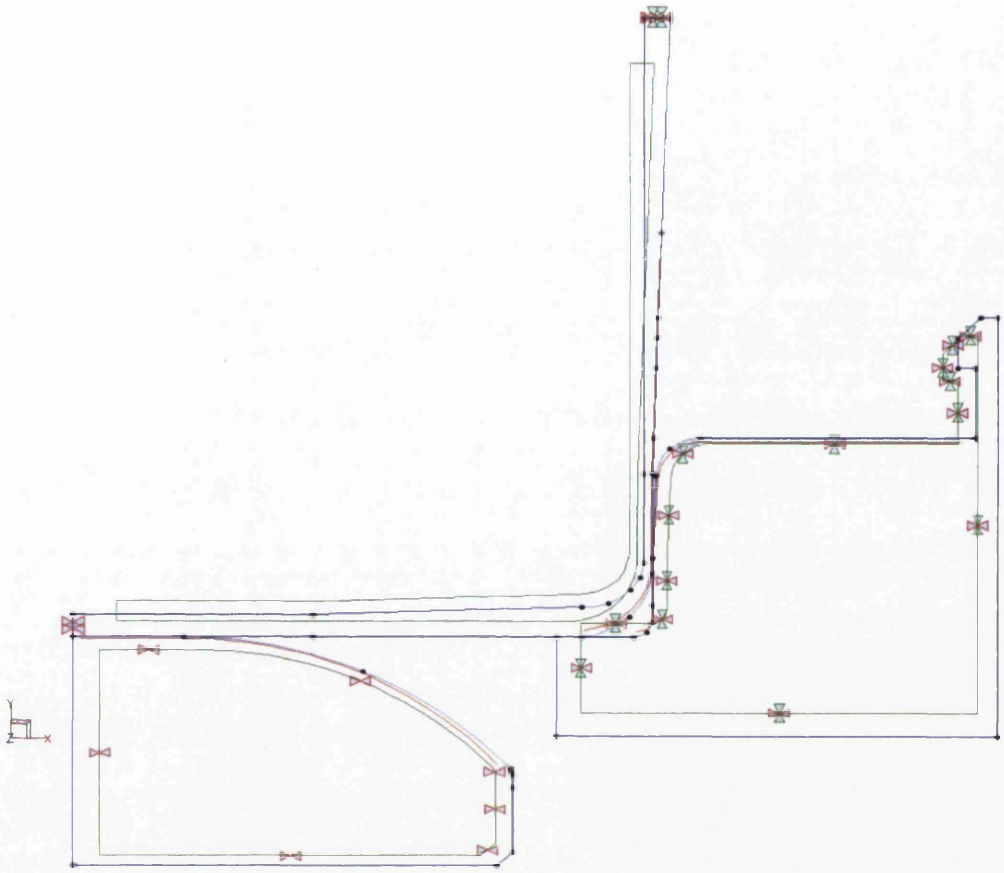

Figure 5.12: Stage 2(a) finite element model boundary conditions

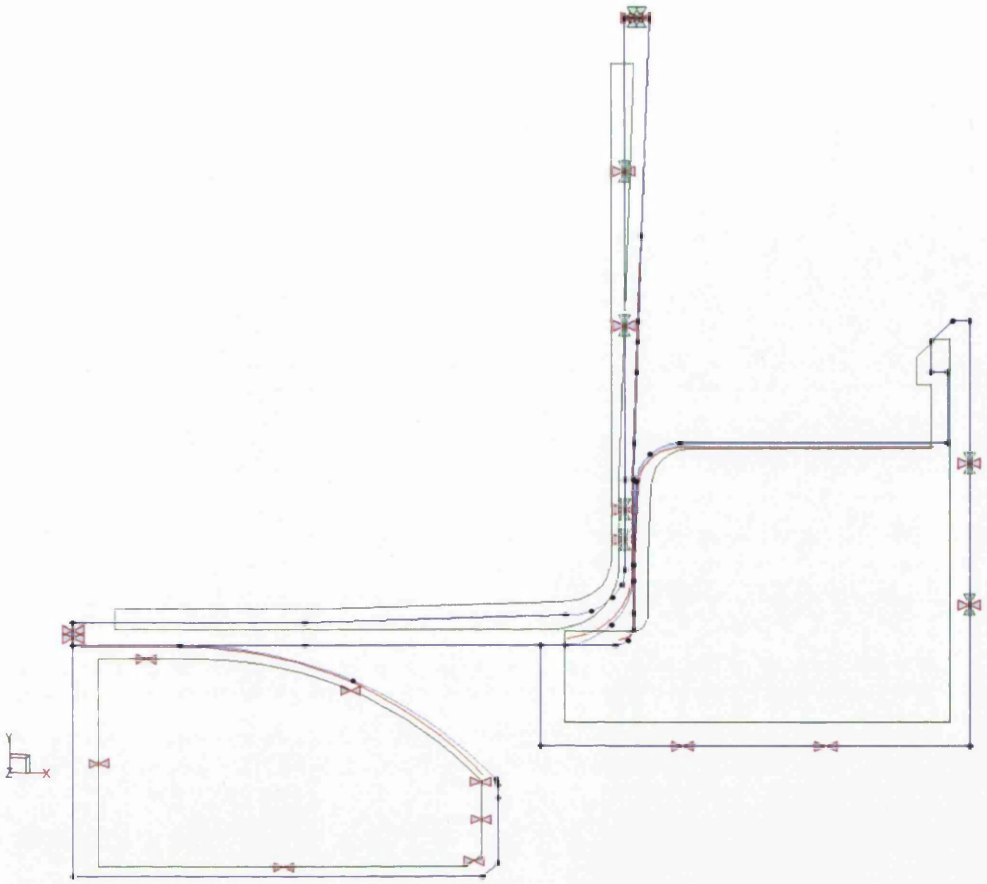

Figure 5.13: Stage 2(b) finite element model boundary conditions

5.3.2.3 Stage 2 loading

A positive displacement of the punch of 8 mm ± 0.5 mm. in the Y direction was used to model the punch travel [57]. Three values of punch displacement in the Y direction of 7.5mm, 8 mm and 8.5 mm were therefore applied to the punch using a rigid body load assigned to the top surface of the punch, as shown in Figure 5.14

.

Objects need to be defined to account for contact between the tooling and the can. These were defined as:

- Outer surface of can

- Inner surface of can
- Top surface of mandrel
- Top surface of punch

Two contact surfaces were defined using updated penalty:

- Punch can
- Can mandrel

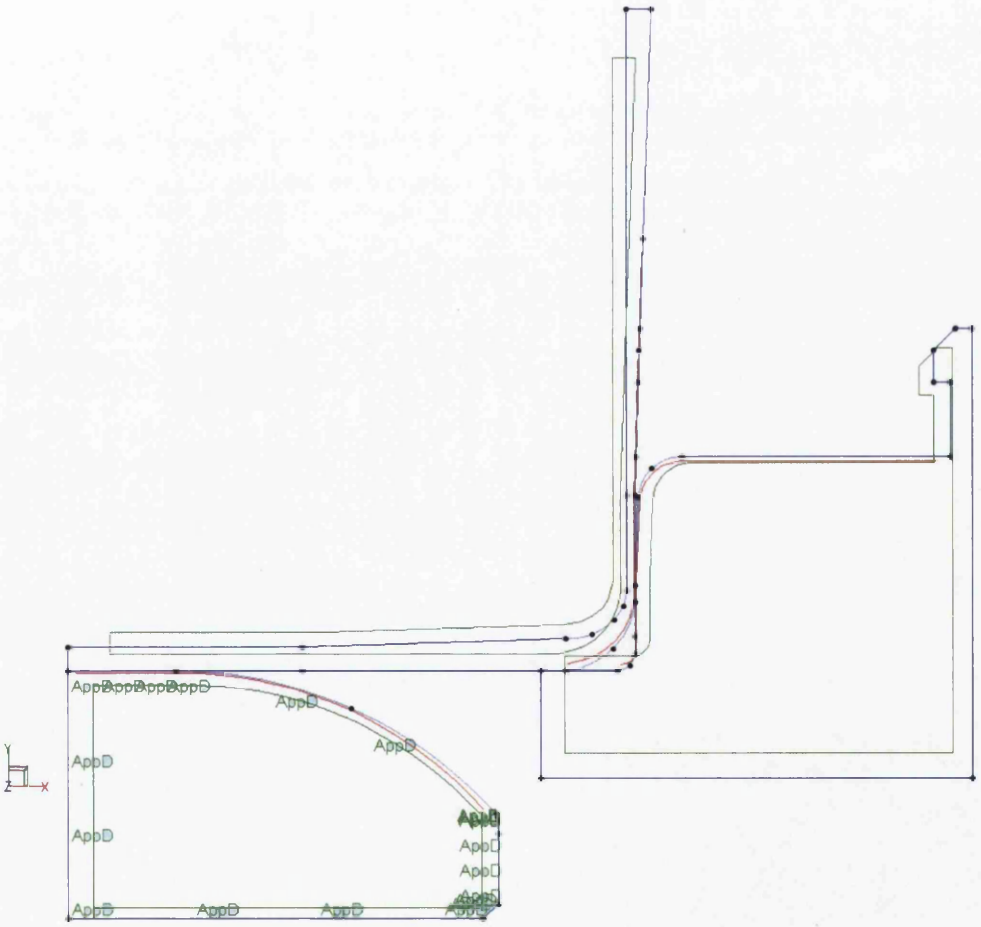

Figure 5.14: Finite element loading

5.3.3 Material models

The material models used are the same as those discussed in Section 5.2.3.

The automatic mesh generation facilities were used to create the mesh shown in Figure 5.15. The resulting model has 1325 four-noded axisymmetric isoparametric elements.

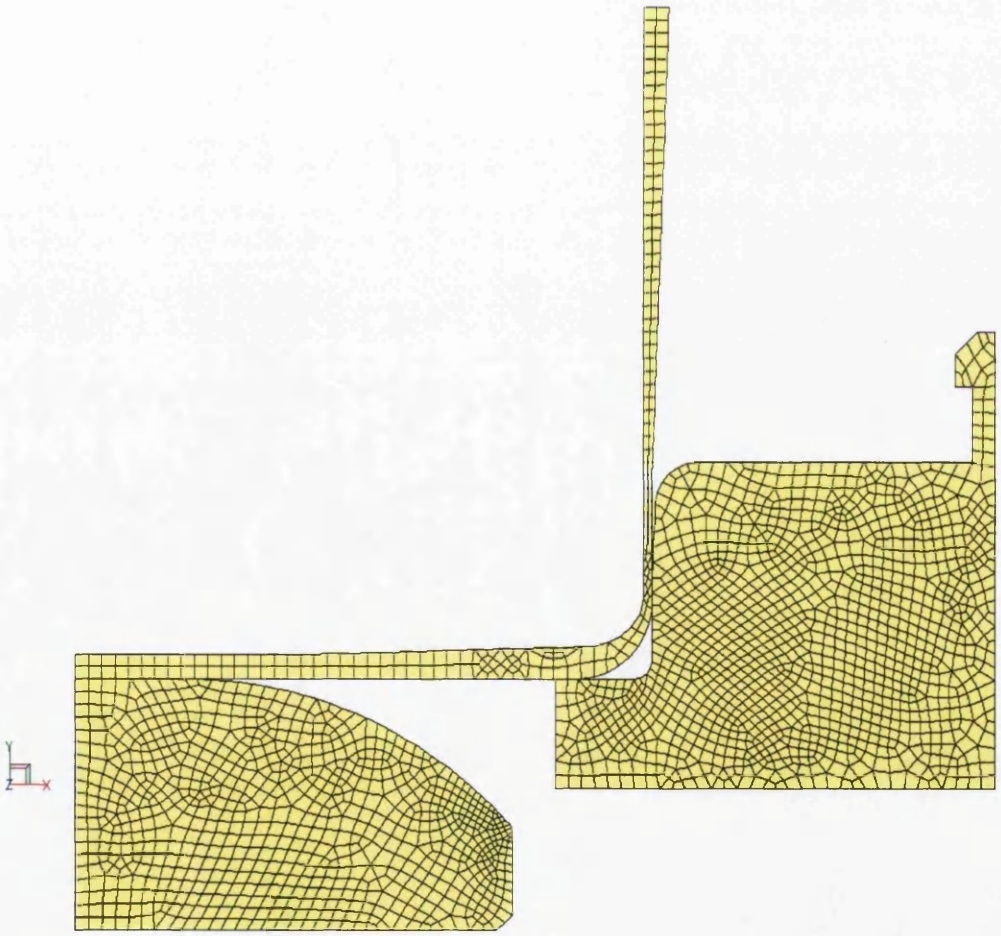

Figure 5.15: Finite element mesh

5.3.4 Finite element predictions ($\mu = 0.25$)

5.3.4.1 Stage 2(a):` pre-decoration boundary conditions

Figure 5.16 shows the bottom forming simulation for a 53 mm aerosol can base at various stages during the loading process, with $\mu = 0.25$. The development of the inverted base shape is clearly visible. It can be seen from figures 5.16(d) (i) and 5.16 (d) (ii) that the highest coefficient of friction the lower punch travel.

The deformed shape after unloading is shown in Figure 5.16(e). It can be seen from this figure that spring back (see Section 2.10.5) does occur, although the level is relative low. And it is clear in point 28 in both figures and nodes 20 that the Y coordinated for this point in figure 5.16 (e) (~ 5.3mm) is bigger than Y coordinate of the same point in figure 5.16(d)(i) (~4 mm).

The predicted thickness-displacement characteristic is shown in Figure 5.17, along with the experimental measurements taken from [2]. Figure 5.17 is discussed in Section 5.3.6.

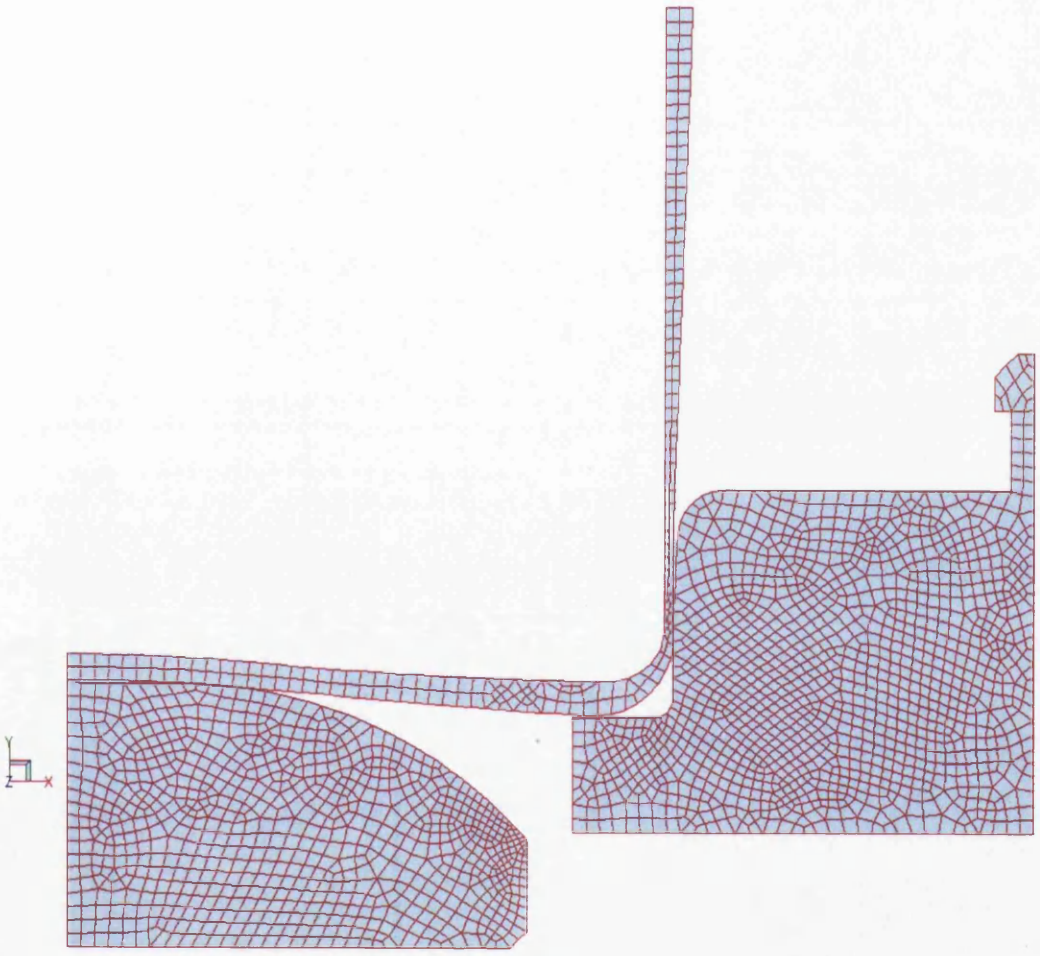

Figure 5.16(a): Stage 2 deformed mesh

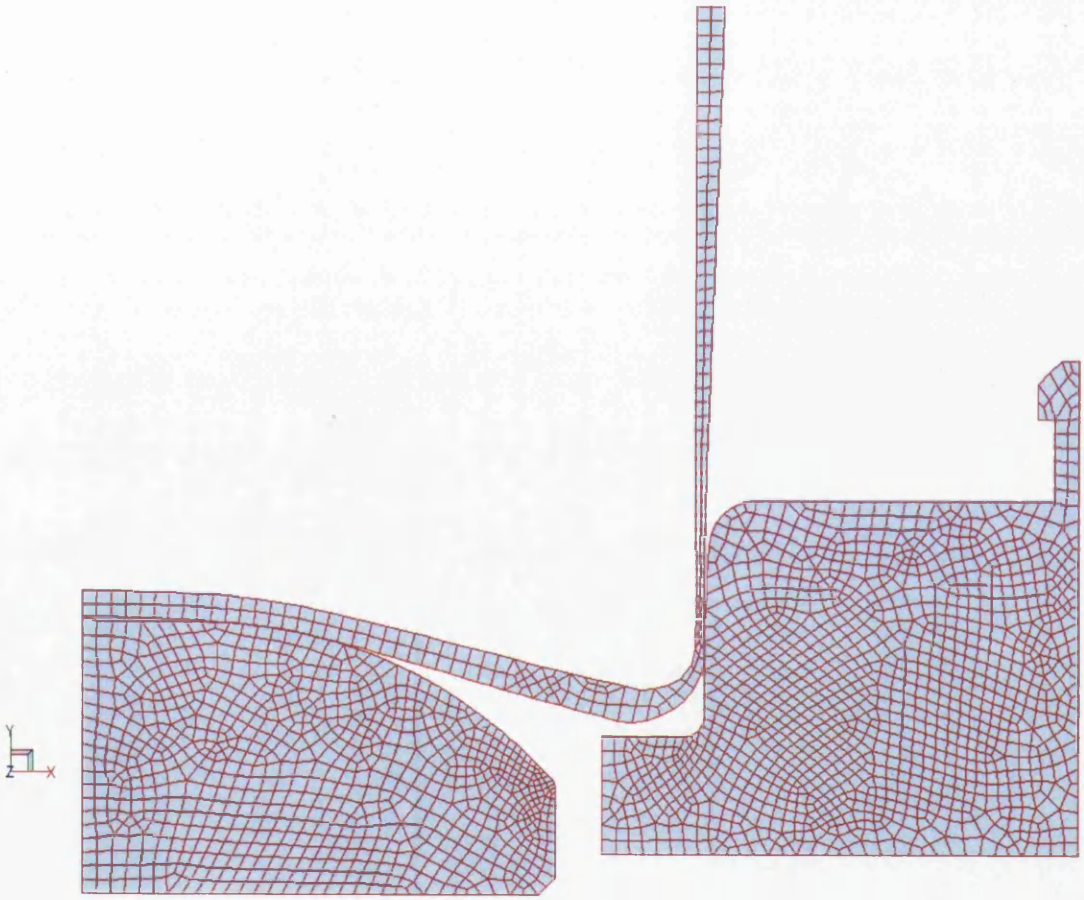

Figure 5.16(b): Stage 2 deformed mesh

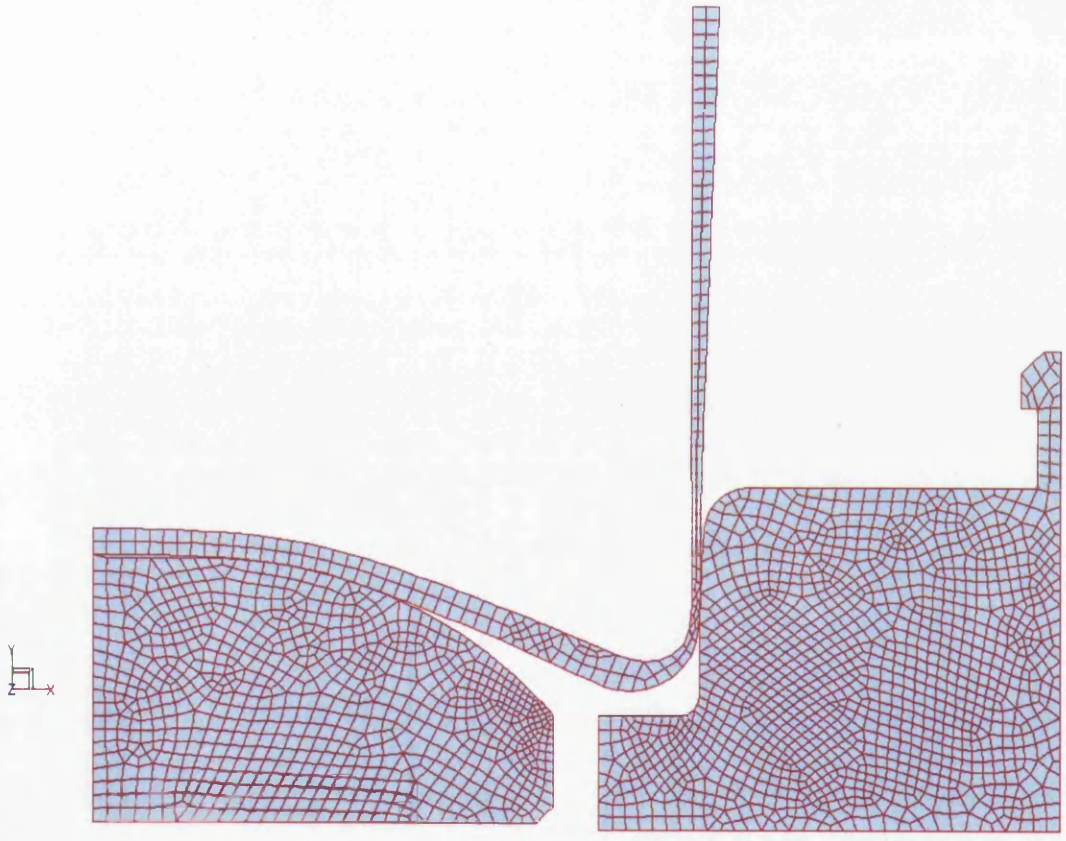

Figure 5.16(c): Stage 2 deformed mesh

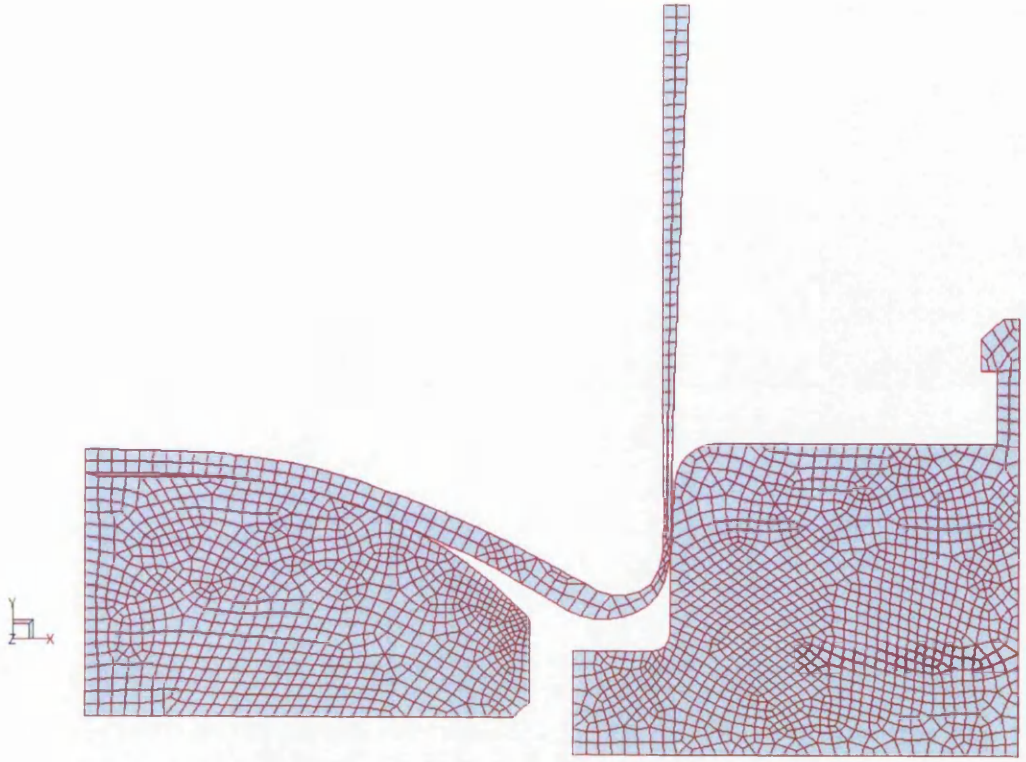

(i) $\mu = 0.25$

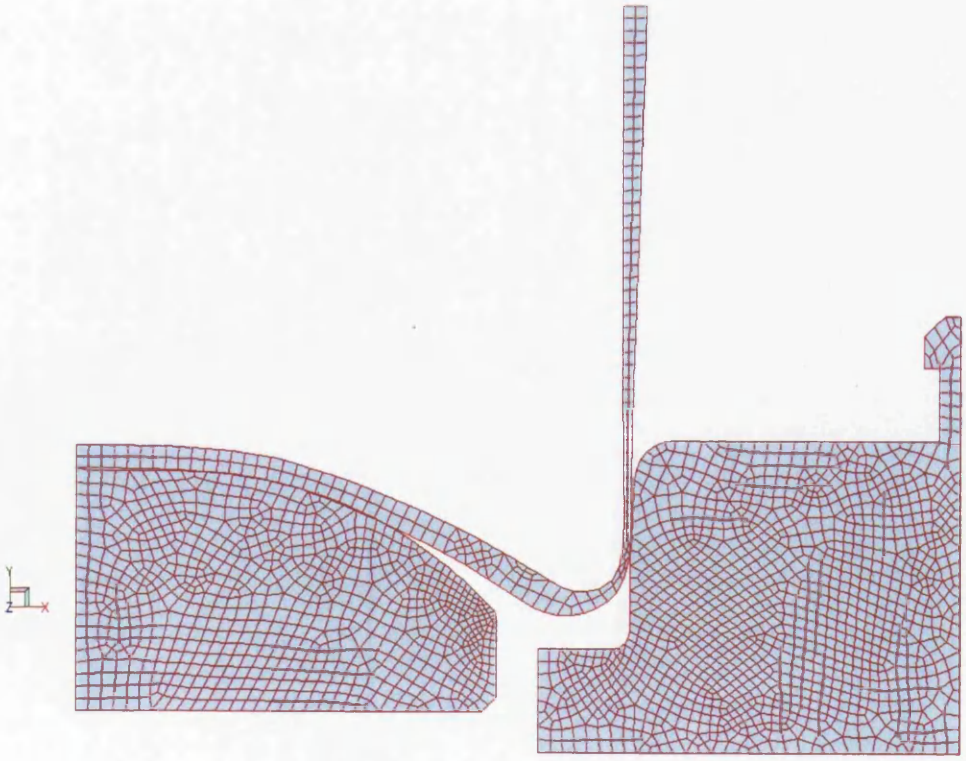

(ii) $\mu = 0$

Figure 5.16(d): Stage 2 fully deformed mesh (max. punch travel 8.5 mm)

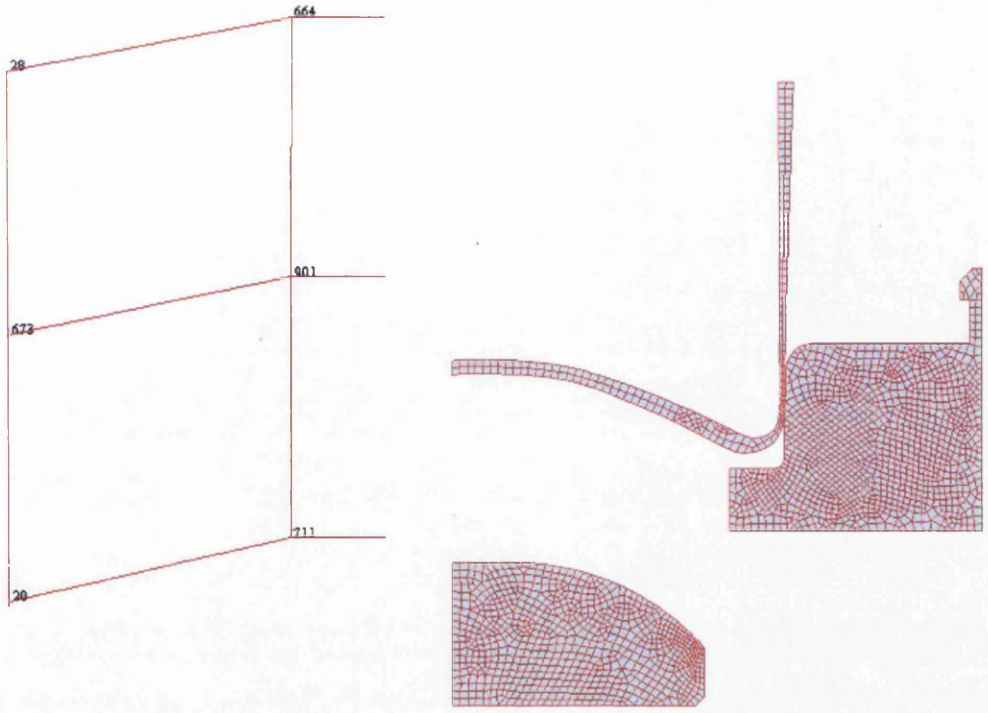

Figure 5.16(e) Stage 2(a) with the punch removed

The deformed mesh for the other two values of maximum punch travel of 8.0 mm and 7.5 mm are shown in Figures 5.16(f) and 5.16(g) respectively. It can be shown from the figures that there are slight differences between the figures.

5.3.4.2 Stage 2(b): post-decoration boundary conditions

The fully deformed shape for Stage 2(b) is shown in Figure 5.18. By comparing this figure with Figure 5.16(d), it is clear that the final deformed shape is affected by the boundary conditions.

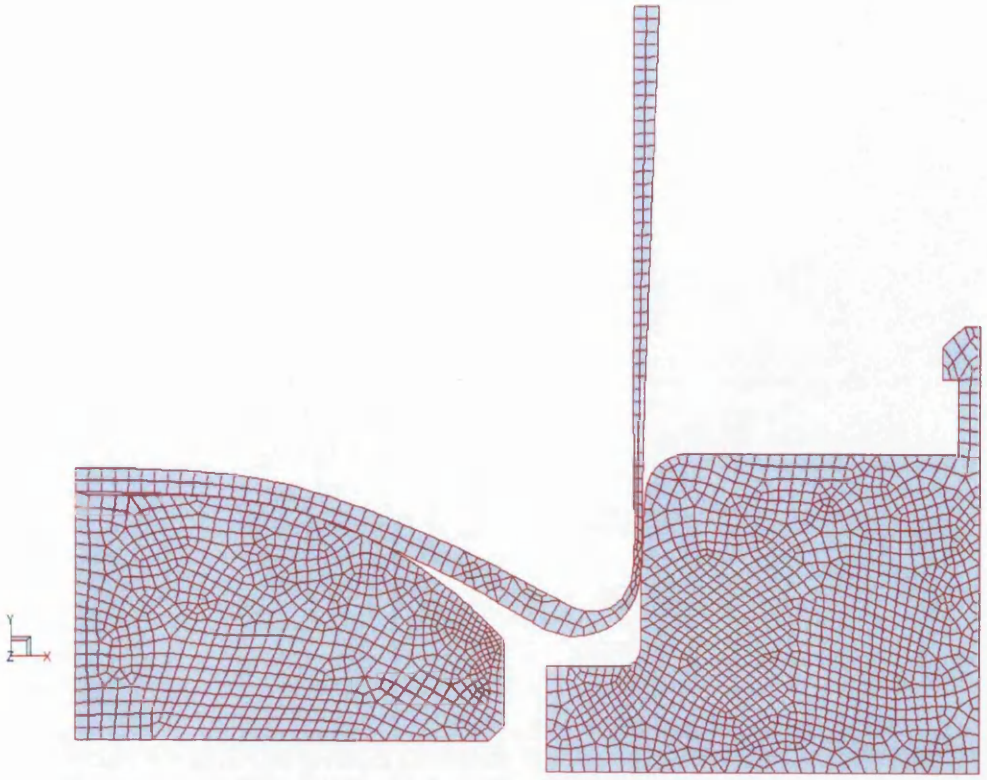

Figure 5.16(f): Stage 2(a) punch travel = 8 mm

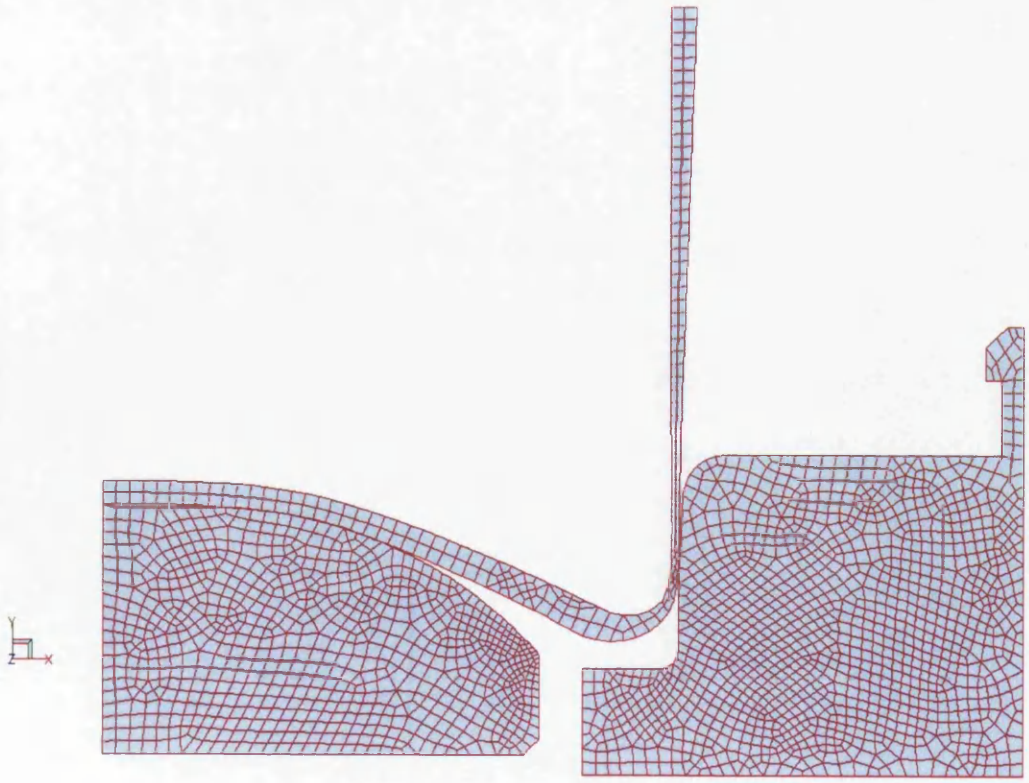

Figure 5.16(g): Stage 2(a) punch travel =7.5 mm

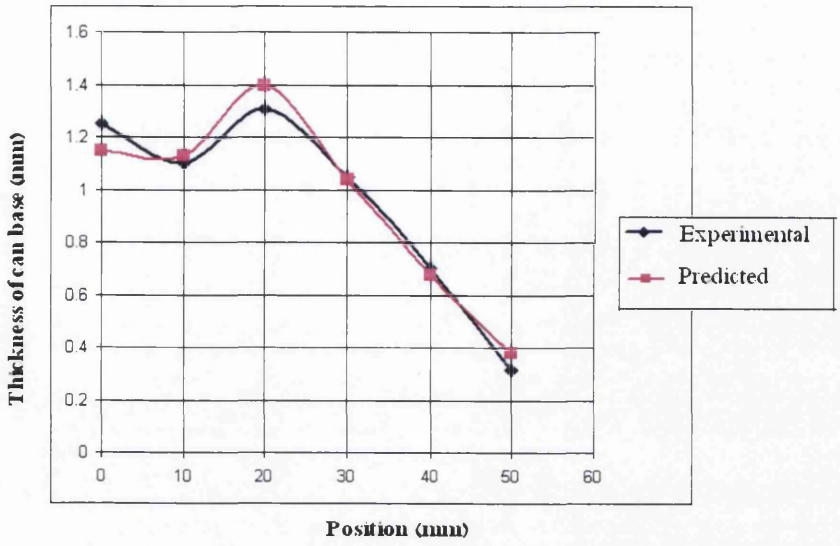

Figure 5.17: Thickness-displacement characteristic after Stage 2(a)

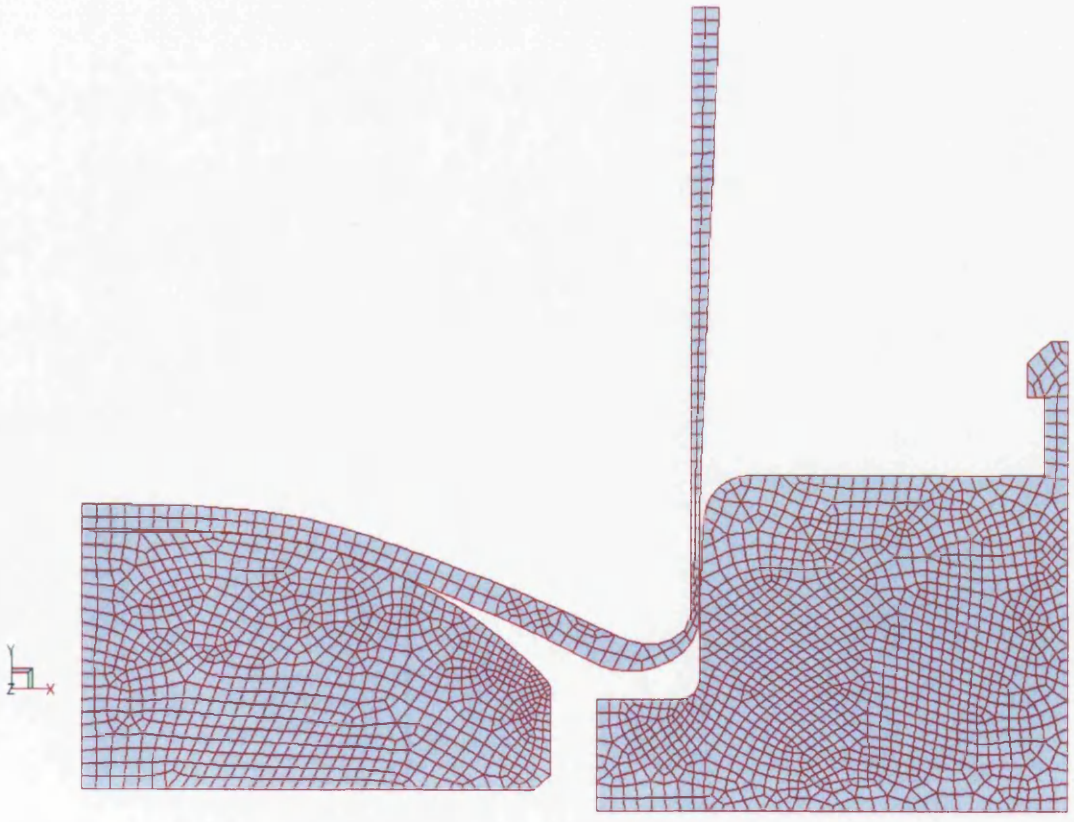

Figure 5.18: Stage 2(b) fully deformed mesh (max. punch travel = 8.5 mm)

5.3.5 Effect of friction coefficient

Figure 5.16(d) shows the punch travel changes by variation in friction coefficient however, the punch travel is slightly different with the coefficient of friction. It can be seen that the lower friction coefficient the higher punch travel.

According to Figures 5.16(f), 5.16(g) that the cans have diverse bottom forming at various punch travel. On the other hand the different coefficient of friction produces the different punch travel.

5.3.6 Comparisons with experimental data

According to the Figure 5.17 that the results from finite element analysis were then validated by comparison with the results of experimental measurements taken from [2] both in terms of the thickness values and the profile, the best correlation is achieved when μ is set to 0.25 in the simulation. The results provide good qualitative agreement. This shows that the finite element analysis predicts that the bottom forming of aerosol cans is accurate to within a maximum error of 0.015 on thickness.

Figures 5.16(d) and 5.18 shows that the different boundary condition predict different can geometries.

5.4 Closure

In this chapter, finite element analysis has been used to model the two-stage back extrusion process for one-piece aerosol cans. The effect of coefficient of friction on the thickness profile and the extrusion punch forces has been investigated.

This work shows that reasonable predictions can be achieved, when compared with experimental data and an analytical solution. The next chapter presents preliminary findings from an optimisation exercise. Having identified an 'optimal' profile, the work in this chapter can be expanded in order to investigate the punch, die and slug geometry requirements to produce this 'optimum' design.

Chapter six

OPTIMISATION

6.1 Introduction

It has been shown in Chapter 3 that these thin-walled cylindrical pressure vessels with inverted bases are 'over designed' in some respects. In particular, it is considered that the base thickness profile could be reduced, while still maintaining the integrity of the vessel. However, care must be taken since the vessels are designed to accommodate any over-pressure by the mechanism of 'dome reversal' (or elastic-plastic buckling) of the base and this inherent safety feature must be retained in any revised design.

In this chapter, a preliminary investigation into the optimisation of the vessel base when under internal pressure, in order to reduce the thickness profile, is described. Initially, a simplistic approach of reducing the base thickness is used to examine the effect on stress distribution and elastic-plastic buckling pressure. Secondly, the DOT optimisation program [58] has been used in conjunction with elastic finite element analysis to provide a more structured approach to optimisation.

6.2 Simplistic approach

6.2.1 Geometry and finite element models

The basic geometry used in Chapter 3 has been modified by removing a horizontal slice of material from the inside of the inner section of the can base. The original and 'sliced' axisymmetric finite element meshes are shown in Figures 6.1 and 6.2

respectively. The thickness at the centreline has been reduced from 1.25 mm to 0.75 mm in increments of 0.1 mm.

The three-dimensional model used to determine the elastic-plastic buckling pressure of the 'sliced' model is discussed in Section 6.2.5.

6.2.2 Loading and boundary conditions

The loading and boundary conditions are identical to those used for the analysis of pressure loading in Chapter 3 and described in Section 3.2 (axisymmetric model) and Section 3.4 (3-D model).

6.2.3 Material models

Elastic and elastic-plastic analyses have been carried out with values for Young's modulus, yield stress and Poisson's ratio of 68.3 GPa, 100 MPa and 0.33 respectively. The multi-linear material hardening curve described in Table 3.5 has been used to model the post-yield stress-plastic strain behaviour.

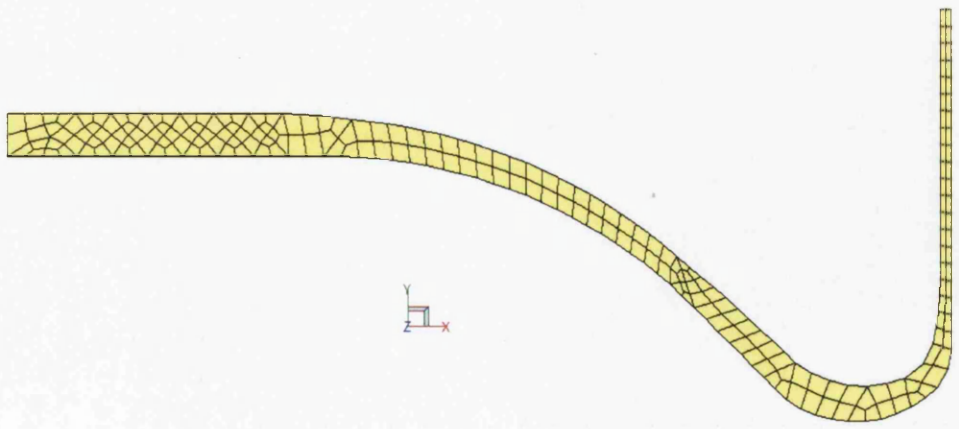

Figure 6.1: Simplistic approach, finite element mesh before reduction (centreline thickness = 1.25 mm)

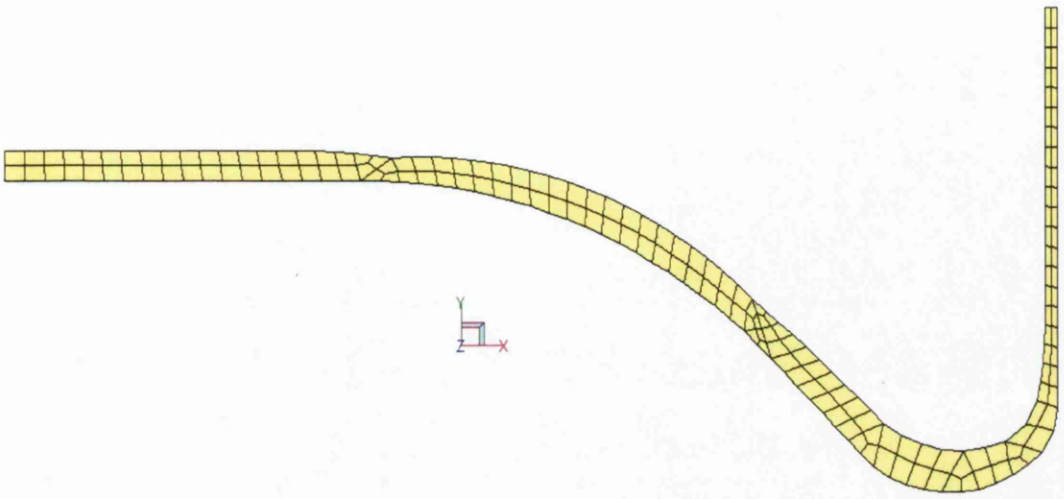

Figure 6.2: Simplistic approach, finite element mesh after reduction (centreline thickness = 0.75 mm)

6.2.4 Results for axisymmetric model

The equivalent stress contour plot for the 'sliced' model with an internal pressure of 1.20 MPa is shown in Figure 6.3 it can be seen from the figure that the equivalent stress varies between 122.66 MPa and 8.35 MPa this result comparison with the corresponding Figure 3.37 in chapter three which has equivalent stress varies between 119.53 MPa and 7.76 MPa and the maximum equivalent stresses in each case are in the corner region. Although Figure 6.4 compared with Figure 3.38 it can be seen from the figures that the collapse load is changes from 1.35 MPa to 1.53 MPa when the thickness of the sliced model decreased by 0.75 mm.

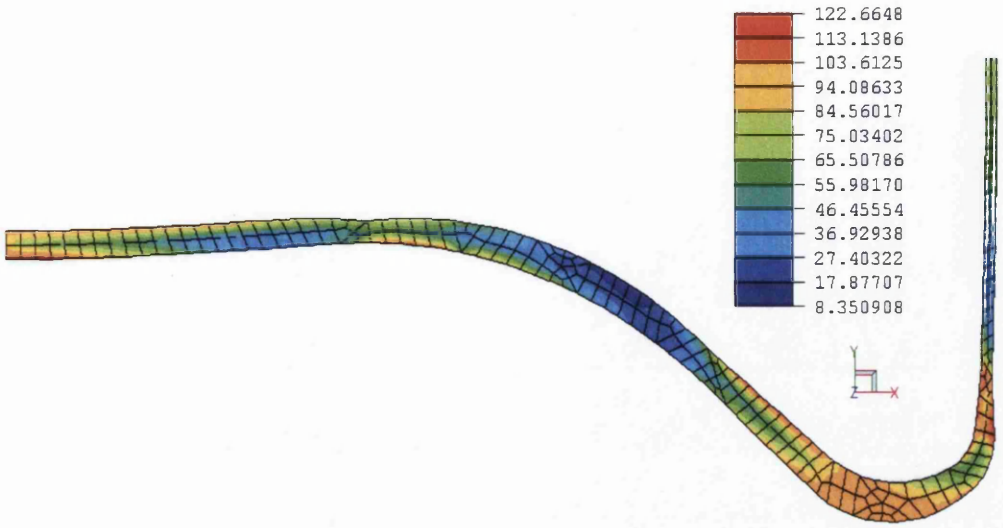

Figure 6.3: Simplistic approach, equivalent stress contour plot for p =1.20 MPa (centreline thickness = 0.75 mm)

The loading was then increased and collapse is predicted when the pressure reaches 1.35 MPa (compared to 1.53 MPa for the original geometry). The corresponding equivalent stress contour plot is shown in Figure 6.4.

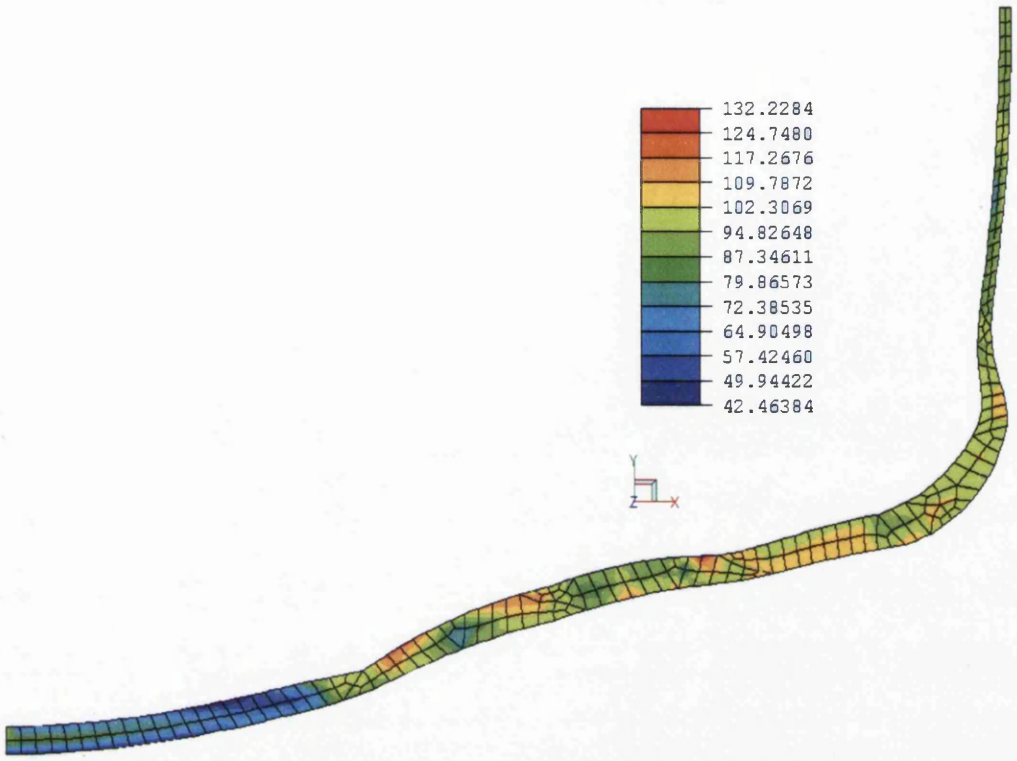

Figure 6.4: Simplistic approach, equivalent stress contour plot for p = 1.35 MPa (centreline thickness = 0.75 mm)

6.2.5 Elastic-plastic buckling results using a 3-D model

Using the approach described in Section 3.4, a three-dimensional model of the 'sliced' geometry has been created and the basic 3D model, constraints, loading and finite element mesh are shown in Figures 6.5, 6.6, 6.7 and 6.8 respectively.

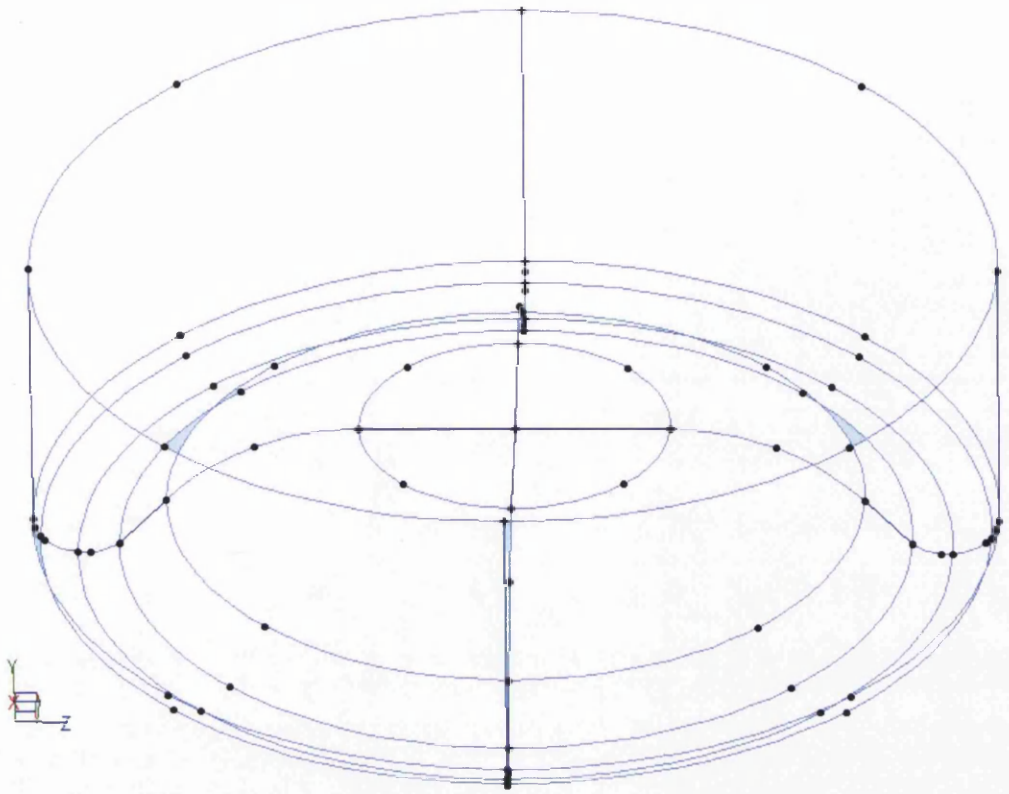

Figure 6.5: Simplistic approach, 3D model (centreline thickness = 0.75 mm)

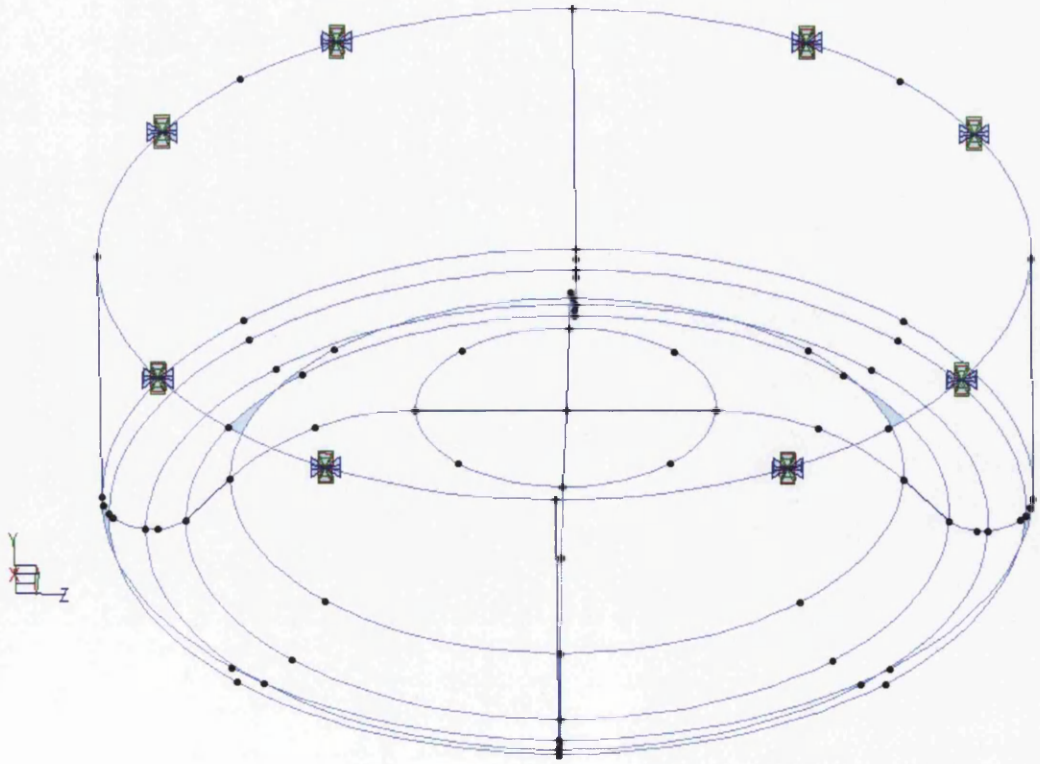

Figure 6.6: Simplistic approach, 3D constraints (centreline thickness = 0.75 mm)

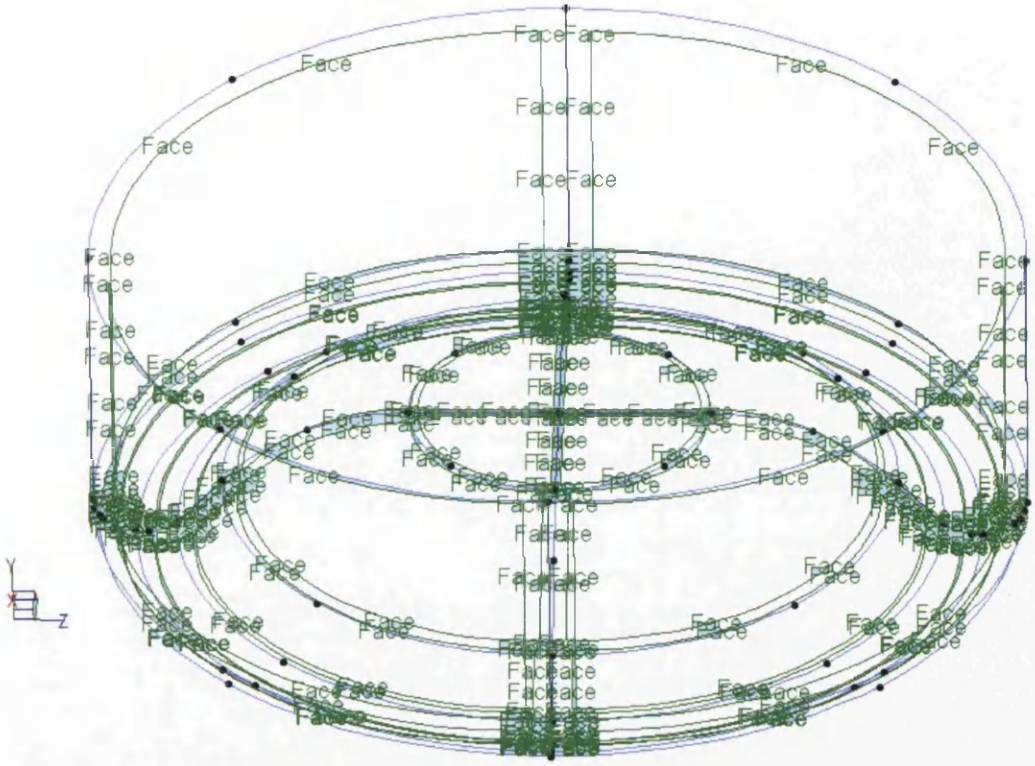

Figure 6.7: Simplistic approach, 3D loading (centreline thickness = 0.75 mm)

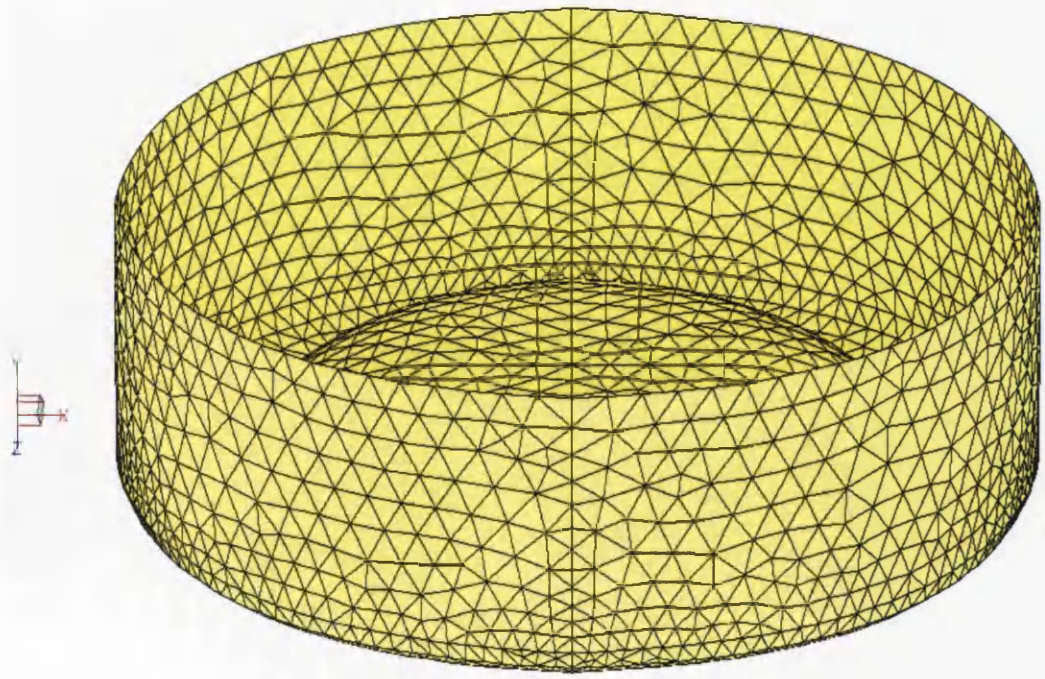

Figure 6.8: Simplistic approach, 3D mesh (centreline thickness = 0.75 mm)

The internal pressure load was increased incrementally until elastic-plastic buckling took place at a pressure of 1.80 MPa (compared to 2.02 MPa for the original model) and the corresponding equivalent stress contour plots for the original model and the 'sliced' model are shown in Figures 6.9 and 6.10 respectively.

In both cases and due to time restrictions, the buckling mode is symmetrical because a symmetrical model (without small-scale perturbations – see Section 3.4) was used. This is an area for further investigation. Figures 6.9 and 6.10 show that the finite element analysis predicts that the aerosol can base will be fully deformed at 2.02 MPa for the actual thickness and 1.80 MPa for the modified geometry and the maximum stresses are now concentrated in the lower section of the can walls in both cases.

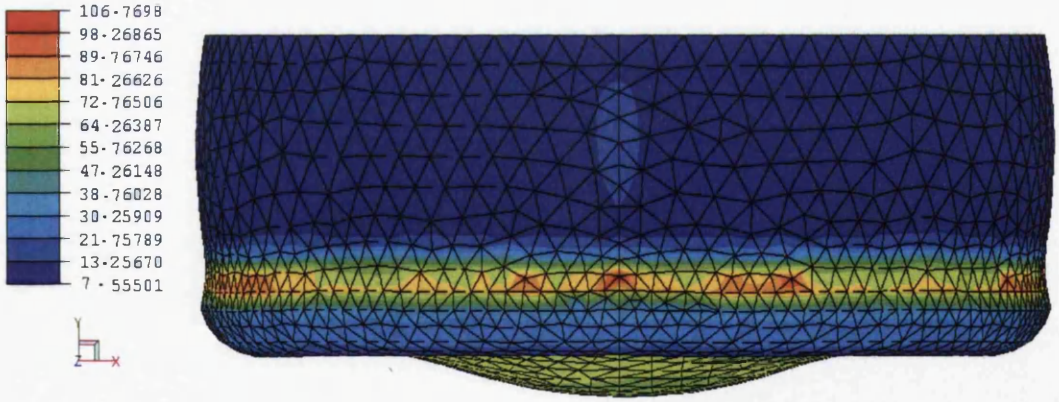

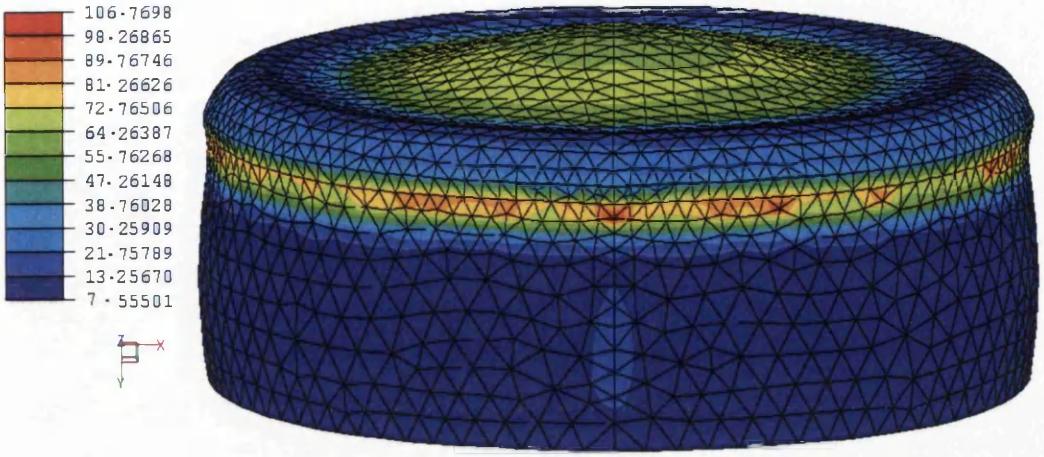

Figure 6.9: Simplistic approach, equivalent stress contour plot at the point of elastic-plastic buckling with p = 2.02 MPa (centreline thickness = 1.25 mm

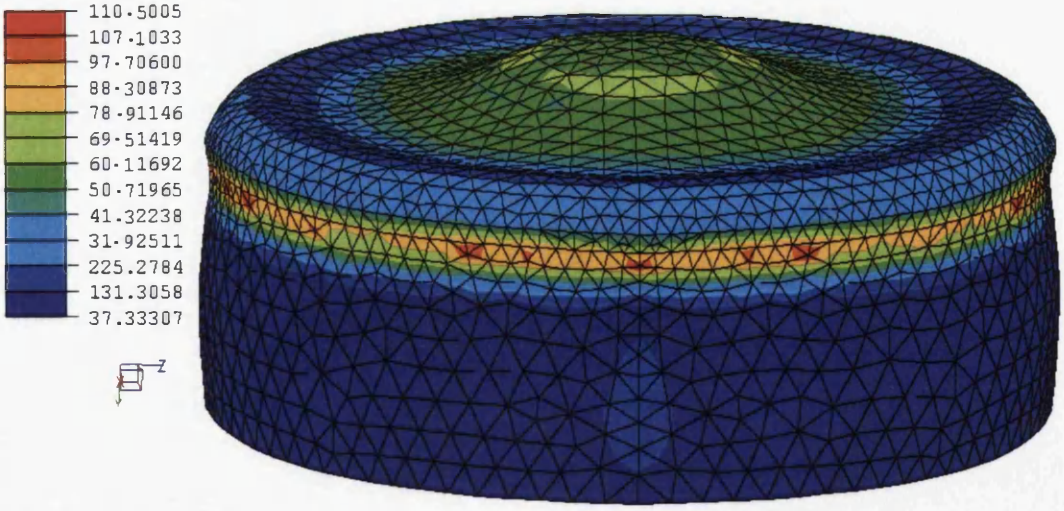

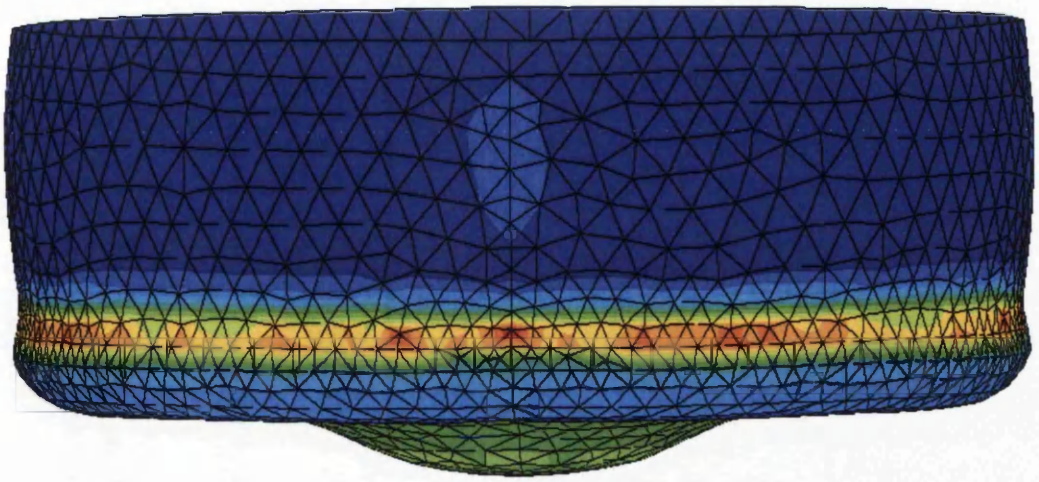

Figure 6.10: Simplistic approach, equivalent stress contour plot at the point of elastic-plastic buckling with p = 1.80 MPa (centreline thickness = 0.75 mm)

6.3 Optimisation procedure

6.3.1 Objective function and constraints

The choice of a suitable design variable (s) is very important as it can affect the degree of non-linear of the objective function or the constraints. It can also result in other implicit constraints, which are not necessarily obvious at first sight. It is recommended to have a direct connection between the values of the design variables and actual geometry [50]. In this work, the volume is indirectly used as the objective function.

An optimisation problem is stated as:

Minimize or maximize the objective function (F(x)), subject to:

$g_j(X) \leq 0$ }

} $j = 1, NCON$ Inequality constraints

$h_j(x) = c_j$ }

and

$X_i^L \leq X_i \leq X_i^U$ }

} $i = 1, NDV$ Side constraints

$X_L \leq X \leq X_U$ }

If the objective functions to be minimised is the cross-sectional area:

$$F(X) = \sum_{i=1}^{n} A_i \qquad \ldots (6.1)$$

where A_i is the CSA of the i th FE.

and n is the number of elements.

Subjected to the constraints that the stresses in each element must be less than the yield stress:

$$\sigma_j(x) \leq \sigma_y \qquad (j = 1 \text{ to } n) \qquad \ldots(6.2)$$

and hence:

$$\frac{\sigma_j(x)}{\sigma_y} \leq 1 \rightarrow \frac{\sigma_j(x)}{\sigma_y} - 1 \leq 0 \qquad \ldots (6.3)$$

where σ_y is the yield stress

The selected design variables are the thickness values at the centre of each element around the profile and the objective function to be minimised becomes:

$$F(X) = t_1 + t_2 + t_3 \ldots\ldots\ldots\ldots + t_n \qquad \ldots (6.4)$$

6.3.2 DOT optimisation program

DOT is a computer program for optimisation. Specifically, it is used to automatically adjust to maximize or minimize a calculated quantity, while satisfying a number of constraints [58].

A computer-based procedure was written using the FORTRAN programming language that reads the output file from an ELFEN analysis and extracts the equivalent stresses at each node in each super-element and determines the maximum values in each of these elements. The DOT program is called and these n values of equivalent stress together with the n thickness values are then used by DOT to generate a new set of thicknesses, based on the constraints in equation (6.3). This information is then used to manually generate a new set of nodal co-ordinates for the n+1 nodes on the inner surface of the profile (i.e. the outer profile is fixed and the cross-section is modified by moving the outside nodes). The new model then provides the input for the next iteration.

Details of the FORTRAN coding can be found in Appendix C.

6.3.3 Geometry and finite element model

The basic geometry, using 6 super-elements, is that shown in Figure 6.11. A mesh of 187 four-noded axisymmetric elements was created from this model, using the automatic mesh generator within ELFEN.

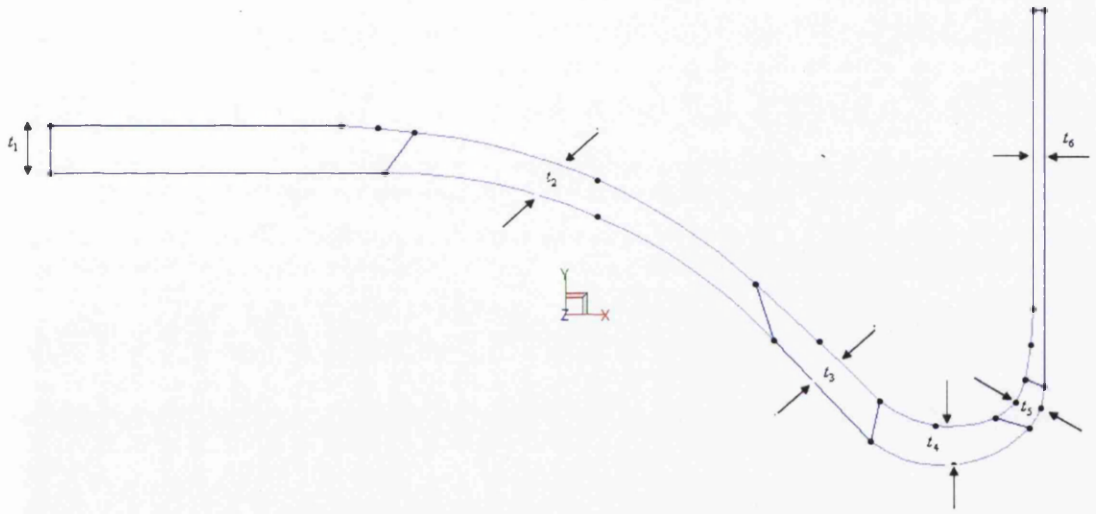

Figure 6.11 Optimisation analysis, basic model with six super-elements and six design variables

6.3.4 Loading and boundary conditions

The loading and boundary conditions are identical to those used for the analysis of pressure loading in Chapter 3 and described in Section 3.2. An arbitrary pressure of 0.50 MPa has been used in the pre-buckling analyses.

6.3.5 Material model

Elastic and elastic-plastic material data are as discussed in Section 6.2.3.

6.3.6 Results

An initial (zero iteration) analysis using the original model in Figure 6.11 was performed and the procedure described in Section 6.3.2 was used to generate a revised model (with new thickness values from DOT) in this analysis the thickness of the base only considered due to the high stress in this region and the wall thickness is constant. ELFEN then re-generated the mesh and the process repeated.

After five iterations, DOT indicated that convergence had been achieved and the resulting 'optimised' shape is shown in Figure 6.12. The original and 'optimised' thickness values are given in Table 6.1 also the optimisation convergence is shown in Figure 6.13.

	Original	Iteration(1)	Iteration2	Iteration3	Iteration4	Iteration5
	1.25	1.15	1.05	0.95	0.82	0.81
	1.1	1	0.9	0.8	0.71	0.70
	1.07	0.95	0.85	0.75	0.63	0.59
	1.13	1.03	0.93	0.83	0.70	0.68
	1.05	0.94	0.84	0.75	0.61	0.59
Σ	5.6	5.07	4.58	4.08	3.47	3.37

Table 6.1: Thickness at each iteration

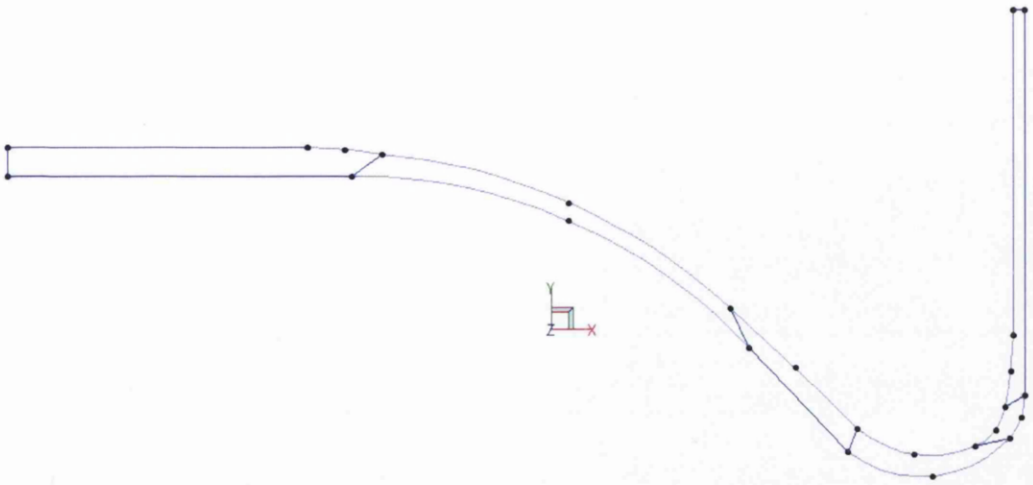

Figure 6.12: Optimisation analysis geometry after optimisation

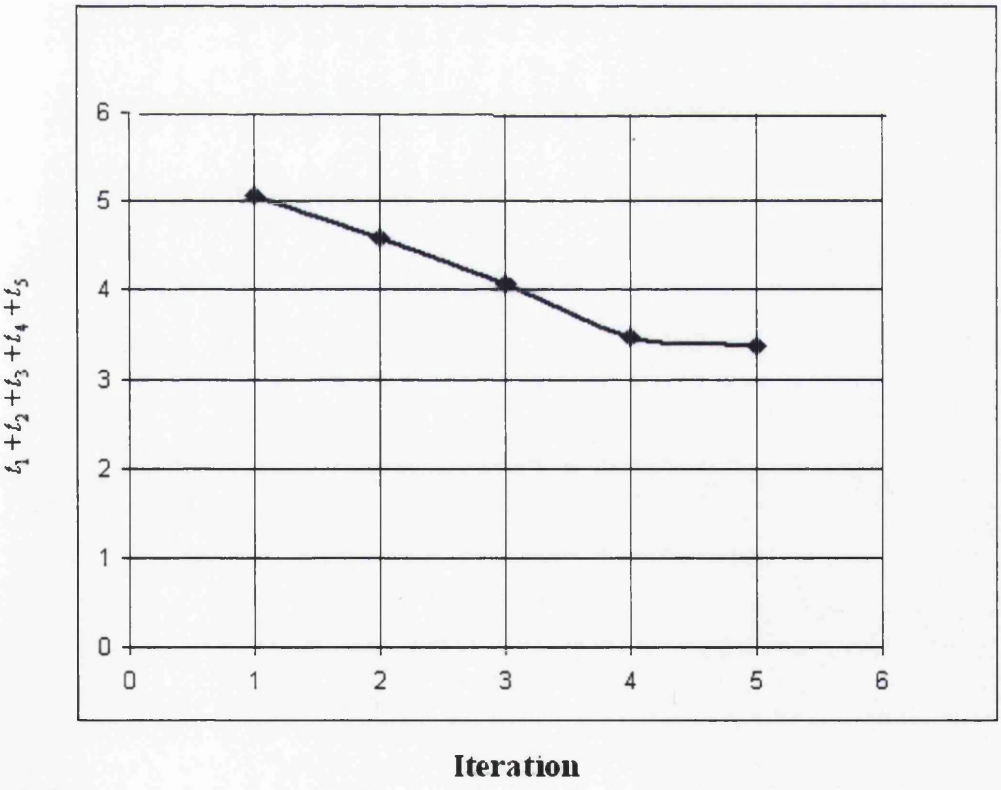

Figure 6.13: The convergence of the solution

The 'optimised' shape was then analysed using the incremental elastic-plastic facilities within ELFEN to establish the pressure at which collapse occurs. (Note that axisymmetric models cannot distinguish between elastic-plastic buckling and collapse, as discussed in Section 3.4).

The equivalent stress contour plot, corresponding to a collapse pressure of 0.62 MPa, is shown in Figure 6.15 also the pre-buckling equivalent stress contour plot of pressure 0.50 MPa is shown in Figure 6.14. The equivalent collapse pressure for the original profile is 1.53 MPa (see Section 3.3.5). It can be seen from the figures that the thickness is reduced then the amount of materials will reduce hence, the collapse pressure also decrease.

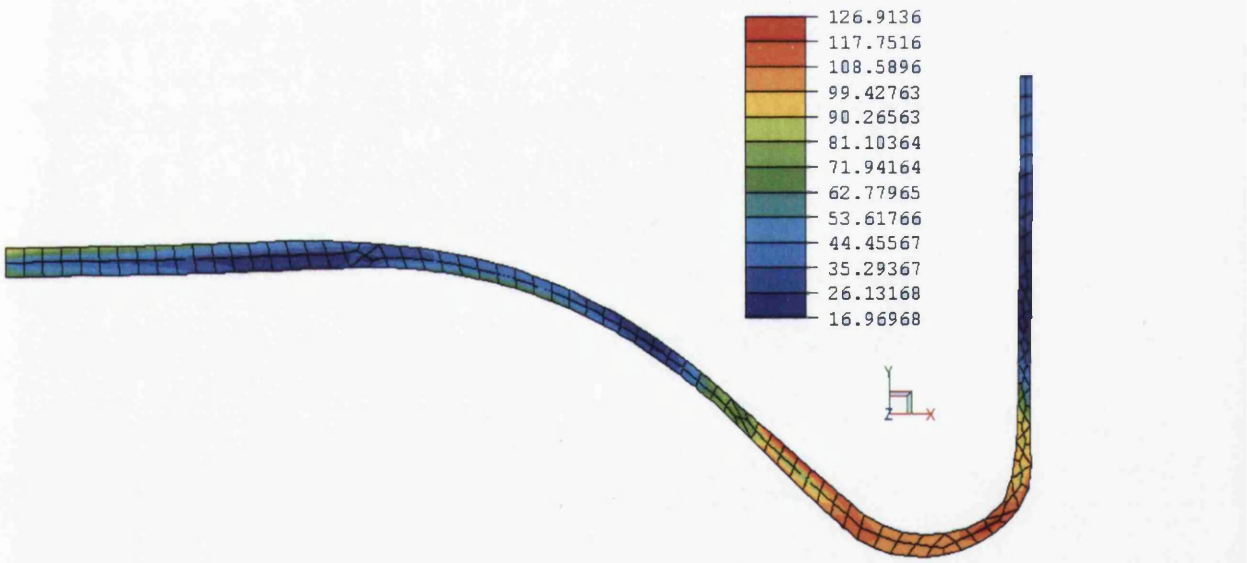

Figure 6.14: Equivalent stress contour plot (pre-buckling, pressure =0.50 MPa)

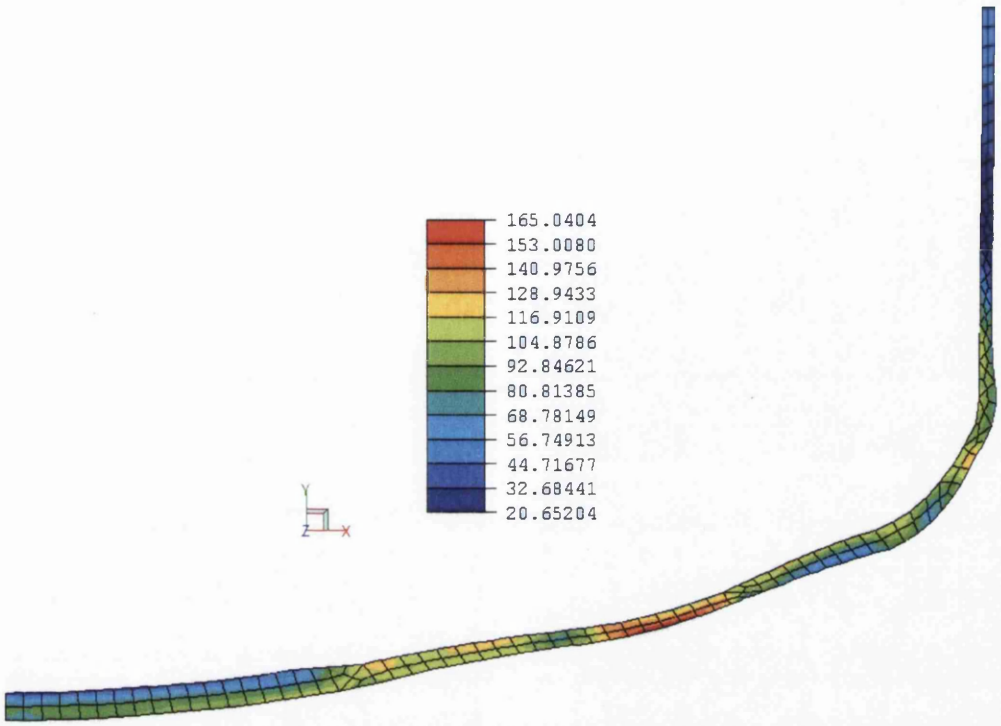

Figure 6.15: Optimisation analysis, equivalent stress contour plot at the point of elastic-plastic buckling with p = 0.62 MPa

6.4 Closure

The results from a preliminary investigation into shape optimisation applied to these thin-walled cylinders have been presented. This work was carried out at a late stage in the project and, therefore, only provides a starting point for further, more detailed analysis. It is clear that significant reductions in the cross-section of the vessel base are possible, within the limits of acceptable burst pressure (which occurs in the plain cylinder region). At the same time, however, the elastic-plastic buckling pressure is significantly affected and this may adversely affect the lower operational pressure limits. The choice of model, objective function and constraints is an area for further investigation and this is discussed in more detail in the final chapters.

Chapter seven

DISCUSSION

7.1 Introduction

The project has looked in-depth at the design and manufacture of aluminium aerosol cans, as a specific form of thin-walled pressure vessel which, due to its complex shape, cannot simply be designed around the traditional British (BS5500) and American (ASME VIII) codes for pressure vessel integrity. Also, the structural integrity of this vessel shape, which consists of an inverted dome end, parallel cylindrical section and truncated cone top, due to external loading is beyond the scope of these codes.

Furthermore, it has been established, from collaboration between the University and a local manufacturer of such vessels (through Knowledge Transfer Partnerships), that competition is fierce and material costs contribute at least 50% of the cost of manufacture. Therefore, it is essential that both the design and the manufacturing processes can be simulated in order to optimise on material usage, whilst still maintaining the integrity of the vessels. This requires:

- a thorough understanding of the yield, elastic-plastic buckling and ultimate failure of the vessels under internal pressure;

- accurate modelling of the buckling behaviour under compressive axial load;

- accurate modelling of the back-extrusion process itself, thus providing the opportunity to investigate the effects of tooling geometry changes on the resulting vessel profile;

- optimisation studies which integrate with the above in order to reduce costs with no loss of integrity and still maintaining the inherent safety feature provided by the inverted base at an acceptable pressure below that at which burst occurs.

These four requirements have formed the basis of the work described in this thesis.

The literature review has concluded that little specific research has been carried out on the structural integrity of these complex vessels (in fact, 'design by test' appears to be the preferred approach) and there is little evidence of finite element analysis being applied to the modelling of the back-extrusion process. Where work has been carried out, it avoids the issue of friction and its influence on thickness profile and extrusion force requirements.

The research work reported in this thesis investigates the linear and non-linear, large displacement behaviour of aluminium thin-walled pressure vessels, in the form of aerosol cans, subject to internal pressure and axial loading using the elastic and elastic-plastic facilities of the ELFEN finite element program. Extensive elastic and elastic-plastic analyses have been preformed using both constant thickness and realistic thickness profile models to obtain a better understanding of the mechanisms of buckling and failure. Similarly, the yielding and flow of material under pressure during the extrusion process has been modelled using ELFEN explicit.

7.2 Internal pressure loading (Chapter 3)

7.2.1 Elastic analyses

Initially, constant thickness (0.4 mm $\leq t \leq 1.4$ mm) axisymmetric finite element models have been used to study the stress patterns that develop and hence establish the conditions for yielding and the variation with thickness profile. A typical geometry (i.e. Geometry 4) with t = 1mm is selected for a full review and the summary results of other geometries are presented. The predictions show that initial yielding will, as expected, occur on the inside surface at the relatively sharp corner close to the plain tube region, which acts as a significant stress concentration feature with K_t values between 4.07 and 13.83 (depending on thickness) being predicted. A non-linear relationship between maximum stress and thickness is also predicted, although when plotted against D/t, the predictions become more linear. However, the relationship between limiting (yield) pressure and thickness, for both the base and plain tube, appear to be reasonably linear. This clearly helps in any investigations into material optimisation.

A similar response is seen for the realistic thickness profile. This is based on experimental observations made by Patten [2], who found that although the cylindrical section is reasonably parallel (~0.31 mm), the variation in thickness along the base is significant (0.7 and 1.31 mm). This results in a reduced elastic stress concentration factor of 3.45 and a greater 'spread' of the stress contours, which is similar to that predicted for the 0.8 mm constant thickness model. The predictions also confirm that the base stresses are very low, compared with the corners and cylinder and this is considered to provide the impetus for material optimisation.

7.2.2 Elastic plastic analyses

Elastic-plastic finite element predictions from the constant thickness axisymmetric models, using both elastic-perfectly-plastic (EPP) and multi-linear kinematic work-hardening (EKH) models for aluminium, have enabled the investigation of the development of the plastic zones as the pressure is increased above that required for initial yielding. A plastic hinge, where the complete cross-section has yielded, is seen to develop and (for the EPP model) no further increases in pressure can be applied. For the EKH model, further increases in pressure are possible until the UTS are reached. A similar response is seen for the realistic thickness model however, it is clear that these axisymmetric models cannot be used to simulate the elastic-plastic buckling (form of elastic-plastic 'snap-through', also referred to as 'dome reversal') characteristic exhibited by actual vessels under pressure.

In reality, the thickness profile is not entirely axisymmetric due to tolerances in the extrusion process and although variations in thickness are very small, they are sufficient to cause a slightly unsymmetrical buckling mode, due to minor radial variations in profile and there is a clear distinction between the elastic-plastic buckling of the base and burst (collapse) pressures, where bursting occurs in the plain tube region.

Consequently, a full three-dimension model was created and a small imperfection was introduced in the base, using results from an eigenvalue analysis (lowest mode) and based on the method described by Robotham *et al* [24]. There is good agreement between the predicted buckling mode (Figure 3.44) and that obtained experimentally (Figure 3.52) and there is reasonable agreement between the predicted buckling

pressure (1.7 MPa) and the experimental value (1.6 MPa). Possible reasons for the discrepancy include:

- Variations in the level of material strain hardening that have occurred during the extrusion process (the material data used is from tests on specimens taken from the cylindrical section, which has been subjected to greater strain hardening than the base)

- The softening effects of temperature increase on material properties. A significant increase in temperature is apparent both during extrusion and internal coating which will cause the aluminium to soften. This effect has not been investigated.

- The approximate nature of the finite element method, particularly for non-linear analysis.

7.2.3 Upper and lower bound pressures

The elastic compensation method proposed by Mackenzie and Boyle has been used to estimate the upper and lower bound limit loads, using only elastic finite element analysis, for both constant thickness axisymmetric and realistic thickness profile models. The use of this method in a limited number of relatively straightforward components and loading arrangements has been reported in the open literature and it is considered that the application described in this thesis provides further, more detailed, information on the nature and limitations of the method which will be of interest and benefit to Engineers and Designers.

The results for the constant thickness models show that the predicted collapse pressures are within the upper and lower bound estimates, closer to the upper bound, and this provides a degree of confidence in these approximate methods. However, the range between the upper and lower bounds is large and, unfortunately, the lower bound is always greater than the yield stress. This limits the use of these approximate methods for this type of geometry and loading to collapse pressure estimates. The upper and lower bound range for the realistic thickness model includes the predicted buckling and collapse pressures but, again, the yield pressure is outside the range. Care should therefore be taken when using this approximate method.

7.3 Axial loading (Chapter 4)

In practice, these components are subjected to axial loading during neck formation and valve insertion/charging. Under these conditions, the can must not collapse and this requirement provides the need for a study of thin-walled, complex shape pressure vessels subjected to axial loading. Again, the results will have direct implications to any subsequent material optimisation study. Also, the effect of strain hardening and temperature on material properties and finite element predictions, discussed in Section 7.2.2, is also relevant here.

7.3.1 Axial loading during neck forming

For this analysis, a model of the plain open cylinder with inverted base (to simulate the first stage of necking) was used with a multi-linear kinematic work-hardening model for aluminium. Small perturbations were introduced into the model to enable buckling, rather than compressive collapse.

Experimental validation tests were also performed and the predictions compare favourably with the experimental results in a number of ways:

- Elastic-plastic buckling occurs at the base, which demonstrates the significance of the sharp corner on the stress distributions. The analytical solution for the equivalent plain cylinder in compression is clearly inappropriate.

- The predicted and experimental load-displacement characteristics are very similar with linear pre-buckling behaviour.

- There is excellent correlation between the predicted and experimental buckling loads.

One experimental test was extended in order to show the post-buckling behaviour with an apparent increase in stiffness prior to a secondary buckling process.

7.3.2 Axial loading during valve insertion/charging

In this case, the top and cylindrical sections of the thin-walled cylinder were modelled. Again, a multi-linear material hardening model was assumed. Small perturbations to the geometry were not necessary since the experimental results show the deformation to occur in the truncated cone-shaped top in preference to the plain cylinder or base.

The finite element predictions indicate a reasonably linear load-displacement curve up to a deflection of ~3 mm, during which time the convex top is being flattened and the stiffness should increase slightly, although noted. After this, there is a reduction in load as the top becomes flatter towards becoming concave. A very different experimental response is observed with low loads up to a deformation of ~2 mm and a rapid increase up to ~3.5 mm. However, the angle of the cone on the finite element model is shallower than that for the components used in the experimental tests and a different response is, therefore, not surprising. A peak load is again shown and it appears that secondary stiffening may be taking place as the displacement approaches ~5 mm.

It is surprising therefore that the predicted and experimental 'collapse' loads are reasonably similar. This cannot be explained and further investigation is necessary.

7.4 Modelling of the extrusion process (Chapter 5)

The modelling of manufacturing processes is a more recent application of non-linear finite element analysis and, in particular, research into the modelling of the back-extrusion process is limited. In this chapter, particular attention has been paid to the effects of friction and boundary conditions on the forces required to extrude the material and the resulting thickness profile, for which no previous results could be found.

There are three independent stages to the deformation process:

- Stage 1 - formation of the side wall and flat base
- Stage 2 - formation of the inverted dome base
- Stage 3 - formation of the truncated cone top

and the first two stages have been simulated in this project. Also, Stage 2 can take place either before or after decoration, in which case the boundary conditions and the subsequent thickness profile are different.

7.4.1 Stage 1 simulation

The effect of friction coefficient on the finite element predictions for the thickness profile has been investigated for $0 \leq \mu \leq 0.25$, based on discussions with colleagues and industrialists. The maximum difference in predicted thickness (~ 0.2 mm) is in the base region close to the sharp corner and round into the first part of the plain cylindrical section. The results suggest that thicker sections in the base and cylinder are produced when μ is low this is described in Section 2.10.4.

Predictions are compared with the predicted profile from a simple model of the punch and die geometry when the punch is fully inserted. It would appear that finite element predictions with $\mu = 0$ provides the best comparison. This seems reasonable as, in practice, a graphite powder is applied to the billet prior to extrusion.

The force-displacement curve for the punch clearly predicts two slopes and it is considered that the change in slope corresponds to the point at which the material starts to flow around the punch corner and up the die. The effect of friction on punch load is significant during the process (~ 5 KN) but the maximum force varies by less than 5% with the range of μ considered. In practice, the predicted machine power requirements will vary little with friction.

Unfortunately, the predicted length of the plain cylindrical section is significantly less than that for the actual cans. This is an area requiring further investigation.

7.4.2 Stage 2 simulation

The effect of friction coefficient on the finite element predictions for the bottom forming process produces the dome in the can base has been investigated for $0 \leq \mu \leq 0.25$. The results suggest that the lower coefficient of friction the higher punch travel.

The finite element result at different boundary conditions shows that the different boundary conditions produce different cans.

The predictions suggest that the effects of springback, due to elastic recovery when the punch is removed, are minimal. This information is useful in the design of dies and punches however, if an optimised can had a thinner base then higher levels of springback would be expected.

7.5 Optimisation studies (Chapter 6)

The need for an 'optimised' thickness profile has been identified in Section 7.1. The results of the research presented in this thesis provide important background information on how thickness affects both the integrity and structural response of these complex thin-walled cylinders under typical loading conditions and it is clear that preferential thinning of the section is possible.

In this chapter, a preliminary look at optimisation has been carried out and it the results are far from conclusive. However, they do provide a valuable insight for future investigation.

7.5.1 Simplistic approach

Assuming that the base is the main section where material could be removed without affecting the integrity, the simplest form of optimisation is to remove a 'slice' of the material from the inner section of the base. In this way, the thickness at the base centreline was reduced from 1.25 mm to 0.75 mm in increments of 0.1 mm.

Using an axisymmetric finite element model, the reduction in 'collapse' pressure is relatively small (from 1.53 MPa to 1.35 MPa for a centreline thickness reduction from 1.25 mm to 0.75 mm). Similarly, using a three-dimensional model (but without any geometrical perturbation), the predicted elastic-plastic buckling pressure falls from 2.02 MPa to 1.80 MPa for the same thickness reduction. These results are encouraging and suggest that material savings may be possible without loss of structural integrity.

7.5.2 Structured approach using DOT

Section 6.3 has described a more structured approach to optimisation, using the DOT optimisation procedure. In this exploratory work, the sum of the thicknesses at particular sections in the model has been the objective function to be minimised with constraints on maximum equivalent stress.

The procedure requires interaction with the finite element program by way of a separate FORTRAN program (see Appendix), which acts as the interface between DOT and ELFEN.

The optimised shape from this preliminary study shows some irregularities. This is probably due to the original stress distribution, since the regions where the thickness has been reduced significantly compare with the regions of high stress in the original model and a more 'smoothed' approach is needed. Also, the ideal situation of a constant stress cannot be achieved in this type of problem because the pressure loading produces a bending moment on the shell and so a stress variation between inside and outside surfaces will always exist in the base and corner. Further work on the choice of objective function and constraints is necessary.

7.6 Closure

The final chapter, Chapter 8, provides a summary of conclusions from the research and some recommendations for further studies.

Chapter eight

CONCLUSIONS AND RECOMMENDATIONS

8.1 Conclusions

The following conclusions are drawn from the research:

1. The finite element method provides a significant advantage over traditional experimental testing methods for proving and improving designs, as the method has the advantages of repeatability, rapid re-analysis of geometry and loading changes and reduced costs.

2. The aim of the research project was to develop a predictive tool that facilitates the can design and optimisation process and, in this respect, the objectives have been achieved. The models are capable of reasonably accurate quantitative assessment of the effect of varying geometry and material properties and are invaluable aids in aerosol can design.

3. Constant thickness (axisymmetric) models can be used in a limited way to study qualitatively the effects of changes in thickness on material and structural response but the actual thickness profile is far from constant and quantitative information can only be obtained when more realistic models are used.

4. Axisymmetric models generally provide some useful information on the behaviour of such structures under pressure and/or compressive axial load. However, they lack

the ability to predict elastic-plastic buckling of the base due to internal pressure and of the side-walls due to axial loading.

5. Full three-dimensional models, with realistic thickness profiles, can be used successfully to predict the buckling and collapse conditions for both pressure and axial loading. However, the models need to be modified (by means of geometric imperfections) to enable the buckling mode to be simulated.

6. The elastic compensation method provides a straight-forward and useful approach, without the need for complex elastic-plastic analysis, which requires knowledge and modelling of the post-yield non-linear material behaviour. However, the method has limited application to this type of geometry. Although estimated elastic-plastic buckling and collapse pressures are below the upper bound estimates, the lower bound estimates are higher than the pressure at which first yield occurs.

7. Finite element analysis can be used successfully to model the back-extrusion process and good comparisons between predicted and experimental data have been demonstrated. The effects of the choice of coefficient of friction and boundary conditions on the extruded profile have been investigated and it appears that the best correlation between experiment and prediction is achieved with a low coefficient of friction being used.

8. In all cases, an accurate model for the non-linear material behaviour is necessary. It has been noted that strain rate variations and elevated temperature may affect the

stress-strain characteristics and lead to variations in material properties across the section.

9. Material optimisation is an important consideration for the manufacturer. However, design constraints limit what can be achieved. The preliminary optimisation study has highlighted both the opportunity for reduced material and the complexities of using a structured approach.

8.2 Recommendations for further work

A number of recommendations for further investigation are drawn from the research:

1. Further studies of the extrusion process are needed in order to identify why the length of the plain cylinder is under-predicted.

2. Stage 2 of the extrusion process should be investigated further (and modelled more accurately) to understand the differences between the experimental results and finite element predictions of load-displacement for the punch.

3. A detailed investigation into shape optimisation is required where further thought and detailed analysis is given to the choice of objective function and constraints. Also the choice of element type and number of elements should be reviewed.

4. The spatial variation in material properties, due to strain rate and temperature effects, may be significant and require further investigation.

5. Finally, there are areas outside the scope of this study, which should be addressed. For example, such components are subjected to radial loading during packaging into bundles. Radial buckling is a possible failure mechanism that needs to be considered, particularly if material optimisation is considered.

REFERENCES

1 **htt://www.cancentral.com** - Can Central is the web site of the Can Manufacturers Institute.

2 **Patten, S.** design and optimisation of aluminium aerosol cans produced by a back extrusion process MSc Thesis, University of Wales Swansea, 2001

3 British Standard Institution **BS5500**; Specification for Unified Fusion Welded Pressure Vessels 1991

4 American Society of Mechanical Engineers, **ASME** Boiler and Pressure Vessel Code, 1991

5 **ELFEN** User Manual Version 3.0.4, 2001, Rockfield Software, Swansea, UK

6 **http://science.howstuffworks.com/aerosol-can.htm**

7 **Cheers, C. F.** Design and optimisation of an ultrasonic for forming metal cans PhD. Thesis, University of Loughborough Leicestershire UK 1995

8 **http://www.yorks.karoo.net/aerosol/link3.htm**

9 **Timoshenko, S. P.** and **Gere, J. M** Theory of elastic stability McGraw-Hill, New York 1961

10 **NAFEMS-** Finite element primer, NAFEMS, 1992

11 **Prinja, N.** and **Clegg. R.** Non linear behaviour of 3-D beams and shells shells NAFEMS BENCHMARK 1993

12 **Zienkiewicz, O. C.** The finite element method, McGraw -Hill, 1984

13 **Prandtl, L.** Spannungsvert eilung in plastischen koerpern proc Of the Ist Int. congress on App.Mech., Delft, Tecnische Boekhandel en Druker, J. Waltman, Jr., 1925, pp 43-54

14 **Reuss, E.** Beruecksichtigung der elastischen formaenderon in der plastizifacts theorie Z. Angew. Math. Mech, 1930, Vol. 10, pp. 266-274

15 **Valliappan, S.** Continum Mechanics Fundemantals, Rotterdam 1981

16 **Owen, D. R. and Hinton, E.** Finite element in plasticity theory and practice pineridge press Lid. 1980

17 **Owen, D. R.** and **Hinton, J. E.** NAFEMS- Introduction to Non-linear finite element analysis, NAFEMS, 1992

18 **Ryder, G. H.** Strength of Materials 1969

19 **Bushnell, D**. Computerized buckling analysis of shell Martinus Nijhoff Publishers 1985

20 **Brush, D. O.** Buckling of bars, plates, and shells 1975

21 **Farshad, M**. Designed and analysis of shell structures Kluwer Academic Publisher 1992

22 **Flugge, W.** Stresses in shells, 2nd Edn., Springer, Berlin, 1973

23 **Karman, T.** and **Tsien, H.** The buckling of thin cylindrical shells under axial compression, J. Aeronout. Sci., 1941, Vol. 8, pp. 303-312

24 **Robotham, W.S., Hyde, T. H. and Williams, E. J**. Finite element torsional buckling analysis and prediction for plain shafts MPSVA 5th

25 **Robotham, W. S.** The elastic-plastic buckling behaviour of shafts PhD. Thesis, University of Nottingham 2000

26 **Rik's, E.** An Incremental Approach to the Solution of snapping and Buckling Problem, Int. J. Solid Structures, 1979, 15,7, pp. 529-551

27 **Mendleson, A.** Plasticity Theory and Application 1968 (Macmillan, London)

28 **Berak, E. G.** and **Gerdeen, J. C.** Finite element technique for limit analysis of structure. Trans. ASME, J. Pressure Vessel Technol, 1990, 112, 138, 144

29 **Dhalla, A. K.** Verification of an elastic procedure to estimate follow-up. In design of elevated temperature piping (Eds R.H. Mallet and R.M. Mello). 1984, pp. 81-96 (American Society of Mechanical Engineers New York)

30 **Marriot, D. L**. Evaluation of Deformation or Load Control of Stresses under Inelastic Conditions using Elastic Finite Element Stress Analysis. In Proceedings of the Pressure Vessel and Piping Conference, Pittsburgh, Pennsylvania, 1988, PVP-Vol. 136 (American Society of Mechanical Engineers, New York

31 **Mackenzie, D** and **Boyle, J.T.** A method of estimating limit loads by iterative elastic analysis. I: simple examples. Int. J Pressure Vessel and piping, 1993, 53, 77, 95

32 **Mackenzie, D., Nadarajah, C., Shi, J. and Boyle, J.T.** Simple bound on limit load by elastic finite element analysis. Trans. ASME, J. Pressure Vessel Technol., 1993, 115,27-31

33 **Gowhari-Anaraki, A. R.** and **Adibi-Asl, R.** Estimation of Upper and Lower bound limit loads and shakedown load for structural frames based on reduced modulus approach. In Proceeding of the 6th International Conference on Civil Engineering Isfahan, Iran, 2003, 399-406

34 **Hardy, S. J., Gowhari-Anaraki, A. R.,** and **Pipelzadeh, M. K.** Upper and Lower bound limit and shakedown loads for hollow tubes with exisymmetric internal projrctions under axial loading. J. Strain Analysis, 2001, 36(6), 595-604

35 **Seshadri, R.** and **Kizhatil, R.K.** Inelastic analysis of pressure components using the `GLOSS` diagram. Proc. ASME, 1990, pp. 186

36 **Sheppard, T.** Extrusion of Aluminium Alloys, Kluwer Academic Publisher 1999

37 **Htenger, H.** Extrusion Process, Machinery, Tooling 1981

38 **Kobayashi, S.** and **Altan. T** Metal forming and the finite element method 1989

39 **Joeri, l.** Developments in finite element simulations of aluminium extrusion. PhD. Thesis, University of Twente 2000

40 **Joachim. D.** Backward can extrusion, PhD. Thesis, University of Aalborg Denmark 2005

41 **Blazynski, T. Z.** Metal forming Tool profiles and flow 1979

42 **GAO, C.** and **FANG. Y.** Investigation on the factors influencing the thickness distribution of super- plastic-formed components. Journal of Zhejiang University Science, 2005, Vol. 6A (7), PP. 711-715

43 **Zienkiewicz, O. C.** and **Godbolet, P. O.** Flow of plastic and visco-plastic solids with special refernce to extrusion and forming process.

International Journal for Numerical Methods in Engineering, 8-16, 1974

44 **Mattiasson, K.** and **Strange. A.** Simulation of spring-back in sheet metal forming NUMIFORM, 1995, PP. 115-124

45 **Akbari, R., Hardy, S. J., Kadkhodayan, M.,** and **Pipelzadeh, M. K.** Simulation of spring back in 2-D draw bending, 2001

46 **Mercer, C., Nagtegaal, J.,** and **Rebelo, N.** Effective application of different solver to formings NUMIFORM 1995, PP. 469-474

47 **Joannic, D** and **Gelin, J.** Accurate simulation of sprinback in 3-D sheet metal forming process. NUMIFORM 1995, PP. 729-734

48 **Narasimhan, N.** Predicting springback in sheet metal forming an implicit and explicit sequential solution proceder, Finite element in analysis and design, 1999, Vol. 33, pp. 29-42

49 **Arwidson, C.** Numerical simulation of sheet metal forming for high strength steels PhD. Thesis, University of Lulea Sweden 2005

50 **Hinton, E. S.** and **Özakca, M.** Analysis and Optimisation of Prismatic and Axisymmetric Shell Structures UK 2003

51 **Sodeik, M.** and **Sauer. R.** Mechanical behaviour of food cans under radial and axial load. 3rd international tinplate conference London, 1984, paper 11

52 **Jing, H. R.** Application of structure optimisation technique to aluminium beverage bottle design, 4th Congress on structural and Multidisciplinary optimisation, 2003, PP. 103-105

53 **Iestyn, B. J.** Computational strategies for design optimisation of food cans, PhD, Thesis, University of Wales Swansea, 1999

54 **Davis, J. R.** Aluminium &Aluminium Alloys, ASME International, 1993

55 **Chilver, L. C** and **Rose, C. T.** Strength of materials and structures, Edward Arnold 1993

56 **Auto CAD** User Manual Version, 2002

57 **Dr Elias, L.** Envases (UK) Ltd, January 2006

58 **DOT** User Manual Version 4.20, Vanderplaats Research and Development, Inc Colorado Springs, 1995

Appendix A

DRAWING OF EXTRUSION TOOLING

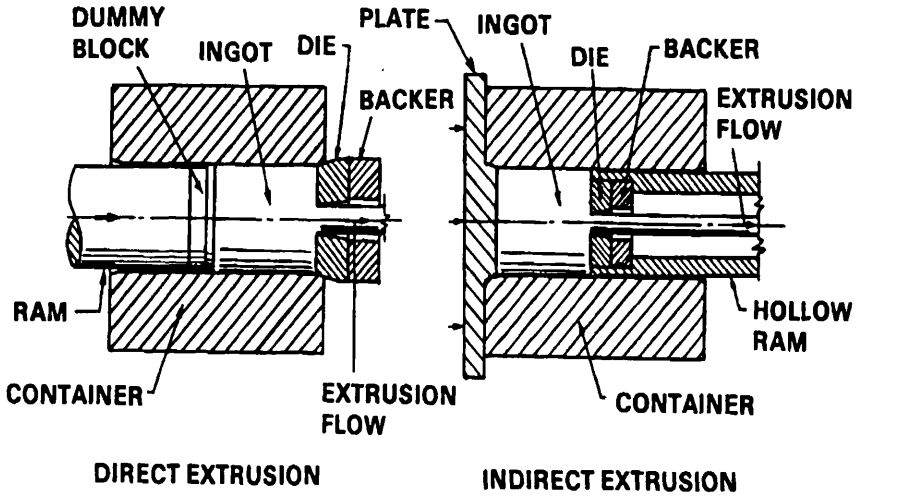

Figure 1: Tooling and metal flow for direct and indirect extrusion process [41]

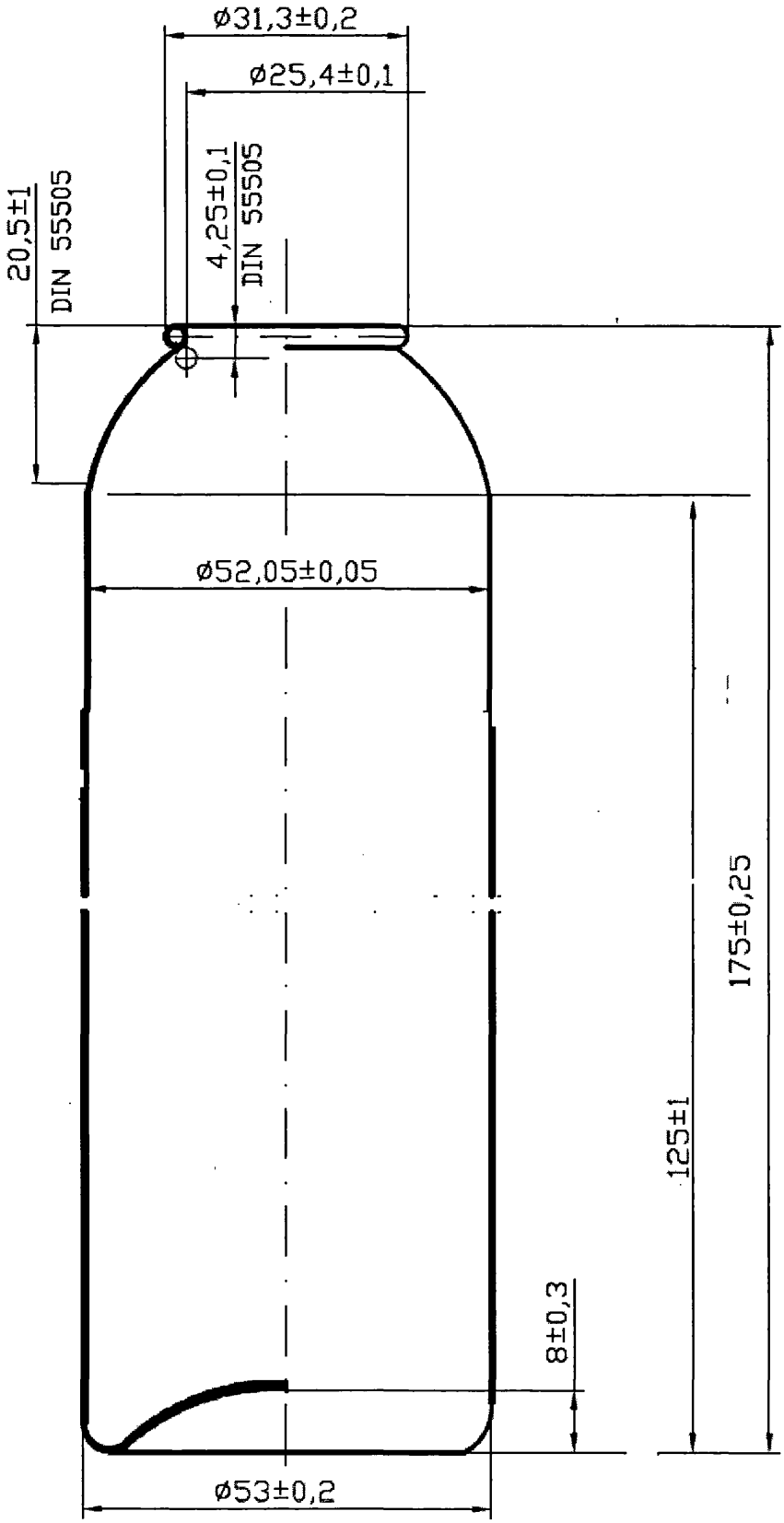

Figure 3: Aerosol can dimension

Appendix B

PROPERTIES OF ALUMINIUM FOR IMPACT EXTRUSION

In order to calculate the strength of the extruded cans and the required thickness of the can walls, the following mechanical properties are required:

- Ultimate Tensile Strength (UTS)
- Yield Strength

Knowledge of the UTS will be used to predict the burst pressure of the cans and the yield strength used to predict the deformation pressure. Both these properties will then determine the required can wall thickness and therefore the cost of each can.
For commercial aluminium, the yield strength is not always a clearly defined point. For this reason, most textbooks refer to percentage proof strains of aluminium rather than yield strengths.

The mechanical properties of aluminium from different manufacturers can vary by large amounts. This is due to differences in alloy content, grain structure and processing (heat treatment, rolling etc.).
At present, Envases (UK) Ltd. use three types of aluminium to produce extruded aerosol cans. These are summarised in the table below:

Supplier	BS Code	Purity	Si, wt%	Fe, wt%	Hardness (Brunell)
Alucenca	1080	99.8	0.076	0.203	16-19
Hydroslug	1070	99.7	0.076	0.127	18-20
Inespal					
Rhienfelden	1050	99.5	0.064	0.243	20-21

The following additional data is assumed about all three types:

Density	$\rho = 2700 Kg / m^3$
Poisson's Ratio	$\upsilon = 0.33$
Cost	£6700 per m^3 (£2.50 per kg)
Thermal Conductivity	$K = 230$ W/m°C
Coefficient of Linear Expansion	$\alpha = 24x10^{-6}$
Young's Modulus	$E = 68.3x10^9$ N/m^2

Chemical Properties

Alloy	Si	Fe	Cu	Mn	Mg	Zn	Ga	Ti	%Pure
1080	0.15	0.15	0.03	0.02	0.02	0.06	0.03	0.02	99.80
1070	0.2	0.25	0.03	0.03	0.03	0.07	----	0.03	99.70
1050	0.25	0.4	0.05	0.05	0.05	0.07	----	0.05	99.50

Manufacturing Processes

Process	**Rhienfelden**	**Alucenca**
1	Melting	Melting
2	Rotary Strip Casting	Rotary Strip Casting
3	Hot Rolling (≈400°C)	Hot Rolling (≈400°C)
4	In line cooling and lubrication	Cooling
5	Cold Rolling (≈60°C)	Coiling
6	Shear	Cool for 48 Hrs Minimum
7	Coil	De-coil
8	Cool for 48 Hrs Minimum	Cold Rolling (≈R.T.)
9	De-Coil	Coil
10	Blank	De-coil
11	Wash	Blank
12	Anneal (500-520°C)	Wash
13	Tumble	Anneal (420-450°C)
14	Pack	Tumble
15		Pack

Appendix C

SIMPLE FORTRAN PROGRAM USING TO CALCULATE YOUNG'S MODULUS (E) AT EACH ITERATION

```
C     PROGRAM ECM
      INTEGER NNODE(8),NELEMENTS,NELEM,IBLANK,NEL
      REAL  EFSTRS(8),ENEW(296),EFFMAX,SIGY,SIGMAD
      NELEMENTS=296
      OPEN(1,FILE='ecm296tempdat.dat',STATUS='OLD')
      DO J=1,NELEMENTS
      READ(1,'(F4.1)') ENEW(J)
      PRINT'(E10.4)', ENEW(J)
      ENDDO
      SIGY=100.0
      SIGMAD=0.0
      DO K=1,NELEMENTS
      EFFMAX=0.0
      DO I=1,8
      READ(1,'(21X,I3)') NELEM
      READ(1,'(I1)') IBLANK
      READ(1,'(91X,F10.5)') EFSTRS(I)
      READ(1,'(I1)') IBLANK
      PRINT*, I
      IF(EFSTRS(I).GT.EFFMAX) THEN
      EFFMAX=EFSTRS(I)
      ELSE
      ENDIF
      ENDDO
      IF(EFFMAX.GT.SIGMAD)THEN
      SIGMAD=EFFMAX
      NEL=K
      ELSE
```

```
ENDIF
PRINT*, EFFMAX
ENEW(K)=2*ENEW(K)*SIGY/(3*EFFMAX)
PRINT*,  ENEW(K)
ENDDO
DO K=1,NELEMENTS
WRITE(1,'(E10.4)') ENEW(K)
 ENDDO
WRITE(1,'(A,F10.5,A,I3)')'SIGMAD = ',SIGMAD,'IN ELEMENT  ',NEL
CLOSE(1)
END PROGRAM ECM
```

```
C    SIMPLE PROGRAM FOR CAN THICKNESS OPTIMISATION

      DIMENSION  X(7),XL(7),XU(7),G(7),SIG(7)
      DIMENSION WK(800),IWK(200),RPRM(20),IPRM(20)

      NRWK=800
      NRIWK=200
      DO 10 I=1,20
      RPRM=1
10    IPRM=1
C     TRY SQP METHOD
      METHOD=3
      NDV=7
      NCON=7
C     INTIAL THICKNESS VALUES
      X(1)=1.25
      X(2)=1.12
      X(3)=1.34
      X(4)=0.71
      X(5)=0.62
      X(6)=0.31
      DO 20 I=1,NDV
      XL(I)=0.0
20    XU(I)=20.0

      SIG(1)=10.766
      SIG(2)=6.641
      SIG(3)=20.648
      SIG(4)=8.265
      SIG(5)=27.078
      SIG(6)=25.035
      SIGMAY=100
      IPRINT=1
```

```
      MINMAX=-1
      INFO=0
  100 CALL DOT (INFO, METHOD, IPRINT, NDV, NCON, X,XL,XU
     *      OBJ, MINMAX, G,RPRM,IPRM,WK,NRWK,IWK,NRIWK)
      IF(INFO.EQ.0)STOP
      call system ("./elfendyn elastic3t 40");
      CALL EVAL (OBJ,X,G)
      GO TO 100
      END
      SUBROUTINE EVAL(OBJ,X,G)
      DIMENSION X(*),G(*)
      OBJ=X(1)+X(2)+X(3)+X(4)+X(5)+X(6)
      DO 30 I = 1,
   30 G(I)=1-SIG(I)/SIGMA
      RETURN
      END
```